REPORT DOCUMENTATION PAGE

Public reporting burden for this collection of information is estimated to average 1 hour per response, including the time for reviewing instructions, searching existing data sources, gathering and maintaining the data needed, and completing and reviewing the collection of information. Send comments regarding this burden estimate or any other aspect of this collection of information, including suggestions for reducing this burden, to Washington Headquarters Services, Directorate for Information Operations and Reports, 1215 Jefferson Davis Highway, Suite 1204, Arlington, VA 22202-4302, and to the Office of Management and Budget, Paperwork Reduction Project (0704-0188), Washington, DC 20503.

1. AGENCY USE ONLY (Leave blank)	2. REPORT DATE 16 Dec 95	3. REPORT TYPE AND DATES COVERED

4. TITLE AND SUBTITLE
Dffects of Confinement on the Failure Mechanism in Cementitious Materials

5. FUNDING NUMBERS

6. AUTHOR(S)

Craig Ashton Rutland

7. PERFORMING ORGANIZATION NAME(S) AND ADDRESS(ES)

AFIT Student Attending:

University of New Mexico

8. PERFORMING ORGANIZATION REPORT NUMBER

96-020D

9. SPONSORING/MONITORING AGENCY NAME(S) AND ADDRESS(ES)

DEPARTMENT OF THE AIR FORCE
AFIT/CI
2950 P STEET, BLDG 125
WRIGHT-PATTERSON AFB OH 45433-7765

10. SPONSORING/MONITORING AGENCY REPORT NUMBER

11. SUPPLEMENTARY NOTES

12a. DISTRIBUTION/AVAILABILITY STATEMENT

Approved for Public Release IAW 190-1
Distribution Unlimited
BRIAN D. GAUTHIER, MSgt, USAF
Chief Administration

12b. DISTRIBUTION CODE

13. ABSTRACT (Maximum 200 words)

19960809 057

14. SUBJECT TERMS			15. NUMBER OF PAGES SB-19
			16. PRICE CODE

17. SECURITY CLASSIFICATION OF REPORT	18. SECURITY CLASSIFICATION OF THIS PAGE	19. SECURITY CLASSIFICATION OF ABSTRACT	20. LIMITATION OF ABSTRACT

DTIC QUALITY INSPECTED 1

Block 1. Agency Use Only (Leave blank).

Block 2. Report Date. Full publication date including day, month, and year, if available (e.g. 1 Jan 88). Must cite at least the year.

Block 3. Type of Report and Dates Covered. State whether report is interim, final, etc. If applicable, enter inclusive report dates (e.g. 10 Jun 87 - 30 Jun 88).

Block 4. Title and Subtitle. A title is taken from the part of the report that provides the most meaningful and complete information. When a report is prepared in more than one volume, repeat the primary title, add volume number, and include subtitle for the specific volume. On classified documents enter the title classification in parentheses.

Block 5. Funding Numbers. To include contract and grant numbers; may include program element number(s), project number(s), task number(s), and work unit number(s). Use the following labels:

C	-	Contract	PR	-	Project
G	-	Grant	TA	-	Task
PE	-	Program Element	WU	-	Work Unit Accession No.

Block 6. Author(s). Name(s) of person(s) responsible for writing the report, performing the research, or credited with the content of the report. If editor or compiler, this should follow the name(s).

Block 7. Performing Organization Name(s) and Address(es). Self-explanatory.

Block 8. Performing Organization Report Number. Enter the unique alphanumeric report number(s) assigned by the organization performing the report.

Block 9. Sponsoring/Monitoring Agency Name(s) and Address(es). Self-explanatory.

Block 10. Sponsoring/Monitoring Agency Report Number. (If known)

Block 11. Supplementary Notes. Enter information not included elsewhere such as: Prepared in cooperation with...; Trans. of...; To be published in.... When a report is revised, include a statement whether the new report supersedes or supplements the older report.

Block 12a. Distribution/Availability Statement. Denotes public availability or limitations. Cite any availability to the public. Enter additional limitations or special markings in all capitals (e.g. NOFORN, REL, ITAR).

DOD	-	See DoDD 5230.24, "Distribution Statements on Technical Documents."
DOE	-	See authorities.
NASA	-	See Handbook NHB 2200.2.
NTIS	-	Leave blank.

Block 12b. Distribution Code.

DOD	-	Leave blank.
DOE	-	Enter DOE distribution categories from the Standard Distribution for Unclassified Scientific and Technical Reports.
NASA	-	Leave blank.
NTIS	-	Leave blank.

Block 13. Abstract. Include a brief (Maximum 200 words) factual summary of the most significant information contained in the report.

Block 14. Subject Terms. Keywords or phrases identifying major subjects in the report.

Block 15. Number of Pages. Enter the total number of pages.

Block 16. Price Code. Enter appropriate price code (NTIS only).

Blocks 17. - 19. Security Classifications. Self-explanatory. Enter U.S. Security Classification in accordance with U.S. Security Regulations (i.e., UNCLASSIFIED). If form contains classified information, stamp classification on the top and bottom of the page.

Block 20. Limitation of Abstract. This block must be completed to assign a limitation to the abstract. Enter either UL (unlimited) or SAR (same as report). An entry in this block is necessary if the abstract is to be limited. If blank, the abstract is assumed to be unlimited.

Craig Ashton Rutland

Candidate

Department of Civil Engineering
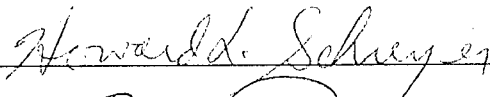
Department

This dissertation is approved, and it is acceptable in quality
and form for publication on microfilm:
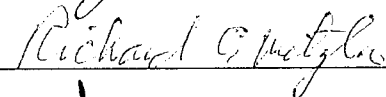
Approved by the Dissertation Committee:
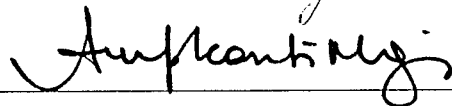
_____ , Chairperson

_____

_____

_____

_____

_____

_____
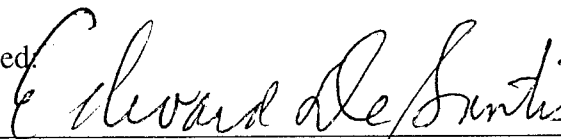
Accepted _____

Dean, Graduate School

DEC 16 1995

Date

EFFECTS OF CONFINEMENT ON THE FAILURE

MECHANISM IN CEMENTITIOUS MATERIALS

BY

CRAIG ASHTON RUTLAND

B.S., University of Illinois, Urbana, 1985

M.S., University of Illinois, Urbana, 1986

DISSERTATION

Submitted in Partial Fulfillment of the
Requirements for the Degree of

Doctor of Philosophy in Engineering

The University of New Mexico
Albuquerque, New Mexico
December 1995

ACKNOWLEDGEMENTS

EFFECTS OF CONFINEMENT ON THE FAILURE

MECHANISM IN CEMENTITIOUS MATERIALS

BY

CRAIG ASHTON RUTLAND

ABSTRACT OF DISSERTATION

Submitted in Partial Fulfillment of the
Requirements for the Degree of

Doctor of Philosophy in Engineering

The University of New Mexico
Albuquerque, New Mexico
December 1995

EFFECTS OF CONFINEMENT ON THE FAILURE
MECHANISM IN CEMENTITIOUS MATERIALS

CRAIG ASHTON RUTLAND

B.S. Civil Engineering, University of Illinois, Urbana, 1985

M.S. Civil Engineering, University of Illinois, Urbana, 1986

Ph.D. Civil Engineering, University of New Mexico, 1995

In this study it is shown that there is a change in the orientation of the failure plane of cementitious materials as confinement increases. It is also found that localized macroscopic behavior begins at or near the peak stress. The implications of this and the stress-strain data on the constitutive model are discussed. Necessary conditions for the prediction of a change in the angle of the failure plane with increasing confining pressure are developed. Conflicting data on the failure mechanism and specifically the orientation of the failure plane under triaxial compression provided the impetus for this study.

An examination of several different methods of relieving friction between the platens and specimens is performed. A new type of specimen is developed using ceramic rods as aggregates to produce a two dimensional specimen. These specimens were tested in biaxial compression and are compared to standard specimens tested in triaxial compression. In addition, a new method for determining strains from the changes in X-ray intensity is developed as part of this study.

TABLE OF CONTENTS

LIST OF FIGURES

LIST OF TABLES

1.0 INTRODUCTION

Triaxial tests on rocks performed by Dunn et al [1973], Wawersik and Brace [1971], and Heard [1966] have shown that at high confining pressures the angle of the failure plane changes with confining pressure for geologic materials. At present there are no data for concrete that relates the confinement to the change in the angle of the principal failure plane at low confining pressures. However, tests by Mills [1967], Zimmerman [1972], and Richart et al. [1928] provide evidence and a concept of failure in which cementitious materials will always fail in a direction parallel to the maximum compressive stress.

Palaniswamy and Shah [1972] commenting on triaxial tests on hardened cement paste state that *"Two distinctly different modes of behavior were observed. For relatively low pressures, the failure was preceded by large strains and the specimen split into several pieces. In contrast, for high lateral pressures, the specimens remained intact, the strains at failure were smaller and crushing and crumbling was evident."* Palaniswamy and Shah [1974] state the same for triaxial tests on mortar and concrete. Balmer [1949] tested oven dried specimens to lateral pressures of 25 ksi with relief of the platen-specimen friction. He states that the Mohr envelope is curved and noted that the angle of the failure plane must change with increasing confining pressure; however, his attempts to measure the angle of the failure plane were thwarted by the presence of cones at the ends of the specimens. These cones were a result of the friction between the platens and specimens.

In this study it is shown that there is a change in the orientation of the failure plane as confinement increases. It is also found that localized macroscopic behavior begins at or near the peak load. The implications of this and the stress-strain data on the constitutive model are discussed. Necessary conditions for the prediction of changing failure angle with increasing confinement are presented in the context of constitutive modeling. Furthermore, it is shown that if the ratios of the eigenvalues of a plastic deformation tensor in a simple plasticity model vary with confining pressure, then the orientation of the failure plane will change with confining pressure. With guidance from experimental data a simple plasticity model is developed that captures the primary feature of the observed change in the failure angle.

A new method for determining strains from the changes in X-ray intensity has been developed as part of this study. In addition, a new type of specimen is developed using ceramic rods as aggregates to produce a two dimensional specimen. These specimens are tested in biaxial compression to compare with standard specimens tested in triaxial compression.

In summary, this study provides a quantitative analysis of the effects of confinement on the failure plane of cementitious materials under quasi-static compressive loads. Emphasis was placed on the relationship of the angle of the failure plane and the confining pressure at pressures between 0 and 8000 psi.

2.0 BACKGROUND

At this point it is necessary to review relevant information about the behavior and modeling of cementitious materials.

Cementitious materials are characterized as being heterogeneous, multi-phase, and quasi-brittle. Cementitious materials are usually made up of aggregates bound together by a pozzolanic binder which usually contains air voids. While such a material is heterogeneous locally, there is some scale at which this material is homogeneous globally. Although cementitious materials fail by developing cracks, classical fracture mechanics cannot explain entirely the global behavior.

2.10 BEHAVIOR

The behavior of cementitious materials is usually described and studied on three different scales: macro, meso, and micro. The macroscopic behavior of the cementitious materials describes the response of the material as a continuum. Therefore, the characteristic length is several times larger than the largest aggregate. For most concretes this length is greater than 3 inches. Behavior at this scale is often described using strength characteristics such as maximum and critical average stress, average stress-strain curves, modulus, angle of the failure plane, etc.

The description of the response at the mesoscopic scale centers on the interactions of the material constituents, usually at the interfaces. For example, the interaction between the cement matrix and the aggregate in concretes usually occurs on a mesoscopic scale. The behavior at this level is described by the initiation and propagation of cracks (debonding) and the mode of fracture. The characteristic length of the mesoscopic scale ranges from 10^{-2} to 1 inch depending on the size of the aggregate.

Microscopic behavior is described by the physical and chemical processes of the material. The characteristic length of this scale is less than 10^{-3} inches. It should be noted that cracks at the meso and microscopic scale are called microcracks.

The general macroscopic behavior of cementitious materials is well documented. Much research has been conducted to examine the factors that affect this macroscopic behavior.

2.11 MACROSCOPIC BEHAVIOR

Figure 2-1 shows the general average stress-strain relationship for typical cementitious materials in uniaxial compression. Such a relationship is usually obtained from uniaxial compression tests, which provide load versus displacement data. The load and the displacement are averaged to obtain the average stress and strain.

When the specimen is initially loaded, the average stress and strain are nearly linearly related up to a point called the proportional limit. This may be as low as 30% of the peak load for uniaxial compression. As the load is increased beyond this point the relationship becomes nonlinear, the modulus will degrade and some permanent deformation will develop (figure 2-2). At a load between 70% and 90% of the maximum this nonlinearity increases rapidly. This point is called the critical stress. The lateral expansion at this point also increases rapidly and the specimen begins to dilate. Further increase in the load leads to a maximum value of load beyond which the material cannot sustain.
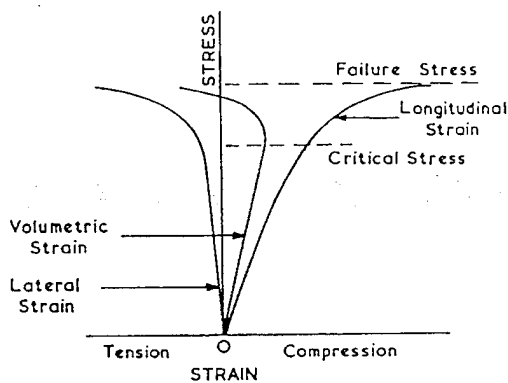
Figure 2-1: Typical Stress-Strain Characteristics under Uniaxial Compression (Schickert [1973])
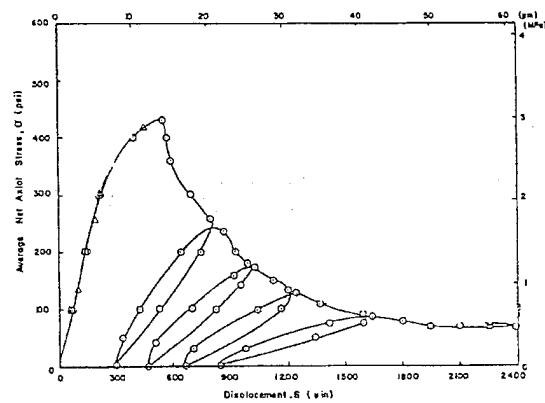
Figure 2-2: Typical Stress-Strain Curve Showing Permanent Deformation and Modulus Degradation (Gopalartnam and Shah [1985])

Usually the tests are either displacement controlled or strain controlled. Displacement controlled unconfined tests often lead to an abrupt or brittle failure with the maximum load being less than for comparable stain controlled tests. Such behavior suggests that the loading device is not stiff enough. Glucklich [1965] placed a spring between a specimen and loading platen and found that the compressive strength was as low as 35% of that obtained without the spring. If the tests are strain controlled or displacement controlled on a sufficiently stiff loading device, additional post-peak behavior can be obtained. This descending portion of the average stress-strain curve is often called softening.

There is debate over the actual cause of softening. Some evidence from tests suggests it may be a material phenomenon, a manifestation of the loading conditions, a result of distributed cracking, or a consequence of

localized strains. Van Mier [1984] has conducted several experiments where the post-peak average stress-strain relation changed as the slenderness of the specimens was increased. Shah and Sankar [1987] found similarly that a different post-peak relation was obtained when using different gauge lengths. Kotsovos [1983] found that the post peak behavior varied with different methods of load application and specifically for different types of friction relief, for example, steel platens, brush platens, steel platens with aluminum sheets and grease. Material softening alone will not predict this. The theory of localized strains provides a possible explanation for this phenomenon.

With the theory of localization there exists a zone where the strains are increasing faster than in the rest of the material. The strains outside of this zone may even decrease as strains increase in the zone. Such a zone is often described as a band where inhomogeneous deformations can occur in a uniformly loaded, initially homogeneous material. Shah and Sankar [1987] suggest that confinement produced by the loading device may cause the unconfined central portion of a specimen to deform more than the confined ends. Figure 2-3a shows that the axial distribution of the lateral deformation for a specimen with no friction relief while 2-3b shows the same data for a test which used 1.5" thick cap blocks to relieve friction. These data suggest that the friction between the specimen and loading device does affect the deformation within the specimen and the development of localized behavior. Torrenti et al. [1988] provide some experimental results that suggest the presence of a zone of localized shear near the peak stress in compressive tests. Dunn et al. [1973] has shown that sandstone has a finite zone over which the principal failure takes place.

(a) No Friction Relief   (b) Cap Blocks for Relief
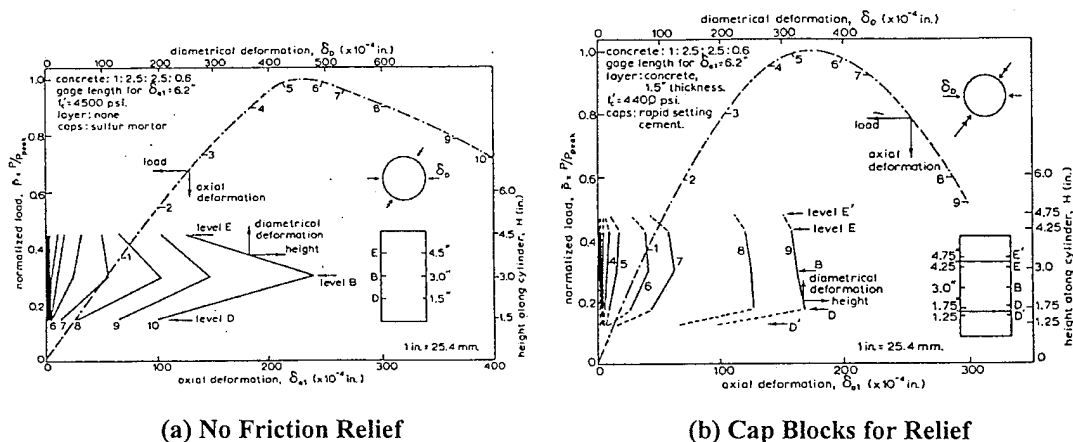
Figure 2-3: Load versus Axial and Diametrical Deformation Profile for Concrete
(Shah and Sanker [1987])

At this point it is necessary to explain what is meant by brittle and ductile behavior. In general, most researchers distinguish between the two types of behavior by considering the post peak response in the load displacement curve. Brittle behavior is characterized by an abrupt loss of load carrying capacity, which generally produces a sharp peak. Ductile behavior is characterized by a gradual loss of load carrying capacity,

which generally produces a rounded peak. Since each persons' definition of gradual is different, the author attempts to discuss the behavior in relativistic terms, i.e., more ductile, which means more gradual reduction of load in the post peak.

Some researchers also use the terms brittle and ductile to describe the failure of the material. Brittle failure are characterized by large (long) cracks with sharp edges. Ductile failures are characterized by many small cracks with dull edges. Horii and Nemat-Nasser [1986] state brittle behavior occurs when the growth of the plastic zone in front of a crack is dominated by the growth of the crack. Ductile behavior occurs when the growth of the plastic zone out paces the growth of the crack.

Palaniswamy and Shah [1974] use brittle and ductile to describe the strain at maximum load. They state that a test with a lower strain than another test at the peak load is more brittle than the other test.

If confining pressure on the sample is increased (triaxial tests) the behavior becomes more ductile (figure 2-4). At very high pressures the deviator stress-strain curve will exhibit stress increasing to a plateau or "yielding" stress. As the confinement is increased the initial modulus, determined from the deviator stress-strain curve, also increases. As in many soils, cementitious materials exhibit shear enhanced compaction under triaxial conditions (figure 2-5a). Such behavior is normally associated with granular materials.

Figure 2-4: Deviator Stress versus Axial and Transverse Strain Under Triaxial Compression (Green and Swanson [1973])

Resende [1987] reports that under a pure hydrostatic load the pressure-volumetric strain curve is shown in figure 2-5b. At first the tangent bulk modulus decreases then increases as pressure increases. During unloading the initial unloading bulk modulus is reported to be constant and equal to the initial loading modulus. As the pressure decreases the modulus drops off dramatically. This behavior may be a result of cracks that were formed or may have been caused by viscous effects. Zimmerman [1965] and Chinn and Zimmerman [1965] found that the uniaxial strength decreases when the specimen is subjected to a hydrostatic load and unloaded prior to applying the uniaxial load. They also noted large permanent deformations to the specimens after the application of the hydrostatic load. Zimmerman [1965] found a .56% reduction in the uniaxial strength for every 1000 psi of hydrostatic pressure applied. Thus, under a purely hydrostatic load, damage may occur, but its effects on the modulus may not be immediately

reflected because the confining pressure keeps the voids and cracks closed.
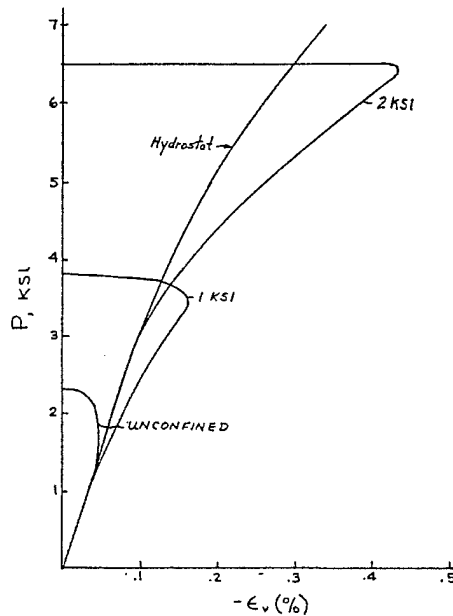
(a) Mean Pressure versus Volumetric Strain
   in Triaxial Compression
   (Green and Swanson [1973])
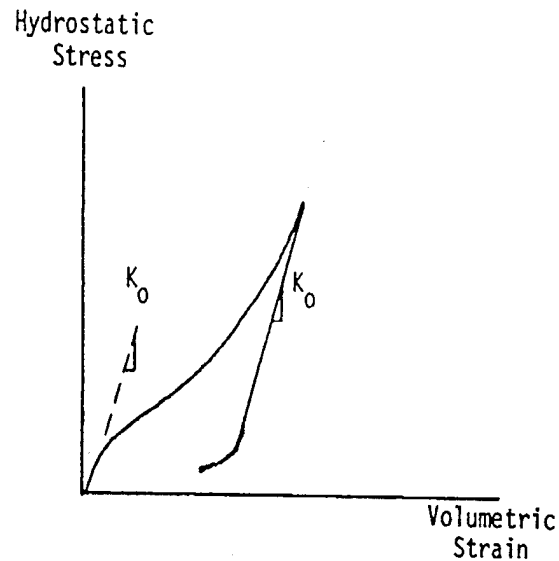
(b) Idealized Pressure versus Volumetric Strain Curve
   (Resende [1987])

Figure 2-5: Hydrostatic Loading

The tensile strength of cementitious materials is only a fraction of their compressive strength. For normal concretes the tensile strength is about one tenth of the compressive strength. Often the tensile strength is taken to be zero in the design of concrete beams. When the tensile strength is used it is usually assumed to be linear elastic to a maximum level at which it fractures. However, carefully designed tests have shown that the shape of the average stress-strain curve for tensile loading is similar to that for compressive loading. Figure 2-6 shows data obtained from a set of tensile tests performed by Evans and Marthe [1968].

The ascending portion of the average tensile stress-strain curve is much more linear than compression of concrete up to a stress, the critical stress, between 70% and 90% of the maximum tensile stress after which the behavior becomes very nonlinear. The initial modulus (computed from the deviator stress-strain curve) of virgin concretes in tension is comparable to that in compression. Evans and Marthe [1968] and Gopalaratnam and Shah [1985] provide evidence that strains localize in tensile tests near the critical stress in the vicinity of the failure plane.
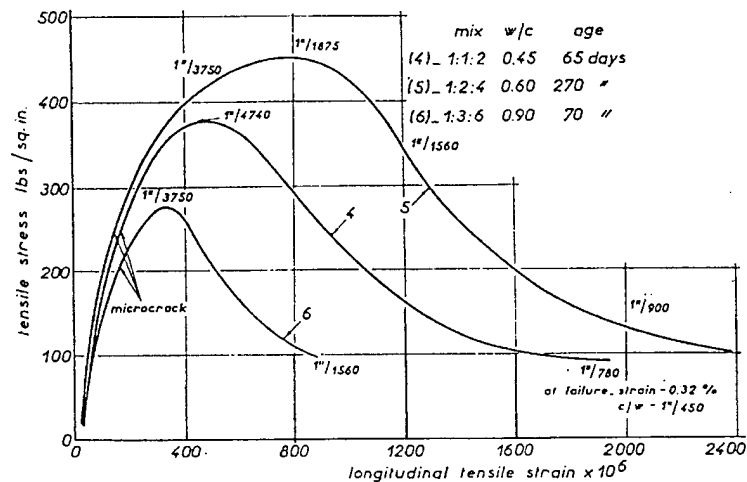
Figure 2-6: **Complete Stress-Strain Curve in Direct Tension (Evans and Marthe [1968])**

Reinhardt and Cornelissen [1984] show that when a cylinder of concrete is cyclically loaded between tension and compression the modulus in compression remained large while the modulus in tension degraded (figure 2-7). This indicates that there is a deactivation of the tensile damage (cracks formed by the tensile loading are closed). They also show that as the maximum compressive stress of the cycle is increased the degradation of the tensile modulus increased. This indicates that the compressive loads may be causing damage perpendicular to the direction of loading or at least enhancing the development of damage which is consistent with the development of cracks parallel to the direction of maximum compression under uniaxial compressive loads.
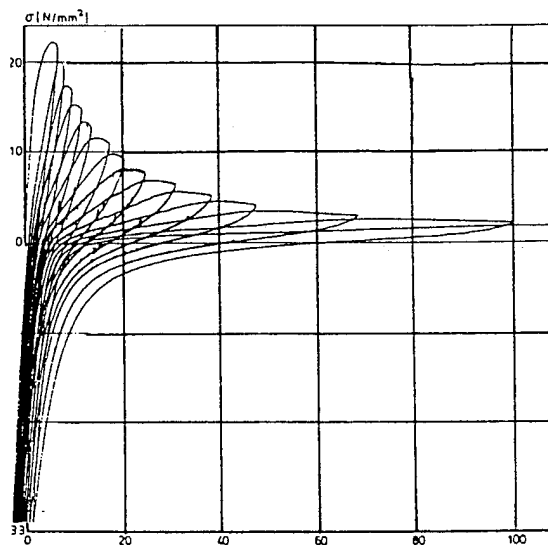
Figure 2-7: Stress Deformation Curve Under Alternating Loads (Reinhardt and Cornelissen [1984])

It is well known that the strength, both tensile and compressive, increases as the strain rate increases. Under long term static loads, the strength of concrete reduces and deflections (strains) increase. This behavior is often called creep. Meyers, Slate, and Winter [1969] studied creep effects in concrete and found that concrete will fail under sustained load (creep) once the rate of load induced (as opposed to pores and shrinkage) mortar crack formation increases significantly. This is typically between 70 and 100% of the peak uniaxial strength under monotonically increasing load. Sustained loads at stresses less than 70% of the peak stress tend to

increase bond cracks. Glucklich [1965] and Shah and Chandra [1970] came to similar conclusions. Tests by Welch [1965] in direct tension and flexure showed similar results.

The average stress-strain curve obtained in compression depends upon the strain gradient in the specimen. Compressive tests performed by Sturman et al. [1965] show that the average stress-strain curve (figure 2-8) changes when the load is applied eccentrically instead of concentrically. The ascending portions of the average stress-strain curves are very similar; however, the peak stress is slightly higher and the strain at failure is much larger for the eccentrically loaded specimen.
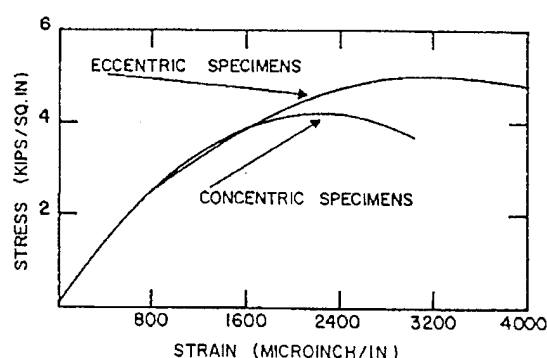
Figure 2-8: Stress-Strain Curves for Eccentric and Concentric Uniaxial Compression (Sturman et al. [1965])

Over the past 50 years the strength and material properties of geotechnical materials have been studied. In particular, the effects of properties such as aggregate size, aggregate shape, aggregate/cement ratio, porosity, etc. on the development of the strength characteristics have been investigated. The geometry of the test samples has been shown to affect the strength characteristics and failure mechanism in concretes. In addition the influences of load path (confinement) on the development of the strength characteristics and failure mechanism have been studied.

2.12 FACTORS INFLUENCING MACROSCOPIC BEHAVIOR

One of the major constituents in concrete is the aggregate. Many researchers have shown that the properties of these aggregates have a large influence on the strength characteristics of concrete. It is well known that the aggregate-cement interface is a source for crack initiation as well as a location of crack arrest. Therefore, it is important to review some of the influences that aggregate properties have on the strength of concrete.

Walker and Bloem [1960] investigated the effects of maximum aggregate size, air entrainment, and aggregate/cement ratio on the compressive, flexural, and tensile strength of concrete. Their study showed that for low aggregate/cement ratios, the compressive strength increases moderately as the aggregate maximum size increases. With higher aggregate/cement ratios the trend is reversed and the compressive strength decreases markedly as the aggregate maximum size increases. The flexural strength followed similar trends but to a far less degree. Similar results were reported by Cordon and Gillespie [1963], Bloem and Gaynor [1963], and Hester [1985].

Kadlecek and Spetla [1967] found that the tensile strength was unaffected by the aggregate top size unless the top-size was greater than one third of the smallest specimen dimension. This provides some indication of the minimum size of the continuum representation. Shah and McGarry [1971] state that the critical stress in tension reduces as maximum size increases.

Kaplan [1959] provides the results of an extensive investigation of the relationship between concrete strength and several aggregate properties. When using aggregates that were stronger than the mortar of concrete, he found no correlation between aggregate strength and concrete strength in compression or flexure. He found that as the aggregate elongation (a measure of shape) increases the flexural strength also increases slightly but the compressive strength does not. Both the flexural and compressive strength increase as the angularity (also a measure of shape) of the aggregate increases. Kaplan [1959] also found that for the most of the aggregates tested, the strength of concrete increases with the roughness of the surface texture of the aggregate.

Kaplan [1959] found a slight increase in the compressive and flexural strength with increasing dynamic modulus of the aggregate. Kaplan [1963] also shows that while changes in the elastic modulus of the aggregate don't influence the strains at the critical or ultimate stresses, they do influence the corresponding stresses for flexure and to a lesser extent, tension. Therefore, an increase in the aggregate modulus produce an increase in the concrete modulus. Hansen [1965] studied the determination of the elastic modulus of concrete based on the moduli of its constituents. Figure 2-9 shows the general trends of the moduli of paste, mortar, concrete, and aggregate.
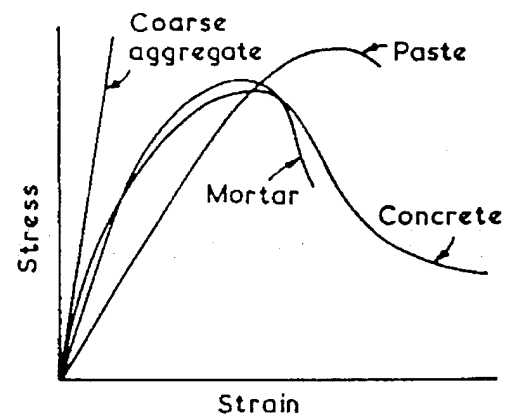
Figure 2-9: Typical Stress-Strain Curves for Concrete and its Constituents (Schickert [1973])

The aggregate/cement ratio is often used in concrete mix. Bloem and Gaynor [1963] report that concrete strength increases with increasing cement content. The effect is most pronounced in the compressive and flexural strength than in the tensile strength. Kaplan [1963] found that the critical and ultimate stresses and strains decrease as the volume of aggregates increases for compression, flexure, and tension.

Pauw [1960] studied the effects of concrete density and strength on the modulus of concrete. He shows that the modulus increases as the density increases. He found empirically that the modulus is directly proportional to the density to the three halves power. These results suggest a relationship between the modulus and the aggregate/cement ratio and the aggregate density. Hansen [1965] obtained similar results.

One way of producing a more dense concrete is to decrease the voids in the cement matrix. Voids in the cement matrix are a natural consequence of the normal preparation of concrete. The volumetric fraction of voids within a specimen is called the porosity. There are five basic types of voids in cement paste, entrapped air, entrained air, capillary pores, "bleeding" pores, and "shrinkage" pores.

Entrapped air is caused by an inadequate mix design in conjunction with improper compaction. These voids have very irregular shapes. In certain circumstances voids can enhance the durability of concretes; therefore, it is sometimes necessary to add chemicals to concrete, which entrain air. Such voids usually have very regular shapes.

Water that is mixed with cement coats and reacts with the many cement particles. As the concrete cures this water is lost and leaves very tiny pores, which are called capillary pores. Sometimes the water that is mixed with the cement begins to collect and migrate upwards. Because migration may be impeded by aggregates in the mix, this water forms lenses, which become voids, or regions of high porosity as the concrete cures. These voids or regions of low porosity below the aggregates create anisotropic behavior.

As the concrete cures the matrix material tends to shrink as it loses water. This produces strains that often exceed the strain capacity of the cement causing cracks to form and open, which are called shrinkage voids.

Popovics [1969] and Hester [1985] studied the influences of porosity on the strength of concrete and concluded that concrete strength decreases with increasing porosity. Kayyali [1989] reports similar results. Tashiro and Urushima [1984] also suggest that the strength increases with a decrease in the size of the maximum pore located in the areas of large tension. Diamond [1985] corroborates this with split tensile tests, which show that pastes always failed at the largest void in the tensile zone. Popovics [1985] provides an empirical equation for the calculation of strength based on porosity.

Roy and Indorn [1985] show that the small pores contribute to the reduction in strength but generally are not a source of failure initiation. Kendall and Birchall [1985] state that the modulus decreases with increasing pore volume; therefore, closure of these voids by confining pressure might be interpreted as "damage deactivation." Dunn et al. [1973] established that the width of the shear zone in sandstone decreases as the porosity decreases. Alford et al. [1982] performed experiments of Micro Defect Free cement, which indicate that the notch sensitivity of a specimen decreases with an increase in the maximum pore size.

Concrete strength increases with decreasing water/cement ratio (w/c). Kaplan [1963] shows that changes in the w/c has little influence on the critical and ultimate strains, but does affect the stresses. Therefore, it follows that the w/c influences the modulus. Tashiro and Urushima [1984] state that the tensile and flexural strengths

are less sensitive to changes in the w/c than the compressive strength. Hester [1985] shows that there is a point at which lowering the w/c decreases the strength. These effects are more pronounced in high strength concretes. Hester also shows that the use of superplasticizers can reduce this sensitivity and increase strength at very low w/c ratios.

Permeability is a measure of the amount and distribution of microcracking and of the pore distribution. In general, permeability increases as porosity increases. Lydon and Mahawish [1989] provide evidence that tensile strength decreases as permeability increases.

The shape and size of test specimens can influence the calculated strength of the concrete. Kaplan [1959] reports that in compression tests on cubes the strength of concrete was less than that of comparable mortars, but, Kaplan [1963] also reports that the reverse was true in similar tests on standard cylinders. Spetla and Kadlecek [1966] studied the effect of slenderness and shape on the tensile strength of concrete. For small slenderness ratios they found that strength decreases rapidly as slenderness increases. At some value of the slenderness this relation changes and there is only a slight decrease with increasing slenderness. They also found that square cross-sections have a higher strength than circular ones of similar slenderness when crushed aggregate is used but when rounded smooth aggregate is used the difference is less than 10%.

Kadlecek and Spetla [1967] also observed that for a given slenderness the tensile strength decreases as the volume of the specimen increases. They also found that the shape of the cross-section had no effect on the strength when comparing specimens of equal volume with large aspect ratios (figure 2-10). Mindess [1984] observed that the fracture energy (the energy required to create one unit of crack area) as determined from flexure tests increases as the size of the beam increases. Such behavior may be a consequence of localization and/or strain gradient effects.
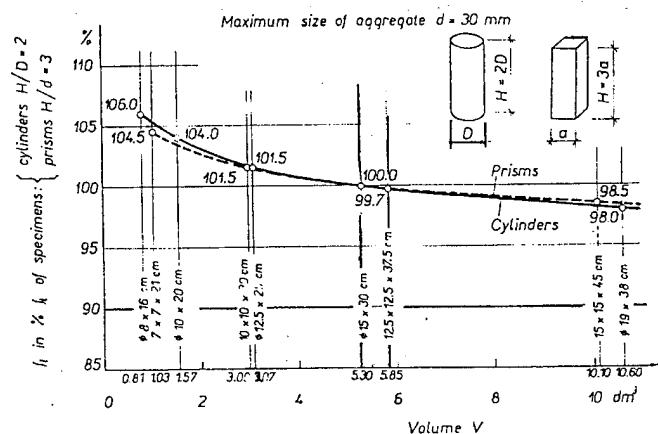
Figure 2-10: Influence of Shape and Volume of Test Specimens on Direct Tensile Strength (Kadlecek and Spetla [1967])

There are extensive data on geotechnical materials indicating a change in the angle of the failure plane under high (> 2000 psi) confining pressures. Tests performed by Dunn et al. [1973] on sandstone, Wawersik and Brace [1971] on Granite and Diabase, Wawersik and Fairhurst [1970] on marble, granite, limestone, basalt,

and slate, Heard [1960] on limestone, dolomite and glass, and Murrell [1965] on sandstone have presented quantitative evidence that there is a change in the angle of the plane of failure with the increase in confining pressure. Specifically, they note that for compression tests the angle of the failure plane with respect to the maximum principal compressive stress increases as confinement increases. These researchers also indicate that macro cracks that make up the failure surface do not appear prior to the peak load.

Horii and Nemat-Nasser [1985] studied the development of cracks and failure in brittle resin specimens with preexisting flaws (cracks). They found that a single preexisting flaw in a barrel shaped specimen would produce unstable crack growth, crack growth under static load, under a uniaxial load (figures 2-11a and b). In contrast they found that a similar crack in a uniaxially loaded bow tie shaped specimen produced stable crack growth, crack growth only under increasing load (figure 2-11b and c). The slight lateral tension produced by loading the barrel shaped specimen, similar to that produced in a split tensile test, promotes unstable crack growth. On the other hand, the slight lateral compression produced in the bow tie shaped specimen tends to inhibit unstable crack growth. They also showed that rectangular resin specimens would produce a failure plane in the direction of maximum compressive stress under uniaxial compression (figure 12a) while producing an angled failure under biaxial compression (figure 12b).

(a) Before Loading   (b) After Loading
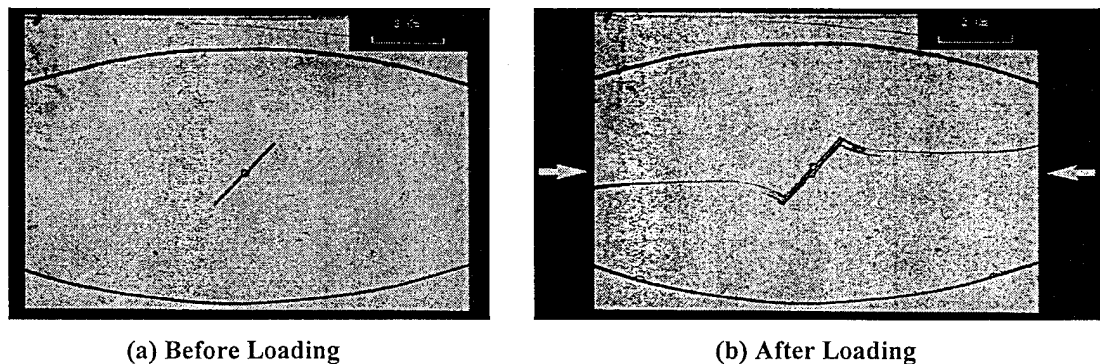
Figure 2-11: Barrel Shaped Resin Specimen with Existing Crack Under Uniaxial Compression
(Horii and Nemat-Nasser [1985])
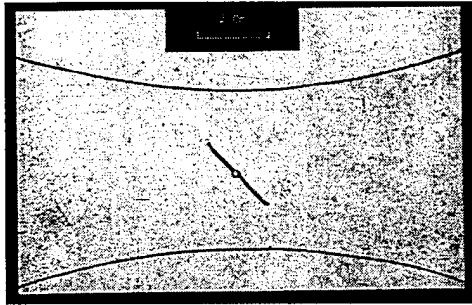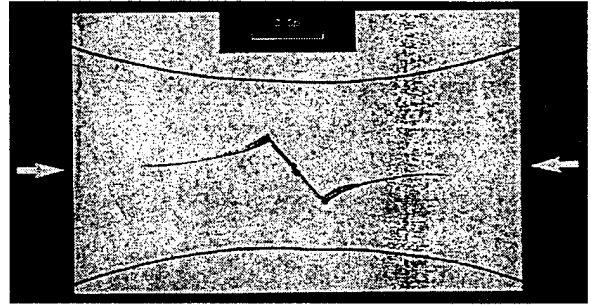
(c) Before Loading   (d) After Loading

Figure 2-11: Bone Shaped Resin Specimen with Existing Crack Under Uniaxial Compression
(Horii and Nemat-Nasser [1985])
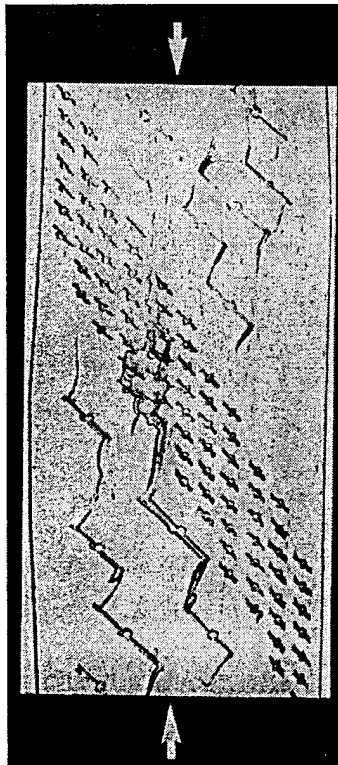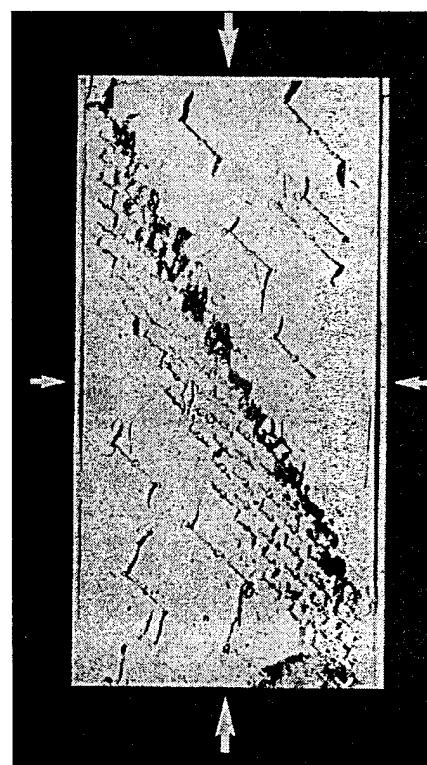
(a) Uniaxial Compression   (b) Biaxial Compression

Figure 2-12: Failure of Brittle Resin Material with Existing Cracks
(Horii and Nemat-Nasser [1985])

Palaniswamy and Shah [1972,1974] state that two distinctly different modes of failure are exhibited by cement paste, mortar, and concrete as confining pressure is increased. Gerstle et al. [1980] performed triaxial tests using various testing machines. Some of these devices applied the lateral confinement via fluid pressure while others used rigid platens. Gerstle et al. [1980] report *"Boundary constraint inhibits transverse specimen deformations, and will therefore result in erroneous material parameters. Unconstrained specimen boundaries are necessary to obtain moduli for prediction of concrete response to general stress states"*. This statement implies that the failure mechanism and the failure plane will be influenced by the method used to apply the lateral loads.

The effects of high confinement on the modulus and "post-peak" behavior was also studied extensively by Mogi [1965, 1966]. He showed that for rocks of differing porosity there was an increase in the modulus as the confining pressure was increased in triaxial compression tests. Furthermore, he noted that the percent increase in the modulus is much larger in the more porous rock than it is in the least porous rocks, which suggests that closure of these pores might be represented as "damage deactivation". He also showed that of the ten types of rocks tested the failure went from brittle to ductile for the most porous materials as the confining pressure was increased. However, the failure remained brittle for the least porous rock as the confining pressure was increased.

Concretes, like rocks, exhibit an increase in the modulus as confining pressure increases. Palaniswamy and Shah [1974] report a decrease in the bulk modulus up to 6000 psi confining pressure then an increase in the bulk modulus for pressures above 6000 psi. This apparent drop in the modulus may have been caused or influenced by the lack friction relief on the ends of the specimen. X-ray tests performed by Wang et al. [1990] show that as a uniaxial load is applied to a specimen the voids close. These same voids begin to reopen after the peak load-deflection curve. The results of these tests suggest that "damage deactivation" may be occurring.

The effects of low confinement have also been investigated. In particular, the effects of end confinement produced by interaction of the test sample with the loading apparatus. Recently these effects have been studied by Kotsovos [1983], Van Mier [1984], Shah and Sankar [1987], Rutland et al. [Appendix A], and Schickert [1973]. Kotsovos shows that for high strength concretes as the end confinement is relieved the post-peak load-displacement response moves from a gradual loss of load carrying capacity to an abrupt loss (figure 2-13). This may be due to the displacement controlled loading or to a loss of structural stability in the cracked specimen. The ascending portion of the load-deflection curve shows a decrease in the modulus and critical to ultimate stress ratio as end confinement decreases. Wang et al. [1990] have noted that as the confinement is relieved the failure plane near the ends of the specimen goes from an angle of about 60 degrees to vertical (figure 2-14).
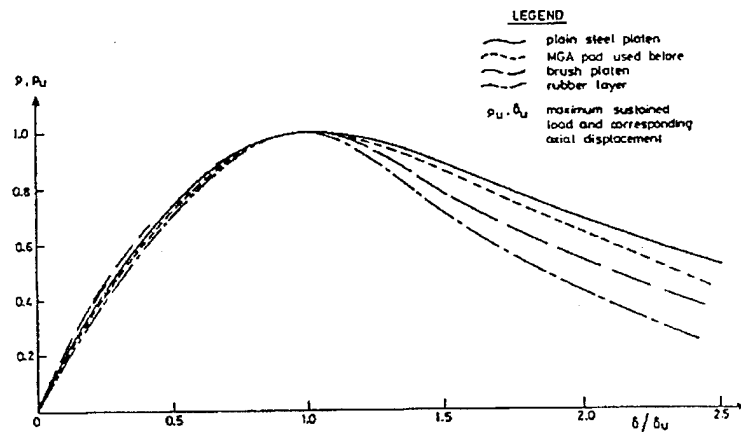
(a) $f_c = 29$ N/mm^2
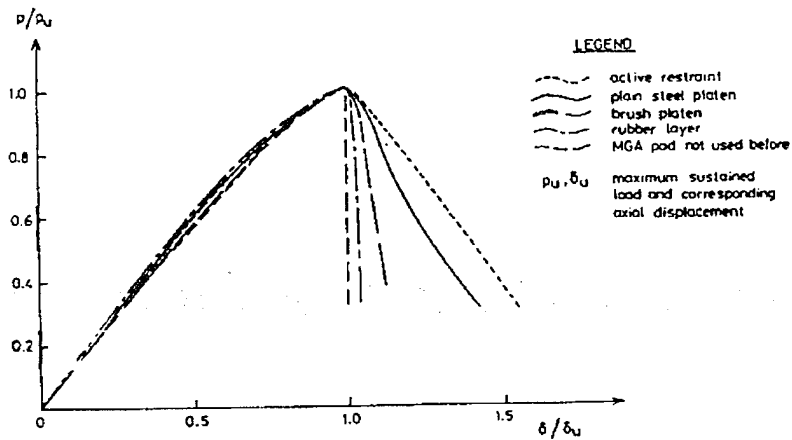
(b) $f_c = 50$ N/mm^2

Figure 2-13: Load-Displacement Relationships Under Various Types of End Restraint
(Kotsovos [1983])

(a)   (b)   (c)   (d)
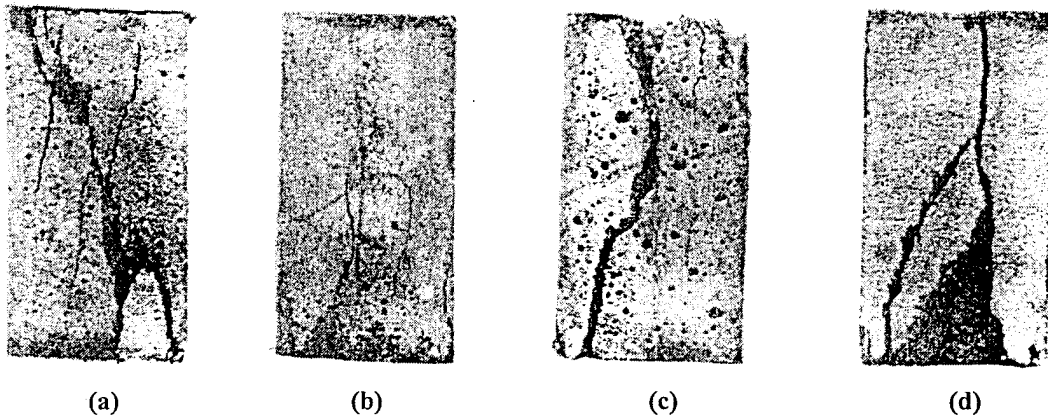
Figure 2-14: Typical Failures of Mortar Under Uniaxial Compression (Wang et al. [1990])
(a) No relief of end friction; (b)-(d) Relief of end friction by aluminum and mylar sheets

Schickert [1973] performed compressive tests using various end conditions on cubic specimens and compared the strains near the ends of the specimens to those at the center of the specimens. For tests where nothing was done to relieve confinement by the platens the ratio of lateral strains near the platens to strains at the center was .25. When aluminum sheets and brush platens were used to relieve confinement this ratio increased to .45 and .5 respectively. Shah and Sankar [1987] found that the most of this confinement could be eliminated by using cement cap blocks cut from the same material as the specimens.

The macroscopic behavior is the global manifestation of the meso and microscopic behavior. The behavior on the mesoscopic scale is best characterized by describing the interaction of the constituents of the concrete. Specifically, the initiation and propagation of cracks along the interfaces is studied. Some of the factors, including some features of the microscopic structure, that influence cracking will be discussed.

2.13 MESOSCOPIC BEHAVIOR

There have been many studies of the relationship between cracking and microcracking of cementitious material and the average stress-strain curve. Such tests usually entail loading a specimen, usually in compression, to a prescribed amount of displacement (strain). Then the specimen is unloaded, impregnated with epoxy, sliced, and viewed under a microscope or X-ray. This is repeated for several different prescribed displacements. The relationship between the amount, type, and location of the cracking can then be associated with various portions of the stress-strain curve. Figure 2-15 provides a view of the general trends found by such tests.
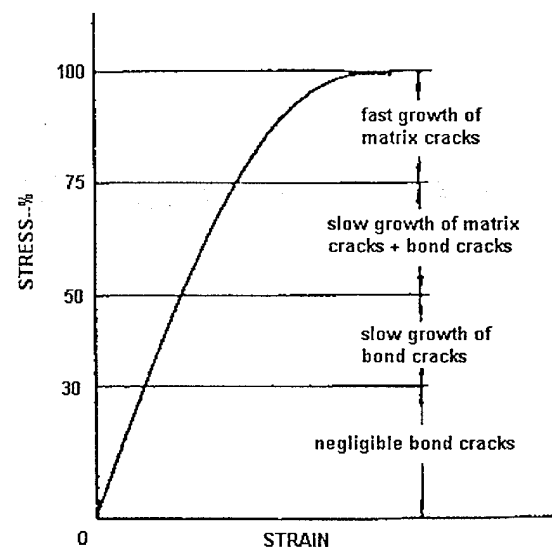
Figure 2-15: Diagrammatic Stress-Strain Curve Under Compression (Glucklich [1965])

Glucklich [1965], Shah and Sankar [1987], Slate and Olsefski [1963], and Hsu et al. [1963] performed compressive tests similar to the procedure described above. These investigators report that microcracking exists before any load is applied. Most of these cracks are located at the mortar-aggregate interface and are called bond cracks. Slate and Olsefski [1963], Jones [1965], and Shah and Sankar [1987] say that bleeding voids often form at the bottom of aggregates, which suggests that the existing "damage" prior to loading is anisotropic.

2-15

As stress is applied up to 30% of the ultimate uniaxial load a few bond cracks develop, usually on the largest aggregates. Glucklich also notes that the stress-strain curve in not truly initially straight (figure 2-16). He states that during the initial loading of a specimen in uniaxial compression, pre-existing microcracks that are perpendicular to the loading axis begin to close. As these microcracks close the specimen becomes stiffer causing the curve to be concave upwards, which is an indication of "damage deactivation". Test results reported by Reinhardt and Cornelissen [1984] support these findings. Tests on mortar by the author produced similar curves.
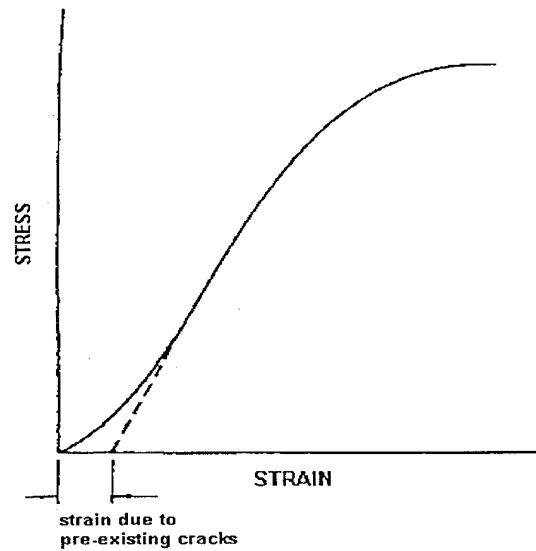
Figure 2-16: Stress-Strain Curve in Compression (Glucklich [1965])

As the stress increases beyond 30% of ultimate uniaxial stress, bond cracking increases. Glucklich also states that the ultrasonic pulse velocity begins to decrease at this point. Shah and Sankar report that these bond cracks occur uniformly in both the transverse and longitudinal directions. These bond cracks form predominately on the large and medium sized aggregates.

At about 50-60% of the ultimate uniaxial load a few mortar (matrix) cracks begin to appear. These cracks bridge existing bond cracks favoring the larger aggregates. There are many more mortar cracks in the longitudinal direction than in the transverse direction. Bond cracks continue to form. Acoustic emissions from the specimen begin to increase at this point.

At about 75-85% of the ultimate load matrix cracking grows significantly. The specimen begins to dilate and acoustic noise increases rapidly. This cracking is predominately in the longitudinal direction. Shah and Sankar [1987] report that the cracking, bond and matrix, localize near the edges of the specimens. Glucklich [1965] notes that the long term compressive strength of hardened cement paste is about 80% of the strength obtained from short term loading. This suggests that cracks forming at this point are unstable and will continue to grow, albeit very slowly, without increasing the load. Meyers et al. [1969] obtained similar results.

Shah and Sankar [1987] say that the cracking remains localized near the edges into the post-peak region to about 80% of the ultimate load. At this point cracking occurs uniformly throughout the specimen in both the longitudinal and transverse directions. They also report that the average angle of the longitudinal cracks was about 10 degrees from the axis of the load.

For very high strength concretes, fewer bond cracks develop. At about 90% of the peak load the aggregates and mortar begin to crack.

Strain gradients appear to delay the onset of mortar cracking. Sturman et al. [1965] show that mortar cracks initiate at much higher strain in eccentrical compressive tests than in concentrical tests. Tests by Kaplan [1963] showed that the strain at first cracking in direct tension tests was about 50% less than those found in flexural tests. Kaplan attributes this to anisotropy of the concrete tested; however, the effect of strain gradients may have also contributed.

In tension, bond cracks form throughout the loading process. Shah and McGarry [1971] state that microcracking begins at about 60% of the ultimate load. At about 80-90% of the ultimate load matrix cracks grow significantly and the stress-strain curve becomes nonlinear. Gopalaratnam and Shah [1985] indicate that cracking localizes near the ultimate failure plane at about 80-90% of the ultimate stress. Tests by Van Mier [1990a] show that cracks appear on the surface of the specimen before the interior cracks. Similar behavior has been reported in flexure by Van Mier [1990b], Shah and McGarry [1971], and Grudemo [1979].

Before discussing the factors that influence this behavior, the topology of the failure surface will be discussed. Uniaxial compression tests by Vonk et al. [1990] showed the spacing of vertical cracks was roughly equal to the size of the largest aggregate. Similarly P-E Petersson [1981] found that in direct tension tests the failure was bounded by a region approximately the width of the largest aggregate. Biaxial compression tests by Van Mier [1984] indicate that the angled "faulting" failures were about the width of the largest aggregate.

Failures under multiaxial compressive loads are very complex. These failures are usually angled failures. Often there are vertical cracks that run through the failure zone (figure 2-17). Figure 2-12 shows the results of tests performed on a brittle resin by Horii and Nemat-Nasser [1986]. Figure 2-12a shows the failure in uniaxial compression. Figure 2-12b shows the failure under biaxial compression. The failure transitions from a very "clean" failure to a very tortuous disruptive failure.

Wawersik and Fairhurst [1970], state that the average crack length is less than in uniaxial compression and decreases continuously as the confining pressure increases. Horii and Nemet-Nasser [1986] show that as confinement increases the number of smaller cracks that develop increases. Chinn and Zimmerman [1965] indicate that bond cracking

Figure 2-17: Typical Failure of Concrete Under Compression (Vonk [1990])

increases as confining pressure increases.

Scanning Electron Microscope (SEM) studies by Mindess and Diamond [1980] provide a closer look at these cracks. They reveal that the cracks are tortuous. Portions of the crack branch off and terminate. Some portions are bridged by aggregates. Cracks may also surround aggregates separating them from the rest of the material. Van Mier reports [1990a, 1990b] similar observations.

Some investigators believe that a process zone of microcracks develops ahead of the macrocrack, which allows some stable crack growth. Recent investigations by Van Mier [1990a] indicate that such a zone is difficult to find. Grudemo [1979] reports that in tests on pastes a very narrow process zone made up of parallel microcracks approximately 100 mm long was observed. Tait et al. [1990] observed in double torsion tests on mortar that the main macrocrack "tip" is difficult to find because it continually branches into ever smaller microcracks (figure 2-18). They report that microcracks open as the macrocrack approaches. Most of these cracks close as the crack tip passes, however, some of the cracks that are very near the macrocrack show no relaxation as the crack tip passes (figure 2-19).

(a)   (b)
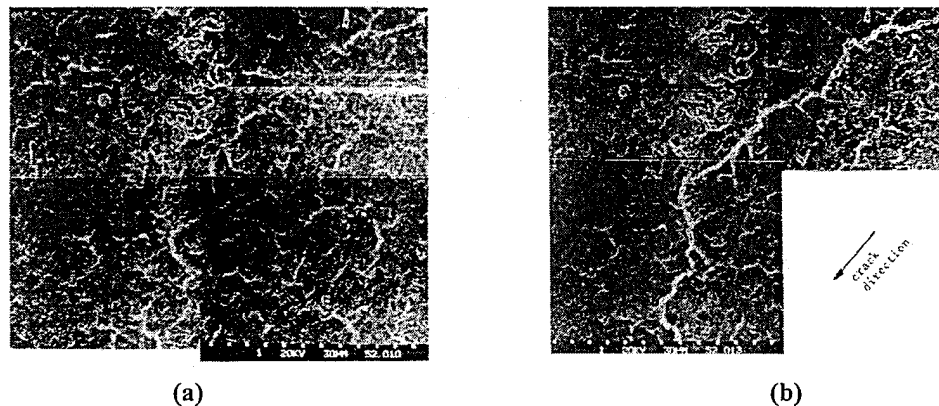
Figure 2-18: Illustration of the Nature of the Macrocrack Process Zone (Tait et al. [1990])

(a)   (b)
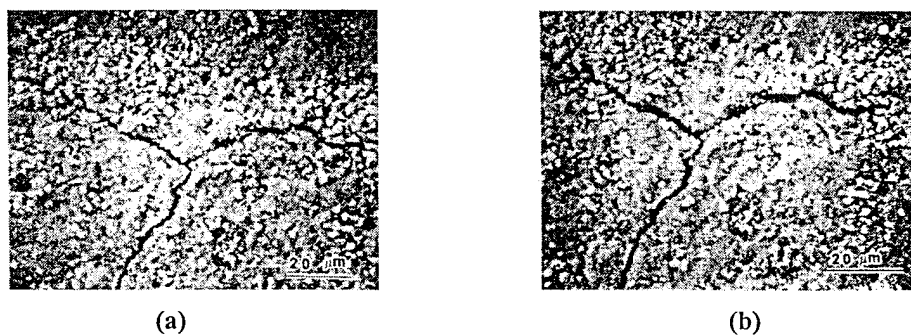
Figure 2-19: Non-Relaxing Microcrack Near a Propagating Crack Tip (Tait et al. [1990])

Tait et al. [1990] also report that there is a significant amount of crack bridging and branching (figure 2-20). Van Mier [1990a] concludes that much of the post-peak load carrying capacity of concrete in tension is due to crack bridging. Analytical studies carried out by Horii and Nirmalendran [1990] show that crack bridging increases the fracture toughness of cementitious materials more than the microcracking in front of the crack tip. Thus, the tortuousness of the crack may be more significant than the microcracking in the crack process zone.
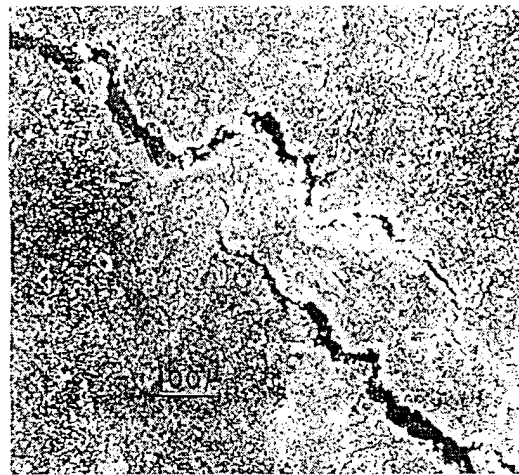
(a) Crack Bridging
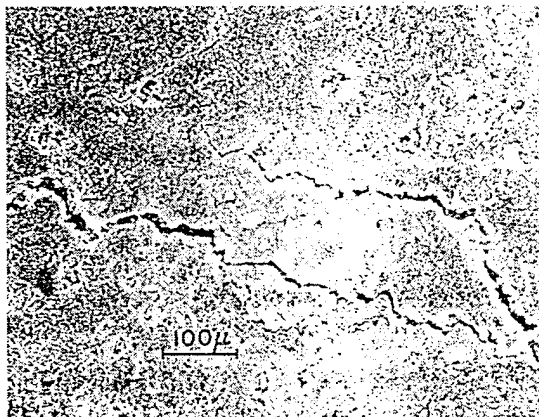
(b) Crack Branching Before Loading
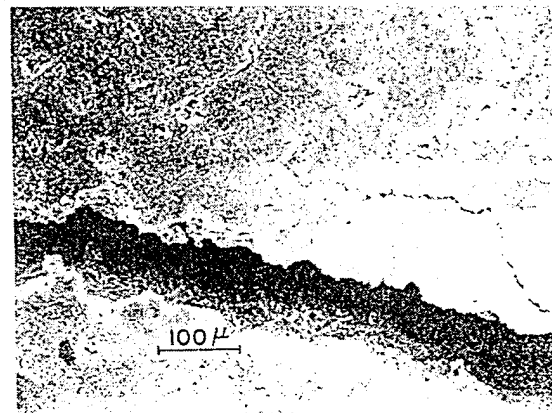
(c) Crack Branching After Loading

Figure 2-20: Crack Process Zone Features (Mindness and Diamond [1980])

Bond strength in normal concretes is the "weak" link in determining the strength of the concrete. Bond is formed by the mechanical interlock of the aggregate and the surrounding cement matrix and the chemical bond between aggregate and cement. In a review of previous studies Struble and Skalny [1980] report that the aggregates are coated with calcium silicate during the hydration process. Calcium silicate represents about 20% of the hydration products in the paste and is one of the weaker hydration products.

Tests by Hsu and Slate [1963] and Alexander et al. [1965] show that the tensile bond strength ranges from 40 to 100% of the tensile strength of the paste. The strength is influenced by the surface texture, aggregate type (chemical make up), water/cement ratio, and age. Although aggregate size does not directly influence bond tensile strength, it does increase the influence of these other factors. Furthermore, increases in the water/cement ratio (w/c) decrease the bond strength faster than the paste strength. The presence of sand in the paste also decreases the tensile bond strength. The tensile bond strength between aggregate and mortar ranges from 30 to 70% of the mortar strength.

Alexander et al. [1965] present the results of bond shear tests. The bond shear strength decreases with aggregate size. Figure 2-21 shows the relationship between normal stress and bond shear strength. They also note that the angle of friction for normal concretes ranges from 30 to 40 degrees. The angle of friction is not affected by the water/cement ratio. However, the shear strength is influenced by the water/cement ratio, surface texture, aggregate type, and concrete age.

Figure 2-21: Normal Stress versus Bond Strength (Alexander et al. [1965])

As concrete hydrates the paste may contract or expand. This contraction or expansion around aggregates leads to stresses, which may exceed the strength of the paste/aggregate bonds or even the paste strength. Experiments by Hansen and Nielsen [1965] show that microcracking increases as that ratio of paste shrinkage to concrete shrinkage increases. Analytical studies by Hsu [1963] show that a 3% shrinkage in the paste volume can cause tensile failure of the bonds when aggregates are separated by a distance equal to .2 times the radius of the aggregate. Similar stresses can also be induced by temperature changes and gradients, and by wetting and drying of the specimen.

2.20 CONTINUUM MODELING

Even with recent advances in computing technology, discrete modeling of concrete can only be used to study a limited scope of problems. By treating concrete as a continuum a much wider variety of problems can be considered. The question arises: "When can the heterogeneous system may be modeled as a continuum?" Use of a continuum model is valid when the macroscopic response of a "continuum element" of the material can be modeled by the response of an appropriate continuum model over the equivalent area.

The size of a "continuum element" for concrete is several times larger than the largest aggregate and may be several inches. By comparison metals have a characteristic length about five orders of magnitude smaller. It is important to consider all the factors that influence the macroscopic behavior of this "continuum element."

To form a complete picture of the constitutive behavior of a material the following must be known:
1. The stress-strain relation
2. The evolution equations for the material parameters
3. The damage surface (or yield or limit surface)
Only two of these are independent. Therefore, with knowledge of two of these items the third can be derived. Often it is easiest to start with the damage surface and the evolution equations.

2.21 CONTINUUM PLASTICITY MODELING

In ideal plasticity the elastic modulus tensor does not change so that all nonlinearities in the tangent stiffness are a result of plastic deformations. The accumulation of plastic deformation is reflected in a monotonically increasing parameter, λ. The model will be strain rate independent.

A surface exists in the stress (or strain) space that separates the region of elastic behavior from the region of states that are not possible. This surface represents the set of states at which plastic deformation may occur. Such a surface may be represented by ϕ, the plasticity function. In general ϕ is a function of the state of stress, σ, an internal kinematic hardening variable, r, and an internal isotropic hardening variable, H. The damage surface becomes

$$\phi(\sigma, r, H) = 0 \qquad \text{2.1}$$

Using the constitutive equation

$$\sigma = E:(e - e^{P}) \qquad \text{2.2}$$

where e is the total strain and e^P is the plastic strain. This leads to

$$\dot{\sigma} = E:(\dot{e} - \dot{e}^P)$$ 2.3

The evolution equations are given by

$$\dot{e}^P = \dot{\lambda}M(\sigma, r, H)$$
$$\dot{r} = \dot{\lambda}R(\sigma, r, H)$$ 2.4
$$\dot{H} = \dot{\lambda}h(\sigma, r, H)$$

The surface is a "limit" surface in so far as the material cannot attain a state of stress outside of this surface. However, the surface may change during loading to accommodate stress states that attempt to evolve to states outside of the plasticity surface. To ensure that the state of stress is either on or contained within the surface the consistency equation is considered.

$$\dot{\phi} = \frac{\partial \phi}{\partial \sigma}:E:(\dot{e} - \dot{e}^P) + \frac{\partial \phi}{\partial r}:\dot{r} + \frac{\partial \phi}{\partial H}\dot{H} = 0$$ 2.5

By substituting equation 2.4 into equation 2.5 and rearranging terms, the rate of change of the plasticity parameter, $\dot{\lambda}$, is given by

$$\dot{\lambda} = \frac{\dfrac{\partial \phi}{\partial \sigma}:E:\dot{e}}{\dfrac{\partial \phi}{\partial \sigma}:E:M - \dfrac{\partial \phi}{\partial H}h - \dfrac{\partial \phi}{\partial r}:R}$$ 2.6

If ϕ is negative then the state of stress is contained within the plasticity surface and the material behaves elastically. If ϕ is zero and $\dot{\phi}$ is negative then the state of stress is on the plasticity surface and elastically moving away from the surface. If ϕ is zero, $\dot{\phi}$ is zero and $\dot{\lambda}$ is zero then the state of stress is moving along the surface elastically. If ϕ is zero, $\dot{\phi}$ is zero, and $\dot{\lambda}$ is positive then the state of stress is moving along the plasticity surface and plastic deformation is occurring.

To study localized behavior of this model it is important to determine the tangent stiffness. For convenience let

$$\frac{\partial \phi}{\partial \sigma} = N$$ 2.7

Define E_P, the hardening modulus, and K as follows:

$$E_P = -(\frac{\partial \phi}{\partial H} h + \frac{\partial \phi}{\partial r} : R)$$
$$K = N:E:M$$

2.8

Define the tangent stiffness tensor, **C**, such that

$$\dot{\sigma} = C:\dot{e}$$

2.9

By substituting equation 2.4 into 2.3 an alternate form for the derivative of the stress is given by

$$\dot{\sigma} = E:\dot{e} - E:M\dot{\lambda}$$

2.10

Using the consistency equation and equation 2.5 which relates the stress rate to the strain, $\dot{\lambda}$ can be written as

$$\dot{\lambda} = \frac{N:\dot{\sigma}}{E_P}$$

2.11

By substituting equation 2.11 into 2.10 and taking the inner product of both sides with **N**, 2.10 becomes

$$N:\dot{\sigma} = N:E:\dot{e} - N:E:M(\frac{N:\dot{\sigma}}{E_P})$$

2.12

Rearranging terms

$$\frac{N:\dot{\sigma}}{E_P} = \frac{N:E:\dot{e}}{E_P + K}$$

2.13

By substituting equations 2.11 and 2.13 into 2.10 and comparing with 2.9, the tangent stiffness, **C**, is given by

$$C = E - \frac{H[\phi]}{E_P + K}(E:M \otimes N:E)$$

2.14

where H[ϕ] is the heaviside function. If **M=N** the flow rule is called associated and **C** is symmetric. If **M≠N** the flow rule is called non-associated and the tangent stiffness, **C**, is non-symmetric. Also note that **C** may become singular if E_p+K gets very small.

2.22 CONTINUUM DAMAGE MODELING

In ideal continuum damage mechanics (CDM) there are no plastic strains; therefore, the stresses and strains are always linearly related through the modulus. However, the modulus does change as damage occurs. The major premise of CDM is that the accumulation of damage is reflected in the degradation of the modulus. This damage is normally associated with the degradation of the material via cracking and increases in the porosity. Increases in density due to hydrostatic loading may be considered as a deactivation of some of this damage. For simplicity it will be assumed that the damage to the continuum can be represented as a scalar, ω. The model will be strain rate independent.

A surface exists in the stress (or strain) space that separates the region of elastic behavior from the region of states that are not possible. This surface represents the set of states at which damage may occur. Such a surface may be represented by ϕ, the damage function. In general ϕ is a function of the state of stress, σ, an internal kinematic hardening variable, r, and an internal isotropic hardening variable, H. The damage surface becomes

$$\phi(\sigma, r, H) = 0 \qquad\qquad 2.15$$

Using the constitutive equation

$$\sigma = e{:}E \qquad\qquad 2.16$$

where E is the secant modulus, the damage surface may be rewritten as

$$\phi(e, E, r, H) = 0 \qquad\qquad 2.17$$

The surface is a "limit" surface in so far as the material cannot attain a state of stress outside of this surface. However, the surface may change during loading to accommodate stress states that tend towards a point outside of the damage surface. This leads to the consistency equation

$$\dot{\phi} = \frac{\partial \phi}{\partial e}{:}\dot{e} + \frac{\partial \phi}{\partial E}{::}\dot{E} + \frac{\partial \phi}{\partial r}{:}\dot{r} + \frac{\partial \phi}{\partial H}\dot{H} = 0 \qquad\qquad 2.18$$

The evolution equations can be written as

$$\begin{aligned}
\dot{E} &= -\dot{\omega}M(e, E, r, H) \\
\dot{r} &= -\dot{\omega}R(e, E, r, H) \\
\dot{H} &= -\dot{\omega}h(e, E, r, H)
\end{aligned} \qquad\qquad 2.19$$

where **M** is a fourth order tensor that represents the change in the secant stiffness tensor per unit of damage, **R** is kinematic hardening function, and h is the isotropic hardening function. By substituting in the evolution equations and rearranging the terms, the damage evolution parameter is obtained

$$\dot{\omega} = \frac{\dfrac{\partial \phi}{\partial e}:\dot{e}}{\dfrac{\partial \phi}{\partial E}::M + \dfrac{\partial \phi}{\partial r}:R + \dfrac{\partial \phi}{\partial H}h}$$ 2.20

If ϕ is negative then the state of stress is contained within the damage surface and the material behaves elastically with no damage. If ϕ is zero and $\dot{\phi}$ is negative then the state of stress is on the damage surface and elastically moving away from the damage surface. If ϕ is zero, $\dot{\phi}$ is zero and $\dot{\omega}$ is zero then the state of stress is moving along the surface elastically. If ϕ is zero, $\dot{\phi}$ is zero, and $\dot{\omega}$ is positive then the state of stress is moving along the damage surface and damage is occurring. It should be noted that as damage is occurring the incremental form of the stress is given by

$$\dot{\sigma} = \dot{E}:e + E:\dot{e}$$ 2.21

When no damage is occurring the stress is given by

$$\dot{\sigma} = E:\dot{e}$$ 2.22

To study localized behavior of this model the tangent stiffness, **C**, must be derived. Define the tangent stiffness tensor, **C**, such that

$$\dot{\sigma} = C:\dot{e}$$ 2.23

By substituting equation 2.19 into 2.21 an alternate form for the derivative of the stress is given by

$$\dot{\sigma} = E:\dot{e} - \dot{\omega}M:e$$ 2.24

The consistency equation can be used to rewrite $\dot{\omega}$ as

$$\dot{\omega} = -\frac{N:\dot{\sigma}}{E_P}$$ 2.25

where $N = \dfrac{\partial \phi}{\partial e}$. By substituting equation 2.25 into 2.24 and taking the inner product of both sides with **N**, 2.24 becomes

$$N:\dot{\sigma} = N:E:\dot{e} + (\frac{N:\dot{\sigma}}{E_P})N:M:e$$ 2.26

Rearranging terms

$$\frac{N:\dot{\sigma}}{E_P} = \frac{N:E:\dot{e}}{E_P - N:M:e} \qquad \text{2.27}$$

By substituting equations 2.25 and 2.27 into 2.24 and comparing with 2.23, the tangent stiffness, **C**, is given by

$$C = E + \frac{H[\phi]}{E_P - N:M:e}(M:e \otimes N:E) \qquad \text{2.28}$$

where H[φ] is the heaviside function.

2.23 THERMODYNAMIC RESTRICTIONS

At this point it is important to review some of the restrictions that the laws of thermodynamics place on the constitutive equations. In particularly, the restrictions that result from the requirement for non-decreasing entropy are considered.

The first law of thermodynamics states that the rate of increase of the energy of any portion of a body equals the rate at which energy is added to that region.

$$\dot{\varepsilon} = P + H \qquad\qquad 2.29$$

where ε is the total energy of the region of the body, P is the rate of mechanical work applied (power) applied to the region, and H represents the rate at which heat is added to the region.

ε, the total energy of the region is given by

$$\varepsilon = \textit{Internal Energy of the Region} + \textit{Kinetic Energy of the Region}$$
$$\varepsilon = \int_R \rho U dvol + \tfrac{1}{2} \int_R \rho v \bullet v dvol \qquad\qquad 2.30$$

where U is the internal energy per unit mass, ρ is the mass density, v is the velocity, and **R** represents the volume of the sub-region of the body. Therefore, the rate of the total energy of the region is given by

$$\dot{\varepsilon} = \frac{d\varepsilon}{dt} = \int_R \rho \ddot{U} dvol + \int_R \rho v \bullet \dot{v} dvol \qquad\qquad 2.31$$

P, the rate of mechanical work applied to the region is given by

$$P = \int_R \rho \mathbf{b} \bullet v dvol + \int_{\partial R} \mathbf{t} \bullet \mathbf{v} ds \qquad\qquad 2.32$$

where **b** is the body force per mass, **t** is the traction on the surface of the portion of the body and **ds** is a differential of surface area of the volume. By utilizing Cauchy's Fundamental theorem, **t** can be transformed

$$\mathbf{t} = \sigma \bullet \mathbf{n} \qquad\qquad 2.33$$

where σ is the Cauchy stress tensor and n is the outward normal to the surface. Equation 2.14 is substituted into equation 2.13 and the divergence theorem is applied to give

$$P = \int_R \rho b \bullet v \, dvol + \int_R (v \bullet \sigma) \bullet \nabla dvol \qquad \qquad \textbf{2.34}$$

which reduces to

$$P = \int_R \rho b \bullet v \, dvol + \int_R (v\nabla) : \sigma dvol + \int_R v \bullet (\sigma \bullet \nabla) dvol \qquad \qquad \textbf{2.35}$$

The spatial gradient of v can be written as the sum of a symmetric tensor and a skew-symmetric tensor. The symmetric tensor is called the rate of deformation tensor, $\mathbf{D}$. Under infinitesimal strains $\mathbf{D}$ can be replaced by rate of change of the strain tensor. The skew-symmetric tensor is called the vorticity. If there are no body moments present then σ is symmetric, which leads to

$$\int_R (v\nabla) : \sigma dvol = \int_R \sigma : \dot{e} \, dvol \qquad \qquad \textbf{2.36}$$

By substituting equation 2.36 into equation 2.35 the rate of mechanical work, P, can be rewritten as

$$P = \int_R \rho b \bullet v \, dvol + \int_R \sigma : \dot{e} \, dvol + \int_R v \bullet (\sigma \bullet \nabla) dvol \qquad \qquad \textbf{2.37}$$

H, the rate at which heat is added to the region is given by

$$H = \int_R \rho Q \, dvol - \int_{\partial R} q \bullet n \, ds \qquad \qquad \textbf{2.38}$$

where Q is the internal heat source per unit mass, q is the heat flux out of the region, and n in the outward normal to the surface of the region. By applying the divergence theorem equation 2.38 can be rewritten as

$$H = \int_R \rho Q \, dvol - \int_R \mathbf{q} \bullet \nabla dvol \qquad \text{2.39}$$

By substituting equations 2.31, 2.37, and 2.39 into 2.29 the first law of thermodynamics can be rewritten as

$$\int_R \rho(\dot{U} + \mathbf{v} \bullet \dot{\mathbf{v}}) dvol = \int_R (\rho \mathbf{b} \bullet \mathbf{v} + \sigma : \dot{\mathbf{e}} + \mathbf{v} \bullet (\sigma \bullet \nabla) + \rho Q - \mathbf{q} \bullet \nabla) dvol \qquad \text{2.40}$$

Since the integration is over an arbitrary volume the integrands must be equal.

$$\rho \dot{U} + \rho \mathbf{v} \bullet \dot{\mathbf{v}} = \rho \mathbf{b} \bullet \mathbf{v} + \sigma : \dot{\mathbf{e}} + \mathbf{v} \bullet (\sigma \bullet \nabla) + \rho Q - \mathbf{q} \bullet \nabla \qquad \text{2.41}$$

Cauchy's first equation of motion states that the divergence of the stress tensor is given by

$$\sigma \bullet \nabla = \rho \dot{\mathbf{v}} - \rho \mathbf{b} \qquad \text{2.42}$$

By substituting equation 2.42 into 2.41 and rearranging terms, the first law of thermodynamics can be written as

$$\rho \dot{U} = \sigma : \dot{\mathbf{e}} + \rho Q - \mathbf{q} \bullet \nabla \qquad \text{2.43}$$

If the internal energy, U, is given as a function of the strain, e, mechanical variables, m_i, and entropy, s, then

$$\rho \dot{U} = \rho \frac{\partial U}{\partial e} \dot{e} + \rho \frac{\partial U}{\partial m_i} \dot{m}_i + \rho \frac{\partial U}{\partial s} \dot{s} \qquad \text{2.44}$$

Equation 2.43 must hold for all $\dot{e}$. One result is the constitutive equation

$$\sigma = \rho \frac{\partial U}{\partial e} \qquad \text{2.45}$$

Define the absolute temperature (always positive) as

$$\theta \equiv \frac{\partial U}{\partial s},$$

<div align="right">2.46</div>

and the thermodynamic tensions as

$$\tau_i \equiv \frac{\partial U}{\partial m_i}$$

<div align="right">2.47</div>

The first law of thermodynamics becomes

$$\rho \tau_i \dot{m}_i + \rho \theta \dot{s} = \rho Q - q \bullet \nabla$$

<div align="right">2.48</div>

If the external heat source, Q, and the heat flux, **q**, are assumed to be zero (a good assumption in most static or quasi static loading situations), then the first law provides an expression for the rate of change of the entropy, given as

$$\dot{s} = -\frac{1}{\theta} \frac{\partial U}{\partial m_i} \dot{m}_i$$

<div align="right">2.49</div>

Define a dissipation function, D_s

$$D_S \equiv -\frac{\partial U}{\partial m_i} \dot{m}_i$$

<div align="right">2.50</div>

The second law of thermodynamics states that entropy never decreases. Alternatively, the second law states that the rate of increase of the internal entropy must be greater than or equal to the rate at which entropy is added to any region of a body by the internal heat source and by the heat flux over the boundary of the region. Using steps similar to those used above the second law can be written as

$$\rho \dot{s} \geq \rho \frac{Q}{\theta} - \frac{(q \bullet \nabla)}{\theta} + \frac{q \bullet (\theta \nabla)}{\theta^2}$$

<div align="right">2.51</div>

By substituting the equation for the first law 2.43 (realizing all of the assumptions that were made to arrive at equation 2.43) into equation 2.51 and rearranging terms then the second law may be given as

$$\rho\dot{s} \geq \frac{q \bullet (\theta\nabla)}{\theta^2} + \frac{\rho\dot{U}}{\theta} - \frac{\sigma:\dot{e}}{\theta} \qquad\qquad 2.52$$

If we define the specific total entropy rate by

$$\dot{\gamma} \equiv \dot{s} - \frac{q \bullet (\theta\nabla)}{\rho\theta^2} - \frac{\dot{U}}{\theta} + \frac{\sigma:\dot{e}}{\rho\theta} \qquad\qquad 2.53$$

then the second law can be written as

$$\dot{\gamma} \geq 0 \qquad\qquad 2.54$$

which is also known as the Clasius-Duhem inequality.

A purely mechanical process is considered in which q=0, Q=0, and $\theta=\theta_0$. Using the equation for the first law as given by equation 2.50, the Clasius-Duhem inequality becomes

$$D_S \geq 0 \qquad\qquad 2.55$$

Restrictions placed on plasticity:

Consider the stored energy function

$$\psi = \frac{1}{2}(e - e^P) : E : (e - e^P) \qquad \text{2.56}$$

The Helmholtz free energy function in separable form is assumed to be

$$\rho A = \psi(e, e^P) - \frac{1}{2} g^2(\eta) \qquad \text{2.57}$$

where η represents the internal mechanical variables. The constitutive equation is given as

$$\sigma = \rho \frac{\partial A}{\partial e} = E : (e - e^P) \qquad \text{2.58}$$

The evolution equations are given as

$$\dot{e}^P = \dot{\lambda} M$$
$$\dot{\eta} = \dot{\lambda} h \qquad \text{2.59}$$

The dissipation is represented by

$$D_S = \frac{\dot{\lambda}}{\rho}\left(\sigma : M + hg(\eta)\frac{\partial(g(\eta))}{\partial \eta}\right) \qquad \text{2.60}$$

If the plasticity surface is represented by

$$\phi = \sigma : M + hg(\eta)\frac{\partial(g(\eta))}{\partial \eta} - C_0^2 \qquad \text{2.61}$$

then during plastic deformation

$$C_0^2 = \sigma : M + hg(\eta)\frac{\partial(g(\eta))}{\partial \eta} \qquad \text{2.62}$$

and the dissipation becomes

$$D_S = \frac{\dot{\lambda} C_0^2}{\rho} \geq 0 \qquad \text{2.63}$$

which implies

$$\dot{\lambda} \geq 0 \qquad \text{2.64}$$

This result indicates

$$\sigma : M \geq -hg(\eta)\frac{\partial(g(\eta))}{\partial \eta} \qquad \text{2.65}$$

2-32

Therefore, the inner product σ:**M** is driven by the hardening function. If the right hand side is 0 then σ and **M** must be at acute angles to one another.

Restrictions placed on damage mechanics:

Consider the stored energy function

$$\psi = \tfrac{1}{2} e \!:\! E \!:\! e \qquad\qquad 2.66$$

The Helmholtz free energy can be written as

$$\rho A = \psi(E, e) - \tfrac{1}{2} g^2(\eta) \qquad\qquad 2.67$$

If the constitutive equation is given as

$$\sigma = \rho \frac{\partial A}{\partial e} = E \!:\! e \qquad\qquad 2.68$$

then the dissipation is given as

$$D_S = -\frac{\partial A}{\partial E} \!::\! \dot{E} - \frac{\partial A}{\partial \eta} \dot{\eta} \qquad\qquad 2.69$$

If the evolution equations are given by

$$\dot{E} = -\dot{\omega} M(E, e)$$
$$\dot{\eta} = \dot{\omega} h(\eta) \qquad\qquad 2.70$$

then the dissipation becomes

$$D_S = \frac{\dot{\omega}}{\rho} \left(\frac{1}{2} e \!:\! M \!:\! e + hg(\eta) \frac{\partial(g(\eta))}{\partial \eta} \right) \qquad\qquad 2.71$$

If the damage surface is represented by

$$\phi = \frac{1}{2} e \!:\! M \!:\! e + hg(\eta) \frac{\partial(g(\eta))}{\partial \eta} - C_0^2 \qquad\qquad 2.72$$

then as damage occurs,

$$C_0^2 = \frac{1}{2} e \colon M \colon e + hg(\eta) \frac{\partial (g(\eta))}{\partial \eta}$$

2.73

The dissipation is rewritten as

$$D_S = \dot{\omega} \, C_0^2$$

2.74

which requires

$$\dot{\omega} \geq 0$$

2.75

If **M** is positive definite then the result implies that the rate of change of the modulus, $\dot{E}$, is negative definite.

2.24 LOCALIZATION AND BIFURCATION

Localized deformations occur when non-homogeneous deformations arise in a homogeneously loaded homogeneous material. The failure plane can be viewed as a zone or band of localized deformations. The angle of such a plane represents the angle of the failure plane.

These localized deformations represent a loss of material stability. A necessary condition for the loss of material stability is the loss of positive definiteness of the second order work (Drucker [1951], Hill [1956, 1957, 1958]) to the perturbed stress and strain fields. The condition for material stability, positive definiteness of the second order work can be written as

$$\dot{\sigma}:\dot{e} = \dot{e}:C:\dot{e} = \dot{e}:C^S:\dot{e} > 0 \qquad \text{2.76}$$

Mathematically speaking these localized zones represent an unbounded solution to a perturbation in the applied force field. To determine when localized behavior may occur and the orientation of this localized behavior it is necessary to consider the concepts of bifurcation and eigen modal analysis.

Bifurcation of a boundary value problem results in either a change in the character of the equation or a change in the character of the solution. If the character of the equation changes the original initial conditions may create an ill-posed problem with the new character. Bifurcation of the solution of a boundary value problem can change the number of solutions, the stability of the solution, or the period of the solution. In this study elliptical equations are considered; therefore, bifurcation of the solution leads to multiple solutions.

Bifurcations can be classified by the mode of the perturbed strain rate produced. There are two basic types discontinuous and diffuse. Discontinuous bifurcations produce a zone across the boundary of which there is a jump in the strain rate with compatible deformations. Maxwell's compatibility equation requires that the jump in the strain rate has the form

$$\Delta\dot{e} = \frac{1}{2}(n \otimes g + g \otimes n) \qquad \text{2.77}$$

where n is the normal to the boundary of the localized zone and g is the relative velocity of the material inside and outside the zone. This form of perturbation to the strain rate field has the special property that one of the eigenvalues is positive, one is zero and one is negative or zero.

Diffuse bifurcations are associated with necking and bulging. The predicted perturbation to the strain rate field is incompatible with the surrounding material. Hill [1967] states that the necking mode initiates in a primary eigen state and grows from a region of zero extent. Neilsen and Schreyer [1993] present similar arguments.

There are four types of bifurcation that can occur that are related to loss of positive definiteness of the second order work, general bifurcation, limit point, loss of strong ellipticity, and loss of ellipticity.

The general bifurcation occurs first. General bifurcation occurs when the symmetric part of the tangent stiffness tensor, $\mathbf{C}^S$, loses positive definiteness. General bifurcations are associated with diffuse bifurcations. The limit point bifurcation is located at the peak of the stress-strain curve where the slope is zero and is a general bifurcation in which the stress state does not change, i.e. $\dot{\sigma} = 0$. The limit point bifurcation occurs when the tangent stiffness, $\mathbf{C}$, obtains a zero eigenvalue. The limit point bifurcation and general bifurcation become the same if the tangent stiffness is symmetric, associated flow.

Recall the requirement for a compatible form of the jump in the strain rate, equation 2.77. By using this compatible form of the strain rate jump, the constitutive relation equation 2.9, and using the minor symmetry of the tangent stiffness tensor the second order work stability requirement can be written as

$$\dot{e}{:}C{:}\dot{e} = \dot{e}{:}C^{S}{:}\dot{e} = g \bullet (n \bullet C^{S} \bullet n) \bullet g = g \bullet Q^{S} \bullet g > 0 \qquad 2.78$$

where $\mathbf{Q}$ is called the acoustic tensor, and $\mathbf{Q}^S$ is the symmetric portion of the acoustic tensor. Material stability is lost when the symmetric portion of the acoustic tensor, $\mathbf{Q}^S$, loses positive definiteness. This is also called the loss of strong ellipticity. If acceleration is considered, i.e. the wave equation is used, then the loss of strong ellipticity corresponds to a change of the wave speed from real and non-zero to one that is imaginary without first becoming zero. This is related to flutter instability in fluid mechanics. The loss of strong ellipticity also produces non-convergence in numerical solutions with increasing mesh refinement.

Consider the existence of a zone of localized material. Assume that the stress rates outside the zone are unchanged by the initiation of the zone. Equilibrium requires that the jump in the traction rates across the boundary of this zone be zero. The jump in the traction rate across the boundary is given by

$$\dot{t} = n \bullet \dot{\sigma} = n \bullet C \bullet \dot{e} = 0 \qquad 2.79$$

where $\mathbf{n}$ is the normal to the boundary of the zone. By substituting the compatible form of the strain rate jump the jump in the traction rate can be rewritten as

$$\dot{t} = (n \bullet C \bullet n) \bullet g = Q \bullet g = 0 \qquad 2.80$$

where $\mathbf{Q}$ is the acoustic tensor. Therefore, $\mathbf{g}$ is non trivial if the acoustic tensor has a zero eigenvalue. This condition is known as the loss of ellipticity which is the classical condition for a discontinuous bifurcation. This condition in the wave equation results in a zero wave speed. As with the loss of strong ellipticity there is a loss of convergence of numerical solution with increasing mesh refinement (Schreyer and Neilsen [1996]).

When the tangent stiffness is symmetric, associated flow, the loss ellipticity and the loss of strong ellipticity become the same.

Ottosen and Runesson [1991A] examined whether the first discontinuous bifurcation was plastic-plastic, plastic deformations both inside and outside the zone of localized deformations, or elastic-plastic, elastic unloading outside the zone and plastic deformations inside the zone of localized deformation. They found that the plastic-plastic bifurcation precedes the elastic plastic deformation.

Ottosen and Runesson [1991A] examined the value of the hardening modulus, H (E_P used in sections 2.21 and 2.22), for the types of bifurcations listed above for the case of associated and non-associated plastic flow. Although, Ottosen and Runesson [1991A] examined each of these types of bifurcation they failed to acknowledge that the loss of strong ellipticity produces a discontinuous bifurcation just as the loss of ellipticity does.

Consider a stress-strain curve that has a hardening and softening regime. The hardening regime is prepeak, positive, and gets smaller closer to the peak. At the peak the hardening modulus is zero. In the post peak regime the hardening modulus is negative and gets more negative (smaller) farther from the peak. Let the hardening modulus at the first possible occurrence of bifurcation be denoted as follows: H^G for the general bifurcation, H^L for the limit point bifurcation, H^{SE} for the loss of strong ellipticity, and H^E for the loss of ellipticity. The results of Ottosen and Runesson [1991A] can be summarized for both associated and non-associated plastic flow by

$$(H^L = H^G = 0) \geq (H^{SE} = H^E) \qquad \textit{Associated Plastic Flow}$$

$$\begin{aligned} H^L &= 0 \\ H^G &> 0 \qquad \textit{Non-associated Plastic Flow} \\ H^G \geq H^{SE} &> H^E \end{aligned}$$

2.81

The most important feature to note is that a non-associated flow model must be used to predict localization prepeak. The first type of bifurcation is the general bifurcation for both associated and non-associated flow. It is possible to have an associated flow model that allows all of the bifurcations to occur at the peak. Ottosen and Runesson [1991B] show that for associated plastic flow with a simple Mohr surface, all bifurcations occur at the peak.

Mandel [1966] states that the positive definiteness of the second order work is a sufficient but not necessary condition for stability of a boundary value problem. He goes on to define stability in the small, material stability, and stability in the large, structural stability. Stability in the large may be maintained even after material stability is lost if the boundaries are properly constrained. Rice [1976] states that the use of

displacement boundary conditions allow solids to proceed past diffuse bifurcations. Neilsen and Schreyer [1993] present similar arguments and note that bifurcation mode in general can be constrained by the prescribed boundary condition. This may explain the difference between the results of Palaniswamy and Shah [1972,1974] or Wawersik and Brace [1971],who used fluid pressure to apply lateral pressure, and Mills [1967] who used platens to apply the lateral pressure which provided a displacement prescribed boundary condition. Gerstle et al. [1980] also noted the constraining affects of using platens to apply lateral pressure.

The loss of strong ellipticity or the loss of positive definiteness of the symmetric portion of the acoustic tensor is used in this study to determine the occurrence of localization, since it is the first discontinuous bifurcation to occur. Furthermore, the orientation of the zone of localized deformations (failure plane) is derived by finding the first **n** that gives a zero determinant for the symmetric portion of the acoustic tensor.

2.25 EIGEN MODAL ANALYSIS AND FAILURE ORIENTATION

The bifurcations mentioned in the previous section occur when positive definiteness is lost in the tangent stiffness tensor, the symmetric part of the tangent stiffness tensor, the acoustic tensor, or the symmetric portion of the acoustic tensor. Since the tensors are initially positive definite then positive definiteness is lost when the smallest eigenvalue of each tensor goes to zero. The general concept of eigen modal analysis, present by Hill [1967] is to set up each bifurcation as an eigenvalue problem and determine when the smallest eigenvalue reduces to zero. The mode of the perturbation to the strain rate can be determined by examining the associated eigen tensor or eigen vector.

Discontinuous bifurcations can be found by examining the loss of positive definiteness in the acoustic tensor or its symmetric component. A direction, **n**, must be assumed to form the acoustic tensor. All directions, **n**, must be checked at each step during the loading process to see which direction if any will produce a loss of positive definiteness in the acoustic tensor. Ottosen and Runneson [1991A] define a right eigenvalue problem for the acoustic tensor that produces an eigen vector, **g**.

$$Q \bullet g^i = \lambda_i g^i \qquad\qquad 2.82$$

where λ_i is an eigenvalue and g^i is its eigen vector. The eigen vector, **g**, associated with the zero eigenvalue along with the associated direction, **n**, make up the eigen mode. **g** represents the relative velocity of the material inside and outside of the zone.

The general bifurcation occurs first and is defined by the loss of positive definiteness of the symmetric portion of the tangent stiffness tensor. Shreyer and Nielsen [1996] consider the eigenvalue problem for the symmetric portion of the tangent stiffness tensor which produces an eigen tensor, equation 2.83. They examine possible discontinuous modes by examining the form of the eigen tensor produced. If the eigen tensor is of the form of equation 2.77 then it is a discontinuous bifurcation.

Consider the eigenvalue problem:

$$C^s : x^i = \omega_i \, x^i \qquad\qquad 2.83$$

where x^i is the ith second order eigen tensor associated with the ith eigenvalue, ω_i.

Since C^s is the symmetric part of the tangent stiffness tensor, the eigen tensors are orthogonal; therefore, any second order tensor can be written as a linear combination of the eigen tensors. The bifurcated strain rate is written as a linear combination of the eigen tensors.

$$\dot{e} = \sum_{i=1}^{6} \alpha_i \, x^i \qquad\qquad 2.84$$

A second order tensor spans a 9 space in general, but since $\mathbf{C}$ has minor symmetry, $\mathbf{C}_{ijkl} = \mathbf{C}_{jikl} = \mathbf{C}_{ijlk}$, the eigen tensors are also symmetric producing a 6 space.

The condition for loss of material stability, equation 2.76 can be rewritten using equations 2.83 and 2.84:

$$\dot{e}:C^S:\dot{e} = \sum_{i=1}^{6} \alpha_i^{\,2} \, \omega_i = 0 \qquad\qquad 2.85$$

where it is assumed that the eigen tensors were normalized such that $X^i:X^j = \delta_{ij}$. Since the tangent stiffness is initially positive definite, the eigenvalues are all greater than zero initially. As the material deforms inelastically, some of the eigenvalues may decrease. Therefore, equation 2.85 is first satisfied when at least one of the eigenvalues, ω_i, reduces to zero. The perturbation to the strain rate must take a form of the eigen tensor associated with the zero eigenvalue, referred to as the zero eigen mode.

The eigen modes can be either diffuse (incompatible mode) or discontinuous (compatible mode) depending upon the form of the eigen mode. If the eigen mode, associated with the zero eigenvalue, has one positive, one zero, and one negative or zero eigenvalue then the perturbation to the strain rate field can take the form of equation 2.77. If the eigen mode takes on this form then the perturbation is compatible. This also means that the loss of strong ellipticity and the general bifurcation coincide. The values of $\mathbf{n}$ and $\mathbf{g}$ can be derived from the eigen mode; however, simple decomposition of the eigen tensor is insufficient to determine which vector represents the normal to the boundary of localized deformation and which is the relative velocity vector. By forming the acoustic tensor with the tangent stiffness and each one of the vectors then the directional vector is the vector which causes the symmetric portion of the acoustic tensor to lose positive definiteness.

Neilsen and Schreyer [1993] present a methodology for determining these eigen modes, eigen tensors. They present the eigen modes for several constitutive models each using various load paths. It should be noted that the eigen mode obtained may depend on the load path. Neilsen and Schreyer [1993] have shown that a Von Mises plastic material with associated flow will produce a diffuse (incompatible) mode under uniaxial tension but the same material will produce a discontinuous (compatible) mode under pure shear.

If the eigen mode is diffuse then the perturbed strain rate is incompatible and will cause discontinuities in the displacement field if treated in the same manner as the discontinuous bifurcation. Hill [1967] states that diffuse bifurcations initiate in a zone of zero extent. Neilsen and Schreyer [1993] argue that the

incompatibility causes the stress state outside the zone to change. These changes in the stress state in turn cause changes in the tangent stiffness which cause changes in the eigen mode which leads an evolving region of necked or bulged material.

Rice [1976] notes that if the boundaries are properly constrained it is possible to proceed past the general bifurcation and even past the first discontinuous bifurcation without the formation of a zone of localized deformations. When the system is constrained the eigen value(s) may become negative allowing for multiple modes. Neilsen and Schreyer [1993] show how the first discontinuous bifurcation can be determined when the general bifurcation is constrained. They also determine the amount of softening required to produce such a bifurcation.

The size of the zone of localized deformations evolves from a zone of zero extent to one of finite extent for incompatible diffuse modes. However, the size of the zone of localized deformations is undefined (infinite extent) for discontinuous bifurcation. When modeling the development of a zone of localized deformations using the finite element method, the zone of (discontinuous) localized deformations depends on the mesh size. As the size of the mesh decreases the size of the zone decreases. Non-local theories can be used to obtain a model that is not mesh dependent.

Non-local theories are based on the assumption that the state of stress at a point depends not only on the strains at that point but on the strains states of the surrounding points as well. Non-local theories produce a finite size to the zone (discontinuous) of localization because they incorporate a length parameter into the formulation.

Alternatively, the length parameter may be incorporated by using Cosserat Theory. The main premise of Cosserat theory is that body moments are allowed. As a result the stress tensor is no longer symmetric. By including the possibility of body moments, a characteristic length, which is a property of the material, is introduced. De Borst [1990] has shown that plasticity can be incorporated into Cosserat theory to obtain a mesh independent model. Considering the finite size of a continuum element when modeling concrete and the evidence that the stress-strain relationship changes as the strain gradient changes such a formulation seems applicable.

In this study the eigen modal method in the form presented above is not used; however, two methods are employed that determine the orientation of n, the normal to the zone of localized deformations (failure plane). The first is a numerical routine that increments the strain in a constitutive model calculating the determinant of the symmetric part of the acoustic tensor by trying various values of n scanning 180 degrees on each of the three primary plane, x_1-x_2, x_1-x_3, x_2-x_3. The second is an explicit method of determining n for the case of a

symmetric tangent stiffness developed by Schreyer and Neilsen [1996]. These methods are applied to simple plasticity models developed directly from the test data.

3.0 EXPERIMENTAL TECHNIQUE

The primary objective of this experimental study was to determine whether the orientation of the failure plane changes as confining pressure increases in cementitious materials. Two types of tests were performed on mortar specimens to provide quantitative data on the orientation of the failure plane versus the confining pressure. Triaxial tests were performed with confining pressures ranging from 0 to 8,000 psi. The triaxial tests were carried out on cylindrical and rectangular specimens. Biaxial (plane stress) tests were performed with confining (lateral) pressures from 0 to 750 psi. The biaxial tests were carried out on rectangular specimens with special "two-dimensional" aggregates.

An essential part of this study was to evaluate how the method of applying the loads affects the behavior. Specifically, it was necessary to evaluate the effect of the methods used to relieve friction between the load platens and the specimens. Uniaxial and triaxial tests were performed to evaluate these effects. In addition, a new technique for obtaining strains from changes in X-ray intensities was developed during this study and was used to help evaluate the effects of the methods to relieve friction. The X-ray tests are explained in detail in Appendix A.

3.10 TRIAXIAL TESTS

3.11 EQUIPMENT SETUP

A Behavioral Science Engineering Laboratories 10 ksi triaxial test cell was used to apply the lateral confining pressure. The test cell had a pressure transducer that was used to monitor fluid pressure inside the cell.

The axial load was applied with a Tinius Olson Super "L" universal testing machine for the triaxial tests. A SATEC Systems, Inc. Baldwin universal testing machine was used for some of the triaxial tests and for some of the uniaxial tests. Most of the uniaxial tests were performed on an Instron 1323 biaxial test machine. All machines were equipped with load platens that could tilt to accommodate specimens with non-parallel load surfaces.

The axial displacement was measured using a Schaevitz LVDT and an ATA-100 analog transducer amplifier during the tests on the Baldwin machine. When using the Tinius Olson Super "L" the LVDT was hooked directly to the internal amplifier of the machine (figure 3-1). The Instron 1323 has an internal displacement measuring capabilities.

A total of 95 cylinders were tested in uniaxial or triaxial compression. A deformation jacket was used in 10% of the tests to obtain strain data. Strain gages were used in 56% of the tests. The remaining tests recorded only load-displacement data.

Strain measurements were taken on 65% of the triaxial tests. Measurements Group, Inc., EA-06-500BL-350 strain gauges were used on 53% of the triaxial tests. A deformation jacket (figure 3-2) with LVDTs attached was used on 12% of the triaxial tests. The deformation jacket measures axial deformations with LVDTs set 120° apart. It also measures the axial displacement from three locations set 120° apart. The measurements made using the deformation jacket proved to be unreliable.
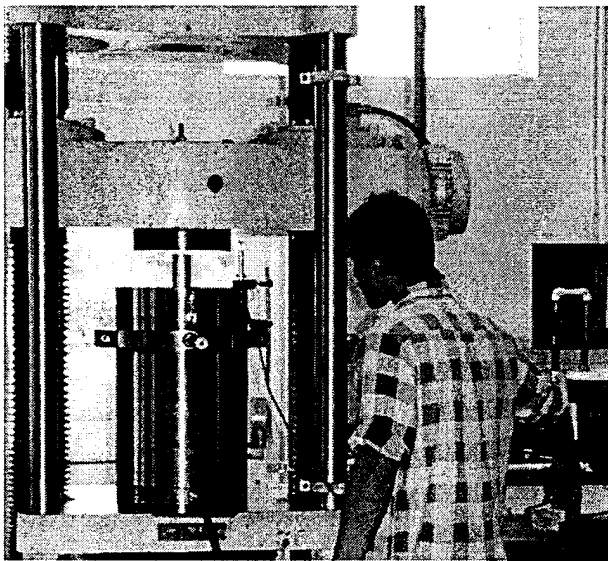
Figure 3-1: Triaxial Cell Setup
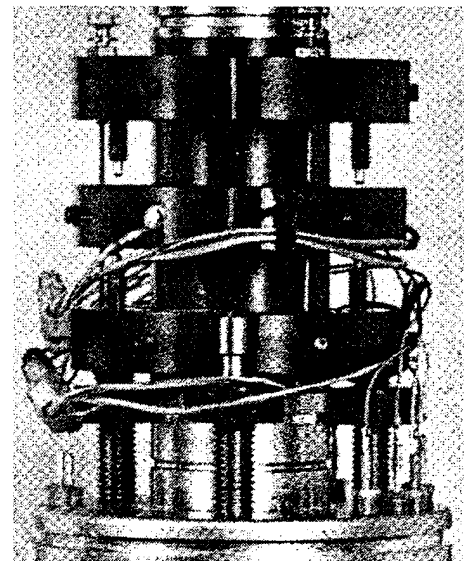
Figure 3-2: Deformation Jacket

Four strain gauges were used on all of the triaxial tests with strain gauges. Two of the gauges were located at the midheight of the specimen. One of the gauges was positioned to measure the axial strain and the other was positioned to measure the circumferential strain. The other two gauges were located near the edge of the specimen and positioned for measuring the axial and circumferential strains.

The deformation jacket was used on 6% of the uniaxial tests while strain gauges were also used on 65% of the uniaxial tests. The uniaxial tests used three different configurations of strain gauges. Tests to determine the material properties used two gauges located at the mid height of the specimen positioned to measure the axial and circumferential strains. Tests to evaluate the effects of different methods of relieving the end confinement used two gauges, each positioned to measure the circumferential strains at the mid height and end of the specimen. Uniaxial tests that were conducted as part of the series of triaxial tests used four gauges configured as for the triaxial tests.

All strain gauges used a quarter bridge setup. The pressure transducer used a full bridge setup. The strain gauges and pressure transducers used a 10 volt DC excitation potential. Data from the strain gages and the pressure transducer was amplified using a Dynamics model 2500 signal conditioner. The LVDTs in the deformation jacket were excited using a sine wave generator at 10 kHz. The data from these LVDTs was demodulated and amplified using a "home made" device shown in figure 3-3 .
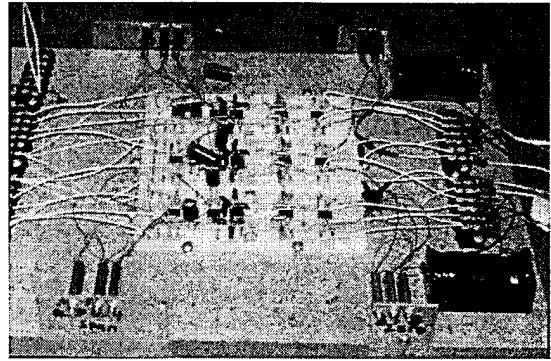
Figure 3-3: Demodulating Amplifier

Axial load and displacement data was recorded on an X-Y plotter. Some of the test data was digitized and stored on an IBM compatible personal computer. Data from tests performed on the INSTRON 1323 Biaxial test machine was digitized at 12 bits using an ISAAC 2000 analog to digital (A to D) conversion system. All other test data was digitized at 16 bits on an ANALOGIC 16 Bit A to D and D to A converter. The ISAAC and ANALOGIC converters had band widths of 0 to +10 volts and ± 5 volts, respectively. This means that when the strains measured by the strain gauges, or loads by the load cells, or displacement by the LVDTs registered voltages outside of the band width then the measurement recorded would be the boundary voltage for all values out side the band. For example a reading of + 15 volts from the gauge would be recorded as +10 volts on the ISAAC and +5 volts on the ANALOGIC. The results of such an occurrence will cause the graph of the value of the gauge to remain constant for some value resulting in plateaus or flat portions on the graphs. When this occurs the gauge or measurement is said to have "over ranged". The ISAAC A to D converter created a large amount of cross-talk (signal from gauge bleeding over to the other gauges). This phenomena would occur when the voltage on one channel exceeded 10 volts, which occurred when gauges broke, shorted, or measurements over ranged.

3.12 SPECIMEN PREPARATION

Mix Design

All triaxial specimens were prepared with a nominal water/cement ratio[1] between .42 and .47. The gradation of the aggregates used is given in table 3-1. The cement/aggregate ratio was .25 by weight. Superplasticizer, Fritz-pak Supercizer 6, was added to increase the workability of the mixes, .3% by weight of cement.

Seventy-five specimens measuring 2" in diameter by 4" tall were cast in three batches of 25. Twelve specimens 2" in diameter by 8" tall were cast in a separate batch. In addition, four batches of 4 rectangular specimens measuring 1.5" by 1.5" by 3" tall were cast.

Eight beams were cast and tested in three point bending to determine the tensile properties of the mix. The beams were 20" X 1.5" X 1.5". The beams were tested in three point bending. The supports were placed 18" apart and the load was applied in the center (figure 3-4). The average modulus of rupture is 987 psi.
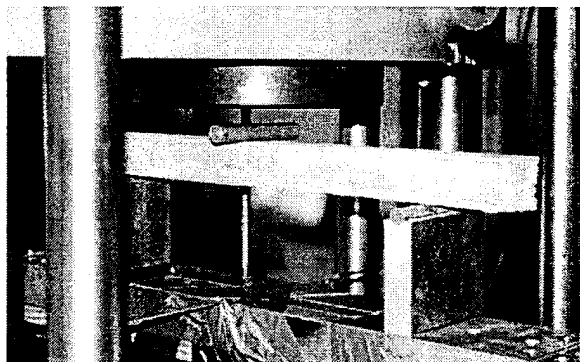
Cap blocks

Figure 3-4: Three Point Bending Test Setup

Cap blocks were used in the majority of the tests to relieve the friction between the platens and the specimens. The cap blocks were cut from 2" diameter by 4" tall cylinders using a concrete saw. The mix design used a water/cement ratio of .35 and a cement/aggregate ratio of .4. The gradation of the aggregate is shown in table 3-1. The ratio of superplasticizer to cement was increased to .5% by weight of cement. Rectangular blocks measuring 1.5" by 1.5" by 3" were also cast for use with the rectangular specimens.

TABLE 3-1

Sand Gradation	
Passing - Retaining Sieve # - Sieve #	% by Weight
#4 - #8	20
#8 - #16	20.5
#16 - #30	21
#30 - #40	15.5
#40 - #50	11
#50 - #100	9.5
#100 - #200	2
< #200	.5

[1]The term nominal is used here because the aggregates used were oven dried when used. Therefore, the actual water available for hydration was probably less.

Molding, Curing, and Cutting

Mortar was vibrated and rodded into molds, covered with damp rags and plastic, and left to set. The cylinders were removed after two days. After the mortar cylinders were removed from the molds, they were wrapped in wet rags. The cylinders were then sealed in plastic bags. The plastic bags were then placed in an oven at 60 degrees Celsius. All specimens and cap block cylinders were removed after 7 to 9 days. Specimens were tested more than 3 weeks after being poured. Exceptions to this were samples 1.01, 1.02, and 1.03 which were tested 14 days after being poured. Samples 1.04, 1.05, and 1.06 were tested 16 days after being poured. Samples 2.01, 2.02, and 2.03 were tested 10 days after being poured. The average strength of samples, 2.01, 2.02, and 2.03 was 42% lower than the average strength of 3.02, 3.05, 3.06, and 3.07 which were tested over 3 weeks after being poured. The average strength of samples 1.01, 1.02, and 1.03 was 12% lower than the average strength of 3.02, 3.05, 3.06, and 3.07. The strengths of all batches from other tests were comparable.

The ends of the 4" tall cylinders were cut off with a concrete saw to obtain flat parallel surfaces. Two of the 8" cylinders were cut down to 6" and two were cut down to 5". The remaining 8" tall cylinders were cut in half to obtain (16) 4" tall cylinders. The rectangular specimens did not require any cutting. Four sets of 1/2" thick cap blocks were cut from 4 of the cap block cylinders. The remaining cap block cylinders, as well as the rectangular cap blocks, were cut into 1" thick slices.

Lapping and Leveling

All specimens and cap blocks were polished on a lap table. The table contained a coarse grit (100) lap pad (figure 3-5). The process of cutting and polishing created surfaces that were smooth; however, they were not parallel and often had a camber or roundness to them. This was due to inaccuracies in the cutting and polishing equipment and methodology. The specimens and cap blocks were out of parallel by a maximum slope of 3% except for 4.08 and 4.13. The maximum camber, calculated as the difference in specimen height measured from the center of the specimen and the edge of the specimen, was no larger than .003". The camber and out of parallel slope of most specimens were smaller than the maximums.
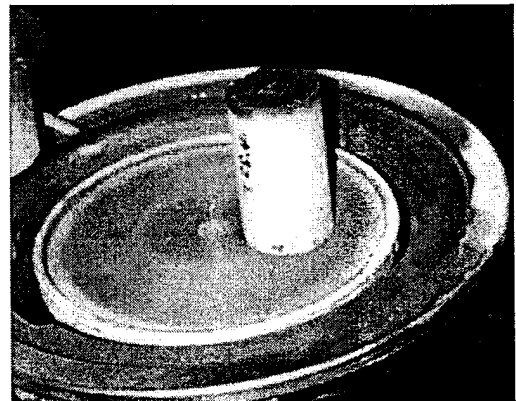
Figure 3-5: Lapping Table

To try and compensate for these problems, the specimens were matched with caps that would produce two load surfaces that were parallel. This was done by trying various combinations of caps and specimens, placing them on a flat level surface, rotating as necessary, and checking the level of the top of the cap block/specimen with a bubble level (figure 3-6). To ensure that the camber did not create small contact
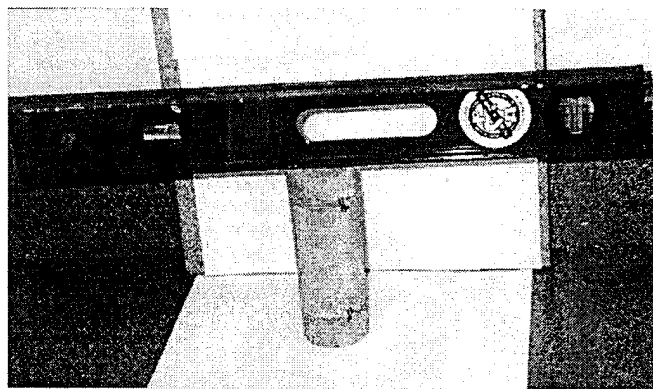
Figure 3-6: Sample Leveling

areas the interface between the cap and the specimen was visually inspected with a light source on the opposite side. If light was visible through the interface then the ends were sanded by hand, cleaned, refitted and re-examined. The caps and specimens were marked to ensure that the final placement and orientation of the specimens and blocks would produce two load surfaces that were parallel.

The loading surfaces on specimens 4.08 and 4.13 were so far out of parallel that a table mounted disk grinder was used to bring the specimens back to parallel. The use of the grinder heated the specimen to the point that several of the aggregates were glowing. The samples were tested; however, the results of the tests on these specimens are out of character with the rest of the samples. These samples were probably damaged by the over heating caused by the disk grinder. This grinding occurred after the gauges had been applied; therefore, data from these gauges is suspect.

Application of gauges

The surfaces where the gauges were to be attached were first sanded with 150 grit sand paper. The surface was washed and wet sanded with increasingly finer grits starting with 220 to 400. The surface was dried. The surface was then cleaned with Measurements Group, Inc., M-Prep Conditioner A. The surface was neutralized with Measurements Group, Inc., M-Prep Neutralizer 5. A thin coat of Measurements Group, Inc., M-Bond AE-10 adhesive was applied to the surface. The adhesive was worked into the surface irregularities and cured for 24 hrs.

The surfaces were again sanded with 150 grit sand paper until the coat of adhesive was removed down to the level of the mortar, leaving only the adhesive that filled the irregularities. Finer grits of sand paper were used to smooth the surface. The M-prep solutions were again used. Additional applications of adhesive were used until all surface irregularities were removed and a flat regular surface was obtained.

After the adhesive had been applied and sanded to obtain a smooth surface, the surface was prepped, using the M-Prep solutions, one final time for the application of the gauges. The gauges and terminal strips were laid out and attached to cellophane tape. Tape helped to position the gauges quickly, accurately, and securely once the adhesive was applied. Next the M-Bond AE-10 adhesive was applied to the surface and the tape with the gauges and terminal strips was pulled tight into position. A small pad of packing foam was placed over the gauges and a spring clamp was placed over the foam to apply pressure to the gauges while the adhesive was curing.

The adhesive cured for 24 hrs. The clamp and tape were then removed. The contacts were cleaned and any tarnish was removed. Wires were then soldered to the contacts using a resin core solder. The resistance of the gauges was checked and any bad gauges, wires, or contacts were replaced. At this point the specimens were ready for the application of a friction reducer and final preparation (figure 3-7).
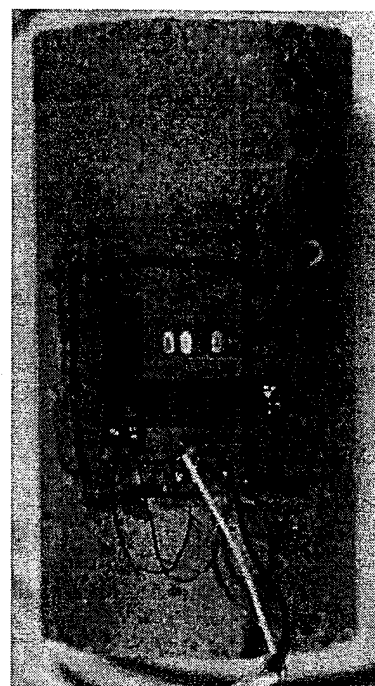
Figure 3-7: Specimen with Gauges, Terminals, and Wires

3.13 FRICTION RELIEF

The method used to relieve the friction between the specimen and the platens affects the failure of the specimen. Several methods of relieving the friction were tested and evaluated using uniaxial tests. Prior to performing the triaxial tests, uniaxial tests were performed on 31 specimens[2] including 4 cap block cylinders.

Fourteen[3] of the 31 specimens were tested without any relief of the friction. This was done to determine material properties for comparison to the cap block material and to the other methods. Six of the uniaxial tests used only a cap block for relieving the friction. Three used cap blocks with grease. The grease is described below. Three used friction reducing pads which are described below. Three used the friction pads and cap block; the pads were placed between the specimens and the cap blocks. For the last two tests a sheet, .01 inches thick, of rubber cut from previously used triaxial membranes was placed between the specimen and platens to relieve the friction.

---

[2]Two of these tests were conducted inside the triaxial cell filled with fluid but not pressurized. Two specimens were tested under hydrostatic pressure and then tested uniaxially that are not included in this number.

[3]This includes four cap block cylinders.

The results of these tests were used to select three methods for use in the triaxial tests. It was decided to use cap blocks alone, cap blocks with grease, and cap blocks with pads to relieve the friction.

Friction reducing grease and pads

The design of the grease selected was obtained from work by Labuz and Bridell [1991]. Labuz and Bridell determined the friction coefficient between steel and concrete for powdered graphite, molybenum disulfide, steric acid grease and a .05 mm thick Teflon sheet. They found that the steric acid grease had the smallest coefficient of friction, about .02. The coefficient of friction was determined using a double shear device. The grease was made by dissolving equal proportions by weight of steric acid into petroleum jelly (Vaseline) at 70 degrees Celsius.

Labuz and Bridell also tested 12 concrete cylinders in uniaxial compression, six 2" dia. and six 6" dia. Half of the specimens were tested using the steric acid grease as a friction reducer. The other half were tested without a friction reducer. They measured the "hoop" (lateral) strain at the center and at the top of the specimen. Figure 3-8 shows the ratio of strain at the center to the strain at the top of the specimen versus the axial stress obtained by Labuz and Bridell. The plot shows that there is a dramatic reduction in the

Figure 3-8: Ratio of Hoop Strain at the Center and the Top versus Axial Stress for the Cases of No Friction Relief and Steric Acid Grease for Relief (Labuz and Bridel [1991])

frictional effects with the use of the grease. Furthermore, the absence of a friction reducer will lead to a barreling affect, i.e. the lateral strains in the center are larger than those on the ends near the application of the friction.

Friction reducing pads were made by sandwiching the steric acid grease between two .004" thick polyethylene sheets. The polyethylene-grease-polyethylene pads are simply referred to as PGP pads. Mills [1967] used polyethylene sheets and axle grease while Zimmerman and Traina [1977] used Teflon sheets and axle grease. Galloway [1989] used Teflon sheets with silicon grease. Bertacchi and Belloti [1972] used polyethylene sheets and molybenum disulfide.

Final Preparation

The cylinders and cap blocks contained air voids on the surfaces which would tear the triaxial membranes (figure 3-9). In order to protect the membranes, the surface voids were filled with clay (figure 3-10). Richart at al [1928] had similar difficulties with air voids and used plaster paris to fill the voids. A small piece of packaging foam was placed over the strain gages and wire terminals to protect them. The specimens and cap blocks were wrapped in duct tape (fig 3-11). The specimens and cap blocks were then wrapped in a thin sheet of tin foil followed by two triaxial membranes (figure 3-12).
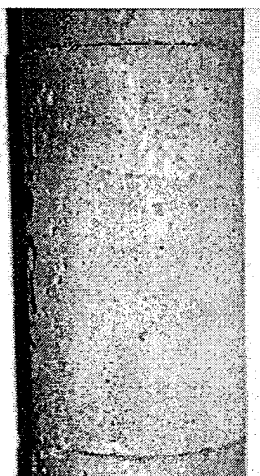
Figure 3-9: Sample with Voids

Figure 3-10: Clay Filled Voids
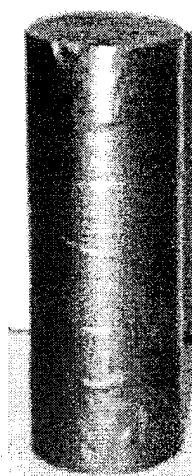
Figure 3-11: Specimen Wrapped in Tape
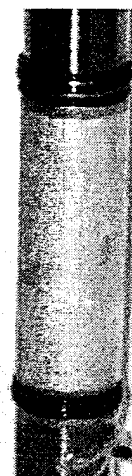
Figure 3-12: Specimen with Membranes and Plunger

The rectangular specimens and cap blocks were prepared in a similar manner. The voids were filled with clay. The specimen and cap blocks were wrapped in duct tape. Then, the specimen was coated with silicon caulk and left to dry in lieu of the aluminum foil and rubber membrane.

Tests on specimens using the cap blocks and PGP pads required a hose clamp to be placed at each interface of the specimen and the cap block to prevent slippage. Even with these clamps these specimens would slip. The amount of slippage increased with increasing confining pressure.

3.14 TEST MATRIX

Table 3-2 provides a summary of the tests with the type of friction relief and the confining pressures given. The tests using a cap block only, C, were performed first followed by the uniaxial tests. The tests using cap blocks with PGP pads, CPGP, were performed next. The tests using the cap blocks with grease,

CG, were performed last. Two specimens were tested in under hydrostatic compression removed from the test cell and retested in uniaxial compression.

TABLE 3-2

TEST SUMMARY

TEST NUM	FRICTN RELIEF	CONFINING PRESSURE	LOAD SEQNCE	TEST NUM	FRICTN RELIEF	CONFINING PRESSURE	LOAD SEQNCE	TEST NUM	FRICTN RELIEF	CONFINING PRESSURE	LOAD SEQNCE
T25.1.4	C	0 PSI	S	T25.4.17	C	4000 PSI	ICY/ICR/R	T25.2.15	CPGP	0250 PSI	ICY/ICR
T25.1.5	C	0 PSI	S	T25.1.14	C	4000 PSI	ICY	T25.3.9	CPGP	0250 PSI	S
T25.1.6	C	0 PSI	S	T25.1.10	C	6000 PSI	S	T25.3.13	CPGP	0250 PSI	ICY
T25.2.8	C	0 PSI	S	T25.1.11	C	6000 PSI	S	T25.3.10	CPGP	0500 PSI	S
T25.4.12	C	0 PSI	ICY	T25.1.12	C	6000 PSI	ICY	T25.3.14	CPGP	0500 PSI	ICY
T25.4.15	C	0 PSI	ICY	T25.2.23	C	6000 PSI	ICY/ICR	T25.3.11	CPGP	1000 PSI	S
T25.2.10	C	0250 PSI	S	T25.1.8	C	8000 PSI	S	T25.3.18	CPGP	1000 PSI	ICY
T25.2.11	C	0250 PSI	S	T25.1.9	C	8000 PSI	S	T25.3.20	CPGP	1000 PSI	ICY/ICR
T25.2.12	C	0250 PSI	ICR/C	T25.1.7	C	9000 PSI	S	T25.2.14	CPGP	2000 PSI	ICY/ICR
T25.4.9	C	0250 PSI	ICY/ICR/R	T25.3.1	CG	0 PSI	S	T25.3.25	CPGP	2000 PSI	S
T25.1.22	C	0500 PSI	ICY/ICR	T25.4.14	CG	0 PSI	ICY	T25.2.20	CPGP	4000 PSI	ICY/ICR/C
T25.1.23	C	0500 PSI	ICY	T25.4.16	CG	0 PSI	ICY	T25.3.23	CPGP	4000 PSI	S
T25.1.24	C	0500 PSI	S/C	T25.3.21	CG	0250 PSI	ICY	T25.3.12	CPGP	6000 PSI	ICY
T25.1.25	C	0500 PSI	S/C	T25.2.9	CG	0500 PSI	S/C	T25.3.24	CPGP	6000 PSI	S
T25.2.4	C	0500 PSI	S/C	T25.2.24	CG	0500 PSI	ICY/ICR	T25.1.1	NONE	0 PSI	S
T25.2.5	C	0500 PSI	S/C	T25.3.22	CG	0500 PSI	ICY/R	T25.1.2	NONE	0 PSI	S
T25.2.6	C	0500 PSI	S	T25.4.6	CG	0500 PSI	ICY	T25.1.3	NONE	0 PSI	S
T25.2.7	C	0500 PSI	S	T25.4.18	CG	1000 PSI	ICY	T25.2.1	NONE	0 PSI	S
T25.2.18	C	0500 PSI	ICY/ICR	T25.2.17	CG	2000 PSI	ICY/ICR	T25.2.2	NONE	0 PSI	S
T25.4.1	C	0500 PSI	S	T25.2.19	CG	2000 PSI	ICY/R	T25.2.3	NONE	0 PSI	S
T25.4.2	C	0500 PSI	S	T25.2.21	CG	2000 PSI	S	T25.3.2	NONE	0 PSI	S
T25.4.3	C	0500 PSI	S	T25.3.16	CG	2000 PSI	ICY/ICR	T25.3.5	NONE	0 PSI	S/R
T25.4.4	C	0500 PSI	S/C	T25.4.8	CG	2000 PSI	S/R	T25.3.6	NONE	0 PSI	ICY
T25.1.19	C	1000 PSI	ICR	T25.2.25	CG	2000 PSI	ICY	T25.3.7	NONE	0 PSI	ICY
T25.1.20	C	1000 PSI	ICY	T25.2.16	CG	4000 PSI	ICY/R	CP1	NONE	0 PSI	ICY
T25.1.21	C	1000 PSI	ICY	T25.3.15	CG	4000 PSI	ICY	CP3	NONE	0 PSI	S
T25.2.13	C	1000 PSI	ICY/ICR	T25.3.17	CG	6000 PSI	ICY	CP4	NONE	0 PSI	ICY
T25.1.16	C	2000 PSI	ICR	T25.4.7	CG	8000 PSI	ICY	CP5	NONE	0 PSI	ICY
T25.1.17	C	2000 PSI	ICR	T25.3.19	CG	hydro/uni	ICY/ICR	T25.3.3	PGP	0 PSI	S
T25.1.18	C	2000 PSI	ICY/C	T25.4.5	CG	hydro/uni	ICY/ICR	T25.4.10	PGP	0 PSI	ICY
T25.2.22	C	2000 PSI	ICY/ICR	T25.3.8	CPGP	0 PSI	S	T25.4.11	PGP	0 PSI	ICY
T25.1.13	C	4000 PSI	ICY	T25.4.19	CPGP	0 PSI	S	T25.3.4	RUB	0 PSI	S
T25.1.15	C	4000 PSI	ICY	T25.4.20	CPGP	0 PSI	ICY	T25.4.13	RUB	0 PSI	S

C - Denotes cap block only

CG - Denotes cap block with grease

CPGP - Denotes cap block with PGP pads

PGP - Denotes PGP pads only

RUB - Denotes rubber sheets only

S- Denoted standard triaxial w/ monotonically increasing displacement

ICY- Denotes intermittent cycling

ICR- Denotes intermittenet creep

C-Denotes creep from prepeak to post peak

R- Denotes relaxation

The rectangular specimens were tested at 0, 500, 1000, and 2000 psi. No strain measurements were taken during these tests. The triaxial tests were performed with cap blocks and PGP pads to relieve the friction.

Several tests were performed at 0, 250, 500, 1000, 2000, 4000, 6000, and 8000 psi. Problems with specimen slippage prevented CPGP tests at 8000 psi. Since the first set of tests on CG specimens were consistent with the results of the other tests it was decided to forego second tests at 250, 1000, 6000 and 8000 psi in favor of extra creep and relaxation tests at 500 and 2000 psi.

During the first tests with cap blocks only the orientation of the failure plane at 500 psi was essentially from one corner (edge) to the opposite. To preclude the possibility that the end effects might be influencing the results four tests were performed with longer specimens, two 5" long and two 6" long, using cap blocks for friction relief again at 500 psi.

Problems with the control of the Tinius Olson Super "L" required the use of a different machine until repairs could be made. Therefore, many of the tests were performed on the SATEC Systems machine. The control problems with the Tinius Olson machine caused sample T25.2.10 to break prior to the beginning of the test.

The tests were conducted using one of three main load sequences. The first was a standard triaxial loading where the displacement was monotonically increased up to and past the peak load (figure 3-13). The second, herein called intermittent cycling, ICY, was a standard triaxial loading but the load was cycled down to the hydrostatic pressure periodically, usually every 5 kips (figure 3-14). These tests were loaded into the post peak regime. The third type, herein called intermittent creep, ICR, was a standard triaxial loading but the loading was stopped at various points and allowed to creep for approximately 4 minutes and then the load was increased (figure 3-15). This was done until the load had gone into the post peak regime. Several of the tests used a combination of ICY and ICR (figure 3-16). Several of the specimens were "creept" from the prepeak regime to the post peak regime. In addition the load was relaxed during several of the tests (figure 3-17). These differing load sequences and the addition of creep and relaxation helped to paint a more complete picture of the behavior of the specimens under triaxial loads.

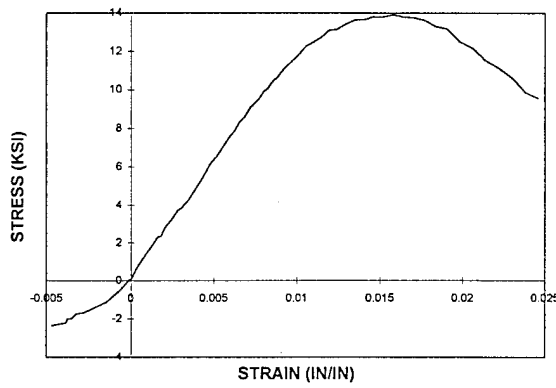**Figure 3-13: Standard Loading (S)**
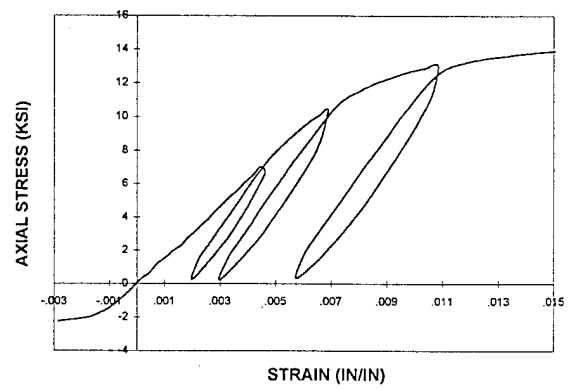**T25.3.25 Stress - Strain Curve**

Figure 3-14: Intermittent Cycling (ICY)
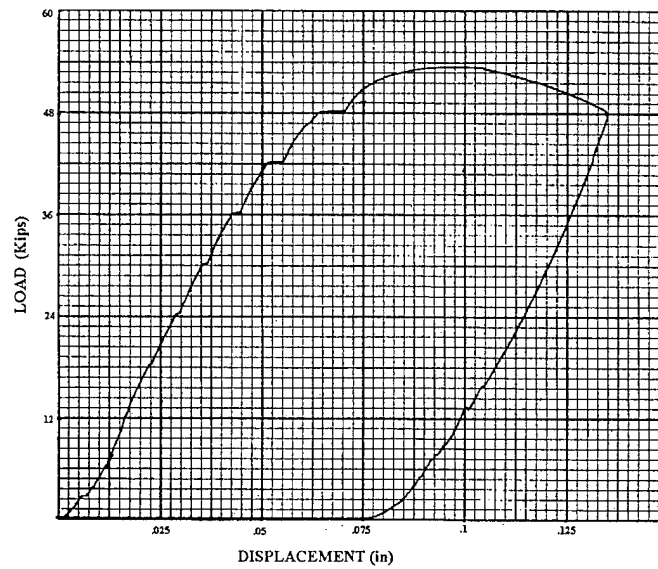**T25.2.25 Stress - Strain Curve**

Figure 3-15: Intermittent Creep (ICR)
T25.1.17 Load - Displacement Curve
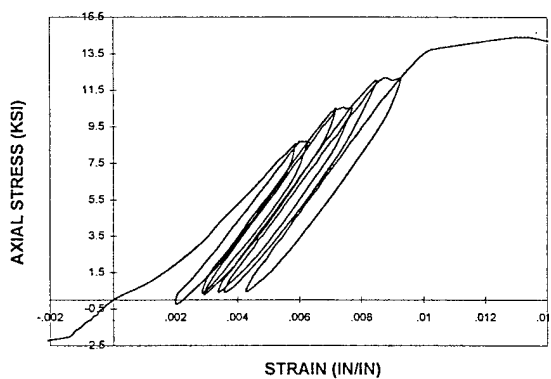
Figure 3-16: Intermittent Cycle/Creep (ICY/ICR)
T25.3.16 Stress - Strain Curve
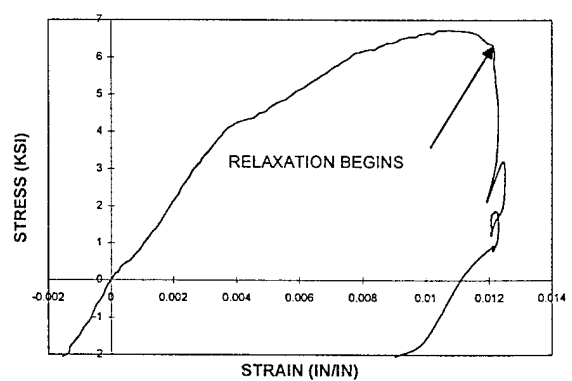
Figure 3-17: Relaxation (R)
T25.4.8 Stress - Strain Curve

Two specimens, T25.3.19 and T25.4.5, were tested under hydrostatic pressure and then tested uniaxially after the hydrostatic tests. The hydrostatic pressure was cyclicly loaded to increasing pressures up to 8 ksi. The pressure was held for 5 to 6 minutes to observe possible creep in the T25.3.19 (figure 3-18a). The pressure was held for 5 minutes at 8 ksi and 40 seconds for all others (figure 3-18b). Test T25.3.19 took 90 minutes and test T25.4.5 took 45 minutes total. The volumetric strains shown in figures 18a and 18b were obtained by simply multiplying the value from one strain gauge by 3. The bulk modulus was calculated to be 2400 ksi.
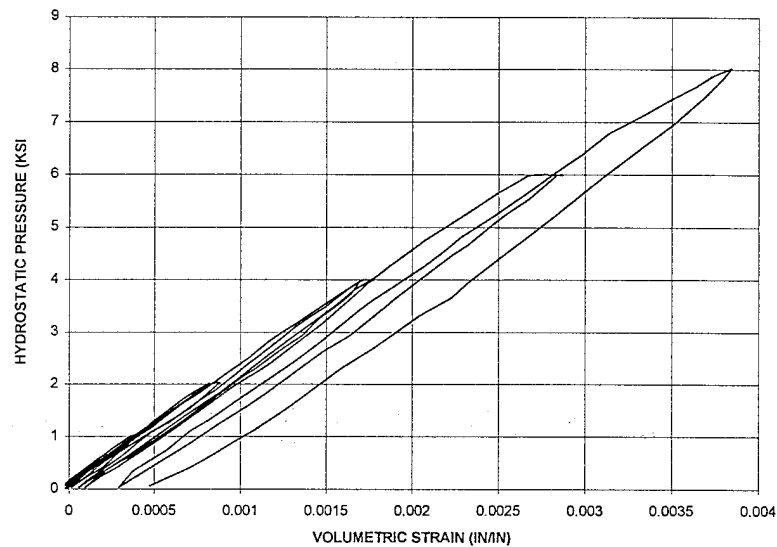
(a) T25.3.19
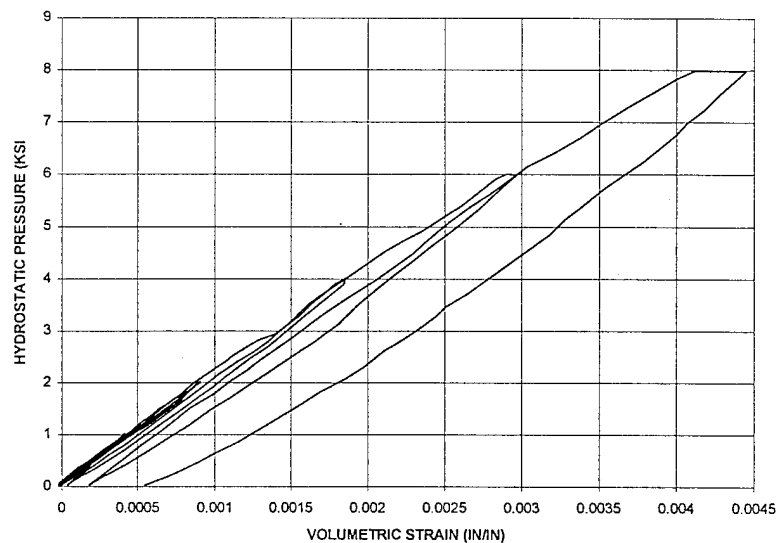
(b) T25.4.5

Figure 3-18: Hydrostatic Pressure versus Volumetric Strain for Hydrostatic Loading

Thirteen of the rectangular specimens were tested using a standard monotonically increasing displacement. Sample TR 4.2 was tested with intermittent cycling of the load. Samples TR 1.3 and TR 2.4 were tested under creep conditions near the maximum loads.

3.15 TEST PROCEDURE

A specimen was placed in the triaxial cell. The cell was then filled with hydraulic fluid. The top of the cell was set into place and the plunger inserted into the top. Air was bled out of the cell prior to starting the test. Five hundred pounds of axial load (159 psi) was applied prior to adding the lateral confining pressure. Then pressure was applied hydrostatically to the specimen, i.e. equal axial and lateral pressure; always maintaining a slight surplus of axial load. Once the desired confining pressure was applied then the confining pressure was maintained while the axial load was increased. The load was removed at or after the peak load.

The displacement was manually controlled except for the uniaxial tests performed on the Instron 1323 which were electronically controlled. The rate of deformation was between .005 in/min and .01 in/min for the tests. The rates varied from tests to test slightly and within a test the rate was not constant. Except for the tests noted below most test rates were close to the range mentioned above. Rate data was not recorded for tests on Batch 1 samples nor on sample T25.2.1 through T25.2.7 and several other miscellaneous tests in which the instrumentation failed.

T25.1.21 was rapidly, "shock", loaded due to a problem with the universal testing machines control unit. The rate changes did not occur at the same location on the loading curve and were not applied for long durations.

The displacement rate was increased from .006 in/min to .014 in/min at several points during the loading sequence for about 30 seconds each for sample T25.2.23. Four increases were applied starting at about 90% of the peak load prior in the prepeak regime and continued into the post peak regime. The displacement rate was increased from .005 in/min to greater than .1 in/min at the peak load 15 seconds for T25.2.17 and T25.2.21. The displacement rate was increased from .005 in/min to .025 in/min at the peak load 45 seconds for T25.4.7.

The displacement rate was increased from .006 in/min to greater than .05 in/min at 98% of the peak load in the post peak regime for sample T25.2.18. The displacement rate was increased from .006 in/min to greater than .015 in/min at 89% of the peak load in the post peak regime for sample T25.2.14.

The displacement rate was slowly and continuously increased during the loading from .005 in/min to greater than .025 in/min for T25.3.23, T25.3.24, and T25.3.25. The displacement rate for sample T25.3.8 was greater than .02 in/min throughout most of the test.

Specimens T25.3.19 and T25.4.5 were hydrostatically loaded prior to loading them uniaxially. The specimens were prepared similar to the other triaxial tests. However, the ends of the triaxial membranes were sealed with thick layers of silicone caulk prior to placing the specimens in the cell. The specimens were set into the cell so that the plunger would not apply an axial load on the specimens. The cell was pressurized to 250, 500, 1000, 2000, 4000, 6000, and 8000 psi. After the hydrostatic tests were concluded the specimens were tested uniaxially.

In tests where data was digitized and stored on computer all equipment was allowed to warm up for thirty minutes prior to testing. The signal conditioners were connected to the gauges at least 5 minutes prior to the beginning of each test.

3.16 TRIAXIAL CELL FRICTION

It is known that there is some friction between the plunger and the test cell. Since the load measurements reflect the load applied to the plunger and not the specimen it stands to reason that the actual load on the specimen was lower than measured under positive displacement rate and higher than measured under negative displacement rate. In an attempt to quantify and correct for this friction a steel sample was tested in the cell and data collected. A model was developed to eliminate the hysterisis in the steel tests. However, application of the method to the mortar specimens rendered an implausible result, a negative hysterisis in the mortar.

Lacking an acceptable alternative for accounting for the friction, the author acknowledges the fact that the friction exists but does not account for it in the load data.

3.20 BIAXIAL TESTS

In previous studies of the behavior of cementitious materials, petrologic studies were performed by Knab et al [1984], Shah and Sankar [1987], Shah and Chandra [1970], Palanswamy and Shah [1974] Shah and Slate [1965], Slate and Olefski [1963], Van Mier [1990b], and Swartz [1991]. This was often done by unloading the specimen and then impregnating it with colored epoxy. After the epoxy cured, the specimens were cut into sections which were then viewed under a microscope. In this study "two-

dimensional" specimens were tested in biaxial compression in hopes that a petrologic study can be performed in real-time without having to unload, impregnate, or cut the specimens.

The specimens used in these tests were intended to be orthotropic, with one direction stronger than the other two. The intent was to create a specimen whose failure plane under biaxial loading would be parallel, not perpendicular, to the direction of zero normal stress. This was accomplished by using ceramic rods as aggregates.

Buyukozturk, Nilson, and Slate [1971] performed similar biaxial tests. They used 1-1/4" diameter limestone cylinders as aggregate rods in a mortar matrix. The specimens measured 5" X 5" X .5". The primary purpose of there study was to examine the development of mortar/aggregate bond cracking and mortar cracks. The load was applied by using brush platens to two directions leaving the axis of the cylinders free from load. The lateral load was varied as a percentage of the axial load (0%, 20%, 50%, and 100%). They found that cracks first initiate at the mortar aggregate interface at 40% of the peak load. Mortar cracks began to form that bridged these bond cracks at 80% of the maximum load. The failure was reported to be vertical in all cases.

3.21 EQUIPMENT SETUP

The axial load was applied with an Instron 1323 biaxial test machine. The machine was equipped with an upper load platen that could tilt to accommodate specimens with non-parallel load surfaces. The lateral load was applied with a hydraulic ram that was mounted to a frame placed on the Instron machine (figure 3-19)
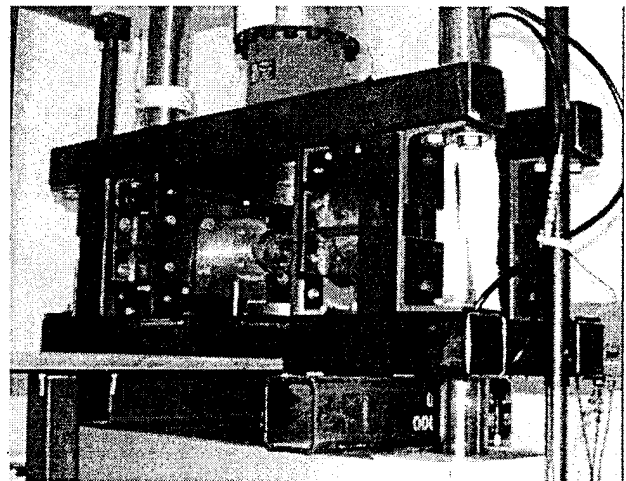
Figure 3-19: Biaxial Testing Machine

The lateral loading device was made by mounting two I beams with stiffeners to two support frames constructed of steel box beams (figures 3-20a-c). Load was applied by a hydraulic ram with a platen on a swivel ball joint. The ram was mounted to one of the I beams. The load was measured with a custom made load cell that was mounted to the I beam directly opposite the ram (figure 3-21).
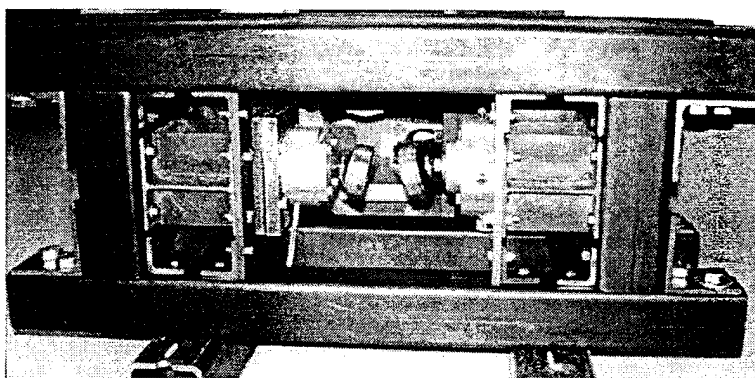
(a) Side View
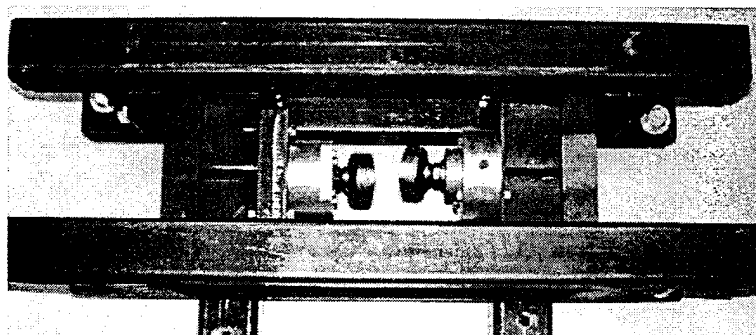
(b) Top View
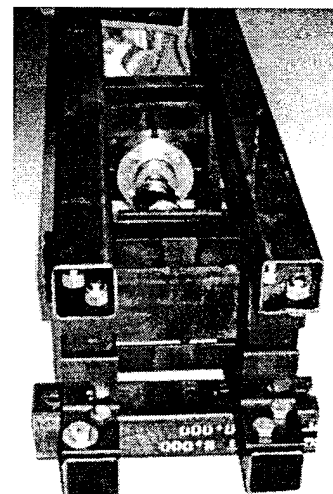
(c) End View

Figure 3-20: Lateral Loading Device
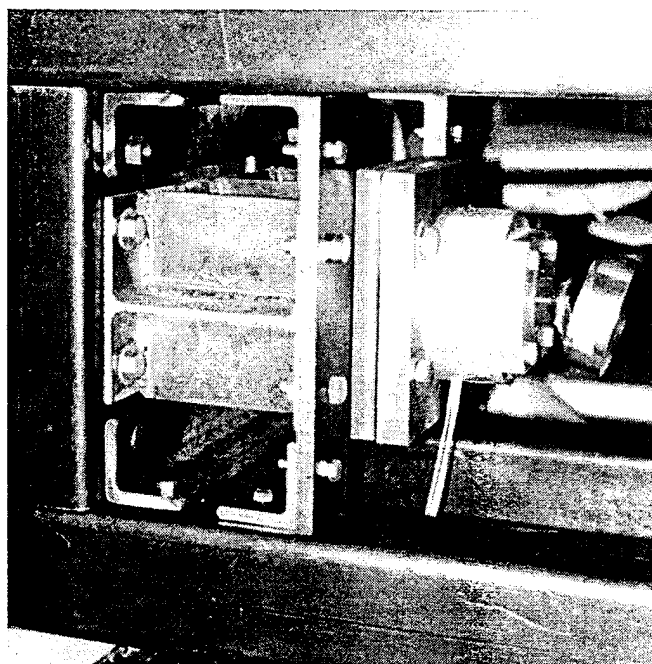
Figure 3-21: Mounted Load Cell

Two load cells were made to handle two different ranges of loads (figures 3-22a and b). Each load cell consisted of an aluminum spool with four strain gauges setup in a full bridge. The spools were threaded for mounting on a steel plate. An aluminum shield was placed over the spool to protect it (figure 3-23). After the shield was in place a platen with swivel ball joint was placed on the spool (figure 3-24).
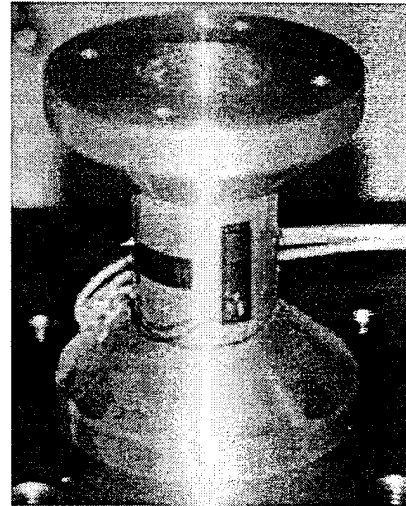
(a) 80 Kip Capacity   (b) 30 Kip Capacity

Figure 3-22: Load Cells
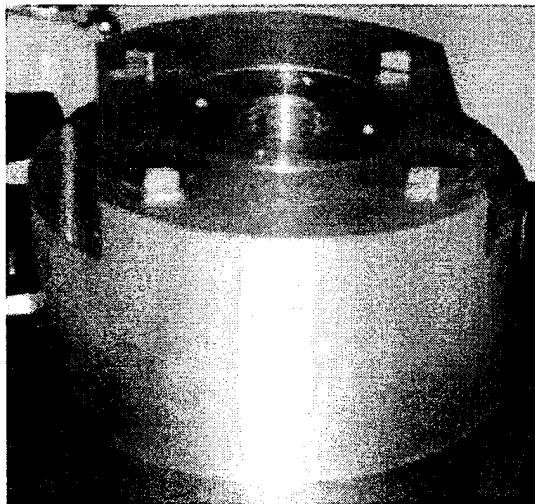
Figure 3-23: Load Cell with Shielding   Figure 3-24: Load Cell with Swivel Platen

The frame with ram and load cell was mounted on the Instron (figure 3-19, 3-25a and b). Four steel rods were placed between the frame and the Instron to allow the frame to move freely as the lateral load was applied (fig 3-26).

(a)

(b)

Figure 3-25: Lateral Load Device Positioned on the Instron Test Machine
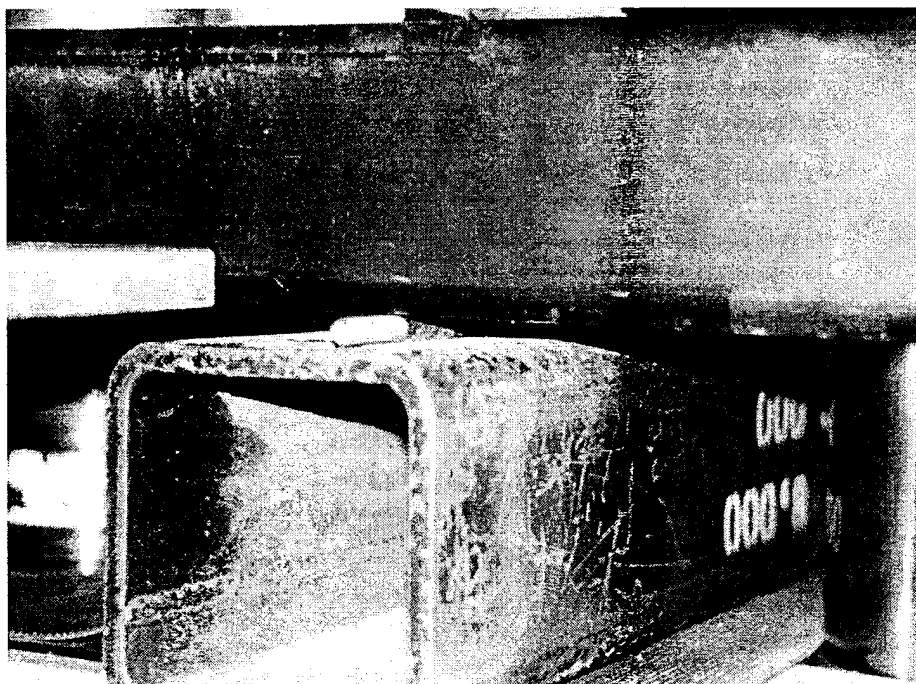
Figure 3-26: Rod Placed Beneath the Lateral Loading Device to Allow Friction Free Lateral Movement

The Instron 1323 has internal displacement measuring capabilities. Strain measurements were taken on all of the biaxial tests. Four Measurements Group, Inc., EA-06-500BL-350 strain gauges were placed on each sample.
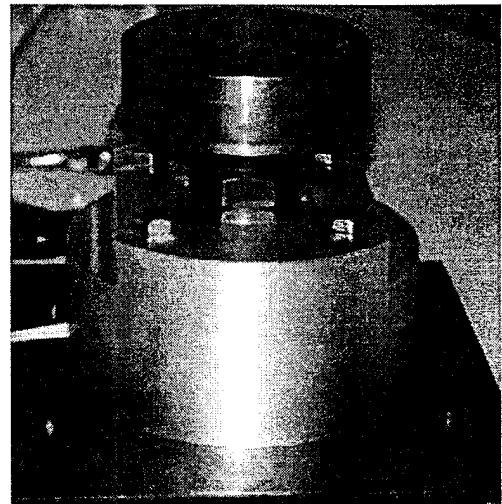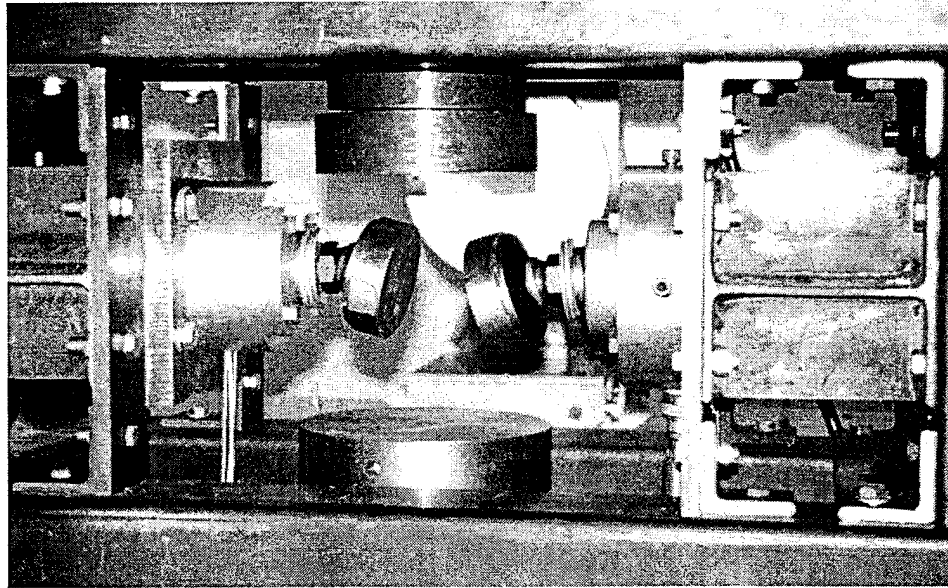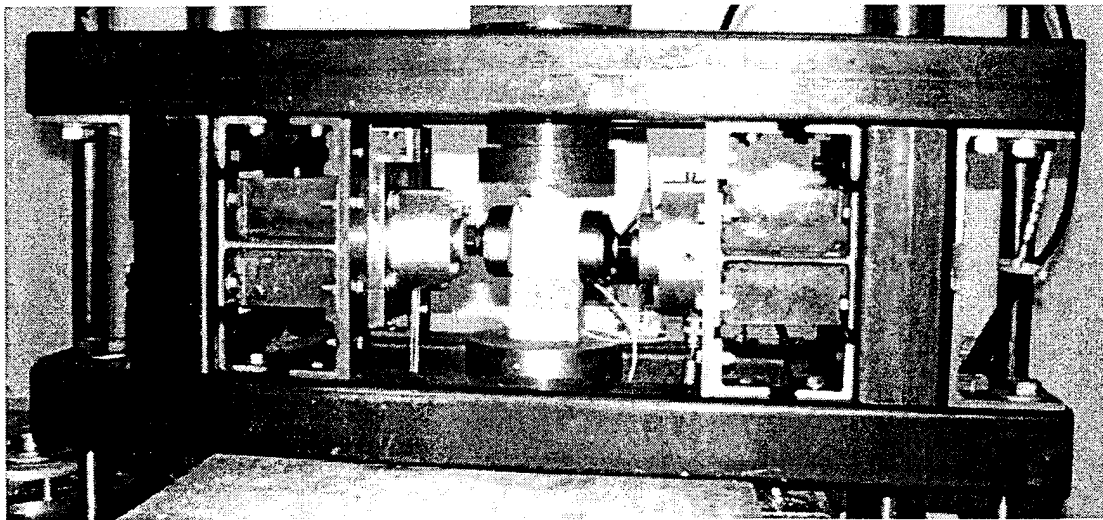
Two of the gauges were located at the midheight of the specimen on the non-loaded faces. One of the gauges was positioned to measure the axial strain and the other was positioned to measure the lateral strain. The other two gauges were located near the bottom edge of the specimen and positioned for measuring the axial and lateral strains. A Schaevitz LVDT and an ATA-100 analog transducer amplifier was used to measure the displacement in the direction out plane to the loading. The LVDT was mounted on a lever to amplify the displacements by a factor of 10.

All strain gauges used a quarter bridge setup. The strain gauges used a 10 volt DC excitation potential. Data from the strain gages was amplified using a Dynamics model 2500 signal conditioner.

Axial load and displacement data was recorded on an X-Y plotter. All of the test data was digitized and stored on an IBM compatible personal computer. Data was digitized at 12 bits using an ISAAC 2000 analog to digital conversion system.

3.22 CERAMIC RODS

Ceramic rods were chosen for the aggregates because they closely resembled rock. The materials were cheap and readily available. Furthermore, a variety of sizes and textures could be obtained easily. Pecos clay was obtained from a local ceramic store. This clay produces a porcelain when sintered at 1200 degrees Celsius for 5.5 hours.

The rods were manufactured by pressing the clay through an extruder (figure 3-27). The extruder consisted of a 2" diameter pipe 12" long with a cap mounted on a wooden stand with a plunger on a lever handle (figure 3-28). The cap had a large hole drilled into it to allow a die to be placed into it (figure 3-29). Four dies were prepared by drilling a hole into a 1/8" thick aluminum disk (figure 3-30). The edges of the hole were chamfered on the side holding the clay. The four sizes of holes used were 3/32", 1/8", 3/16", and 1" diameter.
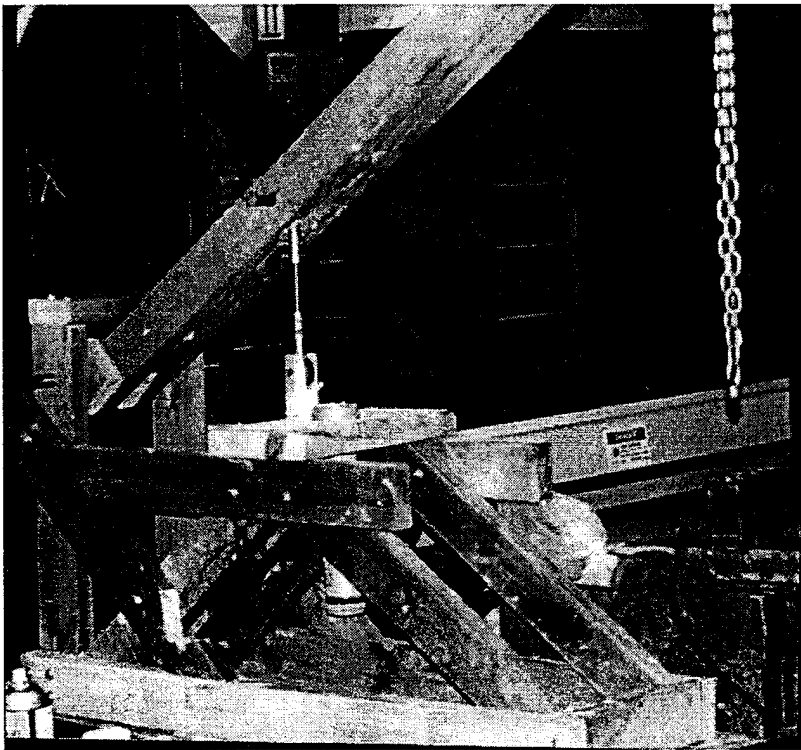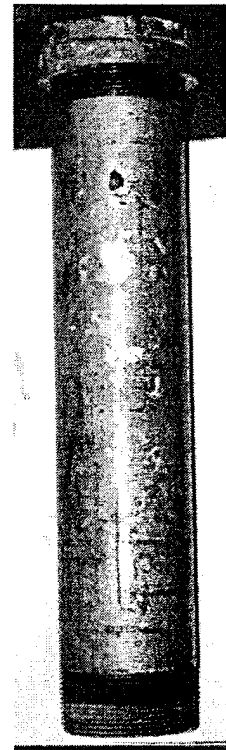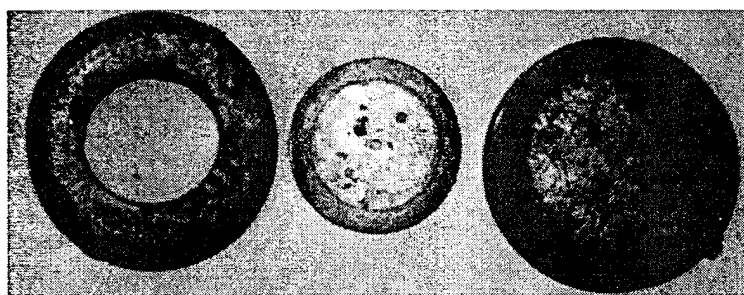

Figure 3-27: Clay Extruder

Figure 3-28: Extruder Tube

(a) Die Retainer   (b) Die Plate   (c) Cap

Figure 3-29: Extruder Cap and Die
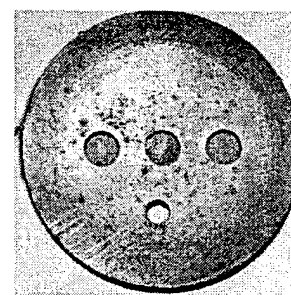
Figure 3-30: Die Plate with Extrusion Holes

Clay was placed in the pipe (figure 3-29). A cap with no holes was placed on the end of the pipe (figure 3-29c). The cap was loosely fitted to allow water to pass through the thread grooves. Weights were placed on the end of the lever arm so that the pressure on the clay was 300 psi. The pressure was applied for 6 hours to consolidate the clay. The weight and cap were removed. The cap was replaced with the die retainer and a die plate (figure 3-29a and b). Weight was applied to the lever until the clay began to flow through the die.

Three samples of clay were taken prior to and after consolidation. These samples were used to determine the moisture content of the clay. The moisture content was 25% prior to consolidation and 22% after consolidation. The density of the sintered rods was (2.4 g/cc).

The clay strands were cut to lengths of approximately 16". The strands were rolled between 2 sheets of sandpaper (40 grit for the 3/16 and 1/8; 80 grit for the 3/32). The use of the sandpaper added texture to increase the bond between the rods and the cement matrix (see fig 3-31). The 1" diameter strands were cut to 2" and 10" lengths. These were not rolled between sandpaper.
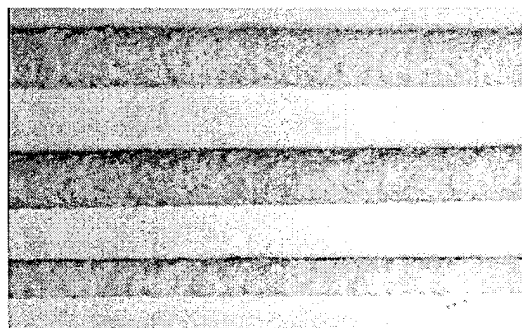
Figure 3-31: Textured Ceramic Rods

The strands were placed on a wood tray with grooves cut into it to keep the strands straight. The 1" diameter strands were dried in an oven at 150 degrees Celsius for three days. The smaller strands were air dried for 24 hours. After drying, the rods were placed in a kiln and heated to 1200 degrees Celsius. The rods were fired at 1200 degrees Celsius for 5.5 hours.

The 1" diameter rods were used to determine the strength properties of the rods. Twelve rods measuring 1" in diameter and 2" long were tested in uniaxial compression. No effort was made to relieve the friction

between the platens and the specimens. The average compressive strength determined from these tests was 12.5 ksi. The tensile strength was determined from 3 point bending tests on seven 10" long rods. The modulus of rupture was 5.1 ksi.

Hunt [1986] presents a table of common rock types and typical engineering properties. The unconfined compressive strength is between 10 and 25 ksi for Granite, 15 and 30 ksi for Basalt, and 15 and 35 ksi for Quartizite. The modulus of rupture is between 400 and 700 psi for Granite, 700 and 1250 psi for basalt, and 600 and 800 psi for Quartzite. Williams and Uy [1978] present data showing ceramic materials with a modulus of rupture 10 to 20 times larger than those obtained from the porcelain used in this study. Typical ceramics have mass densities ranging from 2.0 to 6.5 g/cc. In general the higher the density the higher the strength.

3.23 SPECIMEN PREPARATION

Mix Design

Twenty-one specimens were prepared using three different arrangements of the ceramic rods (7 specimens each). The mix design followed that of the triaxial test specimens. The ceramic rods were considered as aggregates; therefore; the actual amount of sand used was decreased. Table 3-3 shows the gradation of materials. Specifically, the sand that passes the #4 sieve and retained on the #8 sieve was decreased by the weight of the 3/16" and 1/8" rods used. The sand that passed the #8 sieve and retained on the #16 sieve was decreased by the weight of the 3/32" rods used. The 3/32" rods were used to replace some of the #16-#30 sand also.

In the first two mixes the ceramic rods were used to reinforce the mix in one direction. The primary idea was to produce a specimen that would have cracking initiate on the surface of the largest sand aggregate and the rods would impede the development of damage/cracks in a direction perpendicular to them. Furthermore, it was important that the ceramic rods not influence the development of the damage or cracks in a direction parallel to them.

In the first mix (64) 3/16" diameter rods were placed in a square matrix pattern (figure 3-32). The rods were placed 15/32", 2.5 times the diameter, on centers; thus, leaving a space of 1.5 times the diameter of the largest aggregate between adjacent rods. The gradation of rods and sand are shown in table 3-3

The second mix was identical to the first mix with the exception that each row of rods was shifted over 1/2 the diameter of the rod to the right of the row above it (figure 3-33). This second pattern was created to

examine the influence of the rods on the strength and failure characteristics in the plane perpendicular to the rods.

TABLE 3-3

Sand and Rod Gradation for Batches 1 and 2	
Passing - Retaining Sieve # - Sieve #	% by Weight
(64) 3/16" dia rods (#4 - #8)	10
#4 - #8	10
#8 - #16	20.5
#16 - #30	21
#30 - #40	15.5
#40 - #50	11
#50 - #100	12
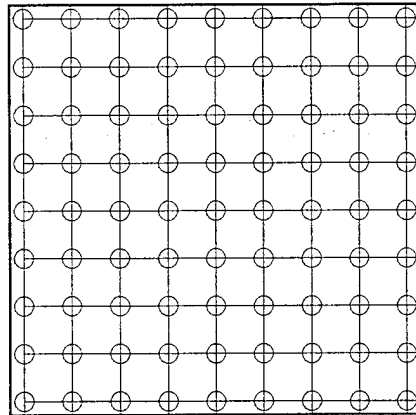
Figure 3-32: Rod Configuration Batch 1   **Figure 3-33: Rod Configuration Batch 2**
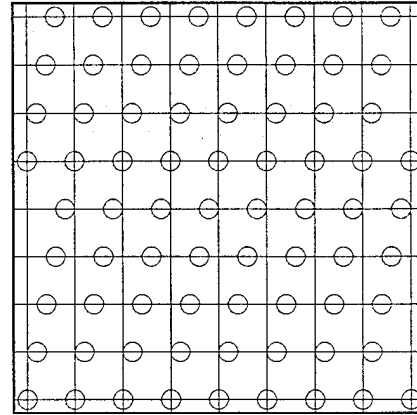
The third mix used (63) 3/16" dia, (142) 1/8" dia. and (500) 3/32" diameter rods (figure 3-34). The rods were randomly mixed and placed in a 4" X 4" X 15" mold with a mortar mix. The water cement ratio was raised to .5 to increase flow around the rods. A "2 dimensional" specimen was produced with similar proportioning to that of the triaxial specimens. The gradation of rods and sand are shown in table 3-4.

TABLE 3-4

Sand and Rod Gradation for Batch 3	
Passing - Retaining Sieve # - Sieve #	% by Weight
(63) 3/16" & (142) 1/8" dia rods (#4 - #8)	20
(446) 3/32" dia rods (#8 - #16)	20.5
(54) 3/32" dia rods (#16 - #30)	2.5
#16 - #30	18
#30 - #40	15.5
#40 - #50	11
#50 - #100	12
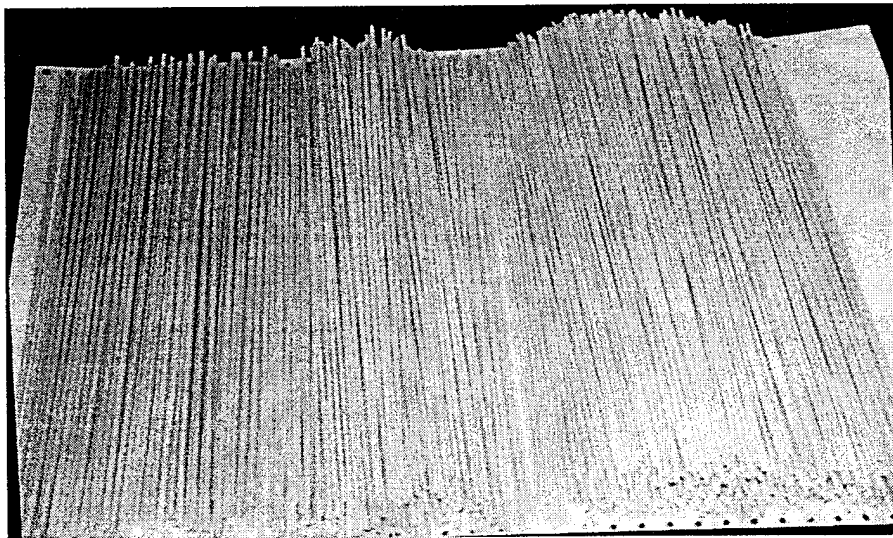
Figure 3-34: (705) Ceramic Rods for Batch 3 Specimens

Cap Blocks

Cap blocks were used in all tests to relieve the friction between the axial load platens and the specimens. The cap blocks were cut from 4" X 4" X 16" using a concrete saw. The mix design used a water/cement ratio of .35 and a cement/aggregate ratio of .4. The gradation of the aggregate is shown in table 3-1. The ratio of superplasticizer to cement was increased to .5% by weight of cement.

The rods for the first two mixes were mounted in forms to hold the rods in the proper relative positions. (figure 3-35). These rods were placed inside the 4" X 4" X 16" mold relative. The mold was placed on a vibrating table. The mortar was placed over the rods and molds in small amounts to pre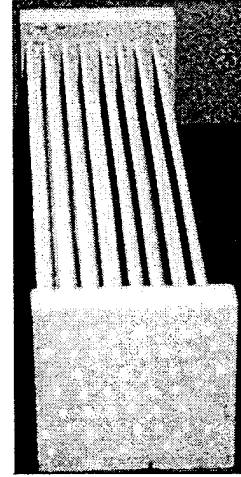clude breaking the rods. The vibration of the table helped the mortar flow around the rods. A thin rod was used to help move and compact the mortar around the rods.
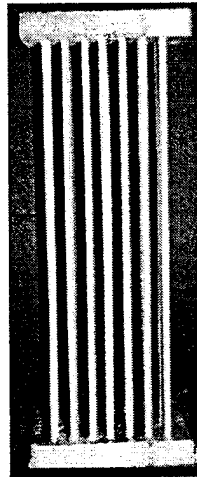
(a) Batch 1 Square Pattern   (b) Batch 2 Offset Pattern

Figure 3-35: Ceramic Rods Mounted on Forms

The last configuration contained too many rods to use a specific form. To cast this brick the mold was placed on the vibrating table. Mortar mix was placed in the form to a depth of about 1/2" (figure 3-36). A hand full of the randomly mixed rod was placed in the form (figure 3-37). While the table was vibrating the rods were hand worked into the mortar (figure 3-38) until just the tops of the top rods are showing (figure 3-39). Additional mortar mix was added, about 1/2" deep. Another handful of rods was added and vibrated into place. This process continued until the mold was filled.

Mortar was vibrated into molds, covered with damp rags and plastic, and left to set. The bricks were removed after two days. After the mortar bricks were removed from the molds, they were wrapped in wet rags. The bricks were sealed in plastic bags. The plastic bags were placed in an oven at 60 degrees Celsius. All bricks were removed after one week.

Figure 3-36: Pour Paste in Form

Figure 3-37: Place Ceramic Rods

Figure 3-38: Work Mortar Around Rods

Figure 3-39: Work Rods Until Lightly Coated

Each brick was cut into (7) 4" X 4" X 1.5" slices. The sides of each slice were trimmed with the concrete saw to remove portions containing large surface irregularities. The resulting samples ranged in height between 3" to 3.4" and ranged in width from 1.6" to 3.7". The samples from batch 3, the batch with the most rods, were smaller than the samples from the other two batches.

Cap blocks approximately 1.5" thick were cut to match each specimen for placement between the specimen and the axial load platens. They were cut .01" to .04" smaller than the width of the samples to ensure the lateral platens loaded the specimen not the cap blocks.

Lapping and Leveling

All specimens and cap blocks were polished on a lap table. The table contained a coarse grit (100) lap pad (figure 3-40). The process of cutting and polishing created surfaces that were smooth; however, they were not parallel and often had a camber or roundness to them. This was due to inaccuracies in the cutting and polishing equipment and methodology. The specimens and cap blocks were out of parallel by a maximum slope of 2%. The maximum camber, calculated as the difference in specimen height measured from the center of the specimen and the edge of the specimen, was no larger than .008". The camber and out of parallel slope of most specimens were smaller than the maximums. The swivel capabilities of the load platens compensated for the out of parallel problem.

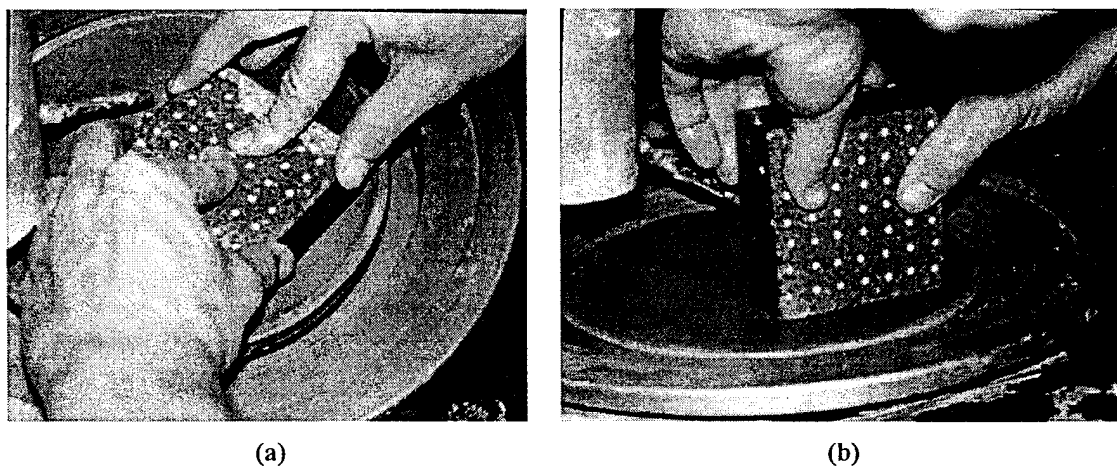(a)   (b)

Figure 3-40: Polishing Specimens on a Lapping Table

Application of gauges

The surfaces where the gauges were to be attached were first sanded with 150 grit sand paper. The surface was washed and wet sanded with increasingly finer grits starting with 220 to 400. The surface was dried.

The surface was then cleaned with Measurements Group, Inc., M-Prep Conditioner A. The surface was neutralized with Measurements Group, Inc., M-Prep Neutralizer 5 (figure 3-41). A thin coat of Measurements Group, Inc., M-Bond AE-10 adhesive was applied to the surface (figure 3-42). The adhesive was worked into the surface irregularities and cured for 24 hrs.

Figure 3-41: Cleaning and Neutralizing
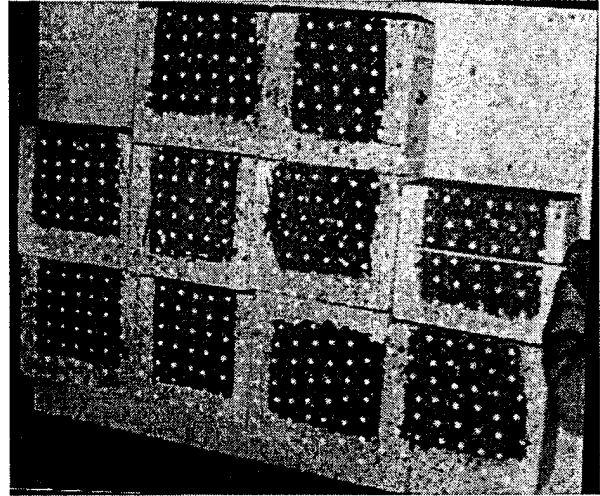
Figure 3-42: Working Adhesive into the Surfaces

The surfaces were again sanded with 150 grit sand paper until the coat of adhesive was removed down to the level of the mortar, leaving only the adhesive that filled the irregularities. Finer grits of sand paper were used to smooth the surface. The M-prep solutions were again used. Additional applications of adhesive were not necessary.

The gauges and terminal strips were laid out and attached to cellophane tape (figure 3-43). Tape helped to position the gauges quickly, accurately, and securely once the adhesive was applied. Next the M-Bond AE-10 adhesive was applied to the surface and the tape with the gauges and terminal strips was pulled tight into position. A small pad of packing foam was placed over the gauges and a spring clamp was placed over the foam. The clamp applied between 10 to 20 psi of pressure to the gauges while the adhesive was curing .
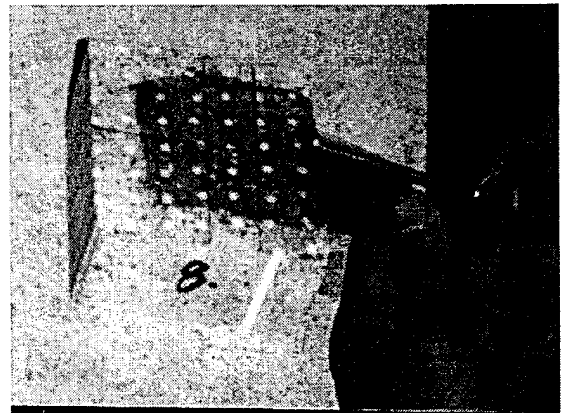
Figure 3-43: Attaching Tape\Gauges

The adhesive cured for 24 hrs. The clamp and tape were then removed. The contacts were cleaned and any tarnish was removed. Wires were then soldered to the contacts using a resin core solder (figure 3-44). The resistance of the gauges was checked and any bad gauges, wires, or contacts were replaced. At this point the specimens were ready for the application of a friction reducer and final preparation.

Figure 3-45 shows the finished surface of several specimens. Figure 3-46 provides a close up view of the rods and the surrounding mortar matrix. Figure 3-47 shows a close-up of the bond between an 1/8" diameter ceramic rod and surrounding matrix for a preliminary test sample containing fewer rods and a higher percentage of larger aggregates.
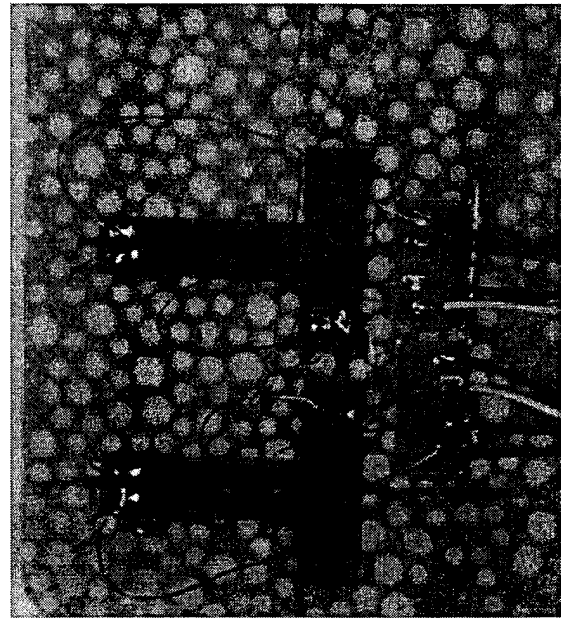
Figure 3-44: Gauges Wired
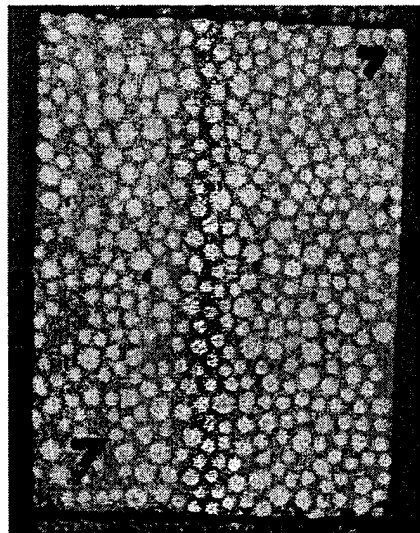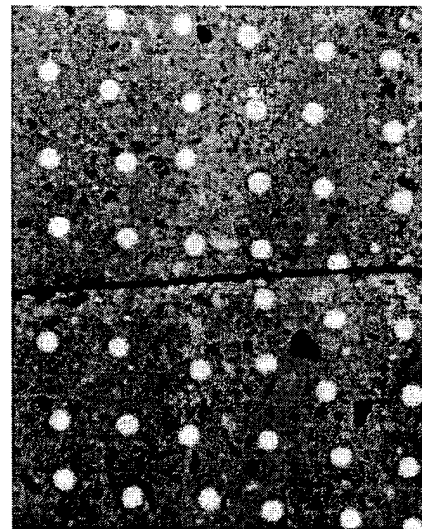
(a) Batch 3
(b) Batches 1 and 2

Figure 3-45: Polished Surfaces of Several Specimens

3-30
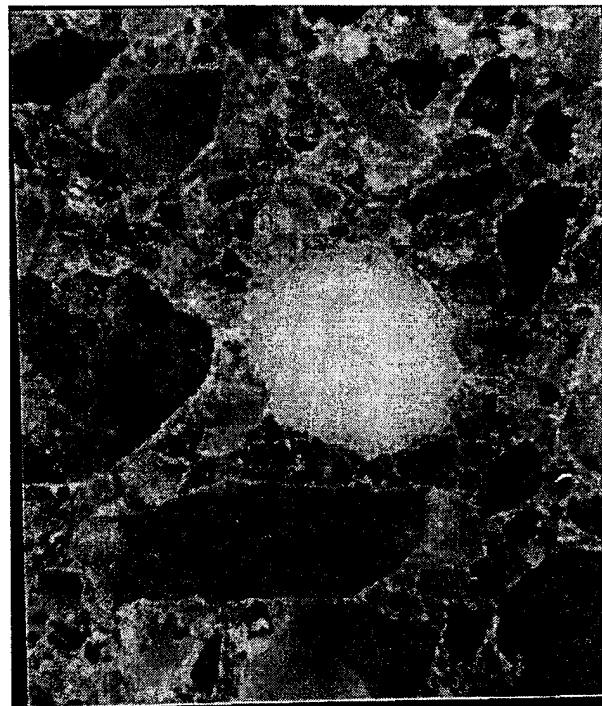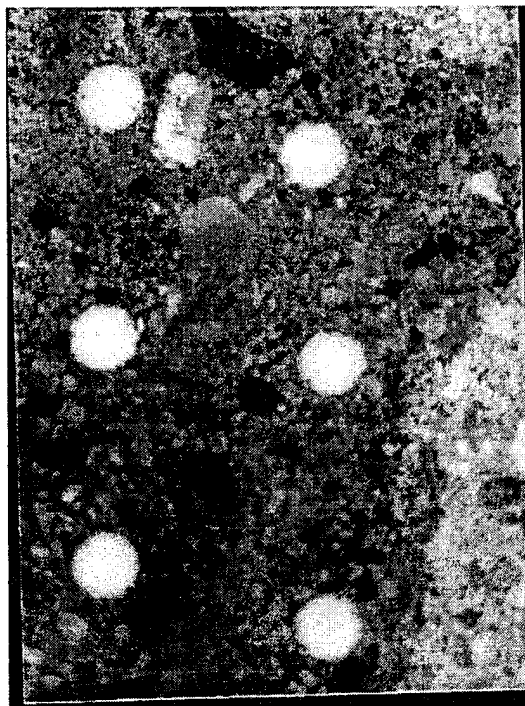
Figure 3-46: Close-up of Rods\Mortar Batch 2 **Figure 3-47: Close-up of Rod\Matrix Interface ·**

3.24 FRICTION RELIEF

Cap blocks were used on all tests to relieve friction between the top platens and the specimens. Grease, the same as for the triaxial tests, was also used to aid in friction relief on all tests except for B.1.1, B.1.2, B.3.1, and B.3.5. Grease was applied to the sides of the specimens to relieve the friction between the side platens and the specimens in all biaxial tests.

3.25 TEST MATRIX

Table 3-5 shows the lateral pressures applied to the samples tested. The samples from batches 1 and 2 that were uniaxially tested broke with failure planes that were not parallel to the direction of zero stress; therefore, the remaining samples from those batches were not tested. The cement matrix material in the samples from these batches was too strong in comparison to the rod strengths. The average uniaxial strength for batches 1 and 2 was 6.75 and 6.5 ksi, respectively. The higher water cement ratio for batch 3 decreased the strength of the cement matrix so that the failures were parallel to the rods, i.e. the normal to the failure plane was in the plane of loading. The uniaxial strength of batch 3 was 3.55 ksi.

TABLE 3-5

BIAXIAL TEST SUMMARY					
SAMPLE	LATERAL PRESSURE (psi)	SAMPLE	LATERAL PRESSURE (psi)	SAMPLE	LATERAL PRESSURE (psi)
B1.1	0	B2.3	0	B3.4	300
B1.2	0	B3.1	0	B3.5	500
B1.3	100	B3.2	100	B3.6	750
B2.1	0	B3.3	200	B3.7	600
B2.2	100				

3.26 TEST PROCEDURE

The biaxial samples were prepared and tested prior to the triaxial tests. The samples were placed between the lateral platens. The axial platens were brought in contact with the specimen. The gauges were then connected to the signal conditioners. Two video cameras were positioned to view the specimen, one from a wide view and the other from a close up view. The close up camera was focused on an area approximately 2.5" by 2.5" square. The signal conditioners were warmed up for 5 minutes and then the gauges/amplifiers were balanced.

The axial load was displacement controlled. The axial displacement was applied at a rate between .003 in/min and .01 in/min. The rate varied from test to test and during each test. The lateral load was applied to the sample using a hand pump for the hydraulic ram. The lateral load was applied so that the axial and lateral pressures were the same up to the prescribed pressure. The lateral pressure was held constant while the axial displacement was increased. The lateral pressure was taken to be the lateral load divided by the area of the lateral face for the specimen. The displacement was held constant at several points during the loading process to examine the specimen. These holds in the load were approximately 30 seconds in length.

3.30 DATA REDUCTION AND ANALYSIS

3.31 DATA COLLECTION

Failure Orientation

The angle of the failure plane was measured relative to the direction of the maximum compressive stress. The angle of the failure plane was taken to be the angle of any plane that separated the specimen or the angle of cracks which appeared to form a plane along which a separation or slip might occur under further loading. The angle was measured using a flat table surface, a straight edge, and a protractor.

To aid in the identification of the failure plane, some of the specimens were soaked in water for 30 minutes. Water collected in the cracks and pores. The samples were surface dried. Typically concrete will darken when it becomes wet. When the surface dried it returned to a light whitish-gray. Water that had penetrated the specimen kept the crack surfaces wet and consequently accentuated any cracks. It was also observed that some of the samples had a band or zone of dark (wet) material around the failure plane even in cases where the crack or failure surface was not readily apparent.

The specimen was placed on the flat surface with the failure oriented perpendicular to the edge of the surface. The straightedge was aligned with the failure plane. The angle between the straightedge and the direction of maximum compressive stress was measured with the protractor. The angle of the failure plane was plotted versus the confining pressure.

Pressure Data

The confining pressure was read from a pressure gauge on the hydraulic pump during the tests. In some tests an electronic pressure gauge was also attached to the cell and the pressures were digitized and recorded on computer for later analysis.

Load and Displacement Data

Load-Displacement curves were plotted on all tests. Maximum loads were taken directly off the plots or the digital read-outs on the test machines. Load data for some tests were also digitized on computer. This data was analyze using a spread sheet program. Load-displacement data was manually digitized from the load-displacement plots and entered into a spread-sheet for publication in this study. Most of the load

cycling and intermittent creep was removed by the selection of the points during the digitizing process. Stress-strain curves obtained from load-displacement data for selected tests are shown in appendix B.

The maximum load was taken from the plots. In the case of creep tests the maximum load was estimated. The deviatoric loads were calculated by subtracting the confining pressure multiplied by the sample area, 3.14 in², from the axial load.

Strain Data

All strain data were digitized and stored on computer for further analysis. All analyses were completed using a spread-sheet program. Data from the deformation jacket and the LVDT measuring out of plane displacements in the biaxial tests proved to be unreliable and was discarded. Average strains were calculated from the displacement data and the initial height of the specimen and the cap blocks.

Stress-strain data for selected tests using strain gauges located in Appendix C. The plots show the axial strain versus the volumetric strain when possible.

Some of the data required redress due to gauge cross talk. Crosstalk was prevalent in the data from the ISAAC 2000. This occurred when one of the gauges produced a signal voltage above 10 volts. This would cause a DC shift or jump in the voltage on the other channels. To preclude this from happening the signal amplifier for the gauge above 10 volts would turned off removing the DC shift from the other gauges. However, in several tests this was not done in a timely manner causing the need for some of the data to be "corrected". Data correction was performed by removing the voltage jump and replacing it with a voltage change equal to the rate of change of the voltage prior to the jump multiplied by the time step to the next data step. The effects can be seen in the graphs of the axial gauge located in the middle of the specimen B3.2 which was not corrected.

Cross talk was also found in the data from the deformation jackets. This was characterized by one of the gauges producing an exact duplicate of the data on another channel. This was caused by an LVDT that was broke and the us of a common input wire. The data from the deformation jacket was disregarded.

In addition to cross talk many gauges over ranged the setting of the A to D converters. This caused the measurement to register a constant maximum voltage while the true voltage was increasing. This can not be corrected.

3.32 DATA ANALYSIS

Prior to testing the signal conditioners were checked by shunt calibration. All of the conditioners were calibrated within 2.5% of each other. In addition the temporal stability was checked by leaving the shunt calibration on for 5 minutes and rechecking the values. The values after 5 minutes were .25 % off the initial readings indicating very good stability.

Localization

Evidence of localized behavior from the gauges was examine. The primary evidence was the reduction in strain from one of the gauges while displacements continue to increase. Plots of the strain gauges versus the displacement strain were used to determine if and when localization may have occurred. It was important to note when this localized behavior has occurred. The stress versus displacement strain curve is overlaid on the graphs to help identify when localization occurs. These graphs for selected tests are located in Appendix D. Fig 3-48 shows a typical graph. The majority of specimens show localization occurring within 94% of the peak stress. The presence of cracks, cracking, and failure planes are also indicators of localized behavior but may also be an indicator of general bifurcation and bulging.
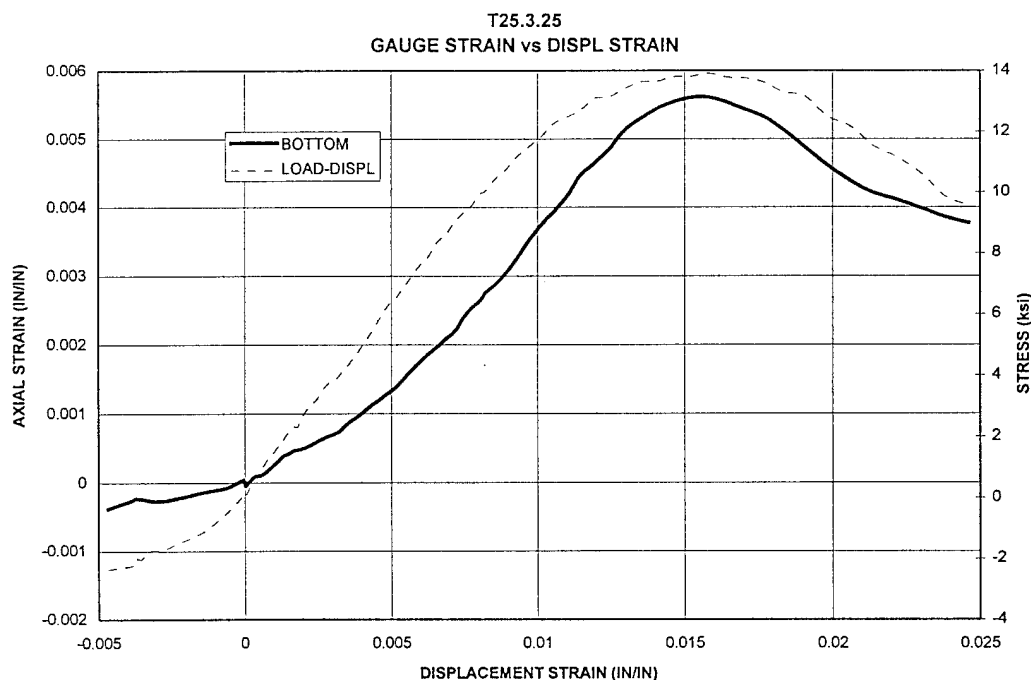

Figure 3-48: Strain Gauge versus Displacement Strain for T25.3.25 Axial Gauge

Friction relief

The effectiveness of the different methods to relief friction between the platens and the specimens was evaluated by comparing the strains measured at the midheight of the specimen and the bottom of the specimen. In addition, a comparison of the failure modes, bulging versus localized failure was examined. The location/direction of the failure surface was examined to provide clues as to the effectiveness of the end friction relief. Appendix A presents a method of strain measure using x-ray intensities that also sheds some light on this matter.

Limit Surfaces

Mohr circles were plotted for the tests. The maximum axial load is plotted against the confining pressure. The octahedral shear stress, $(1/3) \sqrt{\{(\sigma_1-\sigma_2)^2+(\sigma_2-\sigma_3)^2+(\sigma_3-\sigma_1)^2\}}$, was plotted against the octahedral normal stress, $(\sigma_1+\sigma_2+\sigma_3)/3$.

Constitutive Properties

The changes in the amount of plastic strain, reloading modulus, and lateral extension ratio during reloading were investigated for samples with caps and grease to relieve friction and having cyclic loading patterns. Data was taken from tests at 250, 500, 1000, 2000, 4000, and 8000 psi. The following steps were taken to obtain these measures. A line was drawn from the initial reloading point, B, to the point of initial unloading, A, for each cycle, see figure 3-49. This line was used for all of the measurements. This procedure was used for both axial and lateral gauges.
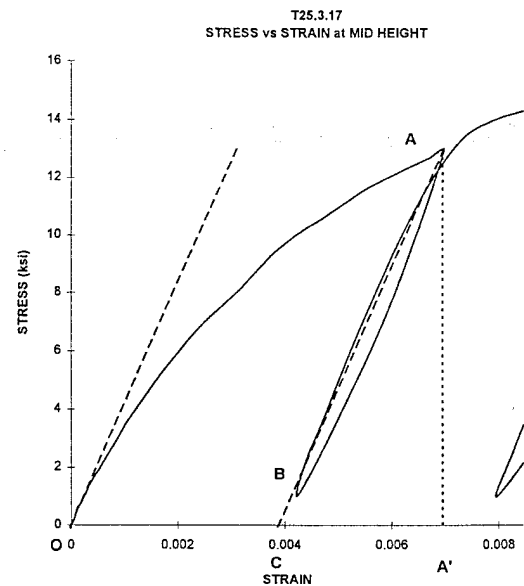
Figure 3-49: Stress-Strain Curve (T25.3.17)

The plastic strain was taken as OC, figure 3-49, while the total strain was taken as OA', figure 3-49. The change in the reloading modulus, slope of CA in figure 3-49, was calculated and compared to the percent of the peak stress at the beginning of the cycle. The change in reloading lateral extension ratio was calculated by dividing the axial elastic strain during reload by the lateral elastic strain during reload and compared to the percent peak stress.

4.0 RESULTS

4.10 FAILURE ORIENTATION

Figure 4-1 shows the relationship between the measured angles and the confining pressure for the cylindrical specimens. Figure 4-1 shows a definite trend of a change in the angle with increasing confining pressure. This result compares well with the results obtained by Wawersik and Brace [1971] shown in figure 4-2. Angles are measured from the direction of the maximum compressive load.
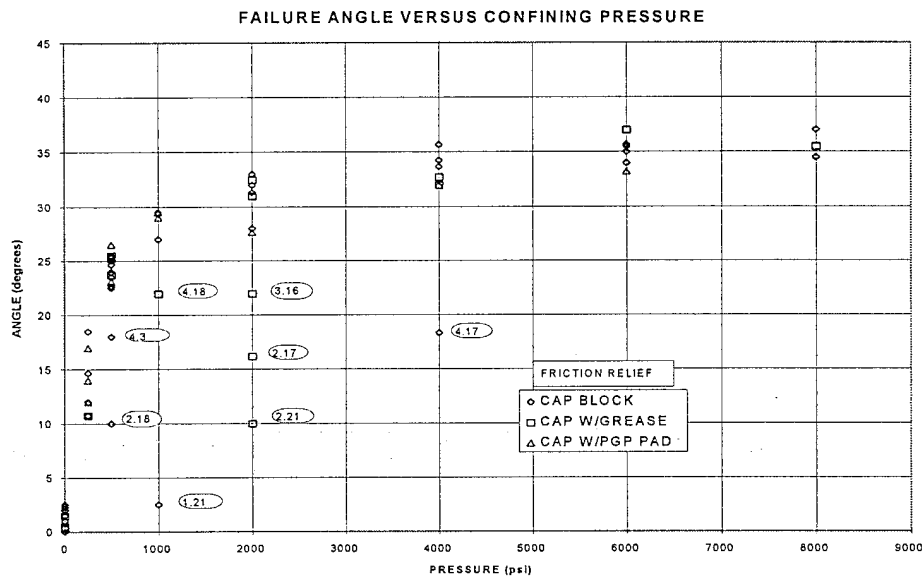

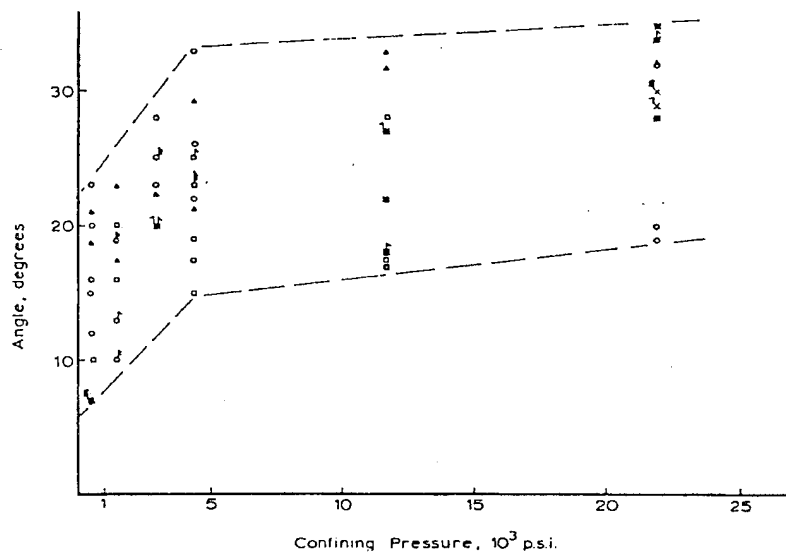Figure 4-1: Failure Angle versus Confining Pressure

Figure 4-2: Failure Angle versus Confining Pressure for Rock (Wawersik and Brace [1971])

Some out-liers are noted in figure 4-1. Sample T25.1.21 was rapidly loaded when the control of the Tinius Olsen Super "L" malfunctioned. This rapid loading occurred prior to the peak loading. The rate of loading for samples T25.2.17 and T25.2.21 was increased at or near the peak. The rate of loading for sample T25.2.18 was increased at 98% of the peak load in the post peak regime.

The load rate was not changed for sample T25.4.17; however, this sample was relaxed in the post peak, i.e., the displacement was held constant while the load decreased. The failure surface for T25.4.17 is a vertical split with a cone on one end. The load displacement curve for T25.4.17 is "jumpy" in the post peak regime just prior to the relaxation. It is unknown if the behavior was due to some possible irregularities in the cap/sample interface or the relaxation process.

The other out-liers did not have any special circumstance noted during the loading that might account for their deviation from the general trend.

Specimen T25.1.8, tested at 8000 psi confining pressure, showed little sign of distress with only small scratches. This may be due to the fact that the specimen was only loaded to the peak load and not loaded into the post peak regime.

Angles were not determined for five of the specimens, T25.1.7, T25.2.14, T25.3.11, T25.3.24, and T25.4.8. T25.1.7 was tested at 9 ksi confining pressure. The cap block broke before the sample did. The sample showed no visible cracking. The load at the time the axial load was released was far below the peak load for 8000 psi confinement. T25.2.14 used cap blocks with PGP pads to relieve friction. The sample had slipped approximately 1/4" from the cap blocks. Although cracking and crumbling was evident an orientation of the failure was not determined. The cap block broke before T25.3.11. T25.3.24 also had cap blocks with PGP pads and slipped from between the cap blocks. No cracks were evident on T25.3.24. Cracks exist on T25.4.8 but an orientation could not be determined. The load was relaxed just after the peak load in this test.

Figure 4-3 shows the relationship between the measured angles and confining pressure for the rectangular specimens. Angles are measured from the direction of the maximum compressive load. The same general trend that is observed for the cylindrical specimens is also seen in figure 4-3 for the rectangular specimens. The data for the rectangular specimens has more variability at each pressure.
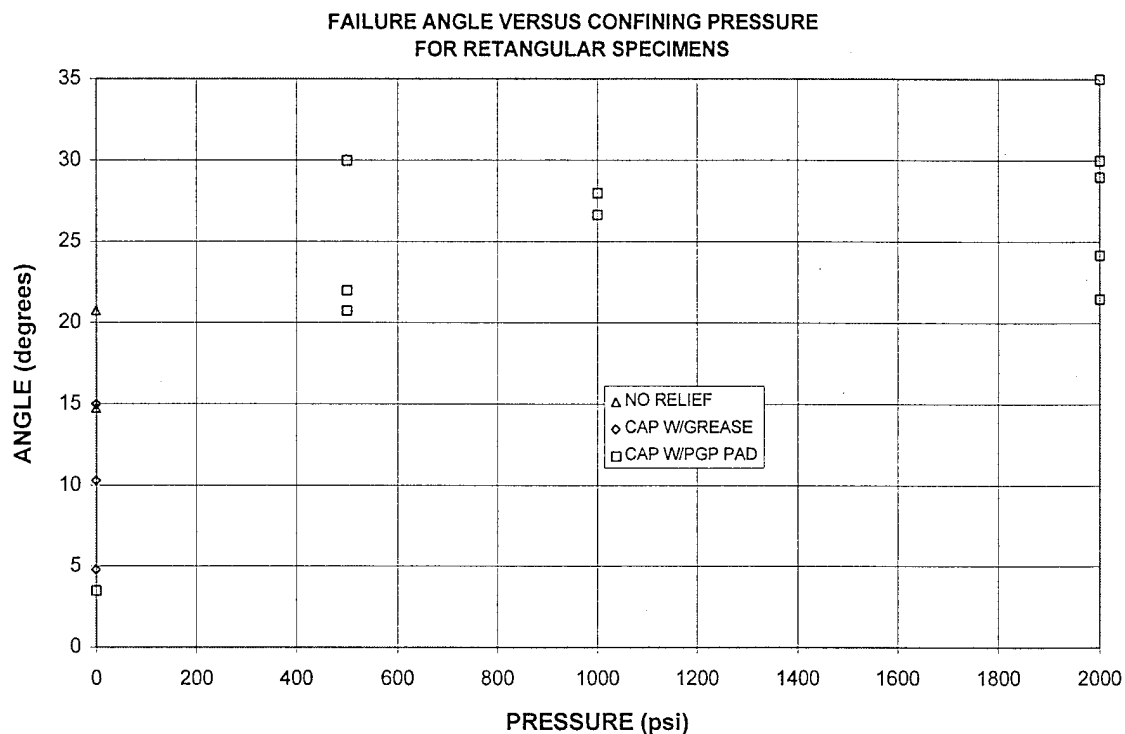
FAILURE ANGLE VERSUS CONFINING PRESSURE FOR RETANGULAR SPECIMENS

Figure 4-3: Failure Angle versus Confining Pressure for Rectangular Specimens

Table 4-1 shows the relationship between the measured angles and confining pressure for the biaxial tests. Angles are measured from the direction of the maximum compressive load. Two angles were measured for the biaxial tests one measuring the angle from the top of the specimen to the bottom and the other measuring the angle in the central third of the specimen. The angle for the bottom two thirds of B3.5 was 5°. The failure surfaces for B3.6 and B3.7 were vertical but with their normals parallel to the direction of the rods.

TABLE 4-1			
FAILURE ANGLES FOR BIAXIAL SPECIMENS			
SAMPLE	LATERAL	ANGLE (DEGREES)	
#	PRESSURE	TOP to BOT	MID 1/3
3.1	0 psi	10.6	3.0
3.2	100 psi	4.8	4.5
3.3	200 psi	21.2	13.6
3.4	300 psi	15.6	13.2
3.5	500 psi	13.6	4.9

The angles in the central third of the specimen are smaller than or equal to those measured from top to bottom which suggests there is some influence from the caps and/or friction. Samples B3.3 and B3.4 and the videos of the tests show that the cap blocks were undersized too much causing a large stress concentration at the corners of the specimens causing the failure surface to emanate from the corner to the central section of the specimen. The video of test B3.5 shows that the cap block failed first. Although it was after cracking began in the center of the specimen, the video indicates that the failure surface near the top deviated from its original path to connect to the crack in the cap block.

The failure surface in test B3.1 consists of three near vertical (5°) surfaces which representing more than 75% of the crack length. These cracks are connected by two angled cracks. There is a fourth crack that extends in a near vertical path from the bottom the vertical crack to a point about 1 inch from the top. This crack appears first in the video but is not part of the ultimate failure surface. Each of the near vertical cracks runs tangential to the rods until the crack runs radial into a large rod. The crack proceeds by following the circumference of the rod. The crack then follows an angled path to the nearest rod again tangential to the next vertical segment (figure 4-4).
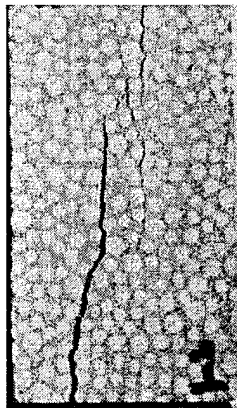

Figure 4-4: Crack Pattern for B3.1

4.20 PETROLOGIC STUDY

An attempt was made to impregnate one of the triaxial specimens, T25.1.12, with a colored epoxy. The epoxy did not penetrate the specimen. The specimen was cut in half. In spite of the inability to impregnate the specimens several features of the failures were noted.

Two specimens were cut in half along the axis., T25.1.12 and T25.1.08. The specimens were tested at 6 and 8 ksi, respectively. Both specimens used a cap block for friction to relief. The saw cut produced a surface that was "crumbly". Aggregates exposed on the surfaces could be separated from the rest of the specimen by simply rubbing the surface. The smaller of the two pieces produced by cutting each specimen broke in two by bending it by hand. The fracture produced many small rounded pieces with many aggregates coming loose. The failures of other samples at high pressures, 4 to 8 ksi, produced similar results: crumbly, dull surfaces with many aggregates coming loose.

The failures of samples at low pressures, 0 to 1 ksi, produced failures with sharp corners. Aggregate would not come loose from simple rubbing action. When the broken remnants of the samples were bent and broken the fracture was "crisp" with no loose aggregates produced, but with sharp edges.

The video cameras used in the biaxial tests also offers some insight in to the shape form and development of the failure. Review of the video tapes shows that in tests B3.1 through B3.5 a slow growing crack could be seen. The crack would bridge from one aggregate to another, presumably from one bond crack to another. In all tests but one, B3.5, the failure crack started near the center of the specimen and moved to the ends. In the case of B3.5 the cap block broke first. A crack was detected near the center which was not part of the primary failure surface.

In an effort to better identify the cracks and their orientation, some of the samples were soaked in water for approximately half an hour. The samples were removed and the surface dried. Water in the cracks accentuate the cracks allowing them to be more visible. It was also observed that in some cases a region or zone of excess surface moisture could be identified even when a well defined crack was not present. This excess water could signify an increase in porosity in the area allowing more water to penetrate and be retained in the zone. This suggests that there is a zone of localized deformation were the damage or cracking is more prevalent then out side the zone. This effect was quite helpful in identifying the orientation of the failure.

4.30 FRICTION RELIEF

Rice [1976] notes that the bifurcations associated with the loss of positive definiteness of the second order work are sensitive to the assumed boundary conditions. Therefore, it is important to know how well an assumed state of stress is being simulated.

The use of cap blocks with PGP pads did relieve friction to a negligible level as evidenced by the slipping of the specimens from between the cap blocks. The slipping caused reduced peak loads in specimens at high

pressures. Furthermore, failure angles were not obtained for specimens T25.2.14 and T25.3.24. The use of cap blocks with grease did not cause slipping; however, the resulting failure under uniaxial stress gave vertical failures similar to the ones produced using the cap blocks with PGP pads and those obtained using rubber sheets. The use of cap blocks alone provided some relief; however, failure surfaces from these tests were more complex with some parts of the surface straight and flat while other parts were curved and cone shaped. Furthermore, use of cap blocks alone produced slight bulging and more surface cracks. These added cracks caused the foil surface of the gauges to "crinkle" much like tin foil that is crunched into a ball and then unraveled.

To assess the friction relief obtained this study examined the material properties of the cap blocks and the specimens, the results of X-ray testing, the ratio of the lateral strains at the bottom of the specimen to the middle of the specimen, and the shape of the failure surface across the ends of the specimens.

The cap blocks were intended to have properties similar to the specimens but have slightly higher strengths. The average strength of the cap blocks was 10.75 ksi compared to 7.04 ksi for the average of specimens[1]. The average initial tangent modulus was 4800 ksi for the cap blocks compared to 5000 ksi for the specimens. The average lateral extension ratio over the same range was .20 for the cap material and .19 for the specimens. The modulus for the specimens tested with the friction relief was slightly lower than the specimens tested without friction relief, approximately 4500 ksi (10% difference). The lateral extension ratio was slightly higher, approximately .21. This result is consistent with the confining nature of the end platens which tends to decrease lateral extension and increases stiffness. The mixes used provided sample and cap materials with the desired properties.

From the X-ray tests presented in Appendix A it is shown that the direct contact of specimen and platen will produce friction between the platen and specimen that will confine the ends of the specimen causing a densification of the sample above that which would occur under true uniaxial conditions. Furthermore, these tests indicate that the use of rubber sheets to relieve the friction tend to induce tensile forces in the specimen causing it to dilate much sooner than it would under true uniaxial conditions. Therefore, to obtain a true state of uniaxial stress in the specimen the relief of the friction must be by a means that lies somewhere "between" no relief and rubber.

Table 4-2 shows the values of the ratio of the lateral strain at bottom compared to those at the middle. The values were taken at 50%, 75%, and 90% of the peak load. Table 4-2 shows the ratios for the first

---

[1] The average strength for the specimens was based on the average of samples T25.1.1, T25.1.2, T25.1.3, T25.3.2, T25.3.5, T25.3.6, and T25.3.7.

occurrence of these loads while table 4-3 shows the values for the last occurrence at 50% and 75% of the peak for those tests that were intermittently cycled.

From Table 4-2 the values of the ratio of lateral strain at bottom to the middle range in value from .7 to over 3.0. However, the majority of the values lie between .8 and 1.8. There does not seem to be a trend in terms of the method of friction relief or for the confining pressure of the tests. Recalling that the lateral gauges do not measure the strain of the entire circumference but only a portion of it and also that the gauges were not necessarily located in line along the axis, it is possible that the imperfection in the cap/specimen interface, sloping of the specimen ends, and minor errors in the placement of the plunger may have contributed to the wide variation in these numbers. Only the specimen that used cap blocks alone for relief showed any signs of bulging; the worst having a diameter in the middle less than .03" larger than the diameter at the ends. Similar measurements were not made on the rectangular or biaxial specimens.

TABLE 4-2										
BOTTOM/MIDDLE LATERAL STRAIN RATIO										
1ST OCCURRENCE										
	FRICTION	CONFINING	% PEAK LOAD				FRICTION	CONFINING	% PEAK LOAD		
TEST	RELIEF	PRESSURE	50%	75%	95%	TEST	RELIEF	PRESSURE	50%	75%	95%
4.10	PGP	0	0.87	1.06	1.2	3.20	cPGP	1000	1.48	1.85	4.83
2.17	cg	2000	0.88	0.77	1.19	3.17	cg	6000	1.54	1.17	1.82
4.18	cg	1000	0.91	0.74	0.62	3.18	cPGP	1000	1.61	1.65	0.98
4.11	PGP	0	0.91	1.33	1.27	4.20	cPGP	0	1.65	1.46	1.5
4.13	RUBBER	0	0.93	1.02	0.87	3.24	cPGP	6000	1.68	5.16	
2.24	cg	500	0.96	0.82	1.08	2.23	cap	6000	1.7	1.11	1.26
4.15	cap	0	1.01	0.95	0.89	4.08	cg	2000	1.78	1.95	1.5
4.17	cap	4000	1.06	1.02	0.91	3.03	PGP	0	1.85	1.73	3.29
2.22	cap	2000	1.07	1.36	1.41	3.02	none	0	2.07	5.46	1.91
2.19	cg	2000	1.07	0.92	4.47	4.06	cg	500	2.14	2.12	1.32
4.14	cg	0	1.15	1.39	2.04	3.25	cPGP	2000	2.16	2.84	1.91
3.21	cg	250	1.16	1.61	2.4	2.13	cap	1000	2.34	2.13	1.44
2.16	cg	4000	1.17	1.53	1.52	3.15	cg	4000	2.5	2.8	2.11
2.14	cPGP	2000	1.39	1.19	1.29	3.22	cg	500	2.82	4.6	1.81
3.16	cg	2000	1.42	1.18	0.82	2.21	cg	2000	3.16	2.65	3.09
4.19	cPGP	0	1.42	1.32	0.82						

TABLE 4-3									
BOTTOM/MIDDLE LATERAL STRAIN RATIO									
LAST OCCURRENCE									
	FRICTION	CONFINING	% PEAK LOAD			FRICTION	CONFINING	% PEAK LOAD	
TEST	RELIEF	PRESSURE	50%	75%	TEST	RELIEF	PRESSURE	50%	75%
4.18	cg	1000	0.58	0.6	2.16	cg	4000	1.23	1.2
4.15	cap	0	0.75	0.86	3.17	cg	6000	1.38	1.2
2.24	cg	500	0.94	1	4.20	cPGP	0	1.48	1.48
2.17	cg	2000	0.97	0.98	4.14	cg	0	1.6	1.6
3.18	cPGP	1000	1.03	0.91	3.15	cg	4000	1.6	1.7
4.17	cap	4000	1.05	0.94	4.11	PGP	0	1.6	1.5
4.06	cg	500	1.11	1.06	3.22	cg	500	1.74	1.78
2.22	cap	2000	1.12	1.17	2.13	cap	1000	1.75	1.93
3.16	cg	2000	1.14	1.05	3.21	cg	250	1.8	1.43
2.23	cap	6000	1.16	1.2	3.20	cPGP	1000	2.01	2.27
2.14	cPGP	2000	1.16	1.14					

Another indicator of the relief of the friction is the shape/direction of the failure plane near the ends of the specimen.

For specimens using no relief there are usually two surface cracks along the sides of the specimen defining the lateral bounds of the failure surface. The connection of these two cracks on the ends, the axial bounds of the surfaces, is not a straight crack but is a crack that runs along the circumferencial edge of the ends, figures 4-5A and 4-5B. Thus, a spoon or shoe horn shaped surface is created with a corresponding cone shape on the other side, figure 4-5C. In a few cases the cracks on the ends were positioned on the end face but were curved towards the edges.

(a) Cap Block   (b) T25.3.2   (c) T25.3.2 Side View
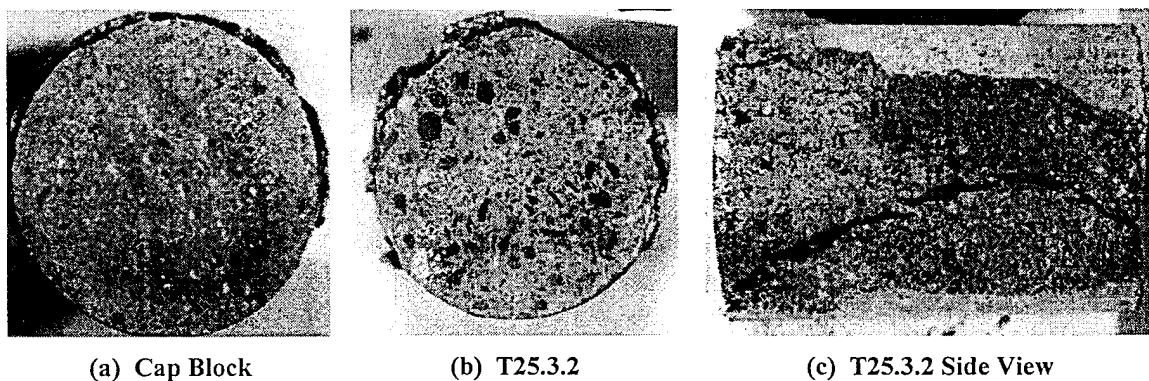
Figure 4-5: Specimens with No Friction Relief

Tests using PGP pads gave mixed results with cracks on one end oriented straight across the end of the specimen while cracks on the other end went around the edges, for example T25.4.10, figures 4-6A and 4-6B. T25.3.3 has cracks that curve close to the edge, figure 4-6C.
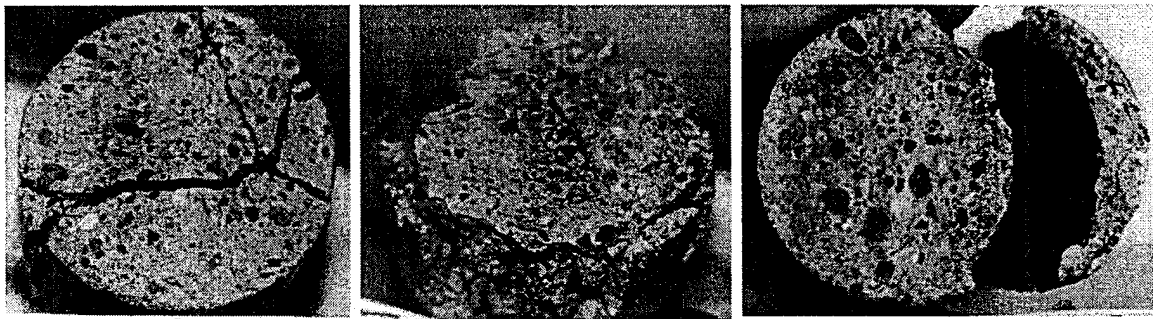
| (a) T25.4.10 | (b) T25.4.10 | (c) T25.3.3 |

Figure 4-6: Specimens Using PGP Pads for Friction Relief

Tests using cap blocks alone for relief produced cracks that were straight across the end and a few cracks that followed the edge of the specimen, figure 4-7C. However, the collection of several cracks on the ends produces a failure with complex surfaces with flat and curved surfaces, figure 4-7A and 4-7B.
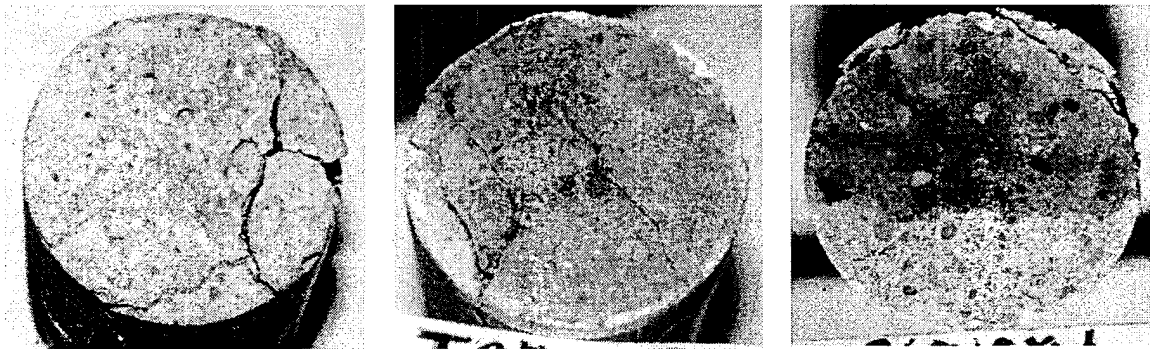

| (a) T25.1.16 | (b) T25.2.8 | (c) T25.2.8 |

Figure 4-7: Specimens Using Cap Blocks for Friction Relief

Tests using caps with grease produced failures with cracks that run straight or near straight across the ends of the sample, figures 4-8A, 4-8B, and 4-8C. Failures often produced three pie shaped pieces, when viewed from the ends, with the angle between the cracks approximately 120° apart, figures 4-8A and 4-8B.
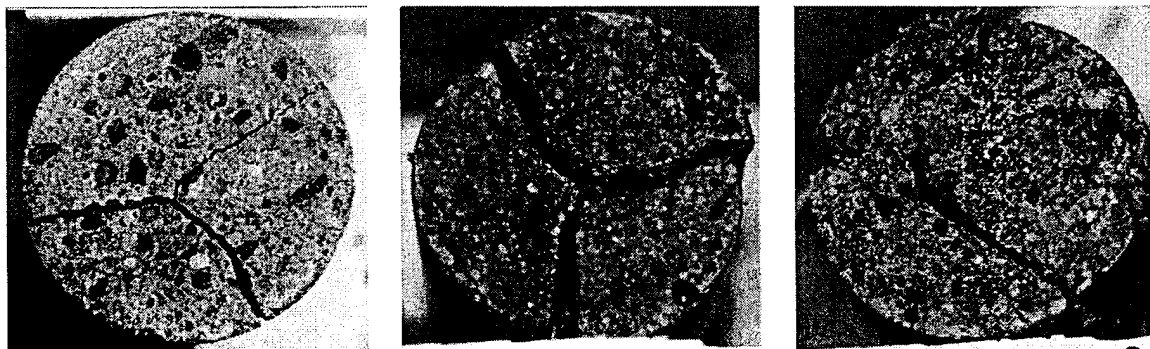
| (a) T25.4.14 | (b) T25.4.16 | (c) T25.4.16 |

Figure 4-8: Specimens Using Cap Blocks and Grease for Friction Relief

For the samples that used PGP pads with cap blocks, the cracks were essentially straight from crack tip to crack tip across the end of the specimens. Furthermore, these samples needed to have a hose clamp placed at the interface of the cap and the specimen because the specimen kept slipping out from between the cap blocks. This slippage continued even with the clamps during the triaxial tests, figure 4-9A and 4-9B. This slippage is further evidence of friction relief.
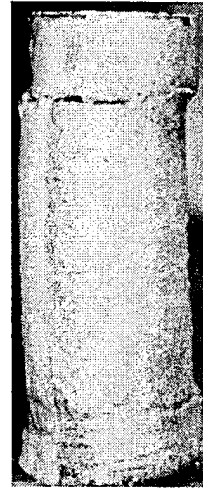
(a) T25.3.24   (b) T25.2.14

Figure 4-9: Specimens Using Cap Blocks with PGP Pads for Friction Relief

When rubber was used to relieve end friction the cracks were through the ends and were straight from one crack tip on the side to the other. The figures, 4-10A and 4-10B, to the right show the result of T25.3.4.
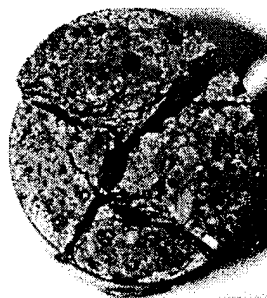
Figure 4-10A: T25.3.4   Figure 4-10B: T25.3.4

Figure 4-10: Specimens Using Rubber Sheets for Friction Relief

4.40 LOCALIZATION

Localization begins when non-homogeneous deformations occur in a uniformly loaded homogeneous material. For the purposes of this study it is assumed that the friction on the ends of the specimens has been relieved sufficiently to consider the specimens homogeneously loaded; however, the results of the previous section indicate that this probably is not true for tests with cap blocks alone. It is further assumed that load variations due to the imperfections, camber and slope, in the cap/specimen interface are negligible. It is also assumed in the case of tests using PGP pads with cap blocks for friction relief that any slippage between the specimen and cap block had a negligible effect on the onset of localization and the resulting failure angle.

One indicator of localized behavior is the presence of one or two failure planes while there is a conspicuous lack of cracking or failure plane development elsewhere in the specimen. Figure 4-11 shows the existence of such planes. Additional photos of the failures of the specimens in this study are located in Appendix E.

| 0 psi | 250 psi | 500 psi | 1000 psi | 2000 psi | 4000 psi |
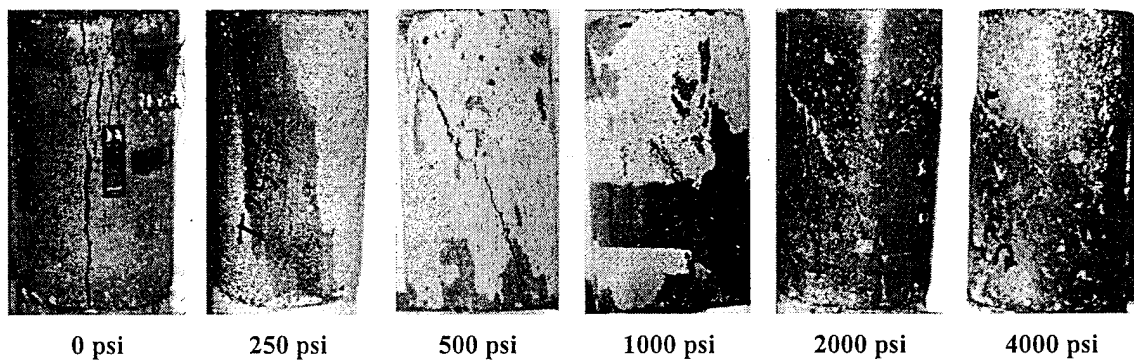
Figure 4-11: Specimen Failures at Various Pressures

Tests using cap blocks alone for friction relief resulted in numerous "slip" surfaces were evident on the samples particularly at high confining pressures. These slip surfaces caused crinkling of the foil gauges. Numerous "slip" surfaces are evident in pictures of samples tested by Chinn and Zimmerman [1965]. Figure 4-12 shows some samples from this report. The number and magnitude of these "slip" planes are far greater than those found in the tests in this study but are similar to those observed. The crinkled foil gauges looked similar to the photos in figure 4-12.
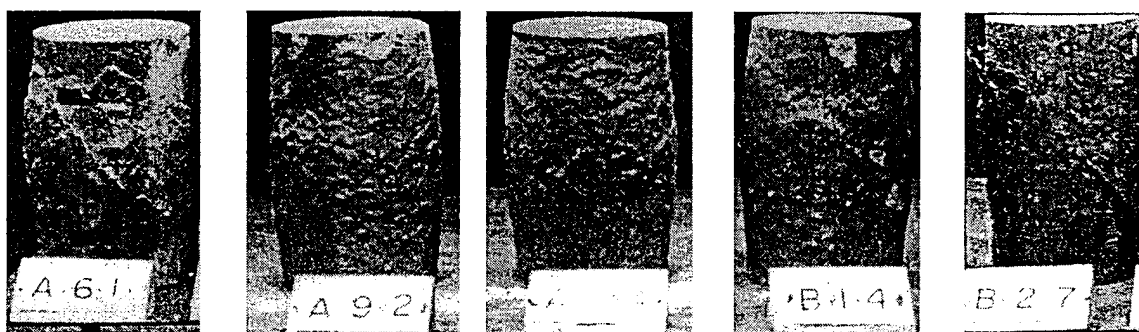
Figure 4-12: Triaxial Test Samples w/No Friction Relief (Chinn and Zimmerman [1965])

A second indicator of localized behavior is the reduction of strain in one or more of the strain gauges under continuing displacement. The point at which this occurs is an indicator of when in the loading process localization occurs. Appendix D contains plots of the strain from the strain gauges versus the displacement strain for selected triaxial and biaxial tests. Figure 4-13 shows a sample plot for specimen T25.3.25. At point A the displacement strain is increasing while the strain gauge is decreasing; thus, at this location on the specimen localized deformation begin at A. Comparing point A with the load-displacement curve indicates that this localized behavior occurred at the peak load.
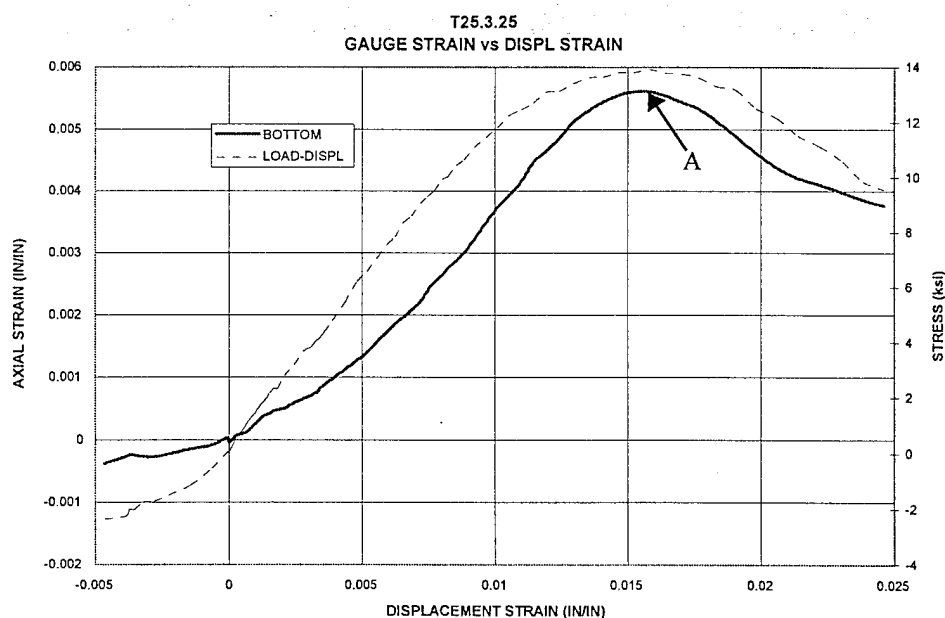
Figure 4-13: Localization from Axial Gauge Strain versus Displacement Strain, T25.3.25

The point at which localization occurs is also of interest. From the plots in Appendix D we can determine at what point during the loading localized behavior is evident in the strain gauges. Table 4-4 shows the result of this analysis. Table 4-4 presents the percent of the maximum stress at which localized behavior is found

4-12

for each gauge. Negative numbers denote localized behavior prior to the peak stress. B denotes the gauge broke before localization. A broken gauge could be an indication of a crack going through the gauge (localization) or separation of the wire from the terminal which occurred in T25.3.24. The absence of a number indicates that localized behavior was not observed. Some gauges had large strain rates at or near peak load.

TABLE 4-4											
PERCENT OF PEAK LOAD AT WHICH LOCALIZATION OCCURS											
Test	Pressure	Axial		Lateral		Test	Pressure	Axial		Lateral	
#	psi	Bottom	Middle	Bottom	Middle	#	psi	Bottom	Middle	Bottom	Middle
3.01	0				100.0%	2.13	1000		94.0%		
3.02	0					3.18	1000	80.0%		79.0%	93.0%
3.03	0			98.0%	100.0%	3.20	1000	99.0%	82.0%	84.0%	99.0%
3.04	0				-80.0%	4.18	1000	97.0%	94.0%	83.0%	B
3.05	0		100.0%		99.0%	2.14	2000		99.9%	98.0%	96.0%
3.06	0				-99.0%	2.17	2000	100.0%	-99.5%	-99.5%	-94.0%
3.07	0		99.5%		100.0%	2.19	2000	-99.0%			
3.19	0	100.0%	100.0%	-84.0%		2.21	2000	B	97.5%	-96.0%	97.5%
4.05	0		100.0%	-99.0%		2.22	2000				
4.10	0		99.0%		99.0%	2.25	2000				B
4.11	0				100.0%	3.16	2000	100.0%	86.0%	95.0%	99.0%
4.12	0					3.25	2000	100.0%		99.0%	99.0%
4.13	0		95.0%	-95.0%	95.0%	4.08	2000	-63.0%	-61.0%	-64.0%	-63.0%
4.14	0		100.0%	100.0%	99.0%	2.16	4000	-99.9%	100.0%		
4.15	0		-99.0%	88.0%	-99.5%	2.20	4000	100.0%		100.0%	
4.16	0		100.0%	-75.0%	100.0%	3.15	4000	91.0%	97.0%	-99.0%	94.0%
4.19	0		100.0%	100.0%		3.23	4000			79.0%	
4.20	0		93.0%	-99.0%	-99.0%	4.17	4000	81.0%	98.0%	97.0%	94.0%
2.15	250					2.23	6000	-97.0%		-98.0%	99.0%
3.13	250	91.0%	93.0%	96.0%	96.0%	3.17	6000	96.0%	100.0%	99.0%	99.5%
3.21	250	100.0%	99.0%		96.0%	3.24	6000	B	B	B	B
4.09	250					4.07	8000	98.0%			
2.18	500					B3.1		100.0%	100.0%	-93.0%	B
2.24	500	96.0%		100.0%		B3.2	100			B	B
3.14	500				85.0%	B3.3	200			-93.0%	B
3.22	500	89.0%	99.0%	94.0%	85.0%	B3.4	300	98.0%		98.0%	98.0%
4.06	500		99.0%			B3.5	500			91.0%	B
NEGATIVE NUMBERS DENOTE PREPEAK						B DENOTES GUAGE BROKE PRIOR TO LOCALIZATION					

The majority of tests indicate localization occurring on or after 94% of the peak load in the prepeak regime. However, the following exceptions are noted. T25.3.4 used rubber to relieve confinement; the bottom lateral gauge had large strains at the peak load. T25.3.19 was previously hydrostatically loaded; the process of loading, unloading, placing, and removing from the cell may have damaged the terminals on the bottom lateral gauge. The graphs indicate base line drift may have caused a false indication of localization. Graphs for T25.4.8 indicate that something happened at 63% of the maximum stress. This specimen was overheated on a table disk grinder during preparation; therefore, it is unknown there was a malfunction in

the gauge or if localization did occur at 63% of the maximum load. Graphs for T25.4.16 show baseline drift of the bottom lateral gauge probably causing a false indication of localization.

The triangular specimens were not equipped with strain gauges; therefore, a similar analysis of the tests on these specimens is not available. Biaxial test data is included in table 4-4.

4.41 OBSERVATIONS OF CRACKING

For uniaxial tests not conducted inside the triaxial cell, cracks/failure planes were detected by sound and with the naked eye at or near the peak, within 98% of the peak load. Dunn et al. [1973] and Wawersik and Fairhurst [1970] report that visible cracking did not appear until after the peak load.

The video tapes of the biaxial tests show surface cracks appearing as early as 61% of the peak load for test B3.2. Tests B3.1, B3.3, B3.4, and B3.5 had visible cracks developing at 95%, 83%, 80%, and 99% of the peak loads, respectively. Although surface cracks were visible prior to the peak these cracks were not always part of the failure surface. Furthermore, in the case of B3.2 there was cracking parallel to the plane of loading, indicating that the load on the surfaces may not have been homogeneous. Tests B3.1, B3.3, B3.4, and B3.5 had no visible cracks parallel to the plane of loading.

The relaxation tests performed on samples T25.2.16, T25.2.19, T25.3.05, T25.4.08, T25.4.09, and T25.4.17 indicate that relaxation prior to 85% of the peak load did not result in complete loss of load. The loss of load that was noted prepeak may be largely attributed to a relaxation of the friction between the plunger and the test cell. Relaxation in the post peak regime resulted in complete loss of load. These results may be interpreted in the following manner. During prepeak relaxation (up to 85% of the peak stress) cracks grow slowly. The rate at which cracks grow increases as the applied load increases. The stress at the crack tip reduces as the axial load decreases. Cracks grow to a stable length while the stress decreases. During post peak relaxation crack growth slows as the stress at the tip decreases. The stress at the crack tip decreases as the load decreases. Energy is dissipated, presumably by cracking, as the stress relaxes. If the cracks grew until all available energy was used up then it is possible that unstable crack growth was occurring because crack growth occurred at/near zero load levels. Alternatively the energy may have been used up in crack nucleation. Both of these possibilities might be interpreted as a loss of material stability but they do not require it to occur. The prepeak relaxation or crack growth will stabilize while post peak crack growth does not stabilize but proceeds until all available energy is used up in crack growth and plastic deformation. The foregoing interpretation does not necessitate localized behavior in the post peak nor does it preclude it in the prepeak. Relaxation was not performed between 85% and 100% of the peak load in the prepeak regime.

The creep tests provide another view of the tests also. The percentage of the maximum load at which the load was held during the creep process was determined by the slope of the load-displacement curve during loading. The level at which it was held was reevaluated after the test by extending the loading and unloading portions of the curve and estimating what the maximum load would have been had the load not been held constant.

Samples T25.2.4 and T25.4.4 were held at approximately 75% of the estimated maximum load for over 210 minutes. The load was increased to 85% in T25.2.4 after 210 minutes and the creep process was continued until the unloading portion of the load-displacement curve was reached. The load was increased after 210 minutes until the unloading portion of the load-displacement curve was reached in test T25.4.4. Sample T25.1.18 was also loaded to 75% of the estimated peak load for 120 minutes the load was then increased to 76% and the load was held for 15 minutes until the unloading portion of the curve was reached.

Sample T25.2.5 was held at 90% of the estimated peak load for 75 minutes until the unloading portion of the curve was reached. T25.1.24 was held at 92.5% of the estimated peak load for 15 minutes until the unloading portion of the curve was reached. T25.2.12 was held at 95% of the estimated peak load for 7 minutes until the unloading portion of the curve was reached.

T25.2.20 was supposed to have a sustained load held at 95% to 99% of the estimated maximum load; however, during the reloading after cycling the load rose to the level prior to the cycling and held constant for 4 minutes while the displacement rate remained constant throughout at .005 in/min. This phenomena of creep by the application of the prescribed displacement rate also occurs in samples T25.2.9, T25.2.23, and T25.3.15 with the rate held constant at .005 in/min.

These creep results could be interpreted as follows. Creep keeps the stress at any crack tip fairly constant. Variations in stress are due only to the change of relative location of other cracks and aggregates as the crack slowly grows. At stresses lower than 75% of the peak stress, the critical stress, intensities at the crack tip are insufficient to cause unstable crack growth. At stresses above 75% of the peak stress intensities at the crack tip are sufficient to cause slow, but unstable crack growth (growth without increasing the applied load). As the sustained stress increases the pace of crack growth increases. Once again the foregoing discussion does not necessitate localized behavior but it does preclude it prior to 75% of the peak; furthermore, discussion of unstable crack growth in concrete is usually centered on a small number of cracks which may be interpreted as localized behavior. This is consistent with the findings of Meyers et al. [1969].

Glucklich [1965] found similar results as well and argues that the true strength of concrete is given by the critical load and not the peak load. At this point it seems possible that a specimen could be loaded so slowly that its peak load is the critical load. Based on these results and previous work the following position is adopted in this study. If the specimens were loaded at a slow enough rate the localization would occur at the peak load. The failure character and orientation would be similar to that found in this study. Furthermore, the Mohr circles would differ but have a similar relative character which is described in the next section.

The assumptions made in taking this position imply that viscous effects (creep) tend to drive localization pre-peak. Further study is needed in the area of the effects of creep to evaluate this position.

4.50 STRENGTH DATA AND LIMIT SURFACES

Tables 4-5, 4-6, and 4-7 present the basic strength data for each of the cylindrical tests. The tables list the test number, the type of friction relief, the confining pressure and the maximum axial stress. Table 4-5 presents the data sorted by batch (test #) while tables 4-6 and 4-7 present the data sorted by the method of friction relief and by the confining pressure respectively. Table 4-7 shows that the use of the table disk grinder did damage T25.4.08 and T25.4.13. Data for the creep tests show the maximum sustained stress.

TABLE 4-5											
STRENGTH DATA SORTED BY BATCH (TEST #)											
Test	Friction Relief	Confine Pressure psi	Axial Stress psi	Test	Friction Relief	Confine Pressure psi	Axial Stress psi	Test	Friction Relief	Confine Pressure psi	Axial Stress psi
1.01	none	0	7,398	2.09	cg	500	11,141	3.17	cg	6000	29,603
1.02	none	0	6,182	2.10	cap	250		3.18	cPGP	1000	12,223
1.03	none	0	5,991	2.11	cap	250	8,403	3.19	cg	0	6,939
1.04	cap	0	5,052	2.12	cap	250	9,440	3.20	cPGP	1000	12,732
1.05	cap	0	4,393	2.13	cap	1000	14,165	3.21	cg	250	8,785
1.06	cap	0	5,112	2.14	cPGP	2000	15,024	3.22	cg	500	10,441
1.07	cap	9000	27,502	2.15	cPGP	250	9,167	3.23	cPGP	4000	23,428
1.08	cap	8000	36,096	2.16	cg	4000	19,099	3.24	cPGP	6000	21,900
1.09	cap	8000	38,897	2.17	cg	2000	14,770	3.25	cPGP	2000	16,297
1.10	cap	6000	29,921	2.18	cap	500	10,345	4.01	cap	500	8,403
1.11	cap	6000	30,685	2.19	cg	2000	15,661	4.02	cap	500	8,149
1.12	cap	6000	31,831	2.20	cPGP	4000	22,918	4.03	cap	500	8,308
1.13	cap	4000	23,428	2.21	cg	2000	14,961	4.04	cap	500	8,750
1.14	cap	4000	24,319	2.22	cap	2000	17,571	4.05	cg	0	5,220
1.15	cap	4000	27,215	2.23	cap	6000	31,067	4.06	cg	500	9,040
1.16	cap	2000	17,316	2.24	cg	500	11,077	4.07	cg	8000	37,688
1.17	cap	2000	17,284	2.25	cg	2000	16,297	4.08	cg	2000	8,913
1.18	cap	2000	18,880	3.01	cg	0	6,844	4.09	cap	250	8,502
1.19	cap	1000	13,910	3.02	none	0	8,117	4.10	PGP	0	6,048
1.20	cap	1000	14,260	3.03	PGP	0	7,401	4.11	PGP	0	6,446
1.21	cap	1000	10,823	3.04	RUB	0	6,685	4.12	cap	0	5,173
1.22	cap	500	10,823	3.05	none	0	7,257	4.13	RUB	0	3,501
1.23	cap	500	12,159	3.06	none	0	6,939	4.14	cg	0	5,411
1.24	cap	500	11,077	3.07	none	0	7,401	4.15	cap	0	5,730
1.25	cap	500		3.08	cPGP	0	6,872	4.16	cg	0	5,252
2.01	none	0	4,504	3.09	cPGP	250	9,021	4.17	cap	4000	20,595
2.02	none	0	4,399	3.10	cPGP	500	11,205	4.18	cg	1000	11,663
2.03	none	0	3,874	3.11	cPGP	1000	12,223	4.19	cPGP	0	4,584
2.04	cap	500	9,550	3.12	cPGP	6000	24,446	4.20	cPGP	0	5,475
2.05	cap	500	11,460	3.13	cPGP	250	8,913	cp1	none	0	10,663
2.06	cap	500	10,823	3.14	cPGP	500	10,313	cp3	none	0	10,106
2.07	cap	500	12,159	3.15	cg	4000	23,046	cp4	none	0	11,539
2.08	cap	0	6,653	3.16	cg	2000	16,616	cp5	none	0	10,743

		TABLE 4-6									
		STRENGTH DATA SORTED BY FRICTION RELIEF METHOD									
Test	Friction Relief	Confine Pressure psi	Axial Stress psi	Test	Friction Relief	Confine Pressure psi	Axial Stress psi	Test	Friction Relief	Confine Pressure psi	Axial Stress psi
1.04	cap	0	5,052	1.15	cap	4000	27,215	2.15	cPGP	250	9,167
1.05	cap	0	4,393	4.17	cap	4000	20,595	3.09	cPGP	250	9,021
1.06	cap	0	5,112	1.11	cap	6000	30,685	3.13	cPGP	250	8,913
2.08	cap	0	6,653	1.12	cap	6000	31,831	3.10	cPGP	500	11,205
4.12	cap	0	5,173	2.23	cap	6000	31,067	3.14	cPGP	500	10,313
4.15	cap	0	5,730	1.10	cap	6000	29,921	3.11	cPGP	1000	12,223
2.10	cap	250		1.08	cap	8000	36,096	3.18	cPGP	1000	12,223
2.11	cap	250	8,403	1.09	cap	8000	38,897	3.20	cPGP	1000	12,732
2.12	cap	250	9,440	1.07	cap	9000	27,502	2.14	cPGP	2000	15,024
4.09	cap	250	8,502	3.01	cg	0	6,844	3.25	cPGP	2000	16,297
1.22	cap	500	10,823	3.19	cg	0	6,939	2.20	cPGP	4000	22,918
1.23	cap	500	12,159	4.05	cg	0	5,220	3.23	cPGP	4000	23,428
1.24	cap	500	11,077	4.14	cg	0	5,411	3.12	cPGP	6000	24,446
1.25	cap	500		4.16	cg	0	5,252	3.24	cPGP	6000	21,900
2.04	cap	500	9,550	3.21	cg	250	8,785	1.01	none	0	7,398
2.05	cap	500	11,460	2.09	cg	500	11,141	1.02	none	0	6,182
2.06	cap	500	10,823	2.24	cg	500	11,077	1.03	none	0	5,991
2.07	cap	500	12,159	3.22	cg	500	10,441	2.01	none	0	4,504
2.18	cap	500	10,345	4.06	cg	500	9,040	2.02	none	0	4,399
4.01	cap	500	8,403	4.18	cg	1000	11,663	2.03	none	0	3,874
4.02	cap	500	8,149	2.17	cg	2000	14,770	3.02	none	0	8,117
4.03	cap	500	8,308	2.19	cg	2000	15,661	3.05	none	0	7,257
4.04	cap	500	8,750	2.21	cg	2000	14,961	3.06	none	0	6,939
1.19	cap	1000	13,910	2.25	cg	2000	16,297	3.07	none	0	7,401
1.21	cap	1000	10,823	3.16	cg	2000	16,616	cp1	none	0	10,663
2.13	cap	1000	14,165	4.08	cg	2000	8,913	cp3	none	0	10,106
1.20	cap	1000	14,260	2.16	cg	4000	19,099	cp4	none	0	11,539
1.16	cap	2000	17,316	3.15	cg	4000	23,046	cp5	none	0	10,743
1.17	cap	2000	17,284	3.17	cg	6000	29,603	3.03	PGP	0	7,401
1.18	cap	2000	18,880	4.07	cg	8000	37,688	4.10	PGP	0	6,048
2.22	cap	2000	17,571	3.08	cPGP	0	6,872	4.11	PGP	0	6,446
1.13	cap	4000	23,428	4.19	cPGP	0	4,584	3.04	RUB	0	6,685
1.14	cap	4000	24,319	4.20	cPGP	0	5,475	4.13	RUB	0	3,501

	TABLE 4-7										
	STRENGTH DATA SORTED BY PRESSURE										
Test	Friction Relief	Confine Pressure psi	Axial Stress psi	Test	Friction Relief	Confine Pressure psi	Axial Stress psi	Test	Friction Relief	Confine Pressure psi	Axial Stress psi
1.04	cap	0	5,052	2.10	cap	250		3.18	cPGP	1000	12,223
1.05	cap	0	4,393	2.11	cap	250	8,403	3.20	cPGP	1000	12,732
1.06	cap	0	5,112	2.12	cap	250	9,440	1.16	cap	2000	17,316
2.08	cap	0	6,653	4.09	cap	250	8,502	1.17	cap	2000	17,284
4.12	cap	0	5,173	3.21	cg	250	8,785	1.18	cap	2000	18,880
4.15	cap	0	5,730	2.15	cPGP	250	9,167	2.22	cap	2000	17,571
3.01	cg	0	6,844	3.09	cPGP	250	9,021	2.17	cg	2000	14,770
3.19	cg	0	6,939	3.13	cPGP	250	8,913	2.19	cg	2000	15,661
4.05	cg	0	5,220	1.22	cap	500	10,823	2.21	cg	2000	14,961
4.14	cg	0	5,411	1.23	cap	500	12,159	2.25	cg	2000	16,297
4.16	cg	0	5,252	1.24	cap	500	11,077	3.16	cg	2000	16,616
3.08	cPGP	0	6,872	1.25	cap	500		4.08	cg	2000	8,913
4.19	cPGP	0	4,584	2.04	cap	500	9,550	2.14	cPGP	2000	15,024
4.20	cPGP	0	5,475	2.05	cap	500	11,460	3.25	cPGP	2000	16,297
1.01	none	0	7,398	2.06	cap	500	10,823	1.13	cap	4000	23,428
1.02	none	0	6,182	2.07	cap	500	12,159	1.14	cap	4000	24,319
1.03	none	0	5,991	2.18	cap	500	10,345	1.15	cap	4000	27,215
2.01	none	0	4,504	4.01	cap	500	8,403	4.17	cap	4000	20,595
2.02	none	0	4,399	4.02	cap	500	8,149	2.16	cg	4000	19,099
2.03	none	0	3,874	4.03	cap	500	8,308	3.15	cg	4000	23,046
3.02	none	0	8,117	4.04	cap	500	8,750	2.20	cPGP	4000	22,918
3.05	none	0	7,257	2.09	cg	500	11,141	3.23	cPGP	4000	23,428
3.06	none	0	6,939	2.24	cg	500	11,077	1.10	cap	6000	29,921
3.07	none	0	7,401	3.22	cg	500	10,441	1.11	cap	6000	30,685
cp1	none	0	10,663	4.06	cg	500	9,040	1.12	cap	6000	31,831
cp3	none	0	10,106	3.10	cPGP	500	11,205	2.23	cap	6000	31,067
cp4	none	0	11,539	3.14	cPGP	500	10,313	3.17	cg	6000	29,603
cp5	none	0	10,743	1.19	cap	1000	13,910	3.12	cPGP	6000	24,446
3.03	PGP	0	7,401	1.20	cap	1000	14,260	3.24	cPGP	6000	21,900
4.11	PGP	0	6,446	1.21	cap	1000	10,823	1.08	cap	8000	36,096
4.10	PGP	0	6,048	2.13	cap	1000	14,165	1.09	cap	8000	38,897
3.04	RUB	0	6,685	4.18	cg	1000	11,663	4.07	cg	8000	37,688
4.13	RUB	0	3,501	3.11	cPGP	1000	12,223	1.07	cap	9000	27,502

Table 4-8 shows the maximum axial and confining pressure for the rectangular specimens.

TABLE 4-8							
STRENGTH DATA FOR RECTANGULAR SPECIMENS							
Test	Friction Relief	Lateral Pressure psi	Axial Stress psi		Test	Friction Relief	Lateral Pressure psi	Axial Stress psi
TR1.1	NONE	0	3730		TR3.1	CG	0	4330
TR1.2	CPGP	0	4130		TR3.2	CPGP	2000	16400
TR1.3	CPGP	1000	11200		TR3.3	CPGP	2000	15700
TR1.4	CPGP	2000	15700		TR3.4	CPGP	1000	11300
TR2.1	CG	0	3000		TR4.1	NONE	0	5900
TR2.2	CG	0	4400		TR4.2	CPGP	2000	16200
TR2.3	CPGP	500	8200		TR4.3	CPGP	500	7300
TR2.4	CPGP	2000	18000		TR4.4	CPGP	500	9000

Table 4-9 shows the maximum axial and lateral pressure for the biaxial tests B3.1 through B3.7.

TABLE 4-9							
BIAXIAL STRENGTH DATA							
Test	Friction Relief	Lateral Pressure psi	Axial Stress psi		Test	Friction Relief	Lateral Pressure psi	Axial Stress psi
B3.1	CAP	0	3,640		B3.5	CAP	500	5,440
B3.2	CG	100	3,690		B3.6	CG	750	7,090
B3.3	CG	200	4,000		B3.7	CG	600	6,460
B3.4	CG	300	4,520					

4.51 MOHR CIRCLES

Figure 4-14 shows the Mohr circles for the tests using cap blocks alone for friction relief. The circle for 9 ksi confining pressure was not plotted. Figures 4-15 and 4-16 show the Mohr circles for tests using caps with grease and PGP pads, respectively. The maximum load for each confining pressure was averaged to generate the Mohr circles. The tensile circle was generated using the Modulus of Rupture from the beam tests.

The graphs for each type of relief are very similar with the exception of the Mohr circle for 6 ksi confining pressure using cap blocks with PGP pads. All the strength data, with the exception of 6 ksi test using cap blocks with PGP pads, was averaged to produce a single graph shown in figure 4-17. In addition to the circles a line, radius, was added to each circle at an angle of 2ϕ, where ϕ depicts the average of the measured angle of the failure plane for each pressure. Two additional lines, radii, were added to each circle at angles of $2\phi - 5°$ and $2\phi + 5°$ to provide for a possible error, $\pm 2.5°$, in the measure of the failure angle. An error of $\pm 1.5°$ was used for the uniaxial circle.
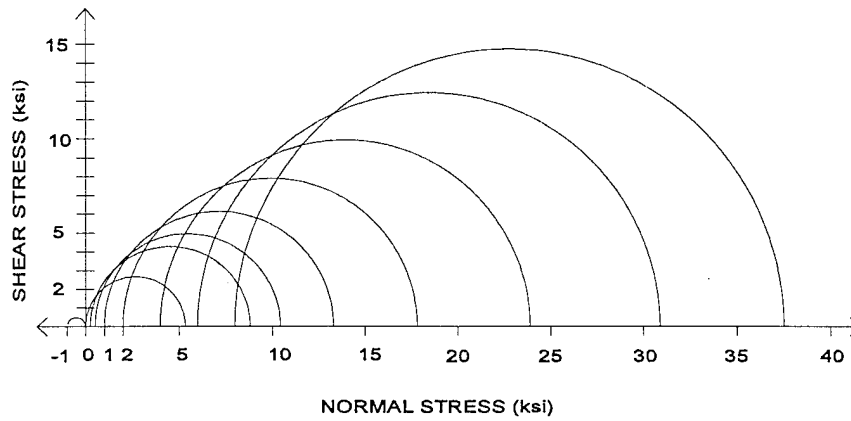
Figure 4-14: Mohr Circles for Tests with Cap Blocks Alone
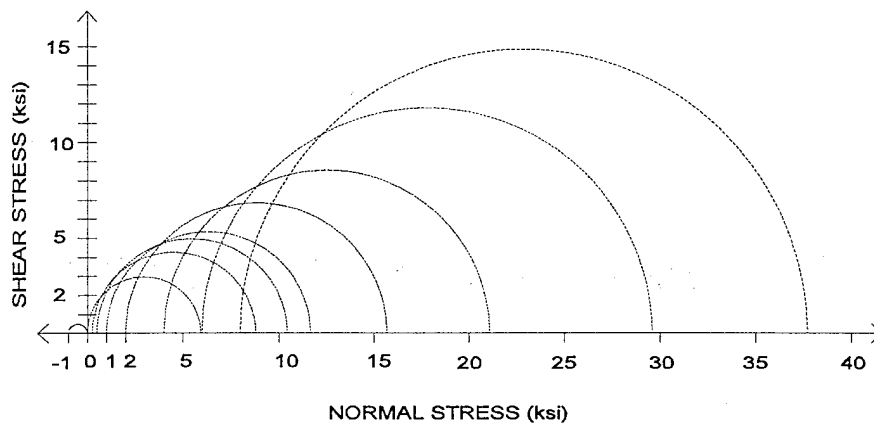
Figure 4-15: Mohr Circles for Tests with Cap Blocks and Grease
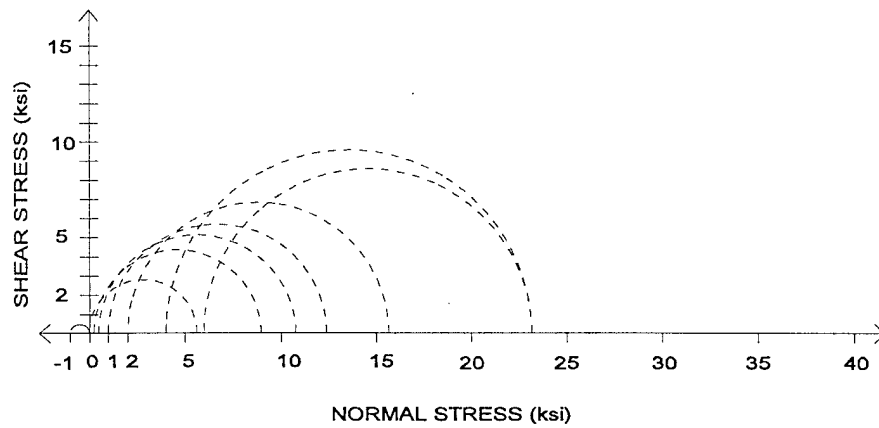
Figure 4-16: Mohr Circles for Tests with Cap Blocks and PGP Pads

A tangent was drawn from the 8 ksi circle to the .5 ksi circle. This tangent is close to being tangent to the 1, 2, 4, and 6 ksi circles. However, it is not very close to the .25 ksi, 0 ksi, and tensile circles. Figure 4-18 shows Mohr circles from tests in the tensile-compression regime by Theocaris and Prassianikis [1974] showing that the circles do not fit the envelope as lateral compressive stress is increase. Theocaris and Prassianikis [1974] conclude that there is a change in the mode of failure as the axial load is moved from tensile to compressive axial stress. They also conclude that the use of the Mohr envelope as a limit surface is invalid. Further examination of figure 4-17 shows that many of the angles measured are not perpendicular to the tangent line, both at low pressures and at high pressures. Furthermore, it is not possible to produce an envelope that runs from the tangent line and touches both the uniaxial and tensile circles. Thus, the use of the Mohr envelope as a damage or plasticity surface in the classical manner is not applicable to the tests in this study, except in the Median pressure region from 500 to 4000 ksi.

The effects of friction between the plunger and triaxial cell have not been accounted for in the graphs for the triaxial tests. Assuming that the affect would be to lower the peak stress by an amount proportional to the lateral pressure then the angle of internal friction would be slightly lower than that measured.
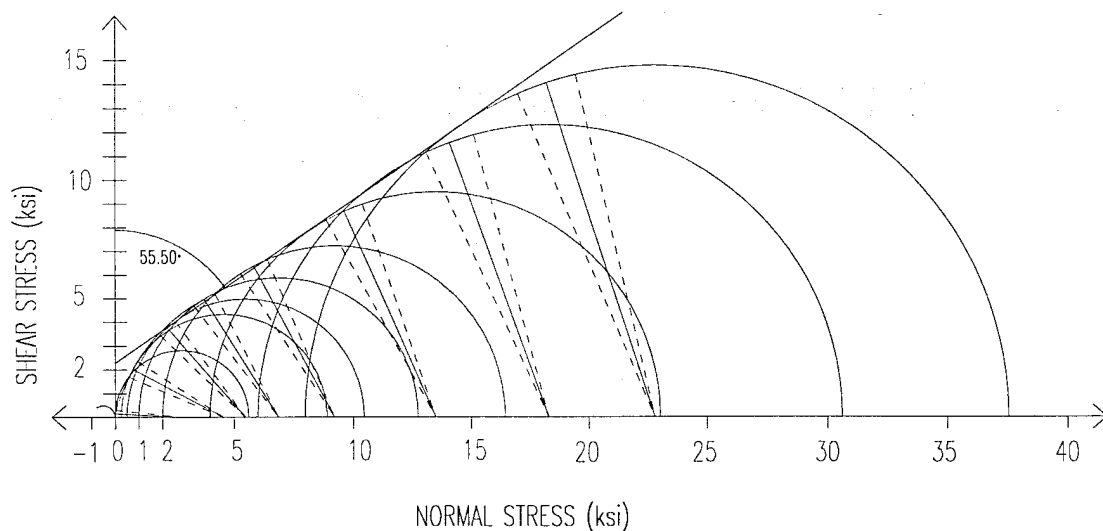
Figure 4-17: Average Mohr Circles for Triaxial Test Series

It should be noted that the maximum stress of increases as the intermediate principal stress increases. This brings up the question "Does the intermediate principal stress affect the orientation of the failure plane?" The tests performed in this study were not designed to answer this question and there is no data available to provide an answer. Furthermore, it should be noted that the stress path and the presence of prior damage may also affect the results obtained.
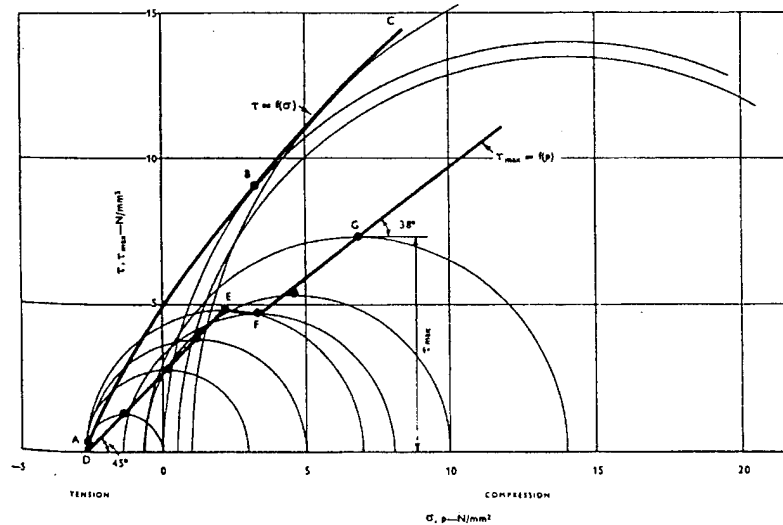
Figure 4-18: Mohr Circles for Tension-Compression Region (Theocaris and Prassianikis [1974])

Mohr circles were not prepared for the rectangular specimens. Figure 4-19 shows the Mohr circles for the biaxial tests B3.1 through B3.7. The direction of zero stress was ignored. The tangent line shown was drawn from the uniaxial, 0 psi, circle to the 500 psi circle. The angle of friction is 90-55.6= 34.6°. If the tangent were run from 0 psi to 750 psi the angle of friction would be 40°.

Based on the friction angle of 34.6° the angle of the failure plane should be 27.8°. None of the measured angles were close to this orientation; thus, the use of Mohr Coulomb criteria is unsuitable. This may be due to the constraint imposed by the lateral platens or the possible inappropriateness of the model in general.
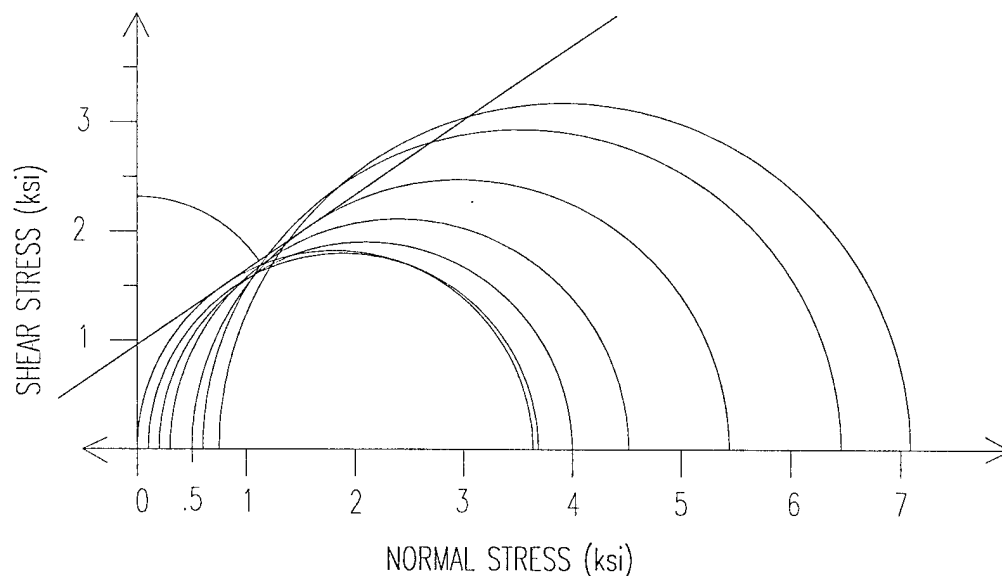
Figure 4-19: Mohr Circles for Biaxial Tests in the Plane of Loading

4.52 MAXIMUM AXIAL STRESS VERSUS CONFINING PRESSURE

Figure 4-20 shows the maximum axial stress versus confining pressure. The data is broken out by the type of friction relief. Several out-liers are noted. Specimen T25.4.08 was damaged during preparation. Specimens T25.3.24 and T25.3.12 slipped during testing. During the testing of specimen T25.1.07 the cap block failed not the sample. The data is broken out by the type of friction relief. A line was fit to all of the data except the uniaxial data and the out-liers.
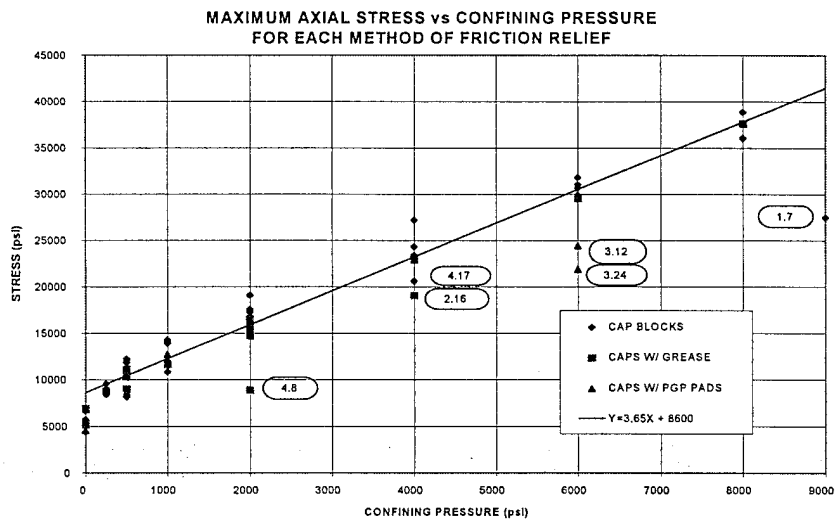
Figure 4-20: Maximum Axial Stress versus Confining Pressure (by Relief Type)

Figure 4-21 shows the maximum axial stress versus the confining pressure broken out by batch. The strength of the samples from batch 4 at 500 psi are lower than those of the other samples.
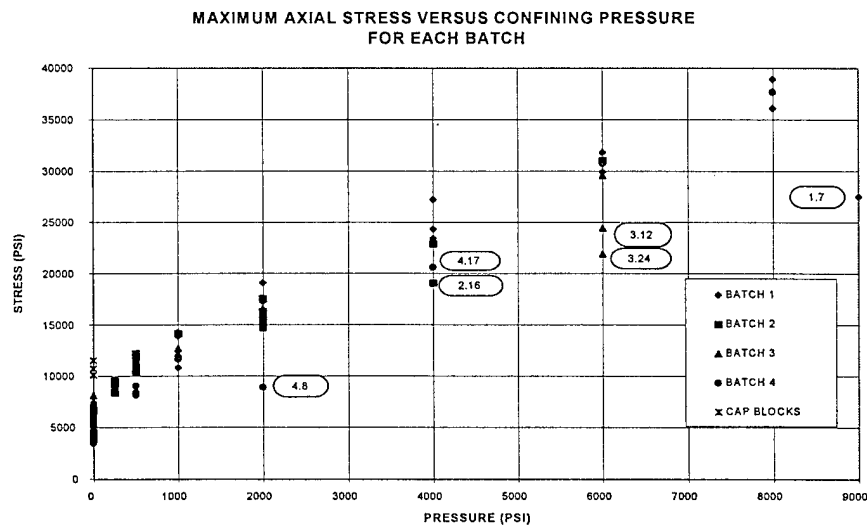
Figure 4-21: Maximum Axial Stress versus Confining Pressure (by Batch)

4-24

Figure 4-22 shows the maximum axial stress versus lateral pressure for the samples from batch 3 of the biaxial tests. Using linear regression, the slope of the best fit line is 4.9 with a coefficient of determination of .962. A quadratic fit produces the following equation with a coefficient of determination of .995:

$$Y = 4.8X^2 + 1.5X + 3.58$$

where X and Y are given in ksi. If linear regression is applied only to tests at pressures less than or equal to 500 psi, as higher pressures resulted in a different failure mode, the slope is 3.73 with a coefficient of determination of .954.

PEAK STRESS VERSUS CONFINEMENT FOR BIAXIAL TESTS

$y = 4.76x^2 + 1.469x + 3.5781$
$R^2 = 0.9951$

$y = 4.9329x + 3.2577$
$R^2 = 0.9617$

AXIAL STRESS (ksi)

LATERAL STRESS (ksi)
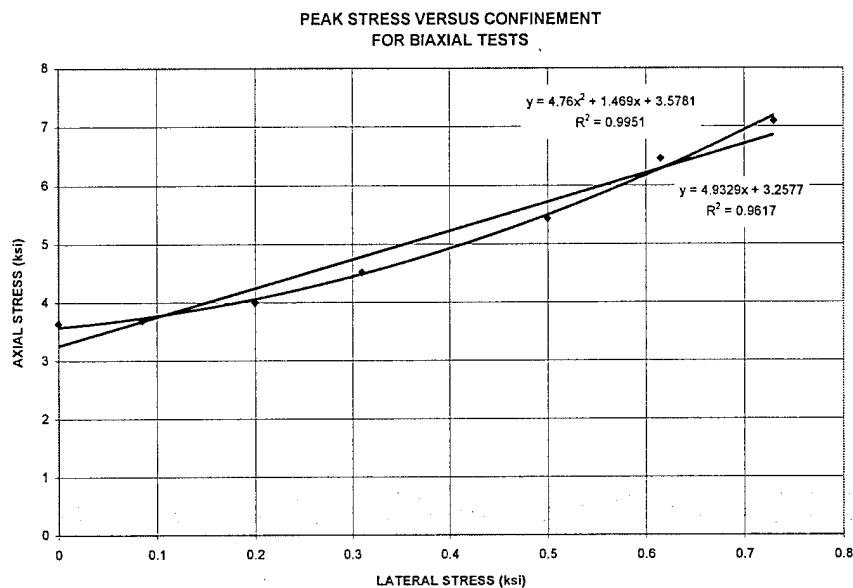
Figure 4-22: Peak Stress versus Confining Pressure (Biaxial Tests)

4.53 OCTAHEDRAL SHEAR VERSUS OCTAHEDRAL NORMAL

Figure 4-23 shows the octahedral shear versus the octahedral normal stress. The line A-A represents the states of equal shear and normal stress. Comparing this data with Figure 4-1, angle versus confining pressure, the slope of the orientation versus confining pressure is large up to about 2 ksi. The slope decreases dramatically at 2 ksi. From figure 4-23 all tests at pressures lower than 2 ksi have peak octahedral shear stresses greater than their corresponding peak octahedral normal stresses. All tests at pressures greater than 2 ksi have peak octahedral shear stresses less than their corresponding octahedral normal stress while tests at 2 ksi are at the point of equal peak octahedral shear and normal stresses. This correlation between the ratio of octahedral shear and normal stresses and the rate of change of the failure orientation with increasing confinement indicates an influence of the ratio of the peak octahedral shear to octahedral normal on the failure mechanism.
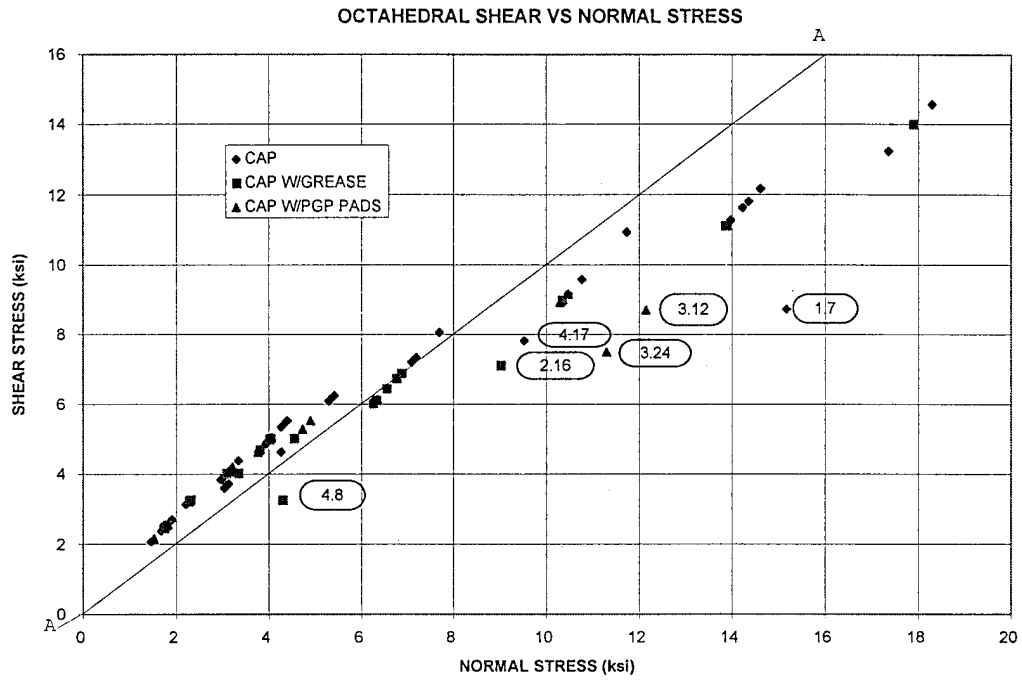
Figure 4-23: Octahedral Shear versus Octahedral Normal Stress

4.60 CONSTITUTIVE PROPERTIES

The changes in the amount of plastic strain, reloading modulus, and lateral extension ratio during reloading were investigated for samples with caps and grease to relieve friction and having cyclic loading patterns. These measures are important since they set the stage for the constitutive model. The plastic deformations were analyzed as well as the "damage" to the material properties of modulus and lateral extension ratio. The following steps were taken to obtain these measures. A line was drawn from the initial reloading point, B, to the point of initial unloading, A, for each cycle (figure 4-24). This line was used for all of the measurements. The percent peak stress refers to the ratio of the applied deviator stress to the peak deviator stress.

T25.3.17
STRESS vs STRAIN at MID HEIGHT
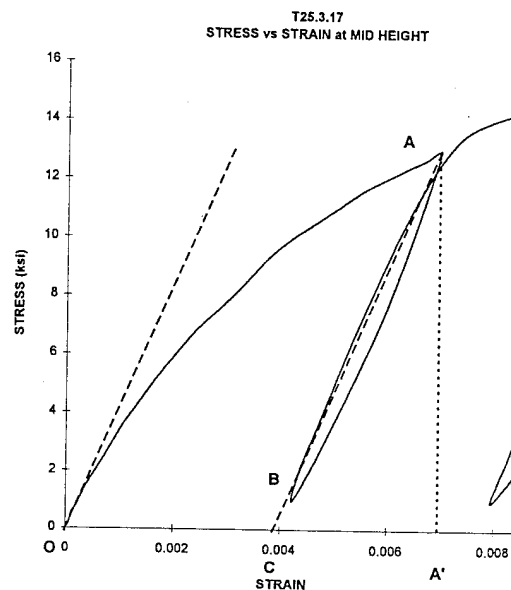
Figure 4-24: Stress-Strain Curve (T25.3.17)

4.61 STRAIN MEASURES (PLASTIC DEFORMATION)

Before examining the results of the tests it is important to review factors that may affect the measurements. There are two main factors that may affect the measurement. The first is creep. The second is the presence of surface irregularities on the sample.

Creep occurred with the application of hydrostatic load as well as with the application of deviatoric load. During triaxial tests creep due to the hydrostatic load tends to increase the axial or compressive strain while it decreases the lateral or tensile strains. From the hydrostatic data the total plastic strain after loading to 6 ksi is between .0001 (in/in) and .0002 (in/in). Since this over a period of about 30 minutes compared to 10 to 20 minutes for the standard triaxial tests the maximum amount of plastic creep strain that may show up on tests to 6 ksi in about .00007 (in/in) which is about 5% of the axial plastic strain and about 10% of the lateral strain.

During specimen preparation voids and rough areas of the specimens were sanded and filled with epoxy. This process created a smooth stable surface for most gauges; however, the confining pressures caused voids beneath some of the gauges that had not been properly filled to collapse. This collapse caused several gauges to fail. Some of the gauges did not fail but deformed to the newly formed depression. The affect of this is to cause the gauge to lengthen as if loaded in tension. This tends to decrease the compressive strains

registered by axial gauges and increase tensile strains in the lateral gauges. In the case of the hydrostatic tests this tends to reduce the strains measured by the gauges. The actual amount depends on the geometry of the depression.

The hydrostatically tested samples were inspected. The results of this inspection are compared to the strain measures. T25.3.19 had a pin hole break in the mid lateral gauge which failed. A small depression was located on the side of the mid axial gauge affecting the outer strand of the gauge. The total plastic strain after the test was .000245 (in/in) The bottom lateral gauge had a depression in the middle third of the gauge. the total plastic strain after the test was .000125 (in/in). The bottom axial gauge had no sign of a depression and a total plastic strain of .000282. Note that the resultant plastic strain for the gauge with the largest depression, the bottom lateral gauge, is half the value of the strain of the gauge with no depression. Since the gauges are measuring opposite direction the result may be interpreted as anisotropy; however, the presence of the depressions may account for the difference.

For T25.4.5 the only two gauges that survived the test were the two gauges at the middle of the specimen. Neither gauge had a depression. However, the data from the lateral gauge is jittery as suggests a poor connection or solder connection in the wiring. The total plastic strain from the mid lateral gauge at the end of the test is .0004 (in/in) while the mid axial gauge had a total plastic strain of .0002 (in/in). The lateral strain is twice the axial strain, which is opposite the result of the test T25.3.19. Since there were no depressions noted this may be an indication of anisotropic behavior.

Given the lack of statistically significant results and the factors that may have affected the results. The possibility of anisotropic behavior is noted but not used in the analysis or discussion of the results. Furthermore, the presence of anisotropy would require far more tests than the scope of these tests would allow to properly model its affect on the constitutive properties and the failure development.

Since the primary objective of this study is to look at the trends of the data and not to consider in minutia the measures taken, the effects of these factors on the actual strains is noted but not employed in the analysis of the data.

Plastic Flow

An essential part of a plasticity model is the plastic flow tensor. Figure 4-25 shows the plastic lateral extension ratio versus the % of peak stress for pressures from 500 psi to 6000 psi. The data for uniaxial tests and tests at 250 psi show very large plastic lateral deformation in comparison to the axial plastic deformations. As the confining pressure increases the majority of the plastic deformation is in the axial not

lateral direction. Creep from the hydrostat tends to magnify this result but can not account for it solely. In the case of the 6 ksi test the axial strain is 5 to 10 times larger than the lateral strain. At 500 psi the axial plastic strain is about 3 times larger than the lateral strain. The amount of lateral strain compared to axial strain increases as the peak stress is approached.

PLASTIC LATETERAL EXTENSION RATIO VERSUS % PEAK STRESS
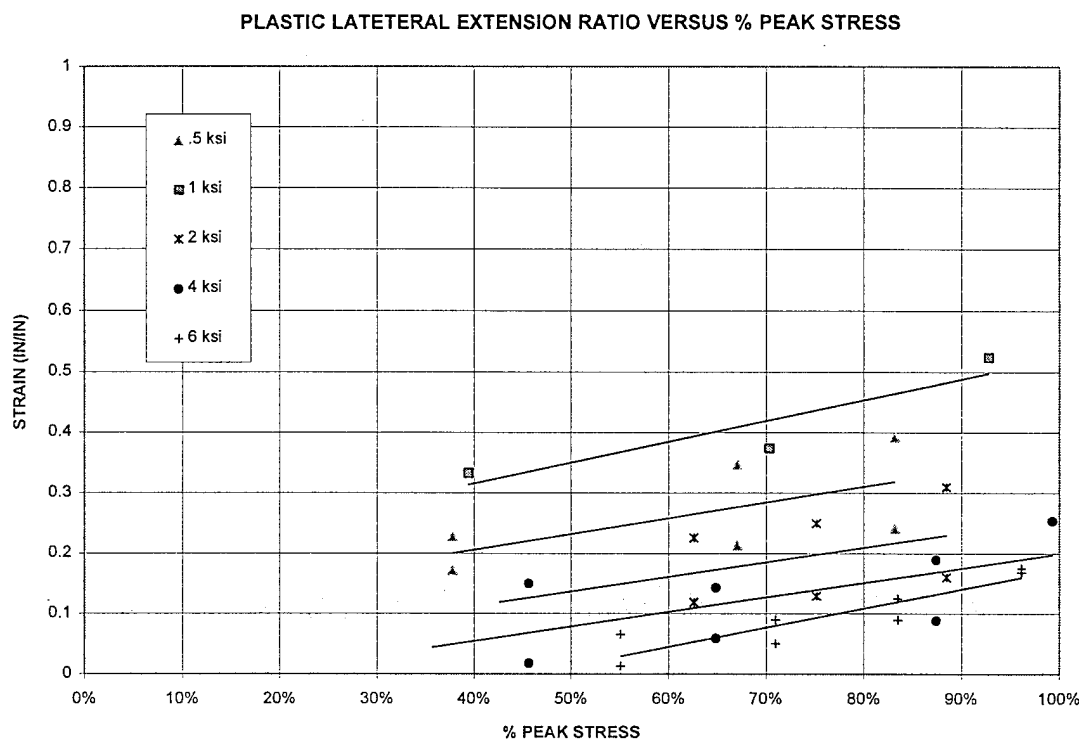
Figure 4-25: Plastic Lateral Extension Ratio versus Percent of Peak Stress

Plastic Strain

The plastic strain during the application of the deviator load was measured, OC on figure 4-24, along with the total strain, OA' on figure 4-24. The percent of the total strain that was plastic was calculated and is herein termed the % plastic strain. The deviator stress at point A was compared with the maximum axial deviator stress to obtain the percentage of the maximum deviator stress at which the cycle was performed. This percentage is termed the % peak stress. The percent plastic strain versus the percent peak stress was plotted for both the axial and lateral gauges in the prepeak regime and are shown in figures 4-26 and 4-27 respectively. If the linear fit for the test at 2 ksi were to exclude the results beyond 80% peak stress, the slope would be .53 and the intercept would be .018%. The slope of each line indicates the rate at which the percent plastic strain changes as the load increases. The intercept indicates the percentage of the initial strain that is plastic from the initial application of deviator load. Values of lateral strains could not be

4-29

obtained for the tests at 8 ksi as all lateral gauges failed during the application of the lateral pressure for these tests.

% PLASTIC STRAIN VERSUS % PEAK STRESS
AXIAL GAUGES
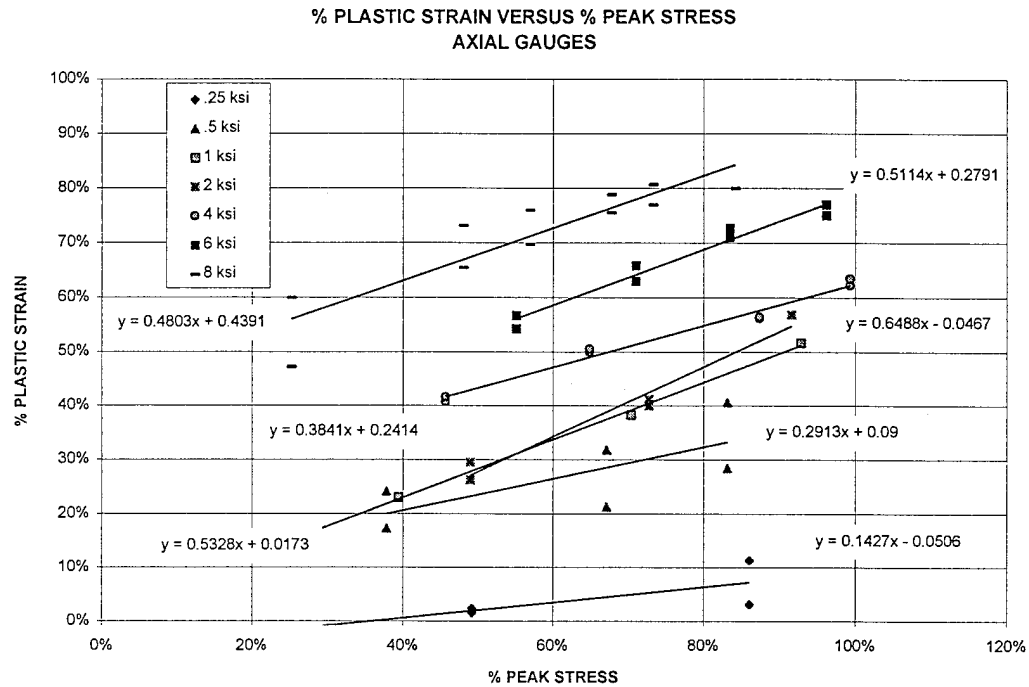
Figure 4-26: Percent Plastic Strain versus Percent Peak Stress (Axial)

% PLASTIC STRAIN VERSUS % PEAK STRESS
LATERAL GAUGES
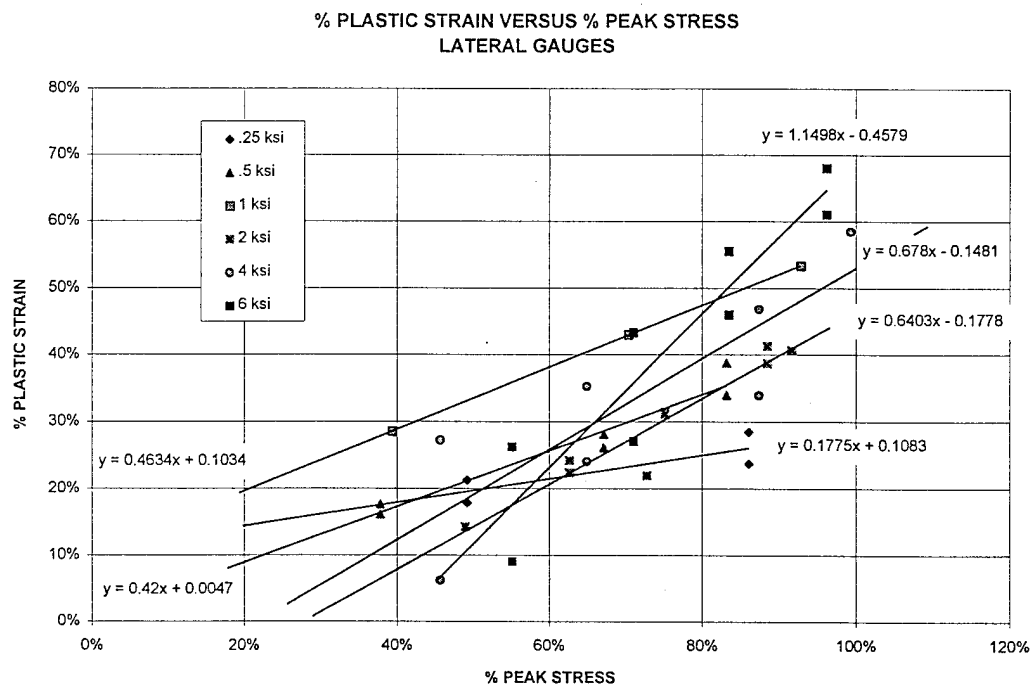
Figure 4-27: Percent Plastic Strain versus Percent Peak Stress (Lateral)

The slopes and Y-intercepts from figure 4-26 were taken for each confining pressure and plotted against confining pressure in figures 4-28 and 4-29 respectively. In figure 4-28 the value of the slope of the lines in figure 4-26 increases rapidly from 0 to 1 ksi. This indicates that the accumulation of plastic strain in the axial direction during loading increases rapidly as confinement increases from 0 to 1 ksi. After 1 ksi the slope of the lines in figure 4-26 tend to level off at about .5. This indicates that the axial plastic strain as a percent of the total strain increases at a rate of 5% for every 10% of the peak stress that is applied and that this rate is constant for pressures greater than or equal to 1 ksi.

The Y-intercepts, figure 4-29, which were taken from the axial gauges, figure 4-26, remain at or near 0% up to 2 ksi and increase to 40% at 8 ksi. This indicates that all of the strain under initial application of the deviator load is all elastic for pressures up to 2 ksi. It also indicates that for confinement of 4, 6, and 8 ksi the strain at the initial application of the deviator load will contain 20%, 30%, and 42% plastic strain. Negative Y-intercepts should be interpreted by looking at the corresponding X-intercept; thus, all strains will be elastic up to the percent of the peak stress represented by the X-intercept.
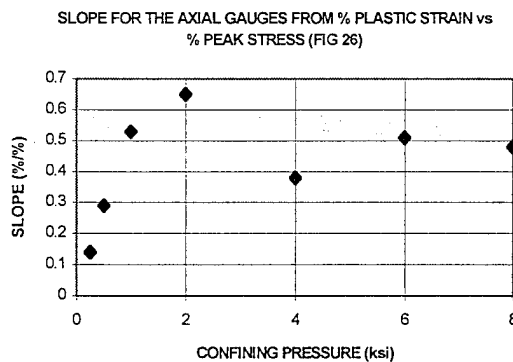
Figure 4-28: Slope from Figure 4-26 (Axial)   Figure 4-29: Y-Intercept from Figure 4-26 (Axial)
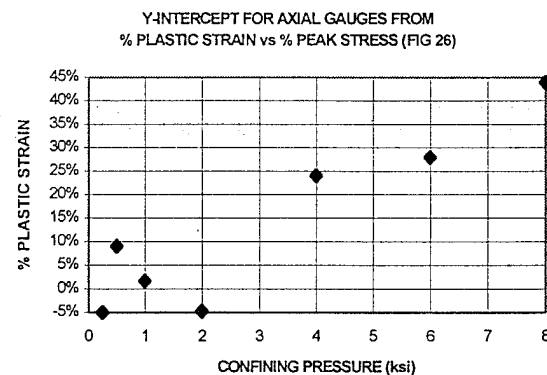
The slopes and Y-intercepts from figure 4-27 were taken for each confining pressure and plotted against confining pressure in figures 4-30 and 4-31 respectively. In figure 4-30 the value of the slope of the lines in figure 4-27 increases monotonically from 0 to 6 ksi. This indicates that the accumulation of lateral plastic strain during loading increases as the confining pressure increases.

The Y-intercepts, figure 4-31, which were taken from the lateral gauges, figure 4-27, remain at or near 0% up to 1 ksi and decrease to -40% at 6 ksi. Negative Y-intercepts should be interpreted by looking at the corresponding X-intercept (fig 4-32). All lateral strains are elastic up to the percent of the peak stress represented by the X-intercept. Once the applied load is equal to the percentage of the peak stress represented by the X-intercept then plastic lateral deformations will begin to occur. The change in X-intercept (fig 4-32) increases in a logarithmic fashion, rapidly at first then leveling off. This result suggests

4-31

that dilatant plastic lateral strains may begin immediately upon loading. At higher pressures lateral strains start out elastic then become plastic well into the loading process , e.g. lateral strains are elastic until 40% of the peak stress then plastic lateral strain begin. Disregarding the possible effects of creep, the results shown in figures 4-27, 4-30, 4-31, and 4-32 show that in general as confining pressure increases plastic lateral strains begin later in the loading process. From figure 4-27 it appears that in all cases plastic lateral strains begin prior to 50% of the peak stress; furthermore, the majority of tests have 20% to 30% plastic strain at 60% of the peak stress.
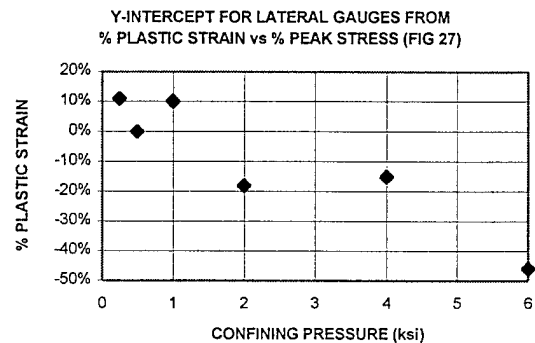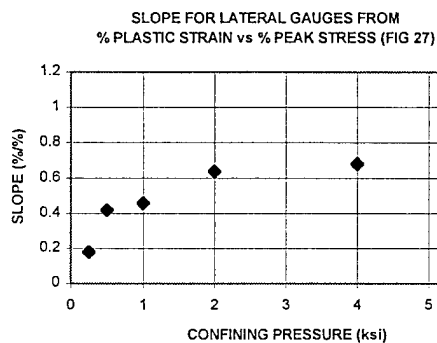
Figure 4-30: Slope from Figure 4-27 (Lateral)   Figure 4-31: Y-Intercept from Figure 4-27 (Lateral)
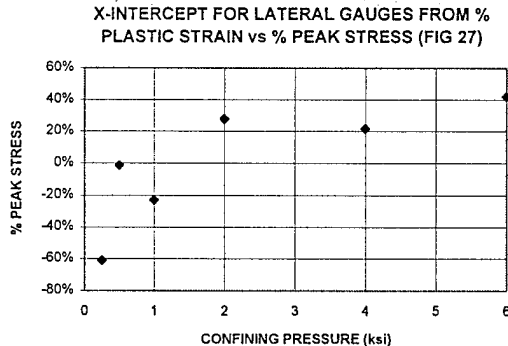
Figure 4-32: Y-Intercept from Figure 4-27 (Lateral)

The effect of the hydrostatic creep was mentioned earlier in this chapter. It was found that the total hydrostatic creep over the entire test was less than 10% of the total plastic lateral strain. However, this result does not preclude the possibility that the creep strains were a significant portion of the total plastic strain at early stages of the loading. Since most of the data were taken above 50% of the peak stress it is unlikely that creep was a significant factor in these results.

4.62 DAMAGE

Classical Damage Mechanics (CDM) focuses on changes to the modulus. Most models consider changes to the bulk modulus, K, and the shear modulus, G. Therefore it is important to investigate changes in these material properties by examining the changes to the axial (sometimes referred to as Young's) modulus, E, and the lateral extension ratio, ν. The bulk modulus, K, and the shear modulus, G, are related to the axial modulus, E, and the lateral extension ratio, ν, by the following equations:

$$K = \frac{E}{3(1-2\nu)} \qquad \qquad 4.1$$

$$G = \frac{E}{2(1+\nu)} \qquad \qquad 4.2$$

The initial modulus, E, and lateral extension ratio were determined to be 5000 ksi and .19, respectively, for the case of samples with no relief of the platen friction and 4500 ksi and .21 for the case with relief of the platen friction. This yields a bulk modulus, K, of 2600 ksi and a shear modulus, G, of 1900 ksi for the case with friction relief. The bulk modulus determined from the hydrostatic data was 2400 ksi which agrees well with the results from using equation 4.1.

The degradation of these values is discussed in detail in the following section. It will be shown that at the peak stress the modulus, E, degrades to approximately 85% of the initial value (figure 4-33) while the lateral extension ratio increases to approximately 120% of the initial value. This produces a bulk modulus, K, equal to the initial modulus, 2600 ksi, and a shear modulus, G, of 1500 ksi which is 75% to 80% of the initial value. This is a reduction of 20% to 25% of the shear modulus while the bulk modulus remains the same. This result is consistent with generally accepted results and numerous damage models. The test data does not provide information to determine if the damage was anisotropic or isotropic.

Modulus

The reloading modulus was obtained by taking the slope of the line formed by points C and A on figure 4-24. The initial modulus was taken as the tangent modulus of the initial loading curve. The reloading modulus is compared to the initial modulus, as a percent of the initial modulus, and is plotted against the percent of the peak deviator stress at which the cycle occurred, figure 4-33. The majority of the tests show the modulus begins to degrade between 60 and 75% of the peak stress. The tests at 8 ksi shows a reduction in the modulus of the central section greater than 10% at 40% of the peak stress while the gauges at the ends of the specimen show little reduction up to 90% of the peak stress. Tests at .5, 2 ksi show no reduction in the modulus up to 90% of the peak stress for the mid or end sections.

CHANGE IN MODULUS vs % PEAK STRESS
AXIAL GAUGES
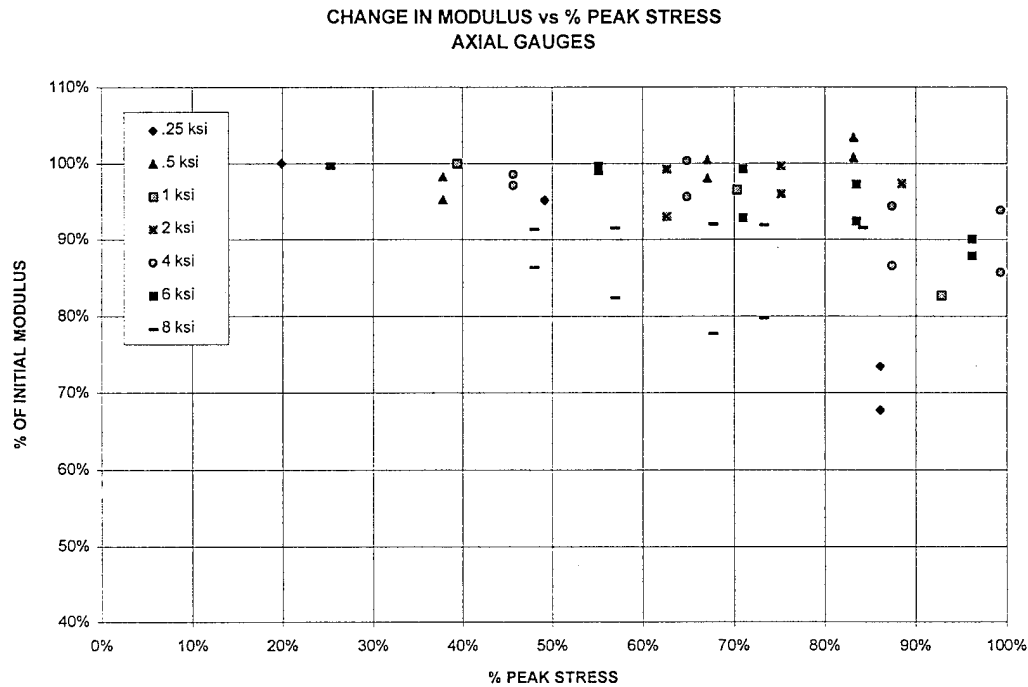
Figure 4-33: Change in Modulus versus Percent Peak Stress (Axial)

Lateral Extension Ratio

The elastic lateral extension ratio during reloading was obtained by taking the ratio of elastic strains in the lateral and axial directions of each set of gauges during reloading. The lateral extension during the first cycle was taken as initial. The elastic lateral extension during each cycle was compared to the initial, as a percent of the initial elastic lateral extension, and is plotted against the percent of the peak deviator stress at which the cycle occurred, figure 4-34. Two of the gauges for the test at 1 ksi with CG relief malfunctioned so that the gauges at the middle and those near the end of the specimen could not be paired as the results from a test at 1 ksi with cap blocks alone for relief was substituted.

Figure 4-34 shows an increase in the elastic lateral extension ratio between 60% and 75% of the peak stress in all specimens. This increase may occur as a consequence of the increase in matrix cracking. These increases also correspond to the reductions in the modulus which is necessary to maintain a constant bulk modulus as seen by the initial and end results. Furthermore, the changes to the elastic lateral extension ratio are more pronounced than changes in the modulus. Therefore, damage in damage models should key on the elastic lateral extension as a measure of the damage in addition to the modulus, E, or alternatively the shear modulus, G, as opposed to the bulk modulus, K. Damage may also be reflected in the modulus in the lateral directions but measures of this were not taken in this study.

4-34

% OF INITIAL LATERAL EXTENSION vs % PEAK STRESS
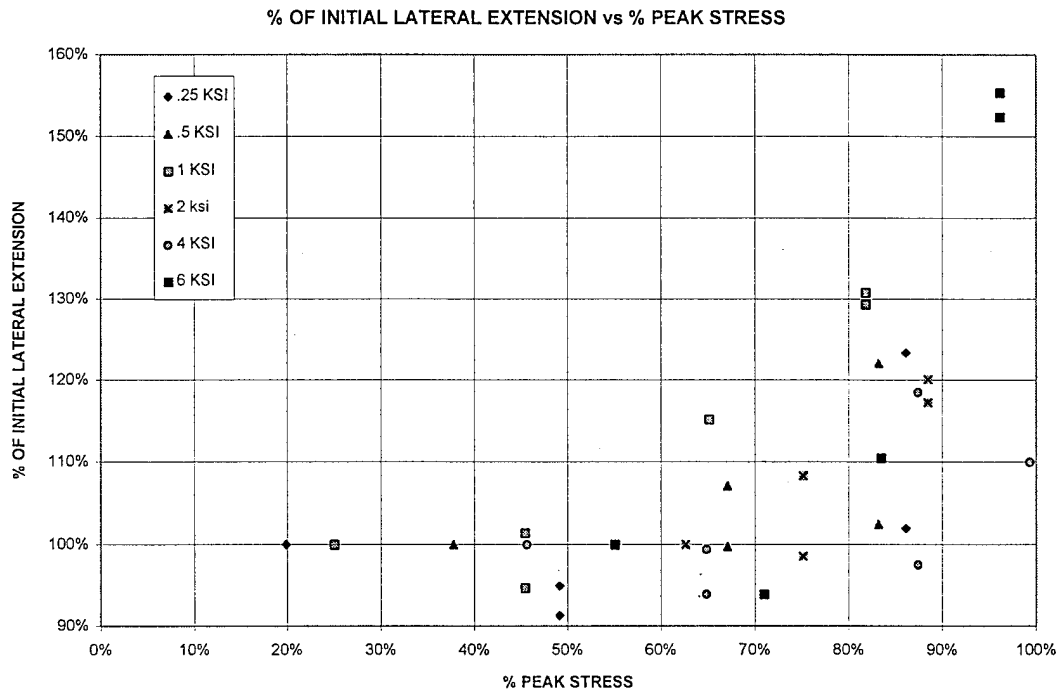
Figure 4-34: Percent of Initial Lateral Extension versus Percent Peak Stress

4.70 SUMMARY OF RESULTS

1. The angle with respect to the maximum compressive stress of the failure plane increases as the confining pressure increases.

2. Cap blocks alone are insufficient to relieve friction between the specimen and the platens. Furthermore, the use of cap blocks with PPG pads does relieve the friction but requires more attention to the specimen preparation to preclude slipping.

3. Localization does occur around 94% of the peak stress. Realizing that specimens can creep to the post peak regime at 75% of the peak stress, one might interpret this result as localization occurs at the peak or in the post peak regime.

4. It is possible to creep the load to failure at 75% of peak stress; furthermore, it is possible to relax the load completely within 90% of the peak stress in the post peak regime but not prior to 85% of the peak stress in the prepeak regime.

5. Use of the Mohr-Coulomb envelope as a model plasticity surface is insufficient to predict the change of angles noted in this study. Application of the angles to the Mohr circles, figure 4-17, reveals deficiencies in the use of the envelope as a plastic limit surface.

6. The graph of octahedral shear versus the octahedral normal stress, figure 4-23, in conjunction with the graph of the failure angle versus confining pressure, figure 4-1, suggest a correlation between the ratio of peak octahedral stress and the failure mechanism.

7. Plastic strain is a major part of the stress-strain relationship for this material.

8. The plastic lateral extension ratio decreases as the confining pressure increases and increases as the deviator stress increases.

9. The percent plastic axial strain at the initiation of the deviator load increases with confining pressure and the percent plastic axial strain increases as the deviator stress increases.

10. Plastic lateral strains begin later in the load sequence, as measured by the percent peak stress, as confinement increases. However, the rate at which the percent plastic lateral strain increases with during loading increases with confining pressure. This leads to the observation that the percent plastic lateral strain at peak stress increases with confining pressure.

11. The modulus, E, begins to reduce between 60% and 75% of the peak stress which corresponds to the formation of numerous matrix cracks.

12. The elastic lateral extension ratio begin to increase between 60% and 75% of the peak stress.

13. The load sequences and materials studied produced little or no change in the bulk modulus but did produce a 20% to 25% reduction in the shear modulus.

5.0 DISCUSSION OF RESULTS

5.10 BEHAVIOR

5.11 ANGLE AND FRICTION

In this study a change in the angle of the failure plane was observed as the confinement on the sample increased. As seen in the previous section there is close agreement between the results of this study and the those obtained by Wawersik and Brace [1971] (figure 4-2). Furthermore, the results are consistent with the findings of Balmer [1949], who states that the angle of the failure plane increases as confinement increases, and are akin to the results of Palaniswamy and Shah [1972, 1974], who found two distinct failure modes for low and high confining pressures.

Friction between the platens and specimen proved to be problematic for Balmer [1949]. To resolve this problem, in this study cap blocks with grease, made from petroleum jelly and steric acid, were used and found sufficient to stop the formation of cones on the ends, allowing the determination of the angle of the failure. Furthermore, the use of cap blocks with pads of grease sandwiched between polyethylene sheets produced slipping which indicates good friction relief.

Mills [1967] and Zimmermann [1972] concluded that the failure plane will always be oriented parallel to the direction of maximum compressive stress. Zimmermann and Traina [1977] state "Failure appears to be by expansion in the direction of the minimum principal stress". Photos of the failed specimens and the loading apparatus suggest that the specimens were constrained from allowing failure (localization) in any direction other than parallel to the maximum compressive stress. This explanation of deviation from the results of this study are corroborated by the results of Gerstle et al. [1980] who have found that boundary constraints inhibit transverse deformations.

Rectangular specimens were tested to investigate the possibility the shape or energy considerations may affect the resulting failure orientation. This would indicate if the failure orientation is a material property or if it is driven by energy concerns. The fact that the samples showed a similar change in angle indicate that there is little or no influence on the angle; however, the location of the failure may be influenced by energy concerns but the data from this study does not support any conclusions regarding this possibility.

The results from the biaxial tests are mixed. Given the argument that the use of displacement based boundary conditions produce lateral constraint which inhibits transverse deformation, the biaxial specimens should have failure planes oriented parallel to the maximum compressive stress. However, all of the

specimens did not. The lack of a trend to the angle of the failure plane as confinement increased, the problems during the specimen preparation, and the video of the biaxial tests lead the author to believe that the specimens tested at 200 and 300 psi produced angled failures because of stress concentrations due to imperfections in the specimen platen interface.

5.12 FAILURE MECHANISM

It is important to review a few salient results from this study prior to discussing the failure mechanism. First, the plastic lateral extension ratio decreases with increasing confinement. This implies that the sample will initially densify at a higher rate as confinement increases. Second, cracks become smaller and more numerous as confining pressure increases. The "crumbly" behavior and "crinkled" gauges provide evidence of this fact as well as the visual inspection of the samples. Since lateral extension is associated with the formation of matrix cracks these results suggest that as confining pressure increases bond crack growth increases early in the load process and matrix cracks are smaller in length and typically bridge bond cracks in the latter portions of the loading for high confining pressures.

Richart, Brandtzaeg, and Brown [1928] and Chinn and Zimmermann [1965] studying cylindrical specimens with lateral fluid pressure, provide a concept of failure that always leads to a vertical failure. This concept is based on a proposal first put forth by Brandtzaeg in which slipping first occurs along angled planes which criss-cross. This slipping induces large tensile strains in the center of the sample which eventually lead to a failure that is oriented parallel to the maximum compressive stress. Examining the work from 1928 shows that none of the samples tested in triaxial compression actually broke. The samples were still intact although the load-displacement curves had gone in to the post peak regime. No effort had been made to relieve the friction between the samples and the axial load application. Furthermore, the samples had a barrel shape when removed similar to the samples shown in figure 4-12. The lack of friction relief led to the development of a conical region of material near the ends that was compressed more than the rest of the sample. The cones acted as wedges driving the material in the center out laterally. The concept of failure fits the observation but is flawed by the fact it does not account for the friction produced between the sample and the axial load platen. This friction produces a non-homogeneous stress field in the material.

Based on the results of this study and the works of Glucklich [1965], Wawersik and Fairhurst [1970] , Dunn at al [1973], Shah and Chandra [1970], Shah and Slate [1965], Horri and Nemat-Nasser [1986] and Meyers, Slate, and Winter [1969], the following concept of failure is presented.

Under uniaxial stress, load induced bond cracking begins at approximately 30% of the peak load and continues until failure. These bond cracks are predominantly parallel to the direction of maximum

compressive stress. Matrix cracks begin bridging between existing bond cracks at 50% of the peak load. These cracks are predominately parallel to the direction of maximum compressive stress. At 75% of the peak load the matrix cracks begin to propagate spontaneously as evidenced by the tests with sustained loads. The initial formation of matrix cracks at 50% correlates with the onset of damage to the lateral extension ratio (Figure 4-30). Glucklich [1965], Shah and Chandra [1970], Shah and Slate [1965], and Meyers et al. [1969] report that the sample begins to dilate at this point, thus, corroborating this finding. Damage to the reloading modulus also began in this region of 50% to 75% of the peak stress.

Under uniaxial stress there is no blunting of the crack growth except for internal variation in stress intensity as the crack propagates from aggregate to aggregate. This allows few large cracks to develop which precipitate failure.

The addition of confining pressure increases the formation of bond cracks and blunts matrix crack growth similar to the crack blunting noted by Horri and Nemat-Nasser [1986]. As the confinement increases the blunted lengths of the matrix cracks are reduced. The increase in bond crack density and the blunting of cracks allow for the formation of numerous, albeit small, matrix cracks in a manner similar to that shown by Horri and Nemat-Nasser [1986]. The increase in bond and matrix crack density increase the probability that the cracks will interact or influence the propagation of one another.

Iqbal and Krokosky [1970] shows that the stress concentrations (intensities) around voids (cracks) decreases as aggregates get closer to the void (crack). They also found that the stress intensity around voids (cracks) and aggregates increases as voids (cracks) get closer to them. As confinement increases the density of cracks increases which reduces the distance between crack (voids). Thus, interaction between the cracks increases causing the cracks to propagate at ever increasing angles to the maximum compressive stress until the material crushes or is dominated by the shear stress.

At pressures below 2000 psi Wawersik and Fairhurst [1970] report the failure is made up of near vertical cracks these cracks get more numerous and shorter as pressure increases. These short near vertical cracks coalesce into a slightly angled failure. At 2000 psi confinement Wawersik and Fairhurst [1970] report that the failure is characterized by an angled failure with short vertical cracks running across it.

At low confining pressures, pressures that result in the peak octahedral shear stress larger than the peak octahedral normal stress, the matrix cracks are blunted allowing the formation of numerous matrix cracks. The length of these cracks is longer than several of the aggregates. The lengths of these cracks get shorter as confinement increases. These cracks interact and form crack bridges across aggregates. The angle of the resulting failure increases as confinement increases. The failure is dominated by the interaction of the

matrix cracks. The blunting of the matrix cracks increases the number of cracks and decreases the length dramatically causing a rapid change in the angle of the failure plane. The angle of the failure plane is typically less than 30 degrees from the maximum compressive stress in this pressure range.

When the pressure is large enough to result in a peak mean stress larger than the peak octahedral shear stress then cracking and subsequent failure is driven by the interaction of bond cracks with the matrix cracks and other bond cracks. The pressures are high enough to produce a density of bond cracks that dominates the failure mechanism. The angle of the failure plane increases slowly with increasing confinement in this pressure range.

This study has shown that some cementious material will exhibit a change in the orientation of the failure plane with increasing confining pressure. It does not preclude the possibility that the angle is affected by the mix design of the material. Furthermore, it may be possible that some mix designs do exhibit a vertical failure under increasing confining pressure or two separate and distinct modes of failure depending on the confining pressure. Further research is needed to determine the affects of mix design on this trend of orientation change with increasing confinement.

This study has shown that the rate of loading can influence the orientation of the failure. In particular it has been found as Galloway [1989] found that the failure plane is oriented parallel to the direction of maximum stress under high strain rates. Although creep tests were run during this study more research is needed to determine the effects of creep loading on the orientation, development, and character of the failure.

During this study the effects of the intermediate principle stress were not studied. However it is known that the intermediate principle stress influences the strength. Biaxial tests produce higher peak loads than uniaxial tests. Mills [1967] provides additional data on the effects of the intermediate principle stress on strength. It is reasonable to assume that the intermediate principle stress may also influence the orientation, development, and character of the failure. More research is needed in this area.

5.20 CONSTITUTIVE MODELING

In this section the requirements placed on an ideal plasticity constitutive model to predict a change in the failure angle with increasing confining pressure are examined. It is found that a change in angle can be predicted if the ratios of the eigen values of the plastic flow tensor change with changes in confining pressure. For the models investigated the value of the hardening modulus at which localized deformations occur increases as confining pressure increases. The value of the hardening modulus at which localization occurs starts off very negative (extreme softening) and moves to the pre-peak hardening regime as confining pressure increases in non associated flow. It is found that non-associativity increases the amount of change in the value of the hardening modulus at which localization occurs and reduces the amount of change in the orientation of the localization zone.

The initial plan of action was to use a simple Mohr Coulomb flow, which produces a localized zone whose orientation is dictated by the internal friction angle. By substituting a function of the confining pressure for the friction angle the orientation would change with confining pressure. However, there are two problems with this approach. First, in order to perform the eigen modal analysis which determined the orientation into which the internal angle function of confinement was substituted, the derivative of the limit function with respect to the stress tensor was taken. If the internal friction had been a function of the confining pressure then this derivative would have been different, producing a different flow tensor and a different tangent stiffness; thus, producing a different result from the eigen modal analysis, not necessarily consistent with the original result in which the internal friction function was originally substituted. Second, the Mohr Coulomb plasticity model fails to predict plastic deformation in the direction of the intermediate stress which is known to be inconsistent with observed results.

5.21 MODEL SETUP

It should be noted that the purpose of this section is not to develop a constitutive model that models all aspects of the behavior of concrete in general or of the mortar tested in this study. The purpose is to identify what feature(s) are needed in an ideal plasticity model in order to predict a change in the failure orientation. Furthermore, the limit surface and plastic flow tensor were derived solely from the triaxial tests in this study and therefore may not apply for situations other than $\sigma_1 > \sigma_2 = \sigma_3$.

Three basic models were considered two associated flow and one non associated flow. Each model followed the concepts of ideal plasticity. All models examined were derived from 2 basic results obtained from the triaxial tests. These results provide a basis for a limit surface and a plastic flow tensor.

The first model uses the limit surface, which will be discussed later, to derive N, the normal to the limit surface which was also used to represent M, the plastic flow tensor $(M = N)$. Thus the first model represents an associate flow model which was analyzed both analytically and numerically.

The second model uses the plastic flow tensor, M, derived from experimental data. The normal to the limit surface, N, is set equal to M $(N = M)$ again producing an associated flow model. A limit surface was not developed for this model since it was analyzed using an analytical method developed by Schreyer and Neilsen [1995] which requires knowledge of N but does not require knowledge of the actual limit surface. The primary purpose of this second model is not to propose a model or form of one but rather to compare the effects of associativity versus non-associativity on the change in the failure angle as confining pressure increases.

The third model is a non-associated flow model that uses the limit surface and the plastic flow tensor, M, derived from the test data. The normal to the limit surface, N, is calculated from the expression derived to fit the data. This model was analyzed numerically and compared to the test data.

Limit Surface

The limit surface represents the point at which the stress state cannot go past without further plastic deformation. The limit surface can be estimated by using the expression for the peak stress as a function of the confining pressure. Figure 5-1 shows the peak stress versus the confining pressure. The following equation is used to estimate the results in figure 5-1

$$\sigma_{11} = 3.65(\frac{\sigma_{22} + \sigma_{33}}{2}) + 8.6 \qquad\qquad 5.1$$

where the stresses are given in ksi. A limit function can be defined by

$$\phi = \sigma_{11} - 3.65(\frac{\sigma_{22} + \sigma_{33}}{2}) - H \qquad\qquad 5.2$$

where the stresses are given in ksi and H is the isotropic hardening function.

MAXIMUM AXIAL STRESS vs CONFINING PRESSURE FOR EACH METHOD OF FRICTION RELIEF

- ♦ CAP BLOCKS
- ■ CAPS W/ GREASE
- ▲ CAPS W/ PGP PADS
- —— Y=3.65X + 8600
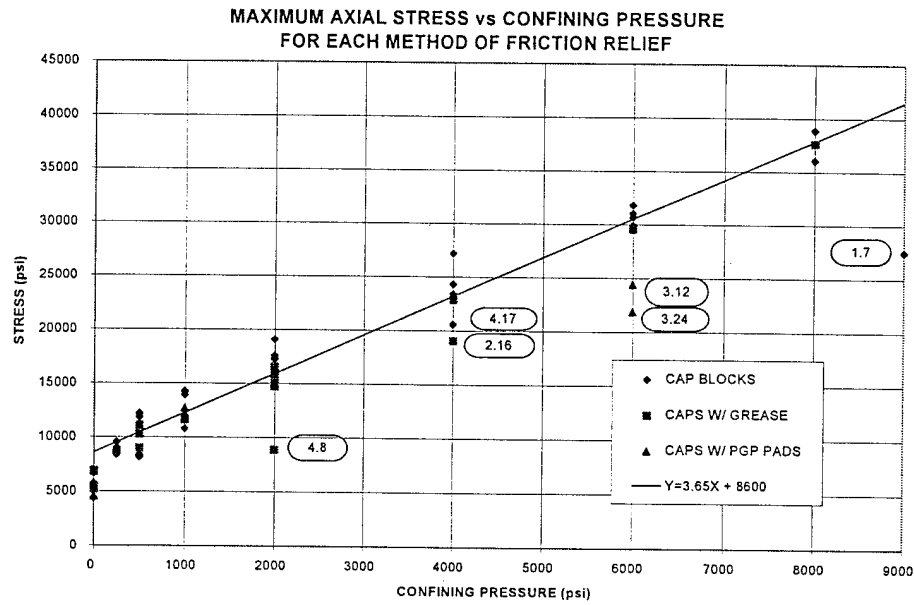
Figure 5-1: Maximum Axial Stress versus Confining Pressure

Herein, the hardening function, H, is considered to have three distinct regimes. The value in each regime is given by the following.

$$H = \begin{cases} H_0 & \bar{e}^P \leq 0 \\ H_0 + (H_L - H_0)\sin(\frac{\pi}{2}(\frac{\bar{e}^P}{\bar{e}_L^P})^Q) & 0 < \bar{e}^P \leq \bar{e}_L^P \\ -\alpha\,(\bar{e}^P - \bar{e}_L^P) + H_L & \bar{e}_L^P < \bar{e}^P \end{cases} \quad 5.3$$

where

$$\bar{e}^P = (\frac{2}{3}(e^P : e^P))^{\frac{1}{2}} \quad 5.4$$

The following values were used for the constants in the equation of the hardening function.

$$\begin{aligned} H_0 &= 4.3 \quad \textbf{\textit{ksi}} \\ H_L &= 8.6 \quad \textbf{\textit{ksi}} \\ \bar{e}_L^P &= .001 \quad \textbf{\textit{in/in}} \\ Q &= .5 \end{aligned} \quad 5.5$$

The value of α was changed to determine the hardening modulus at localization. The linear function was used due to problems with model stability and the need for a large amount of softening with associated and near associated flow.

Plastic Flow Tensor

Figure 5-2 shows the plastic lateral extension ratio (ratio of the lateral plastic strain to axial plastic strain) versus confining pressure from the triaxial tests. The plastic lateral extension ratios were obtained from the last cycle of loading prior to the peak stress in the tests where the cyclical loading occurred. The last cycle occurred between 75% and 95% of the peak stress. No attempt was made to normalize or interpolate the result to the peak stress. These ratios were averaged for each confining pressure and the result is plotted in figure 5-2.
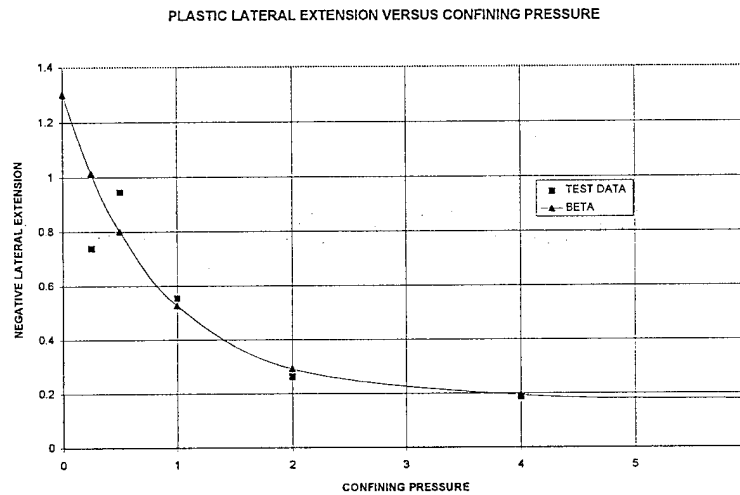
Figure 5-2: Plastic Lateral Extension (Beta) versus Confining Pressure

Using the result in figure 5-2 the plastic flow tensor, **M**, for the triaxial tests may be represented in the following form.

$$M = \begin{bmatrix} 1 & 0 & 0 \\ 0 & -\beta & 0 \\ 0 & 0 & -\beta \end{bmatrix} \qquad \text{5.6}$$

where -β is the plastic lateral extension ratio. The following function is used to represent β and is plotted in figure 5-2.

$$\beta = 1.1 e^{(-1.2(\frac{\sigma_{22} + \sigma_{33}}{2}))} + .2 e^{(-.02(\frac{\sigma_{22} + \sigma_{33}}{2}))} \qquad \text{5.7}$$

where the stresses are given in ksi.

Constitutive and Evolution Equations

The constitutive equation can be written as

$$\dot{\sigma} = E:(\dot{e} - \dot{e}^P)$$

5.8

or

$$\dot{\sigma} = C:\dot{e}$$

5.9

where **C** is the tangent stiffness tensor and is given by

$$C = E - \frac{(E:M \otimes N:E)}{E_P + K}$$

5.10

E_p is the hardening modulus and $K = N:E:M$. The evolution equations are given by

$$\dot{e}^P = \dot{\lambda} M$$
$$\dot{H} = \dot{\lambda} h$$

5.11

Hardening Modulus, E_p

The value of the hardening modulus is important in examining when localization occurs and how much hardening or softening is needed to obtain localization. It is necessary to determine h in order to determine the hardening modulus.

$$\dot{H} = \frac{\partial H}{\partial \bar{e}^P} \frac{\partial \bar{e}^P}{\partial e^P} : \dot{e}^P = \frac{\partial H}{\partial \bar{e}^P} \frac{\partial \bar{e}^P}{\partial e^P} : M\dot{\lambda} = \frac{\partial H}{\partial \bar{e}^P} \frac{2}{3\bar{e}^P} e^P : M\dot{\lambda}$$

5.12

Comparing equation 5.11 with equation 5.12, h can be written as

$$h = \frac{\partial H}{\partial \bar{e}^P} \frac{2}{3\bar{e}^P} e^P : M$$

5.13

The hardening modulus is defined by

$$E_p = -\frac{\partial \phi}{\partial H} h = -\frac{\partial \phi}{\partial H} \frac{\partial H}{\partial \bar{e}^P} \frac{2}{3\bar{e}^P} e^P : M$$

5.14

Using the hardening function, H, the hardening modulus, E_p, can be rewritten as

$$E_P = (H_L - H_0)(\frac{Q\pi}{2\bar{e}_L^P})(\frac{\bar{e}^P}{\bar{e}_L^P})^{Q-1}(\frac{2}{3\bar{e}^P}e^P:M)\cos(\frac{\pi}{2}(\frac{\bar{e}^P}{\bar{e}_L^P})^Q) \quad \begin{matrix} 0 & \bar{e}^P \leq 0 \\ & 0 < \bar{e}^P \leq \bar{e}_L^P \end{matrix} \quad 5.15$$

$$-\alpha(\frac{2}{3\bar{e}^P}e^P:M) \qquad\qquad \bar{e}_L^P < \bar{e}^P$$

5.22 ANALYSIS

Both analytical and numerical analysis of the models were performed. First the associated flow models were analyzed using an explicit method developed by Schreyer and Neilsen [1995]. This method provides an explicit method to determine the orientation of the zone of localization and the value of the hardening modulus at localization for associated plastic flow isotropic constitutive models. The method centers on the loss of ellipticity as the failure criteria; thus, the first occurrence of the discontinuous bifurcation dictates when localization occurs and the orientation of the zone of localized deformations. Next the associated flow case of **M=N** was analyzed numerically by placing the model in a simple driver program for comparison with the analytical results. Finally the non-associated flow rule was examined numerically in the same manner.

Consider the setup of the axis and stress show below (all compression will be considered positive)
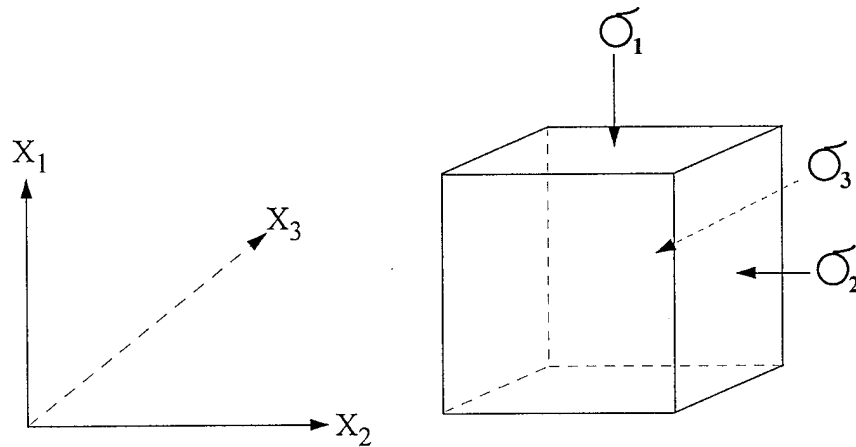
Figure 5-3: Coordinate Axis Orientation

Analytical (Explicit)

The methodology presented by Schreyer and Neilsen [1995] begins by placing the tangent stiffness tensor in the form

$$C = E - f\psi \otimes \psi \qquad \qquad 5.16$$

where

$$\psi = \frac{E:N}{(E:N:E:N)^{\frac{1}{2}}} \qquad \qquad 5.17$$

Therefore, the hardening modulus is determined by

$$E_P = \frac{(E:N:N:E)}{f} - K \qquad \qquad 5.18$$

Schreyer and Neilsen [1995] break the possible solutions in to three types based on how many of the eigen values, ψ_i, of ψ are identical. For triaxial compression with $\sigma_1 > \sigma_2 = \sigma_3$ two of the eigen values are equal. For each type of problem several possible solutions for the orientation are presented with a corresponding value of f for each solution. The minimum value of f is an indictaion of the first possible discontinuous bifurcation and the corresponding orientation is taken as the orientation of the failure plane.

Consider the case of associated plastic flow under triaxial compression, $\sigma_1 > \sigma_2 = \sigma_3$ (compression is positive) with the limit surface, $\phi = \sigma_{11} - 1.825(\sigma_{22} + \sigma_{33}) - H$. The plastic flow tensor, M, and normal to the limit surface, N, can be expressed as

$$M = N = \begin{bmatrix} 1 & 0 & 0 \\ 0 & -1.825 & 0 \\ 0 & 0 & -1.825 \end{bmatrix} \qquad \qquad 5.19$$

Let the hardening function, H, be given in equation 5.3. Let Young's Modulus, E, equal 5000 ksi and Poison's ratio, v, equal .19. The shear modulus, G, becomes 2101 ksi. ψ becomes

$$\psi = \begin{bmatrix} .1973 & 0 & 0 \\ 0 & -.6932 & 0 \\ 0 & 0 & -.6932 \end{bmatrix} \qquad \qquad 5.20$$

with obvious eigen values.

Schreyer and Neilsen [1995] identify three possible solutions for the normal to the localized zone with corresponding values of f when 2 eigen values of ψ are identical.

$$A)\ n_1 = 0, n_2 = 1, n_3 = 0 \quad f = \frac{2G(1-\upsilon)}{\psi_2^{\,2}(1-2\upsilon)}$$

$$B)\ n_1 = 0, n_2^{\,2} + n_3^{\,2} = 1 \quad f = \frac{2G(1-\upsilon)}{\psi_1^{\,2}(1-2\upsilon)} \tag{5.21}$$

$$C)\ n_1 = \sqrt{\frac{(1-\upsilon)\psi_1 - \upsilon\psi_2}{(\psi_2 - \psi_1)}}, n_2^{\,2} + n_3^{\,2} = 1 - n_1^{\,2} \quad f = \frac{2G}{(1-\upsilon)(\psi_1^{\,2} + \psi_2^{\,2}) - 2\upsilon\psi_1\psi_2}$$

Using the numbers stipulated above the value of f is determined for each possible solution, a) $f = 2 \times 10^6$, b) $f = 11006$, and c) $f = 10015$. Since the value of f is a minimum in case c) the normal to the first possible zone of localized deformation is given by the direction in c). Let $n_3 = 0$ and the normal to the localized zone becomes:

$$n_1 = .48087, n_2 = .87679, n_3 = 0 \tag{5.22}$$

Therefore, the angle of the normal to the zone of localization with respect to the X_1 direction, θ_n, is 61.3°. The angle of the zone of localization with respect to the X_1 direction, θ, is 90° - 61.3° = 28.7° (figure 5-4). The value of the hardening modulus, E_P, is found from f to be -16653 at the onset of localization.
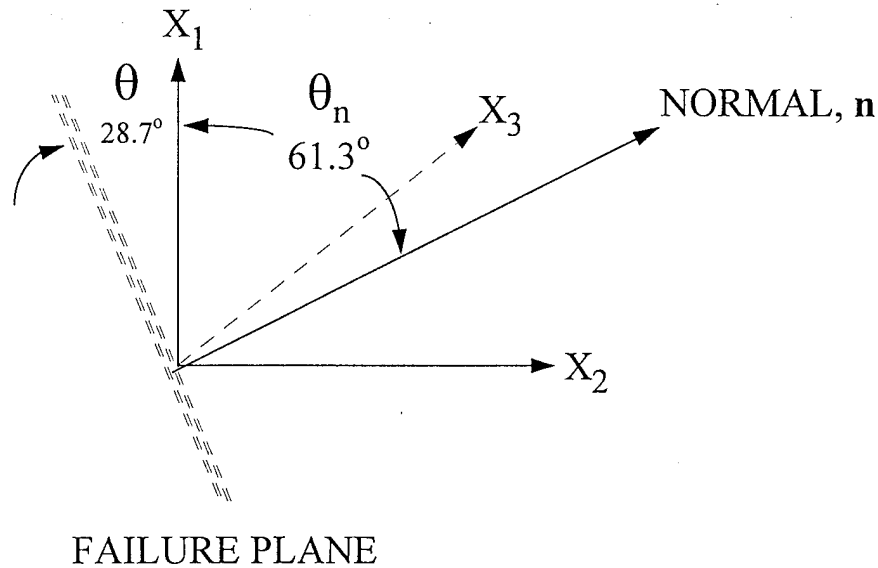
Figure 5-4: Orientation of Failure Plane and Normal

Next the case of **N=M** was analyzed, with **N** and **M** given by

$$N = M = \begin{bmatrix} 1 & 0 & 0 \\ 0 & -\beta & 0 \\ 0 & 0 & -\beta \end{bmatrix} \qquad\qquad 5.23$$

where

$$\beta = 1.1 e^{(-1.2(\frac{\sigma_{22}+\sigma_{33}}{2}))} + .2 e^{(-.02(\frac{\sigma_{22}+\sigma_{33}}{2}))} \qquad\qquad 5.24$$

Therefore, the ratio of the eigen values of M and N vary with confining pressure. There were three possible solutions for the normal to the zone of localization as before and again the value of f was a minimum for case c). Table 5-1 shows the results of this analysis for the various pressures used in this study (note that the angles are the angle of the zone with respect to the X_1 direction). Figure 5-4 shows the angle of the failure plane, or zone of localization (not the normal to the zone), versus the confining pressure for associated flow with $N=M$, non-associated flow, and the angles measured from the triaxial tests. These results will be discussed later in this section. Figure 5-7 shows the value of the hardening modulus at localization versus the confining pressure for associated flow with $N=M$ and non-associated flow.

TABLE 5-1

ORIENTATION OF THE FAILURE PLANE VERSUS CONFINING PRESSURE						
FOR N = M (n_3 =0)						
PRESSURE ksi	β	f	n_1	n_2	ANGLE θ degrees	HARDENING MODULUS, E_P
0	1.3	8888	.5722	.8201	34.9	-8450
.25	1.01	7778	.6341	.7733	39.4	-5101
.5	.8	6713	.6864	.7273	43.3	-3200
1	.53	5352	.7667	.6421	50.1	-1405
2	.29	4965	.8559	.5172	58.9	-420
4	.19	5187	.9	.4359	64.2	-180
6	.18	5221	.9047	.4261	64.8	-162
8	.17	5257	.9095	.4158	65.4	-145

Numerical

The driver program, Appendix F, steps through added strain increments and calculated the stress, elastic strain and plastic strain at each step. The driver program also calculates the value of the hardening modulus

and the determinant of the tangent stiffness tensor, the symmetric portion of the tangent stiffness tensor, and the symmetric portion of the acoustic tensor, $Q^s = .5((n \bullet C \bullet n) + (n \bullet C \bullet n)^T)$

The acoustic tensor was determined using a subroutine which selected a form of the vector n. The vector n started in the principal direction X_2 and was rotated over a 180° arc in 1° increments in the X_1-X_2 plane each time recalculating the determinant of the symmetric portion of the acoustic tensor. The same procedure was performed for the X_2-X_3 and X_1-X_3 planes. The orientation of the zone of localization was determined by examining a plot of the direction of n versus the determinant of the symmetric portion of the acoustic tensor, Q^s.

First the associated flow model with $M = N$ was run. Figure 5-5 shows the determinant of the symmetric portion of the acoustic tensor, Q^s, versus the direction of n for the case of associated flow with $M = N$ (equation 5.19). The angle of n associated with the minimum value of the determinant is approximately 61° which is in good agreement with the analytical result of 61.3°. Furthermore, the value of hardening modulus that produces a zero valued determinant, localized behavior, is approximately -16660 which agrees well with the analytical result of -16653; thus, providing corroborating evidence that the computer model is consistent.

DETERMINANT OF $(Q + Q^T)/2$ VERSUS THE ORIENTATION OF n
The angle is measured from the X_1 direction
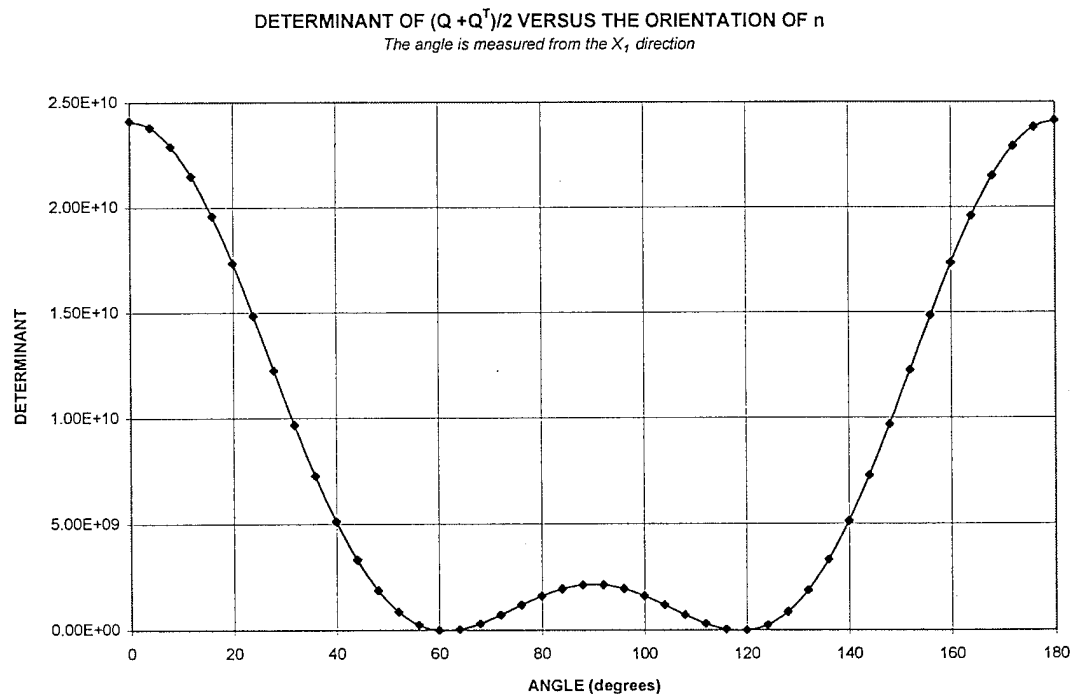
Figure 5-5: Determinant of Q^s versus the Orientation of n

The last step in the analysis was to run the non-associated flow model through the program driver. Recall that the limit function, ϕ, is defined by

$$\phi = \sigma_{11} - 3.65(\frac{\sigma_{22} + \sigma_{33}}{2}) - H \qquad 5.25$$

where H is defined by equation 5.3. The plastic flow tensor, **M**, is defined by

$$M = \begin{bmatrix} 1 & 0 & 0 \\ 0 & -\beta & 0 \\ 0 & 0 & -\beta \end{bmatrix} \qquad 5.26$$

where

$$\beta = 1.1e^{(-1.2(\frac{\sigma_{22}+\sigma_{33}}{2}))} + .2e^{(-.02(\frac{\sigma_{22}+\sigma_{33}}{2}))} \qquad 5.27$$

Table 5-2 summarizes the results of the driver program. The confining pressure is tabulated with the orientation of the normal to the localized zone, the orientation of the localized zone with respect to the X_1 direction, and the value of the hardening modulus at which localization occurred.

TABLE 5-2

ORIENTATION OF THE FAILURE PLANE VERSUS CONFINING PRESSURE FOR NON-ASSOCIATED FLOW			
PRESSURE (ksi)	ANGLE OF NORMAL θ_n **n** (degrees)	ANGLE OF PLANE θ (degrees)	HARDENING MODULUS, E_P
0	58.9	31.1	-12000
.25	56.3	33.7	-9400
.5	54.2	35.8	-7300
1	50.4	39.6	-4300
2	46.0	44.0	-1200
4	44.0	46.0	200
6	43.76	46.24	480
8	43.74	46.26	590

Figure 5-6 shows the angle of the failure plane (zone of localization) versus confining pressure for the analysis of associated flow associated flow with **N** and **M** given by equation 5.23 and for non-associated flow with **N** and **M** given by 5.19 and 5.26 respectively. The test data from the triaxial tests on mortars are plotted for comparison. It is easy to see that this methodology does predict a change in angle with confining pressure. However, the implementation in the ideal plasticity model considered creates a larger angle than

is observed. The angles from the associated flow model fall over a larger range, 35°-65°, than the non-associated flow, 31°-46°, thus, predicting a change in the orientation of the failure plane that is twice as large as that predicted by the non-associated flow model over the same pressure change. In general the curves seem to follow the same type of path as the experimental data but are shifted upwards.

ANGLE OF THE FAILURE PLANE VERSUS CONFINING PRESSURE
The angles are referenced to the direction of maximum compressive stress, X_1
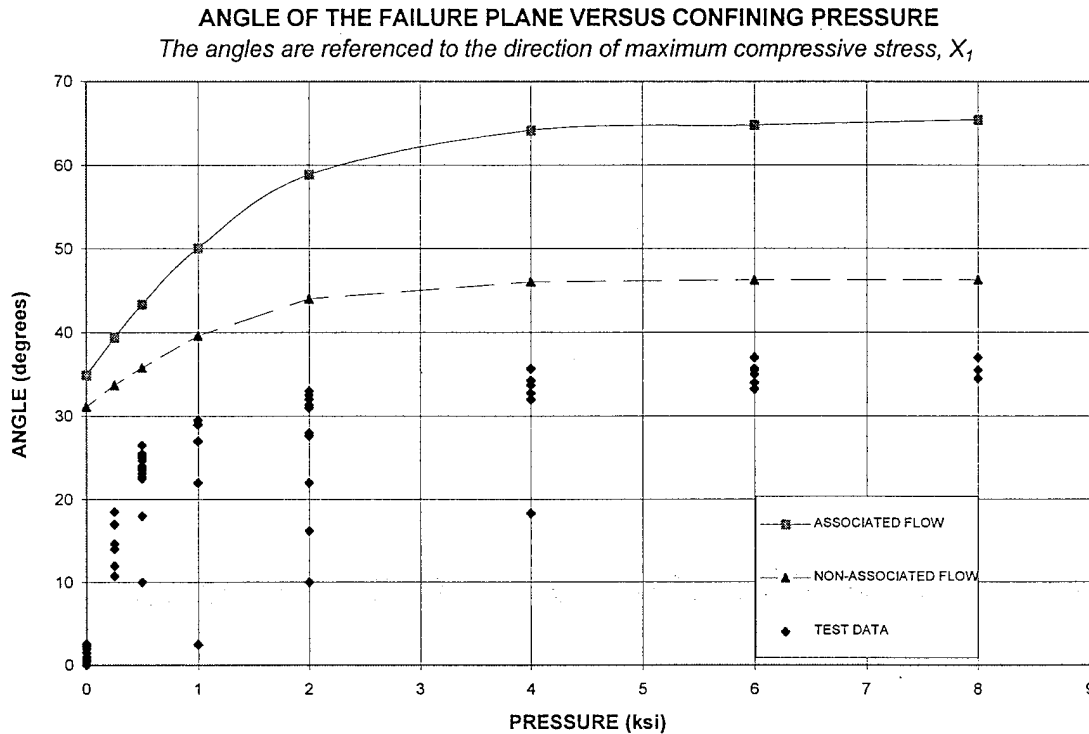
Figure 5-6: Failure Plane Orientation versus Confining Pressure

Figure 5-7 shows the value of the hardening modulus, Ep, required to achieve localization. Figure 5-7 indicates that under uniaxial stress conditions the localization occurs well into the post peak region, which is contrary to the test observations. The localization rapidly approaches the peak as the confining pressure increases to 2 ksi. The hardening modulus for the case of the associated flow model slowly approaches the peak stress at confining pressures above 2 ksi. The hardening modulus for the non-associated flow model moves from post peak to prepeak as the pressure increases to 4 ksi and levels off at 6 ksi. This move to the prepeak region signals the point at which localization can occur prepeak.
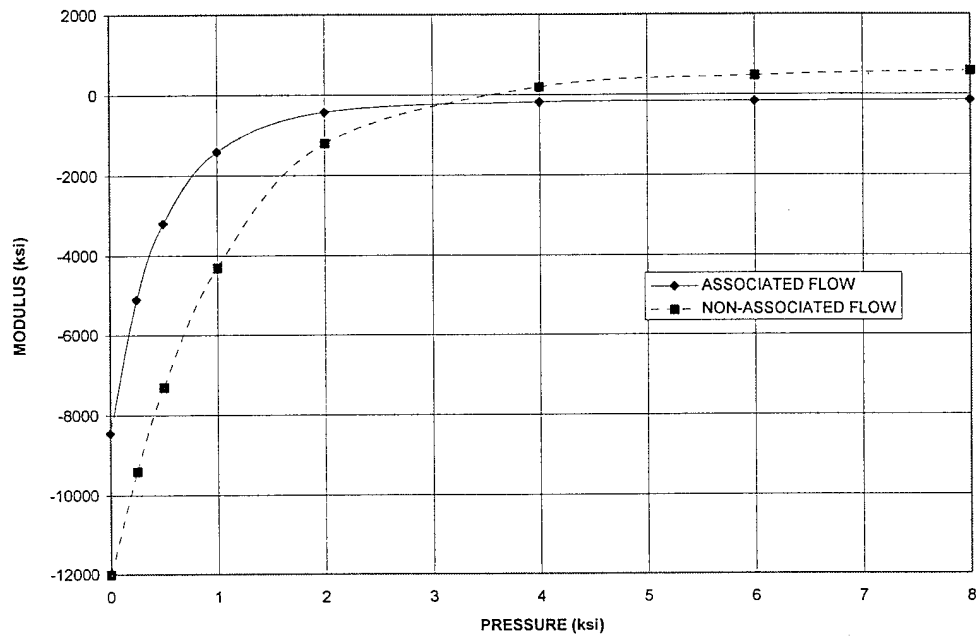
Figure 5-7: Hardening Modulus at Localization versus Confining Pressure

Figure 5-8 presents the same data as figure 5-6; however, the data from the models was shifted by a constant angle down so that the angles predicted at 8 ksi would match the experimental data points. This resulted in a shift of 30° down for the associated flow model and 11° for the non-associated flow model. The shifted graphs show that the non-associated flow model provides a good fit to the data at pressures above .25 ksi but overestimate the angle under low pressure and uniaxial conditions. The shifted graph of the associated flow provides a better fit under uniaxial and .25 ksi pressure conditions; however, it under predicts the angle for intermediate pressures from .5 ksi to 2 ksi. The shifted associated flow graph also provides a good fit at and above 4 ksi confining pressure.

ANGLE OF THE FAILURE PLANE VERSUS CONFINING PRESSURE

The angles are referenced to the direction of maximum compressive stress, X_1

Legend:
- ASSOCIATED SHIFTED
- NON-ASSOCIATED SHIFTED
- TEST DATA

Axis labels: ANGLE (degrees) vs PRESSURE (ksi)
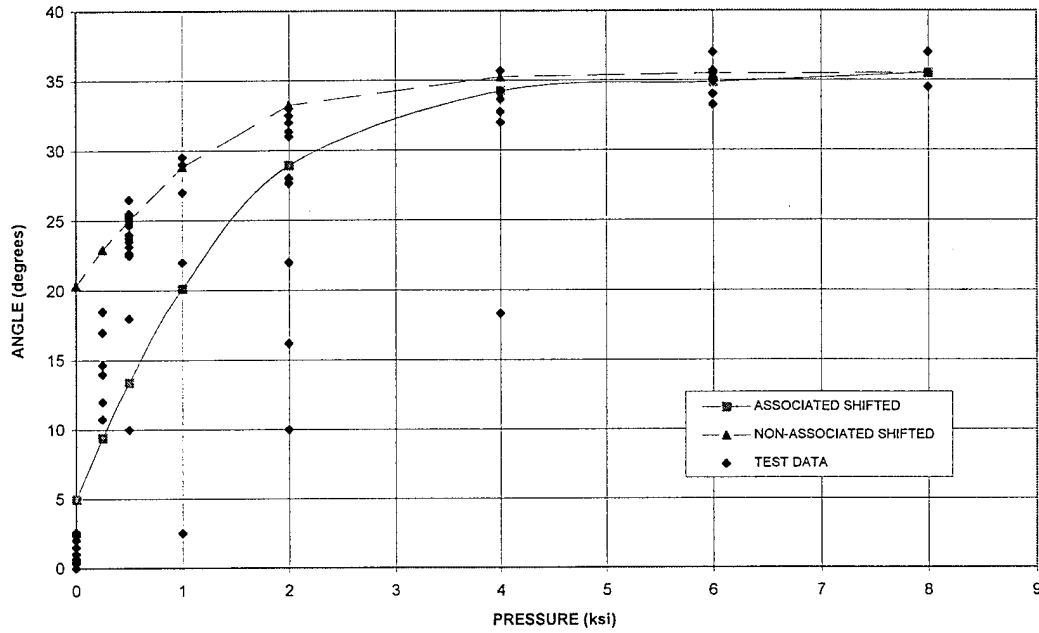
Figure 5-8: Shifted Angles versus Confining Pressure

At this point it is important to investigate possible sources of this shift. Since damage to the elastic parameters was noted during the tests the influence of isotropic damage on the angles was investigated. This was accomplished by using the numerical algorithm but setting the values of the elastic parameters E, the modulus, and ν, the lateral extension ratio, to 4032 ksi and .25 respectively. This represents a constant bulk modulus, K, and a 25% reduction of the shear modulus, G. The resulting change in angle versus confining pressure is shown in figure 5-9. The un-shifted values from the"non-damage" code are shown for comparison. It is easy to see that this "damage", which is isotropic in nature, shifts the values in the right direction but the shift is too small to compensate for the large shift.

5-18

ANGLE OF THE FAILURE PLANE VERSUS CONFINING PRESSURE

The angles are referenced to the direction of maximum compressive stress, X_1
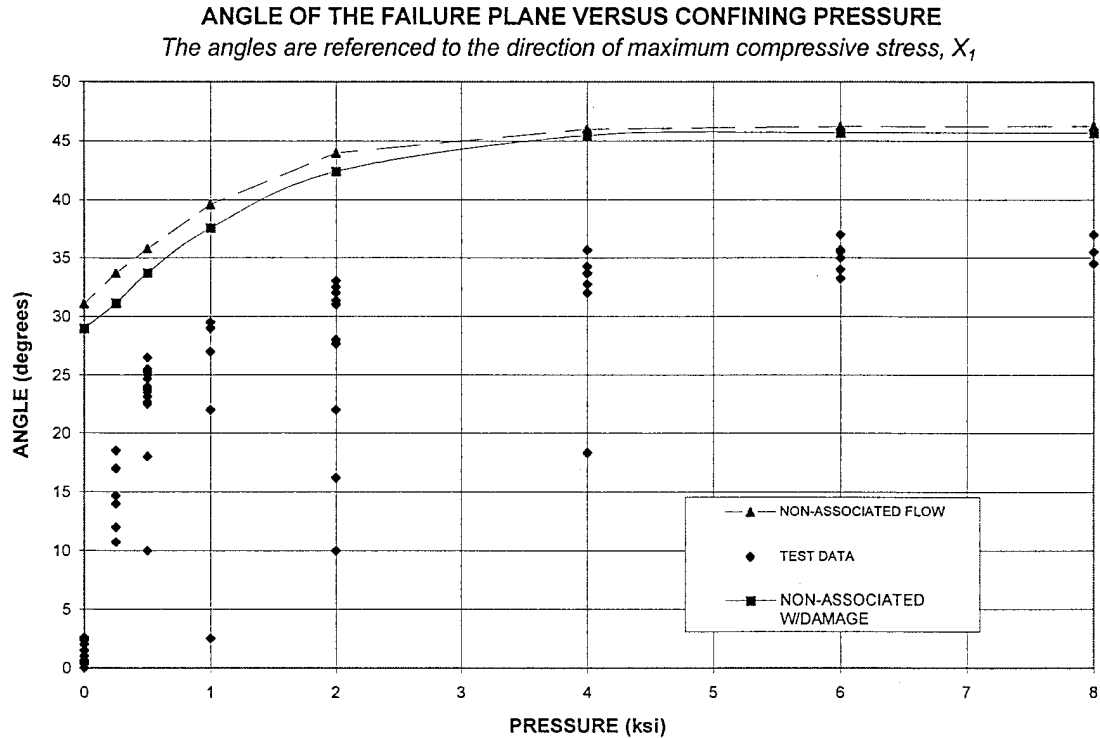
Figure 5-9: Angle of the Failure Plane versus Confining Pressure for Simulated Isotropic Damage

Next the values used in the model were examined. The data used to determine the plastic flow tensor was obtained from the last cycle in the test and not at the point at which localization occurred nor at the peak. The test data indicates that the plastic lateral extension ratio increases as stress increases, figure 4-25. It is possible that the lateral plastic strains increase dramatically at the onset of localization; therefore, the driver program was modified to allow for larger values of β. First the equation for beta was redefined as

$$\beta = 16.5 e^{(-3(\frac{\sigma_{22} + \sigma_{33}}{2}))} + 1.5 e^{(-.08(\frac{\sigma_{22} + \sigma_{33}}{2}))}$$

5.28

Figure 5-10 shows the angle of the failure plane versus the value of beta for the non-associated flow model. As a limiting case β was set to 1000 and 100,000,000 and the driver program run for the case of uniaxial compression resulting in angle of 20°. This indicates that the minimum angle that can be obtained by only allowing for a larger value of β is 20°.

ANGLE OF THE FAILURE PLANE VERSUS BETA
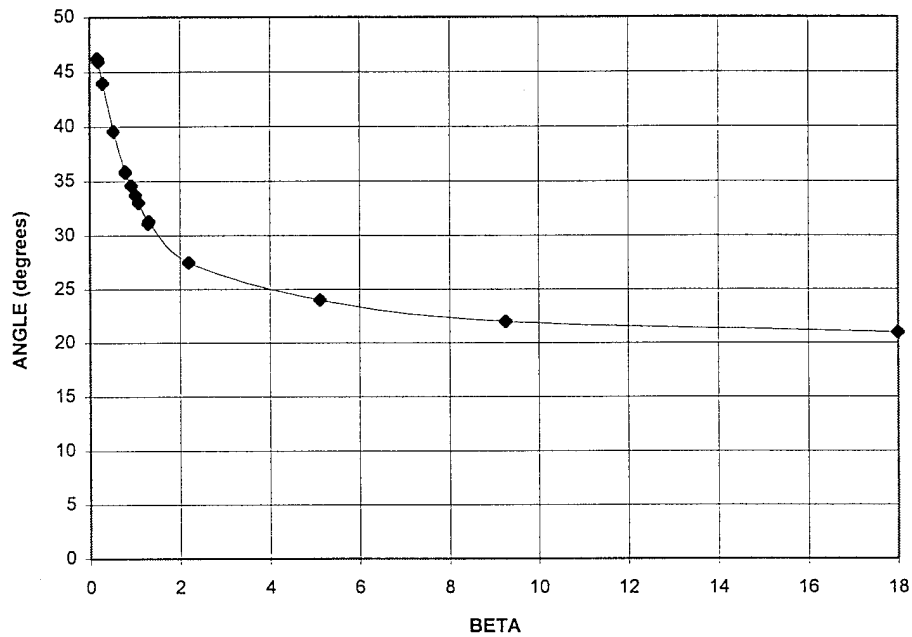
Figure 5-10: Angle of the Failure Plane versus Beta

The limit surface was reexamined. The surface fits well for all values above 500 psi but does not accurately reflect the values at 0 and 250 psi. An exponentially decreasing function was subtracted from the original limit surface to create a new surface that captures the strength at these low pressures (figure 5-11). The revised limit surface is defined by

$$\phi = \sigma_{11} - 3.65(\frac{\sigma_{22} + \sigma_{33}}{2}) + 2.74e^{-6.36(\frac{\sigma_{22} + \sigma_{33}}{2})} - H \qquad\qquad 5.29$$

where the stress are given in ksi.

Figure 5-12 shows the angles obtained by using this revised surface. As expected the angles do not change at the higher pressures; however, there is a dramatic change in the angles predicted at lower pressures. The angle decreases approximately 15° in the uniaxial case. This does not solve the problem of the shift at the higher pressures but does open the door again to the possibility that the value of beta may be larger. It is interesting to note the large change in the angle predicted with such a small change in the limit surface when the large change in the shear modulus created virtually no change.

MAXIMUM AXIAL STRESS vs CONFINING PRESSURE

Legend:
- ◆ CAP BLOCKS
- ■ CAPS W/ GREASE
- ▲ CAPS W/ PGP PADS
- —— Y=3.65X + 8.6
- — — Y=3.65X+8.6-2.74EXP(-6.35X)

Y-axis: STRESS (ksi)
X-axis: CONFINING PRESSURE (ksi)
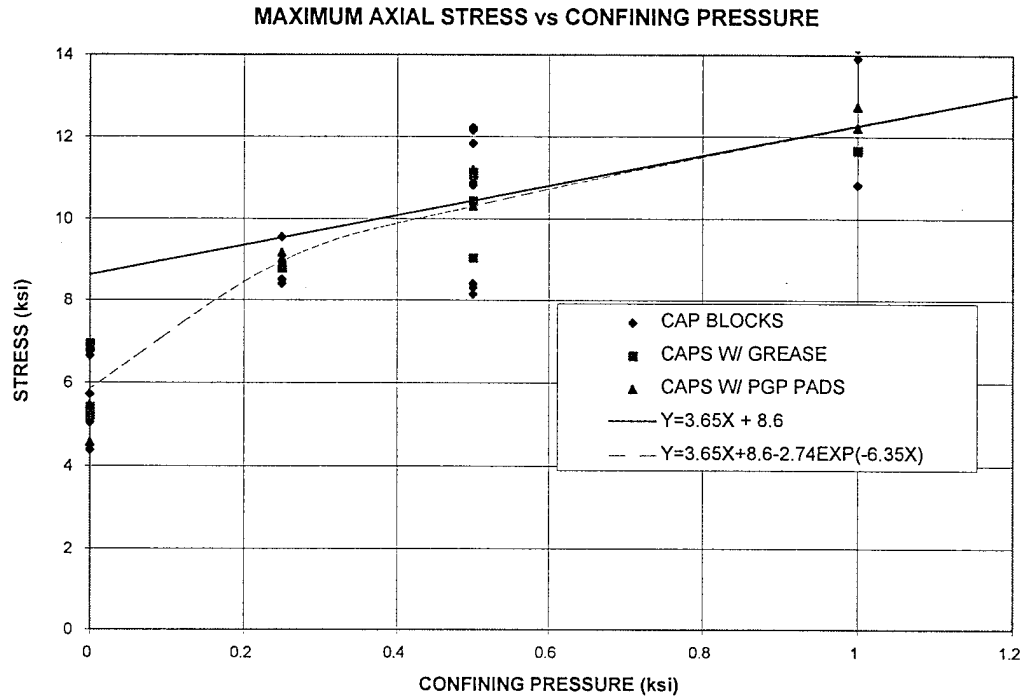
Figure 5-11: Maximum Stress versus Confining Pressure with Revised Limit Surface

ANGLE OF THE FAILURE PLANE VERSUS CONFINING PRESSURE
The angles are referenced to the direction of maximum compressive stress, X_1

Legend:
- —▲— USING OLD LIMIT SURFACE
- ◆ TEST DATA
- —✕— USING NEW LIMIT SURFACE

Y-axis: ANGLE (degrees)
X-axis: PRESSURE (ksi)
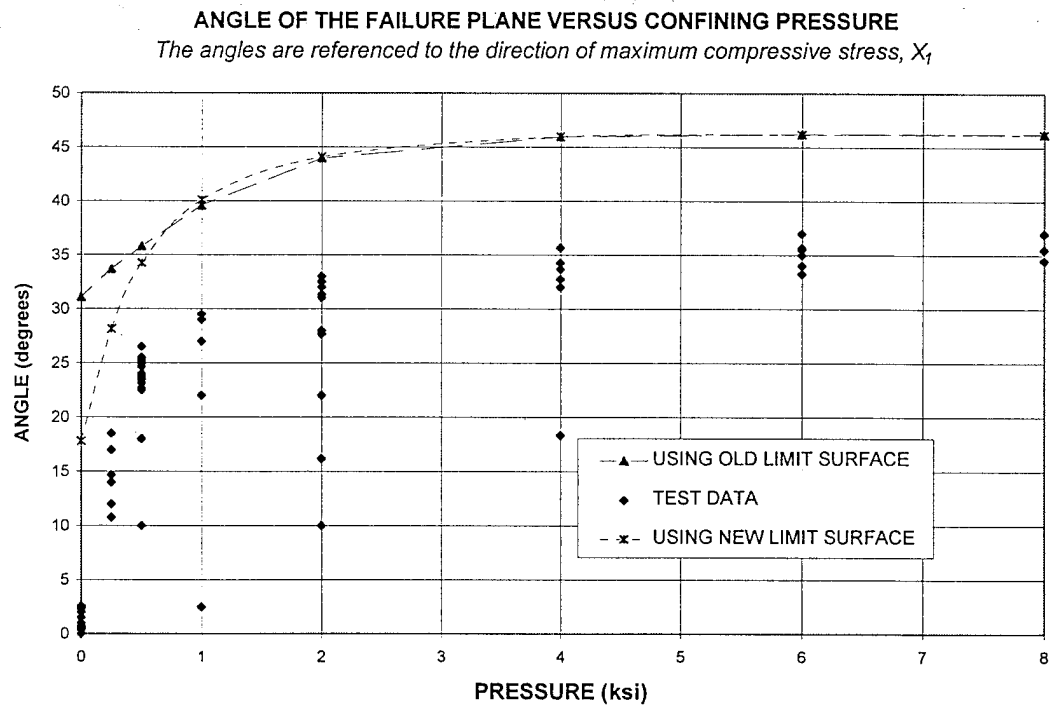
Figure 5-12: Angle versus Confining Pressure Using the Revised Limit Surface

The problem of the shift is now re-engineered to determine what beta must be in order to fit the data and is this new beta reasonable for the material. For each pressure an array of betas are used to develop a graph of angle versus beta for each pressure. The value of beta corresponding to the experimental value of the angle for each pressure is obtained and plotted against the confining pressure (figure 5-13). Thus the beta required to predict the angles determined from the tests is defined by

$$\beta = 3.5e^{-2(\frac{\sigma_{22}+\sigma_{33}}{2})} + 1.2e^{-.04((\frac{\sigma_{22}+\sigma_{33}}{2})}$$ 5.30

Figure 5-14 shows the predicted angle versus confining pressure using the revised limit surface and beta.

From figure 5-13 the required value of beta for a good fit to the data is 3 to 5 times larger that the plastic lateral extension ratios obtained from the tests. Due to the rapid nature of the failure under uniaxial conditions it is difficult to assess weather a 4 fold increase in the plastic lateral extension ratio is reasonable. The values at the higher pressures do seem unreasonable given the to lethargic response of the specimens to the loads up to 8 ksi. However, it possible that the actual strains may have been higher for the specimen as a whole than those recorded by the strain gauges due to the fact that they are local measures   This means that a larger beta may be warranted and account for some of the shift but it probably does not account for all of the shift.

BETA VERSUS CONFINING PRESSURE
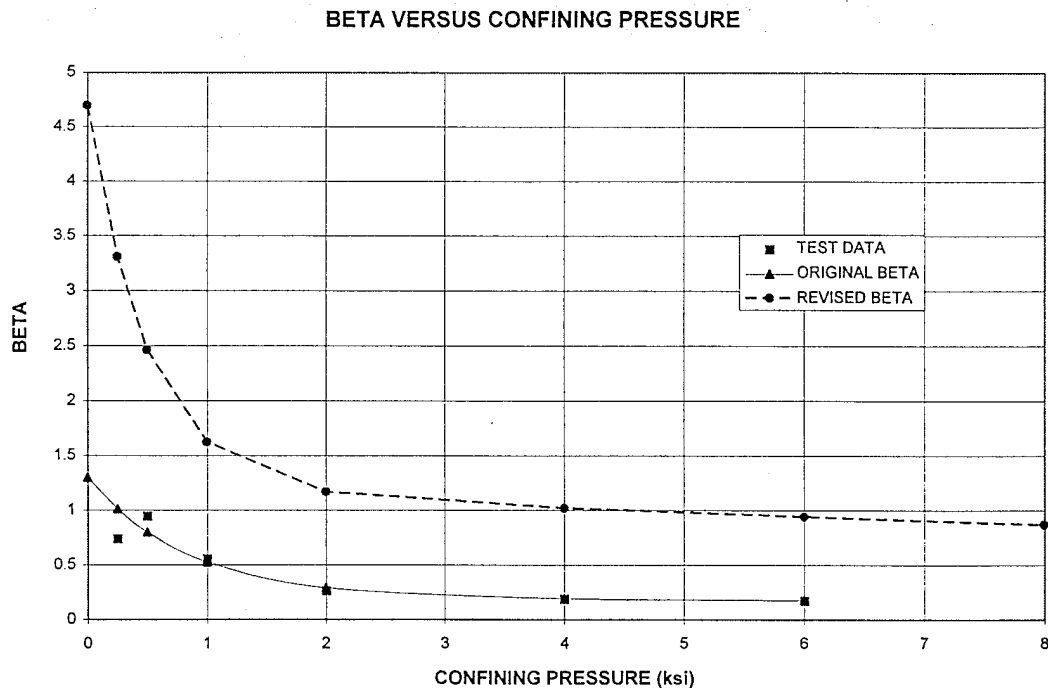
Figure 5-13: Beta versus Confining Pressure Using the Revised Beta

ANGLE OF THE FAILURE PLANE VERSUS CONFINING PRESSURE

The angles are referenced to the direction of maximum compressive stress, X_1
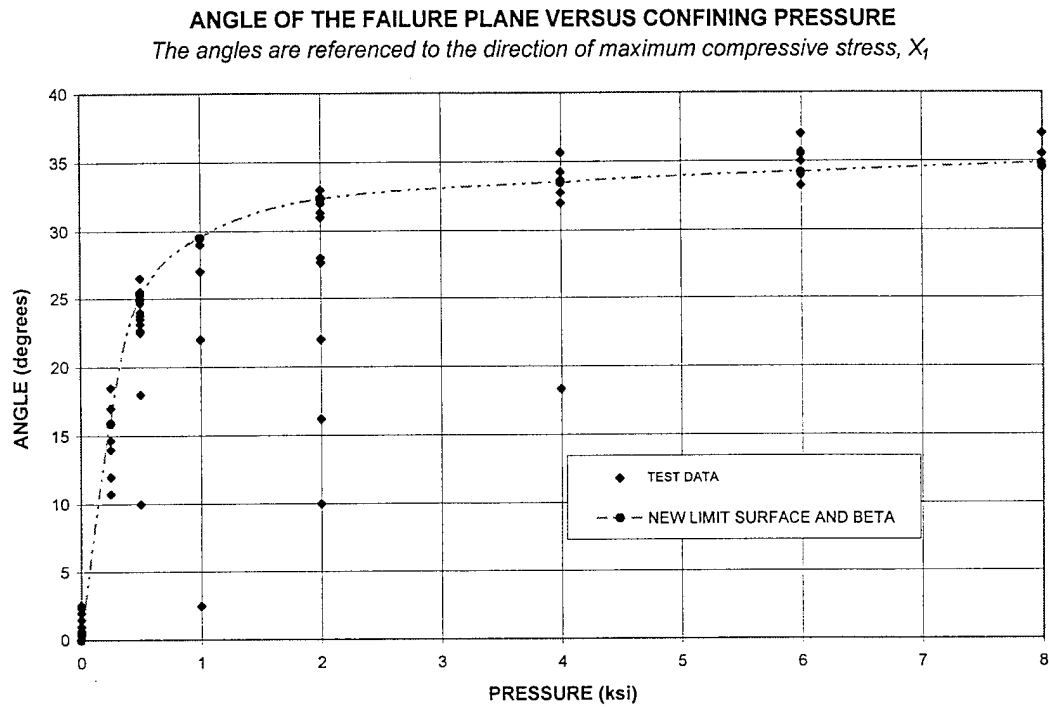
Figure 5-14: Angle versus Confining Pressure Using Revised Limit Surface and Beta

There are two other possible sources of the shift that are not explored in this study. The first is the assumption of the parameters in the hardening function are not constants but change with confining pressure. The second is anisotropic damage. Although the use of isotropic damage had little effect on the predicted angle, the incorporation of anisotropy may cause a larger effect as it changes the components of the tangent stiffness matrix at different rates. Since there is no data on the possibility of anisotropic damage it will not be considered in this modeling section but will be discussed further in the next section as the conditions necessary to obtain a changing failure orientation are discussed.

5.23 ANALYTICAL CONSIDERATIONS

To determine the conditions necessary to predict a change in the failure angle with increasing confinement the determinant of the symmetric portion of the acoustic tensor, Q^s, is analyzed. To simplify the analysis several assumptions are made and will be discussed when they are made.

First, assume the failure plane is parallel to the X_3 direction. This is reasonable in the case of a material loaded as they were in the tests in this study with $\sigma_{22} = \sigma_{33}$ equal to the confining pressure and if the material properties with respect to the X_2 and X_3 directions are the same as they are for the material in this study. This assumption allows the normal to the failure plane, n, to be defined as (see figures 5-3 and 5-4):

$$n = \cos\theta_n X_1 + \sin\theta_n X_2 + 0X_3 \qquad 5.31$$

The failure angle or orientation of the zone of localization is dictated by the n that first produces a zero determinant of Q^s. This n can be found by examining the extrema of the determinant of Q^s, $|Q^s|$, with respect to the angle θ_n. First, the components of Q and Q^s must be determined.

$$Q_{ij} = n_k C_{kijl} n_l \qquad 5.32$$

where C_{ijkl} are the components of the tangent stiffness tensor. Removing terms involving n_3, Q_{11} is defined

$$Q_{11} = n_1 C_{1111} n_1 + n_1 C_{1112} n_2 + n_2 C_{2111} n_1 + n_2 C_{2112} n_2 \qquad 5.33$$

Since C_{1112} and C_{2111} are zero, Q_{11} simplifies to

$$Q_{11} = n_1 C_{1111} n_1 + n_2 C_{2112} n_2 = n_1^2 C_{1111} + n_2^2 C_{2112} \qquad 5.34$$

The other component are determined in a similar manner.

$$\begin{aligned}
Q_{12} &= n_1 n_2 (C_{1122} + C_{2121}) \\
Q_{13} &= 0 \\
Q_{21} &= n_1 n_2 (C_{2211} + C_{1212}) \\
Q_{22} &= n_1^2 C_{1221} + n_2^2 C_{2222} \\
Q_{23} &= 0 \\
Q_{31} &= 0 \\
Q_{32} &= 0 \\
Q_{33} &= n_1^2 C_{1331} + n_2^2 C_{2332}
\end{aligned} \qquad 5.35$$

Using equations 5.34, 5.35 and minor symmetry of the stiffness tensor (no body moments) the symmetric portion of the acoustic tensor, Q^s, is defined by

$$Q^S = \begin{bmatrix} n_1^2 C_{1111} + n_2^2 C_{2112} & \frac{n_1 n_2}{2}(C_{2211} + 2C_{1212} + C_{1122}) & 0 \\ \frac{n_1 n_2}{2}(C_{2211} + 2C_{1212} + C_{1122}) & n_1^2 C_{1221} + n_2^2 C_{2222} & 0 \\ 0 & 0 & n_1^2 C_{1331} + n_2^2 C_{2332} \end{bmatrix} \qquad 5.36$$

The determinant of Q^S is defined by

$$|Q^S| = [(n_1^2 C_{1111} + n_2^2 C_{2112})(n_1^2 C_{1221} + n_2^2 C_{2222})(n_1^2 C_{1331} + n_2^2 C_{2332})]$$

$$- [(n_1^2 C_{1331} + n_2^2 C_{2332})\left(\frac{n_1 n_2}{2}(C_{2211} + 2C_{1212} + C_{1122})\right)^2] \qquad 5.37$$

By multiplying out, using minor symmetry of the tangent stiffness, and assembling like terms the determinant can be rewritten as

$$|Q^S| = n_1^6 (C_{1111} C_{1212} C_{1313})$$

$$+ n_2^6 (C_{1212} C_{2222} C_{2323})$$

$$+ (\frac{n_1^4 n_2^2}{4})(C_{1313}\{4C_{1111} C_{2222} - C_{1122}^2 - C_{2211}^2 - 2C_{1122} C_{2211}$$

$$- 4C_{1122} C_{1212} - 4C_{2211} C_{1212}\} + 4C_{1111} C_{1212} C_{2323}) \qquad 5.38$$

$$+ (\frac{n_1^2 n_2^4}{4})(C_{2323}\{4C_{1111} C_{2222} - C_{1122}^2 - C_{2211}^2 - 2C_{1122} C_{2211}$$

$$- 4C_{1122} C_{1212} - 4C_{2211} C_{1212}\} + 4C_{2222} C_{1212} C_{1313})$$

Let q_1, $q2$, q3, and q_4 represent the coefficients of n_1^6, n_2^6, $(n_1^4 n_2^2)$, and $(n_1^2 n_2^4)$, respectively. Thus, the determinant of the symmetric portion of the acoustic tensor becomes

$$|Q^S| = n_1^6 q_1 + n_2^6 q_2 + n_1^4 n_2^2 q_3 + n_1^2 n_2^4 q_4 \qquad 5.39$$

The components of n (equation 5.31) are substituted into equation 5.39 to obtain

$$|Q^S| = q_1 \cos^6 \theta_n + q_2 \sin^6 \theta_n + q_3 \cos^4 \theta_n \sin^2 \theta_n + q_4 \cos^2 \theta_n \sin^4 \theta_n \qquad 5.40$$

The extrema of this determinant with respect to the orientation of the normal to the failure plane can be found by setting the derivative of the determinant with respect to θ_n to zero and finding the roots.

$$\frac{\partial |Q^S|}{\partial \theta_n} = 0 \qquad 5.41$$

The substitution of equation 5.40 into equation 5.41 leads to

$$6q_1 \cos^5\theta_n(-\sin\theta_n)$$

$$+6q_2 \cos\theta_n(\sin^5\theta_n)$$

$$+4q_3 \cos^3\theta_n(-\sin^3\theta_n) + 2q_3 \cos^5\theta_n(\sin\theta_n)$$

$$+2q_4 \cos\theta_n(-\sin^5\theta_n) + 4q_4 \cos^3\theta_n(\sin^3\theta_n) = 0$$

5.42

Like terms are collected and the expression simplified to obtain

$$-2\cos\theta_n \sin\theta_n \{\cos^4\theta_n(3q_1 - q_3) + 2\cos^2\theta_n \sin^2\theta_n(q_3 - q_4)$$

$$+ \sin^4\theta_n(q_4 - 3q_2)\} = 0$$

5.43

Half angle formulas are applied to the portion in parenthesis, like terms collected, and simplified to obtain

$$-\frac{\cos\theta_n \sin\theta_n}{2}\{A\cos^2 2\theta_n + B\cos 2\theta_n + D\} = 0$$

5.44

where

$$A = 3(q_1 - q_2 - q_3 + q_4)$$
$$B = 2(3q_1 + 3q_2 - q_3 - q_4)$$
$$D = (3q_1 - 3q_2 + q_3 - q_4)$$

5.45

Therefore, the determinant of the acoustic tensor, $|Q^s|$, is a maximum, minimum, or point of inflection when

$$\cos\theta_n = 0$$ 5.46

$$\sin\theta_n = 0$$ 5.47

$$A\cos^2 2\theta_n + B\cos 2\theta_n + D = 0$$ 5.48

The solutions to equations 5.46 and 5.47 are obvious, 0 or 90° (0,90,180,270,360, etc.). The solutions for equation 5.48 depend on the value of A.

$$\theta_n = (\frac{1}{2})\arccos\left(-\frac{B}{2A} \pm \sqrt{\left(\frac{B}{2A}\right)^2 - \left(\frac{D}{A}\right)}\right)$$ $A \neq 0$ 5.49

$$\theta_n = (\frac{1}{2})\arccos\left(\frac{-D}{B}\right)$$ $A = 0$ 5.50

Therefore, the determinant of the symmetric portion of the acoustic tensor, $|Q^s|$, will have maximum or minimums at 0, 90°, and the values of θ_n given in equations 5.49 and 5.50.

Since the tangent stiffness tensor begins positive definite, $|Q^s|$ begins positive and reduces as the tangent stiffness degrades. Therefore, it is the minimum value of the determinant that will first reach zero. The

minimums and maximums can be distinguished by evaluating second derivative of $|Q^s|$ with respect to θ_n at the θ_n equal to the values 0, 90°, and the values of θ_n given in equations 5.49 and 5.50.

$$\frac{\partial^2 |Q^s|}{(\partial \theta_n)^2} = \cos^6 \theta_n (-6q_1 + 2q_3) + \sin^6 \theta_n (-6q_2 + 2q_4)$$

$$+ \cos^4 \theta_n \sin^2 \theta_n (30q_1 - 22q_3 + 12q_4) \qquad \textbf{5.51}$$

$$+ \cos^2 \theta_n \sin^4 \theta_n (30q_2 + 12q_3 - 22q_4)$$

using the values 0, 90°, and the values of θ_n given in equations 5.49 and 5.50, 5.51 is rewritten

$$\left.\frac{\partial^2 |Q^s|}{(\partial \theta_n)^2}\right|_{\theta_n = 0} = (-6q_1 + 2q_3) \qquad \textbf{5.52}$$

$$\left.\frac{\partial^2 |Q^s|}{(\partial \theta_n)^2}\right|_{\theta_n = 90°} = (-6q_2 + 2q_4) \qquad \textbf{5.53}$$

$$\left.\frac{\partial^2 |Q^s|}{(\partial \theta_n)^2}\right|_{\theta_n = from\ 5.49} = \left(\frac{2A - B \pm \sqrt{B^2 - 4AD}}{2A}\right)\left(\frac{2A + B \mp \sqrt{B^2 - 4AD}}{2A}\right)\left(\frac{\pm\sqrt{B^2 - 4AD}}{2}\right) \quad A \neq 0 \quad \textbf{5.54}$$

$$\left.\frac{\partial^2 |Q^s|}{(\partial \theta_n)^2}\right|_{\theta_n = from\ 5.50} = \frac{(B^2 - D^2)}{2B} \quad A = 0 \qquad \textbf{5.55}$$

where A, B, and D are given by equation 5.45. If the result is positive then the point is a minimum, if negative it is a maximum, and if it is 0 then it is a point of inflection.

This processes is completed by taking the value of θ_n for which the determinant of the acoustic tensor is a minimum (either 0, 90°, or the values of θ_n given in equations 5.49 and 5.50) and substituting it into equation 5.38. The result of this substitution is not shown here but will create an equation that can be evaluate at each increment of strain in the constitutive model driver to determine if localization has occurred. Thus, the equation resulting from this substitution and the angles 0, 90° and those given in 5.49 and 5.50 remove the need to perform computationally intensive searches for a minimum angle and to determine if the value has reached zero.

The previous analysis could have been accomplished with the more general case of the failure not oriented in the X_3 direction. This would have introduced one other angle and the rest of the components of the tangent stiffness tensor. In order to determine the orientation derivatives with respect to both angles would have been required.

Recall that it is the necessary condition for a change in angle with increasing confinement that is sought. In order for the angle of the failure plane to change with confining pressure the minimum value of the determinant must occur when the angle is given by 5.49 or 5.50 (i.e. equation 5.54 or 5.55 is positive); furthermore, the ratio of B/A and/or the ratio of D/A must be a function of the confining pressure (for A ≠ 0) or the ratio of D/B must be a function of confining pressure (for A = 0). This is a necessary condition in order to have a change in the angle of the failure plane with increasing confining pressure.

Recall that A, B, and D are algebraic sums of the components of the acoustic tensor which in turn are sums of components of the tangent stiffness tensor multiplied by one another to the power 3. Using equation 5.45 the ratios can be written as

$$\frac{B}{A} = \frac{2(3q_1 + 3q_2 - q_3 - q_4)}{3(q_1 - q_2 - q_3 + q_4)} \qquad 5.56$$

$$\frac{D}{A} = \frac{(3q_1 - 3q_2 + q_3 - q_4)}{3(q_1 - q_2 - q_3 + q_4)} \qquad 5.57$$

$$\frac{D}{B} = \frac{(3q_1 - 3q_2 + q_3 - q_4)}{2(3q_1 + 3q_2 - q_3 - q_4)} \qquad 5.58$$

To examine these ratios let $q_2 = aq_1$, $q_3 = bq_1$, and $q_4 = cq_1$. The ratios become

$$\frac{B}{A} = \frac{2(3 + 3a - b - c)}{3(1 - a - b + c)} \qquad 5.59$$

$$\frac{D}{A} = \frac{(3 - 3a + b - c)}{3(1 - a - b + c)} \qquad 5.60$$

$$\frac{D}{B} = \frac{(3 - 3a + b - c)}{2(3 + 3a - b - c)} \qquad 5.61$$

The ratio (a) is given by

$$a = \frac{C_{2222} C_{1212} C_{2323}}{C_{1111} C_{1212} C_{1313}} \qquad 5.62$$

which can be viewed as a ratio of the stiffness or modulus in the X_2 direction to the stiffness in the X_1 direction. Increases in (a) tend to increase B/A, decrease D/B and tend to accentuate changes in D/A produced by changes in (b) and (c). The uses of anisotropic damage would change this ratio more than isotropic damage; therefore, the use of anisotropic damage may increase or decrease the change in the predicted angle. The ratio (a) would be expected to be higher for low confining pressures if the damage at low pressures is more prevalent in the X_1 direction than the X_2 direction. As confining pressure increases the damage in the two directions would be expected to be similar; therefore, the ratio (a) would tend to decrease as confinement increased. Thus, as confinement increases the angle of the normal would decrease

but the angle of the failure plane would increase with confinement. Furthermore, (a) would stay relatively constant at high pressures compared to low pressures producing a smaller change in the angle at higher pressures compared to lower pressures which is consistent with the test results.

The ratios (b) and (c) which contain several terms such as

$$\frac{C_{1122}}{C_{1111}} \qquad 5.63$$

which can be thought of a measure of the lateral extension ratio. As changes to the lateral extension ratio increase the changes to the ratios (b) and (c) decreases which leads ultimately to a decrease in the predicted angle of the failure plane. Thus, at low pressures where the lateral extension ratio is large the predicted angle is nearly vertical. As the lateral extension decreases (more densification as seen with higher confining pressures) the predicted angle of the failure plane with respect to the direction of maximum stress increases. This again is consistent with the tests results.

It is important to note that the absolute values of the components of the tangent stiffness matrix are unimportant to the determination of the failure angle, although they do affect when localization occurs. It is the relative values of the components that will determine whether there is a change in the angle with increasing confinement. Therefore, it can be said that the relative values of the components of the tangent stiffness tensor must change as confinement changes in order to predict a change in the angle with increasing confining pressure.

For the case of ideal plasticity the tangent stiffness tensor is defined by

$$C_{ijkl} = E_{ijkl} - \left(\frac{1}{E_P + K}\right)\left(N_{fg}E_{gfij}E_{klop}M_{op}\right) \qquad 5.64$$

where

$$E_P = -(\frac{\partial \phi}{\partial H}h + \frac{\partial \phi}{\partial r}:R) \qquad 5.65$$

and

$$K = N:E:M \qquad 5.66$$

Therefore, the values of the components of the tangent stiffness depend upon three possible variables, the tensors N and M and the scalar E_P. Since N and M appear in both the numerator and the denominator, the change in orientation of the failure plane is tied more to the relative values of the eigen values of the matrices N and M as pressure increases than to changes in the absolute values of their components. However, changes in the absolute values of the components of M and N will create changes in the angle when there is a also a change in the relative values of K and E_P. Changes in E_P can also create changes in

the relative values of the components of the tangent stiffness tensor; however, since changes in E_P are reflected in all values of tangent stiffness components in similar manner it is expected that changes in E_P with increasing confinement do not not create large changes in the predicted failure angle.

6.0 SUMMARY AND CONCLUSIONS

6.1 SUMMARY

Triaxial tests were performed on cylindrical and rectangular mortar specimens. These tests resulted in failure orientations which increased relative to the direction of maximum compressive stress as confinement increased. Several methods of friction relief were investigated. It was found that the use of cap blocks with grease (made from steric acid and petroleum jelly) and polyethylene sheets removed virtually all of the friction but created slipping problems during testing. The use of cap blocks and grease seemed to work best. The use of cap blocks alone provided enough confinement to create some cone areas at the ends of some specimens.

Analysis of the strain gauge data indicates that localized deformations occurred within 94% of the peak stress. The data also indicate that plastic deformations are a large part of the behavior of this material. Damage reflected in the degradation of the material properties was noted, specifically the shear modulus reduced by about 25% at the peak stress while the bulk modulus remained constant.

A simple plasticity model was developed from the test data which produced a change in the failure angle similar to that measured during the tests; however, the predicted angles were approximately 10 degrees larger than the measured angles. Analysis of the determinant of the symmetric portion of the acoustic tensor reveals that a necessary condition for the prediction of a change in the orientation of the failure plane with increasing confining pressure is that the ratios of the components of the tangent stiffness tensor change with increasing confining pressure. The analysis also reveals that the change in angle may be accentuated by the use of anisotropic damage which was not measured during the tests. The analysis also reveals that for simple plasticity models the predicted angle may change if the ratios of the eigenvalues of the plastic deformation tensor and/or the normal to the limit surface change with confining pressure as they do in the simple model developed from the test data.

Biaxial tests were conducted on two dimensional specimens. These specimens used ceramic rods to preclude failures in the plane of loading. This methodology worked at pressures up to 500 psi. The matrix material was too strong to allow this methodology to work at higher pressures. The investigation of the failure angle of these specimens was hampered by the use of platens to apply the lateral load which constrained possible modes of failure and by the lack of a sufficient number of samples.

6.2 CONCLUSIONS

While these conclusions are definitive for the material studied here, it is surmised that these conclusions apply universally to all cementitious materials; however, further study is required to confirm this.

1) The angle of the failure plane relative to the direction of maximum compressive stress increases with increasing confining pressure.

2) The orientation of the failure is principally a material property largely independent of shape but may be influenced by boundary constraints.

3) The angle of the failure plane relative to the direction of maximum compressive stress decreases with increasing strain rate.

4) Use of platens to apply lateral pressure constrain possible failure modes.

5) Constraint due to end friction will influence the resulting failure.

6) Use of cap blocks alone is insufficient to relieve end friction and may cause cones to form near the ends.

7) A necessary condition for the prediction of a change in angle of the failure plane with increasing confinement is that the ratio of the components of the tangent stiffness tensor change with increasing confinement. The amount of change in the orientation of the failure plane is dictated by the amount of change in the relative values of the components of the tangent stiffness tensor. In addition it is required that the result of equation 5.54 or equation 5.55 be positive.

8) By formulating the deformation tensor and the normal to the limit surface such that the ratio of the eigen values of each of these tensors changes with confining pressure a simple plasticity model can be constructed that captures the main features of the observed change in orientation with increasing confinement.

9) Localized deformations occur within 94% of the peak stress.

10) Ceramic rods can be used as aggregate to produce "two dimensional" specimens. However, their utility in the examination of material behavior may be limited by the loading device used to apply the loads.

APPENDIX A
STRAIN MEASUREMENTS FROM CHANGES IN
X-RAY INTENSITIES

ABSTRACT

Recent tests by Wang et al [1990] have shown that X-ray equipment is now sufficiently sensitive so that changes in densities due to changes in loads on specimens can be detected when X-ray images of the specimen are enhanced and compared. Prism specimens of aluminum and cement mortar were tested in uniaxial compression and simultaneously X-rayed. The gray levels from X-ray images taken during loading are compared. Results show that the strains in the specimen can be determined from the changes in the gray levels.

INTRODUCTION

X-ray radiography has been widely used to determine density distributions and displacement fields within various materials and, in particular, soils (Roscoe et al [1963], Arthur [1977], and Wong and Arthur [1985]). Using X-ray radiographs of sand specimens, Vardoulakis and Graf [1985] has shown that dilatation occurred in a thin shear zone at failure and that the density of this zone was qualitatively different from the soil outside of this shear zone. Similar qualitative changes in the density of cementitious specimens has been shown by Wang et al [1990].

The purpose of this study is to investigate the possibility of using these X-ray images to quantitatively examine these density changes and to use this as an alternative method of determining strains within a specimen. The theoretical relationship between strain and image intensity is first derived for general loading situations. Then simplifying assumptions are made to make the relationship tractable. Experimental data are given to show the feasibility of the procedure for measuring strains.

Currently, there are primarily two methods by which quantitative measures are made using X-ray images in a broad beam geometry. The first method, Digital Tracking (Wang et al [1990]), determines the displacement in a plane parallel to the image plane. The position of discrete points in the sample are tracked from image to image throughout the loading process. Once the displacements have been calculated the strains can be determined. In many cases, to track material points it is necessary to place inclusions, such as a wire mesh or lead balls, in the material. A plot of the displacements of these points provides a representation of the displacement field within the sample at the location of the points.

The accuracy of this technique relies on the abilities of the operator and on the dimensions represented by one pixel of the digitized image. The technique is very time consuming and labor intensive. When inclusions such as a mesh or lead balls are used the behavior of the specimen may be changed. However, one of the advantages of this technique is that it provides the displacements (two dimensionally) of a point within the specimen as opposed to providing an average through the specimen.

In the second technique, Cross Correlation (Wang and Ross [1991]), a two dimensional cross correlation is performed on a subregion of two X-ray images at different loadings. Displacements are calculated by finding the point of maximum correlation. The strains are then determined from the displacements. This technique may be used in conjunction with digital tracking to provide an automated way of determining the displacements of mesh points.

The second technique, although automated, may take several days (on a PC/386) to analyze two images because of the large number of computations required. In many cases, it may require substantial preprocessing of the image. It also requires a high amount of contrast within the portion of the image being analyzed. When not used in conjunction with the tracking of discrete points the results obtained represent an average through the specimen. One advantage of this technique is that it is capable of discerning subpixel displacements.

In this study the change in gray level of a region is calculated from images taken during the loading. These changes are used to directly calculate the strains. Two of the drawbacks to this technique are that it provides an average measure of strain through the specimen and that it requires some knowledge of the lateral extension (Poisson) effect. Two of the advantages of using changes in gray levels are that it requires orders of magnitude fewer computations than the cross correlation technique and it provides a direct measure of strain, not displacement.

THEORETICAL ANALYSIS

At various times during the test, images are digitized (captured) and stored on a computer for later analysis. When an image is captured it is broken into discrete elements called pixels. The shade of gray (gray level) of each pixel is a measure of the average of the light intensity that made up the originally viewed analog image. In the case of X-ray fluoroscopy the gray levels are a measure of the intensity of the X-rays striking the X-ray detector. Each pixel is representative of an area that is parallel to the X-ray detector and perpendicular to the path of the X-rays. The actual dimension of the area represented depends on the magnification of the image and the capabilities of the image capturing system.

In general, the intensity of X-rays passing through a material can be calculated using the following formula (McMaster [1959]):

$$I = I_0 \, \beta(\mu x) \, e^{-(\frac{\mu}{\rho})\rho x} \tag{1}$$

where I_0 is the intensity of the X-rays entering the material and I is the transmitted intensity of the X-rays. The linear attenuation factor is denoted by μ and ρ is the mass density. The mass attenuation factor is μ/ρ which is only a function of the material composition and the energy of the photons of the X-ray. The path length that the X-rays must travel through the material is denoted by x. $\beta((\mu/\rho)\rho x)$ is the build-up factor or forward scatter and is a function of the mass attenuation factor, mass density, path length, and beam geometry. For narrow beam tests $\beta((\mu/\rho)\rho x) = 1$.

For wide beam tests the calculation of the build-up factor based on theoretical considerations is very complex (Goldstein and Wilkins [1954]). However, empirical forms prove to be adequate for most situations. The empirical forms used vary from simple linear assumptions to complex power laws. Figure A-1 shows the build-up factor versus thickness for iron at various X-ray energies (Halmshaw [1966]). Due to the asymptotic behavior of the build-up factor, Taylor [1954] proposed the following form:

$$\beta(\mu x) = \omega \, e^{-\alpha_1 \mu x} + (1 - \omega) \, e^{-\alpha_2 \mu x}$$

where ω, α_1, α_2, and μ are constant for a given X-ray energy and can be determined experimentally. In many situations a cubic polynomial is sufficient.

$$\beta(\mu x) = 1 + A(\mu x) + B(\mu x)^2 + C(\mu x)^3$$

where A, B, C, and μ are constant for a given X-ray energy.

As a specimen is loaded, both the density and the X-ray path length change. Therefore, the intensity of the X-rays exiting the specimen will change. These changes in path length and density are functions of the applied strain (ε) and the lateral extension (Poisson) ratio (υ)[1]. It should be noted that if a specimen is loaded in pure shear, there is no change in density. However, there may be a change in the X-ray path length depending on the orientation of the X-rays.

---

[1] Poisson's ratio reflects the ratio of lateral contraction to longitudinal extension for uniaxial stress. Since the ratio is normally defined in the linear elastic regime, it is a material constant analogous to Young's modulus. Therefore, in the subsequent text, the lateral extension ratio is used to denote the fact that, due to inelastic behavior and microcracking, the ratio is not constant.

Suppose a specimen with nominal height, width, and depth of H, W, and D, respectively, is subjected to a multiaxial strain. The specimen is oriented with one face perpendicular to the X-rays which pass through a material path of length D. Let ρ_1 and D_1 represent the density and X-ray path length prior to loading. The density after loading can be expressed in terms of the density prior to loading using the continuity relation:

$$\rho_2 = \frac{\rho_1}{(1 + \varepsilon_{vol})} \tag{2}$$

where $\varepsilon_{vol} = \varepsilon_h + \varepsilon_w + \varepsilon_d$ for small strains. The normal components of strain in the directions denoted by H, W, and D are ε_h, ε_w, and ε_d, respectively. These components are considered positive in tension. Similarly, the X-ray path length after loading can be expressed as:

$$D_2 = D_1 (1 + \varepsilon_d) \tag{3}$$

The intensity of the X-rays prior to loading is given by:

$$I_1 = I_0 \, \beta_1 \, e^{-(\frac{\mu}{\rho})\rho_1 D_1} \tag{4}$$

where $\beta_1 = \beta((\mu/\rho)\rho_1 D_1)$. Similarly, the intensity after loading is:

$$I_2 = I_0 \, \beta_2 \, e^{-(\frac{\mu}{\rho})\rho_2 D_2} \tag{5}$$

where $\beta_2 = \beta((\mu/\rho)\rho_2 D_2)$. The substitution of equations (2) and (3) into (5) yields:

$$I_2 = I_0 \, \beta_2 \, e^{-(\frac{\mu}{\rho})\rho_1 D_1 \xi} \tag{6a}$$

where

$$\xi = \frac{(1 + \varepsilon_d)}{(1 + \varepsilon_{vol})} = \frac{1}{(1 + \varepsilon_h)(1 + \varepsilon_w)} \tag{6b}$$

The subtraction of (6a) from (4) provides the change in intensity for a given strain:

$$I_1 - I_2 = \beta_1 \, I_0 \, e^{-(\frac{\mu}{\rho})\rho_1 D_1} \, [1 - (\frac{\beta_2}{\beta_1}) \, e^{(\frac{\mu}{\rho})\rho_1 D_1 (1 - \xi)}] \tag{7}$$

Therefore, the change in intensity (ΔI) during the loading will be:

$$\Delta I = I_1 \left[1 - \psi \, e^{(\frac{\mu}{\rho})\rho_1 D_1(1 - \xi)} \right]$$ (8)

in which

$$\psi = \frac{1 + A\left((\frac{\mu}{\rho})\rho_1 D_1 \xi\right) + B\left((\frac{\mu}{\rho})\rho_1 D_1 \xi\right)^2 + C\left((\frac{\mu}{\rho})\rho_1 D_1 \xi\right)^3}{1 + A\left((\frac{\mu}{\rho})\rho_1 D_1\right) + B\left((\frac{\mu}{\rho})\rho_1 D_1\right)^2 + C\left((\frac{\mu}{\rho})\rho_1 D_1\right)^3}$$

During the test only one measure of ΔI is obtained for a load increment, but, equation (6) has two unknowns (ε_{vol} and ε_d or ε_h and ε_w). Therefore, additional measures of the strains must be obtained or the number of unknowns must be reduced to make this procedure tractable. Next, two useful stress paths will be considered, uniaxial stress and plane stress.

Uniaxial Stress:

Suppose the specimen is subjected to uniaxial stress in the direction associated with H. X-rays pass through the depth (D). When the specimen is compressed by an amount δ_h in the vertical direction, it expands by δ_w and δ_d in the other directions. Suppose the material is orthotropic. If the lateral extension ratios for the H-W and H-D planes are υ_w and υ_d, respectively, then the lateral strains are

$$\varepsilon_w = -v_w \varepsilon_h$$

$$\varepsilon_d = -v_d \varepsilon_h$$

The density after loading can be expressed in terms of the density prior to loading by the following relation:

$$\rho_2 = \frac{\rho_1}{(1 + \varepsilon_h)(1 - v_w \varepsilon_h)(1 - v_d \varepsilon_h)}$$ (9)

Similarly, the X-ray path length after loading can be expressed in terms of the density prior to loading:

$$D_2 = D_1 (1 - v_d \varepsilon_h)$$ (10)

The substitution of equations (9) and (10) into (5) yields:

$$I_2 = I_0 \, \beta_2 \, e^{-(\frac{\mu}{\rho})\frac{\rho_1 D_1}{(1 + \varepsilon_h)(1 - v_w \varepsilon_h)}}$$ (11)

The difference between terms in (11) and (4) provides the change in intensity for a given axial strain (ε_h):

$$I_1 - I_2 = \beta_1 \, I_0 \, e^{-(\frac{\mu}{\rho})\rho_1 D_1} \, [1 - (\frac{\beta_2}{\beta_1}) \, e^{(\frac{\mu}{\rho})\rho_1 D_1 (1 - \lambda)}]$$

(12a)

where

$$\lambda = \frac{1}{(1 + \varepsilon_h)(1 - \nu_w \varepsilon_h)})$$

(12b)

Therefore, the change in intensity (ΔI) during the loading will be:

$$\Delta I = I_1 \, [1 - \psi \, e^{(\frac{\mu}{\rho})\rho_1 D_1 (1 - \lambda)}]$$

(13)

in which

$$\psi = \frac{1 + A\,((\frac{\mu}{\rho})\rho_1 D_1 \lambda) + B\,((\frac{\mu}{\rho})\rho_1 D_1 \lambda)^2 + C\,((\frac{\mu}{\rho})\rho_1 D_1 \lambda)^3}{1 + A\,((\frac{\mu}{\rho})\rho_1 D_1) + B\,((\frac{\mu}{\rho})\rho_1 D_1)^2 + C\,((\frac{\mu}{\rho})\rho_1 D_1)^3}$$

and one equation with two unknowns (ε_h and ν_w) is obtained. In many situations the lateral extension ratio, ν_w, is known or can be bounded. In other cases the strain may be known or bounded and it is the lateral extension ratio we seek to find. The ratio of build-up factors is approximately one when the deformations in the D direction and when the density changes are very small. The accuracy of this approximation decreases as the photon energy of the X-rays decreases and the initial thickness of the specimen increases (Figure A-1). Equation (13) is inverted to obtain:

$$\varepsilon_h = \frac{(\nu_w - 1) + \sqrt{(1 - \nu_w)^2 + 4\nu_w \gamma}}{2\nu_w}$$

where

$$\gamma = \frac{\ln(1 - \frac{\Delta I}{I_1})}{(\frac{\mu}{\rho})\rho_1 D_1 - \ln(1 - \frac{\Delta I}{I_1})}$$

In other words, with the lateral extension ratio assumed to be known, the strain component, ε_h, can be determined directly from the change in gray level when the ratio of build-up factors is assumed to be one.

Plane Stress:

Suppose the strain components $(\varepsilon_h, \varepsilon_w)$ occur in the vertical (height) and lateral (width) directions, respectively, as a result of loading in the H-W plane. The specimen is X-rayed perpendicular to the applied loads. Suppose the material behaves orthotropically, specifically, the lateral extension ratio in the unloaded direction, υ_d, is different from the lateral extension ratios in the other two directions, which are assumed to be equal, $\upsilon_{hw} = \upsilon_h = \upsilon_w$. Then ε_d can be written as:

$$\varepsilon_d = [\frac{-\nu_d}{1 - \nu_{h\text{-}w}}](\varepsilon_h + \varepsilon_w) \tag{14}$$

As before, the density and the X-ray path after loading are expressed in terms of the values prior to loading:

$$\rho_2 = \frac{\rho_1}{(1 + \varepsilon_h)(1 + \varepsilon_w)(1 + \varepsilon_d)}$$

$$D_2 = D_1(1 + \varepsilon_d) \tag{15}$$

$$\rho_2 D_2 = \frac{\rho_1 D_1}{(1 + \varepsilon_h)(1 + \varepsilon_w)} \tag{16}$$

In the case of small strains the denominator can be rewritten:

$$(1 + \varepsilon_h)(1 + \varepsilon_w) \approx 1 + \varepsilon_h + \varepsilon_w \tag{17}$$

ε_d is added and subtracted from equation (17) to obtain:

$$(1 + \varepsilon_h)(1 + \varepsilon_w) \approx 1 + \varepsilon_{vol} - \varepsilon_d$$

When this equation is combined with equation (14), it follows that:

$$(1 + \varepsilon_h)(1 + \varepsilon_w) \approx 1 + \varepsilon_{vol}(\frac{1 - \nu_{h\text{-}w}}{1 - \nu_{h\text{-}w} - \nu_d}) \tag{18}$$

With a procedure similar to that used for the uniaxial case it can be shown that:

$$\Delta I = I_1 \left[1 - \psi\, e^{(\frac{\mu}{\rho})\rho_1 D_1 (1 - \frac{1}{1 + \varepsilon_{vol}\tau})} \right] \tag{19}$$

in which

$$\psi = \frac{\beta\!\left((\frac{\mu}{\rho}) \dfrac{\rho_1 D_1}{1 + \varepsilon_{vol}\tau}\right)}{\beta\!\left((\frac{\mu}{\rho})\rho_1 D_1\right)}$$

$$\tau = \frac{1 - v_{h\text{-}w}}{1 - v_{h\text{-}w} - v_d}$$

The change in intensity is expressed in terms of the volumetric strain and the lateral extension ratios. Therefore, the volumetric strain can be obtained if the lateral extension ratios are known.

Attenuation and Build-up Factors:

It should be noted that when small deformations occur the buildup factor in the strained state is essentially the same as that in the unstrained state. Therefore, the ratio of the build-up factors used in equations (8), (13), and (19) can be set to 1. This makes the calculation of the strains from the measured change in gray levels much easier.

If the attenuation factor for the materials tested are to be determined experimentally using a broad beam geometry then it is essential that the build-up factor be considered. By utilizing equation (1), the attenuation factor, μ, can be determined by testing specimens of various thicknesses of the same material. The actual procedures used will be discussed later in more detail.

<div align="center">

EXPERIMENTAL TECHNIQUE

</div>

Equipment:

All specimens were loaded in uniaxial compression using an Instron 1323 Biaxial Loading System. Continuous X-rays of the specimens were taken with an IRT IXRS 160/3200 Industrial X-ray System. The fluoroscopy was accomplished using a six inch image intensified area X-ray detector and a CCD camera. Images from the tests were digitized using an IMAGING Technologies, Inc. FG100-1024 Video capturing board in an IBM AT computer.

The X-ray source was placed approximately 5 feet from the specimen and 7 feet from the image intensifier. This was done to produce an essentially planar X-ray beam striking the specimen and to reduce the spherical attenuation through the specimen to a negligible level.

Specimens:

Seven prismatic specimens were tested. Three aluminum specimens (approximately 3" X 2" X 1.5" blocks) were tested as were four specimens made from Densified Systems containing ultrafine Particles, "DSP", cement mortar (1.5" X 1.5" X 3"). Strain gauges were attached to opposite sides of the specimens. Two gauges were placed on each side, one for axial strain, the other for lateral strain. Each set of gauges was placed at the mid height of the specimen. These gauges were used to determine the lateral extension ratio and to provide a measure of the axial strain to compare with the results obtained from the changes in gray levels.

The DSP mortar was prepared using 500 grams of cement (Type I&II), 120 grams of silica fume, 1000 grams of sand (#16-#100 sieve), 155 grams of water, and 15 ml of superplasticizer.

Test Procedure:

The aluminum specimens were tested in uniaxial compression up to 100 kips. The loading system was load controlled at a rate of .1 kips per second. Load-displacement, strain, and X-ray data were collected. No steps were taken to relieve the lateral confinement produced by the friction between the platens and the specimen.

Each DSP sample was tested in uniaxial compression. The loading system was displacement controlled at a rate of .0025 inches per minute. The samples were loaded to failure. Load-displacement, strain, and X-ray data were collected.

No steps were taken to relieve the lateral confinement produced by the friction between the platens and the specimen for the first two tests on the DSP. The resulting failure zones were angled and passed through the corners of the specimens. On the third test 1.5 inch cubes of DSP were placed between the platens and the specimen. The confinement was relieved in the fourth test by placing a .01 inch thick sheet of rubber between the platens and the specimen. The failure zones resulting from these last two tests were characterized as vertical splitting.

In all tests a piece of aluminum (not loaded) was placed near the specimen so that it could be seen in the X-ray images. This aluminum acted as a control, which allowed the images to be corrected for slight temporal

variations in the X-ray intensity. It should be noted that for the materials and energy levels used the expected change in gray levels are approximately .1% to .5% of the intensity of the original image, I_1. Therefore, it is critical that any changes in the intensity of the source X-ray beam be accounted for.

The specimens were continuously X-rayed with a photon energy of 100 Kev. Approximately 24 images were captured during each test. Each captured image is the average of 32 consecutive frames taken at a rate of 30 frames per second. This averaging also helps reduce spatial and temporal fluctuations.

Attenuation and Build-up Factors:

Attenuation factors were obtained experimentally for the aluminum. Nine plates of aluminum of various thicknesses were X-rayed at a photon energy of 100 Kev. The samples were placed next to a one inch thick plate in the X-ray. One image was captured for each plate thickness. The use of a control plate removes the dependence of the equation on I_0. The attenuation and build-up factors were not experimentally determined for the DSP samples because suitable samples have not been manufactured.

DATA REDUCTION AND ANALYSIS

During the tests the apparent intensity of the X-rays was highest in the center of the image and decreased towards the edges in a smooth manner. A similar effect was noted by Temper, Gruner, and Eikenberry [1988]. Most of this non-uniformity is caused by the image intensifier, which is optimized for low distortion of the image at the expense of uniformity. The spatial non-uniformity was stable and not accounted for in the reduction of the image data. This spatial non-uniformity has no effect on the analysis when the displacements are small and when there are no large inclusions with intensities that are significantly different than the rest of the sample.

The average gray level of the unloaded image (I_1) was calculated. Then the difference in gray levels between to the loaded and unloaded images was calculated ($I_1 - I_2$). These differences in gray levels were averaged over a large portion of the specimen (image). The average differences were normalized by dividing by the average intensity of the original image, I_1. These normalized average differences in gray levels were then plotted against the corresponding strain (measured from the axial strain gauges).

Data from the strain gauges were used to determine the value of the lateral extension ratio and how it varies with axial strain, in the case of the DSP mortar. The lateral extension ratios obtained from these gauges were substituted in equation (13) to obtain the theoretical relationship between change in gray level and axial strain.

The theoretical relation between axial strain and normalized change in gray level was plotted and compared to experimental results.

The differences in gray levels were averaged over a region for three reasons.

First, in order to determine the change in intensity (gray level) at a particular point (line through the depth D) the point must be followed in the image during the loading. Since each pixel represents the average intensity over a finite region, interpolation would be required to find the intensity at a particular point within the pixel. Furthermore, the position of the point in succeeding images must be known. This can be accomplished by placing lead pins in the specimen as reference points; which works well for materials with homogeneous deformations. Such considerations are computationally expensive to account for and are not the main emphasis of this study.

Secondly, in the case of the DSP specimen, the strain to failure is so small the change in intensity from the beginning of load to failure may be only a fraction of a gray level. However, gray level differences for any individual pixel may be as large as four gray levels. By examining the gray levels of an unloaded specimen over time and throughout the specimen, temporal and spatial changes of approximately one to four gray level values for most specimens were observed. At this point it is assumed that the noise is a "white" noise. To avoid time consuming image processing to filter out this noise, the intensities were averaged over a large area to remove the effects of this noise.

Finally, as stated before, the change in gray level measured in this test configuration is a fraction of a gray level. However, the image capturing card only digitizes in integer values. By noting that the gray level varies slightly within the specimen, accurate sub-integer values of the changes in intensity can be obtained if the intensities are averaged over a large enough region. Accurate results were obtained for the aluminum with a region 25 pixels by 25 pixels (.14 by .14 inches). The minimum size of the region for the DSP was governed by the inhomogeneities in the specimens. Regions were no smaller than 75 by 75 pixels (.42 by .42 inches) for the DSP.

Attenuation and Build-up Factors:

Equation (1) and a suitable representation of the build-up factor can be used to calculate the attenuation and build-up factor coefficients for each material. When two plates of a material having two thicknesses are X-rayed at the same time the dependence on the incoming X-ray intensity, I_0, can be removed by dividing the average intensity over one of the plates by the average intensity over the other plate. The following equation is obtain by this division:

$$\frac{I_{1\,D1}}{I_{1\,D2}} = [\frac{\beta(\mu D1)}{\beta(\mu D2)}] e^{(\mu(D2-D1))} \tag{20}$$

where D1 and D2 are the thicknesses of the two plates. μ is the linear attenuation factor for the material for the density of the plates examined. $I_{1\,D1}$ and $I_{1\,D2}$ are the average intensity of the plates with thicknesses of D1 and D2 respectively. By using this equation and a nonlinear regression analysis, the build-up and attenuation factors can be determined.

In addition, a lower bound for the attenuation factor can be found graphically. If D2 is kept constant, at 1 inch for example, then the ratio of build up factors becomes the build-up factor for the material divided by a constant. The exponential in equation (20) is brought to the other side of the equation to obtain:

$$\frac{I_{1\,D1}}{I_{1\,D2}} e^{(\mu(D1-D2))} = [\frac{\beta(\mu D1)}{\beta(\mu D2)}] \tag{21}$$

By assuming values for the attenuation factor m and the data derived from the images of the pairs of plates, graphs of the shape of the build-up factor can be drawn. As the attenuation factor is varied the shape changes. At some minimum value of the attenuation factor the shape of the attenuation factor will have negative slopes which are not possible and, therefore, a lower bound can be established for the value of the linear attenuation factor, μ.

The mass attenuation factor, μ/ρ, was obtained for concrete by Hubbell (Bray and Stanley [1989]). By multiplying the mass attenuation factor for concrete by the unloaded density of the DSP samples, ρ_1, the linear attenuation factor, μ, for DSP is found to be .93 in^{-1}. This is the value used to analyze the DSP data.

An alternate method for the calculation of attenuation factors is presented by Bryant and McIntire [1985]. The method requires knowledge of the chemical make-up of the material by mass. With the use of this information and tables of mass attenuation factors for each chemical element in the material, the mass attenuation factor for the whole material can be calculated.

RESULTS

ALUMINUM:

With the methods discussed above the linear attenuation factor for aluminum was determined to be 1.17/in and 1.02 /in, when using a cubic polynomial and Taylor's formulation for the build-up factor, respectively. This

A-12

agrees well with the value published by Bryant and McIntire [1985] of 1.1684/in. Further analysis of equation (20) shows that the equation is very sensitive in the range of values for μ and the thicknesses being considered. Large changes in μ produce small changes in ratio of intensities. Several steps which can be taken to reduce this sensitivity will be discussed later.

The lateral extension ratio that was determined from the strain gauge data was .32 for the aluminum. The linear attenuation factor, μ, for aluminum X-rayed at a photon energy of 100 Kev was taken from Bryant and McIntire [1985] to be 1.1684/in. Figure A-2 shows predicted and experimental values of the normalized average change in gray level, $\Delta I/I_1$, versus the strain for the three aluminum samples. The predicted values follow the observed values closely.

DSP:

For the DSP specimens the lateral extension ratio increased as load was applied. A plot of the lateral extension ratio versus the axial strain is shown in Figure A-3 for the first test without relief of end confinement. Figure A-3 also shows the values of the lateral extension ratio that were used to analyze the data from that test. Figure A-4 shows the predicted (using the data from Figure A-3) and observed average change in gray level versus axial strain. The observed values show that there is more compaction than predicted. Dilatation occurred later than predicted. Furthermore, the specimen begins to dilate in the center much sooner than in the regions close to the platens. The failure zone for the specimen was angled and passed through the corners of the specimen. Such results are expected when there is additional confinement on the specimen from the platens.

Figure A-5 shows the results of a uniaxial test with rubber sheets between the platens and the specimen. The specimen begins to dilate at approximately .0005 (in/in), while the predicted dilatation doesn't occur until an axial strain of .0019 (in/in) is attained. Investigation of smaller regions of the images shows that dilatation occurs at the ends of the specimens almost immediately. Dilatation in the center of the specimen occurs at a strain of .0019 (in/in). This matches well with the predicted behavior indicating that the center of the specimen is fairly close to uniaxial conditions. The failure zone of this specimen is characterized as vertical splitting. These results are consistent with an outward lateral shear stress being applied at the ends of the specimen by the rubber.

The results of the tests on the mortar specimens indicate that the technique is sensitive enough to small changes in gray level to detect small deviations from the assumed stress path. It is sensitive enough to evaluate how close the loading technique simulates a specific stress path and where within a specimen a stress path is best simulated.

In the test in which cap blocks were used to relieve the end confinement, the data are too noisy to evaluate the performance of the test procedure. However, the failure for this case is also characterized by vertical splitting.

RECOMMENDATIONS FOR FUTURE WORK

The basic principle of this technique is that changes in the X-ray intensity passing through a specimen represents changes in both the density of the material and the X-ray path length. Therefore, it is advantageous to set up the tests in such a way that the expected changes in intensity are as large as possible. Equation (8) points to several ways this can be done.

First, I_1 could be increased. By increasing the current to the X-ray emitter the number of photon emitted is increased causing an increase in the intensity of the X-ray image. The equipment used for these tests provided a limit of 256 possible values for the intensity. If a 12 bit A/D converter was used on the video capturing board then there would be 4096 possible value. In cases where the intensity of the image is very low and limited by the capabilities of the X-ray emitter or the thickness of the sample, a video amplifier may be needed.

Second, the linear attenuation factor, μ, can be increased by X-raying at a lower photon energy. For example, if the DSP was X-rayed at a photon energy of 50 Kev instead of 100 Kev, the linear attenuation factor changes from .93 to 2.05 (1/in). Therefore, the expected change in gray level would double for the 1.5 in thick specimens provided the intensity of the original image, I_1, remains the same. The provision of the same initial intensity would require an increase in the current to the X-ray emitter and/or an increase in the aperture opening of the CCD camera. If the average intensity of the unloaded specimen decreases when switching to a lower photon energy then the advantages of increasing the attenuation factor may be negated.

The expected change in gray level can also be increased by using a thicker specimen (larger value for D). This also reduces the initial intensity. Therefore, it will be necessary to increase the current to the emitter and open the camera aperture to maintain the same initial intensity.

It may be desirable to test a specimen in such a way that the ratio of the build up factor in the strained state to the unstrained state is significantly different from one. This leads to a problem inverting the equation to obtain strains from changes in gray level. The setup can be changed to a narrow beam geometry by columnating the X-ray beam between the specimen and the image intensifier. Then the build-up factor would be 1 for all thicknesses.

At this time, the results have depended on obtaining some knowledge of the lateral extension effect. For the case of plane strain, $\varepsilon_d = 0$, it is easy to see that equation (8) depends only on the volumetric strain. Therefore, this technique may prove useful in the determination of volumetric strains in plane strain tests on sands.

The development presented in this paper always leads to one equation with two unknowns. If additional measures of the strains are obtained the equations may prove more accurate and comprehensive. By combining this technique with others such as digital tracking one might be able to determine strains more accurately and more efficiently than by utilizing only one method or the other. By using tomographic techniques it may be feasible to obtain a complete picture of the strains within a specimen utilizing only the changes in gray level. The result would be a very valuable tool for non-destructive testing.

CONCLUSIONS

Strain data can be obtained by measuring the change in gray level of X-ray images. With some knowledge of the lateral extension effect and loading conditions, strains can be obtained with very little computation. In the case of uniaxial stress the strains can be obtained real time with state of the art video processing equipment; therefore, the technique may be used as a non-invasive means to provide strain control for materials testing.

Preliminary tests on mortar specimens indicate that this technique will provide a means of quantifying how well an experimental setup simulates a homogeneous state of strain under uniaxial and biaxial states of stress. Alternatively, it may be used to show which subdomain of the specimen is experiencing a homogeneous strain field.

If the technique is used in conjunction with other strain measuring techniques such as cross correlation of X-ray images or digital tracking a more complete record of the strain history may be obtained non-invasively. Furthermore, if this technique can be applied to a specimen in several directions, for example by utilizing tomographic techniques, it may be possible to derive a complete description of the strain field solely from the change in gray levels.
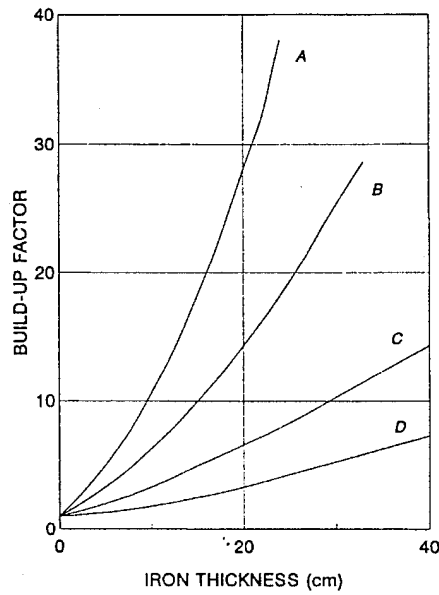
Figure A-1: Build-up Factor for Iron for Various Photon Energies:
A) .5 MeV, B) 1 MeV, C) 2 MeV, D) 4 MeV
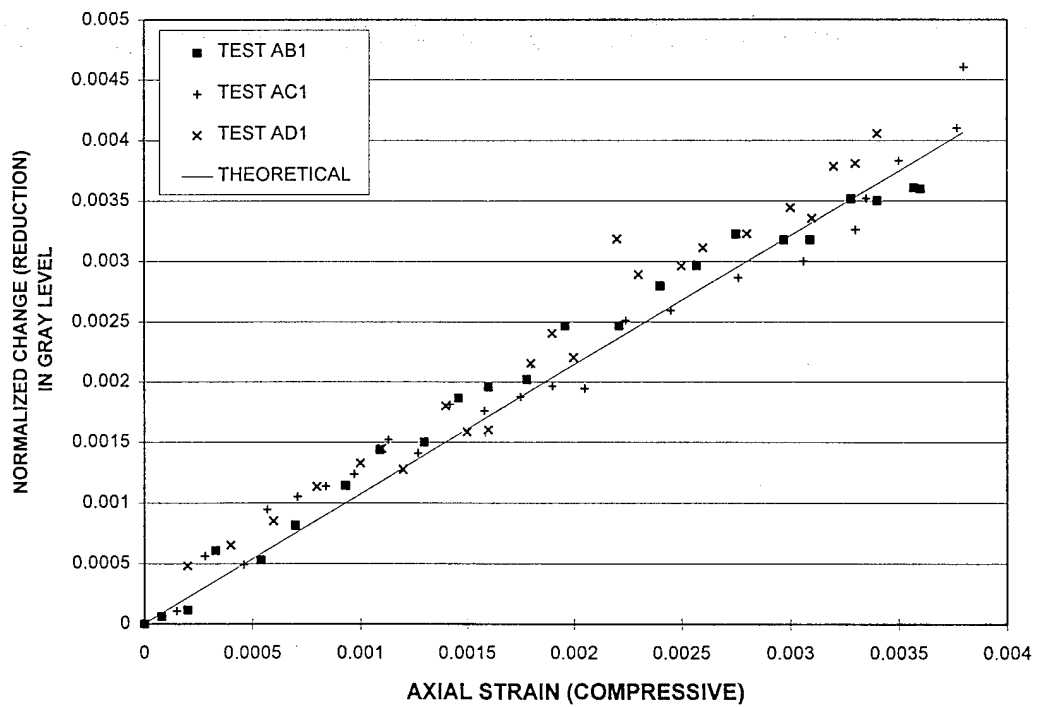
Figure A-2: Normalized Change in Gray Level versus Axial Strain
for Aluminum with Poisson's Ratio = .32
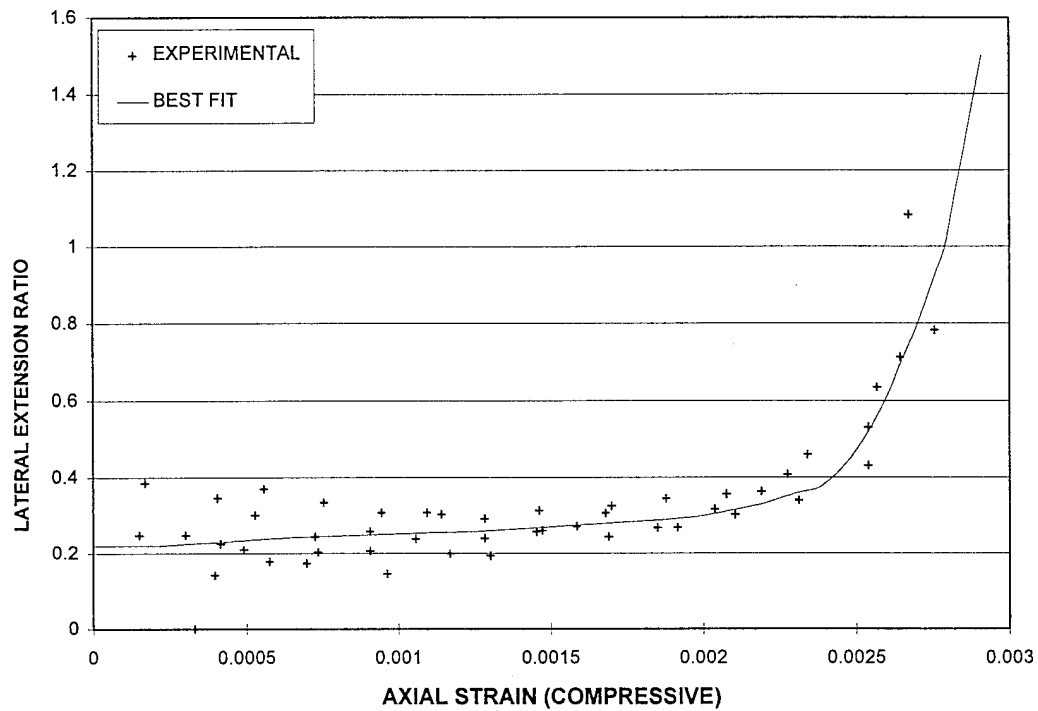
Figure A-3: Lateral Extension Ratio versus Axial Strain
for DSP Test C11 with No Friction Relief
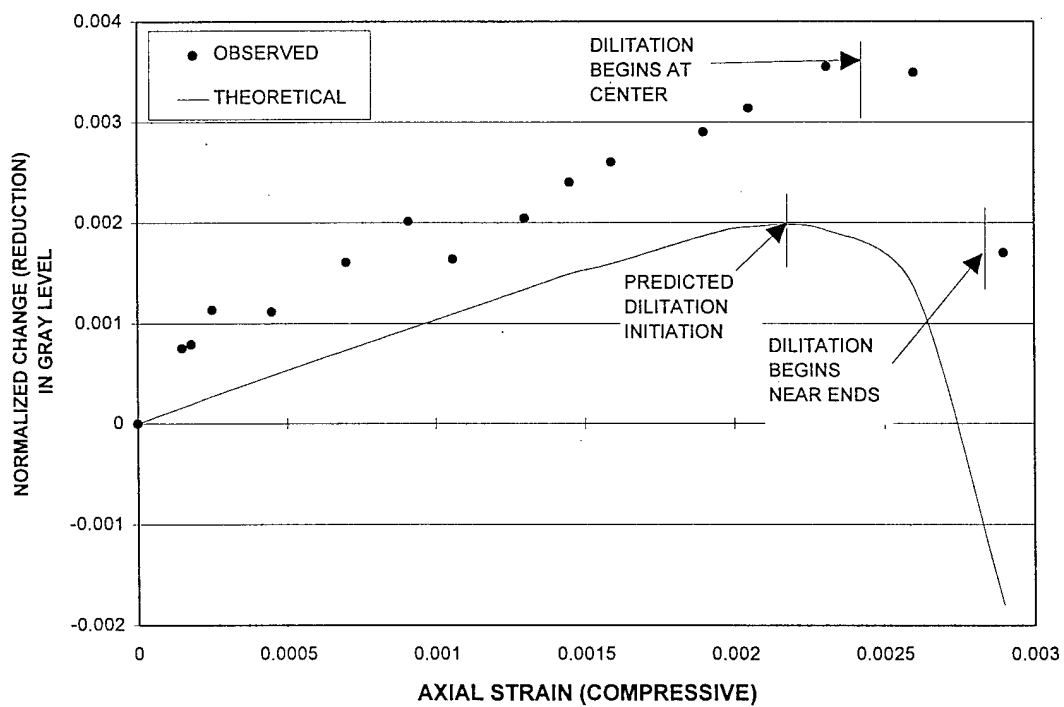
Figure A-4: Normalized Change in Gray Level versus Axial Strain
for DSP Test C11 with No Friction Relief

A-17
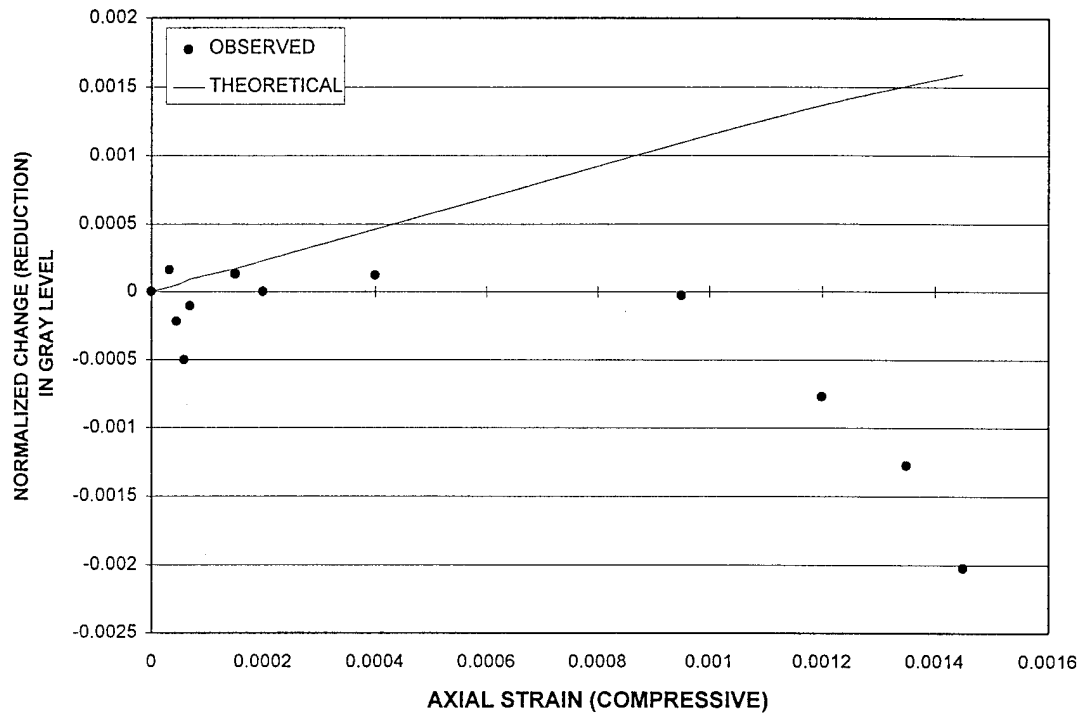
Figure A-5: Normalized Change in Gray Level versus Axial Strain
for DSP Test C411 with Rubber Sheets for Friction Relief

REFERENCES

J. R. F. Arthur "Industrial Radiography in Soil Mechanics," British Jnl. of Non-destructive Testing, Vol. 29, No. 1, Jan 1977, pp. 9-13.

D. E. Bray and R. K. Stanley, Nondestructive Evaluation, McGraw Hill Book Company, 1989, pp. 386.

L. E. Bryant and P. McIntire, The Society for Nondestructive Testing "Nondestructive Testing Handbook," Vol. 3, "Radiography and Radiation Testing," 1985, pp. 836-878.

H. Goldstein and J. E. Wilkins, Jr. "Calculation of Penetration of Gamma Rays," U.S. Atomic Energy Comm., NYO-3075 (1954).

R. Halmshaw, "Physics of Industrial Radiology," American Elsevier Publishing Company Inc., 1966, pp. 142-143.

R. C. McMaster, The Society for Nondestructive Testing "Nondestructive Testing Handbook," 1959, Vol.1, pp. 13.17-15.39.

K. H. Roscoe, J. R. F. Arthur, and R. G. James "The Determination of Strains in Soils By an X-ray Method," Civil Engineering and Public Works Review, July 1963, pp. 873-876.

J. J. Taylor, "Application of Gamma Ray Build-up Data to Shield Design," WAPD Memo, RM-217, 25 January 1954.

R. H. Templer, S. M. Gruner, and E. F. Eikenberry "An Image-intensified CCD Area X-ray Detector for Use with Sychrotron Radiation," 1988, Advances in Electronics and Electron Physics, Vol. 74, pp. 275-283.

I. Vardoulakis and B. Graf, "Calibration of Constitutive Models for Granular Materials Using Data from Biaxial Experiments," Geotechnique, Vol. 35, No. 3, 1985, pp. 288-317.

M. L. Wang and T. J. Ross "Deformation Measurements at a Crack Tip using a Fast-Scanning Electron Microscope," Fracture Processes in Concrete, Rock and Ceramics, Edited by J. G. M. van Mier, J.G. Rots, and A. Bakker, RILEM, E. & F.N. Spon, 1991, pp. 61-71

M. L. Wang, H. L. Schreyer, and C. A. Rutland "Internal Deformation Measurements with the Use of Real Time X-rays," Micromechanics of Failure of Quasi-Brittle Materials, Editor S. P. Shah, S. E. Swartz, and M. L. Wang, Elsevier Applied Science, 1990, pp. 81-94.

R. K. S. Wong and J.R.F. Arthur "Determination and Uses of Strain Distributions in Sand Samples," Geotechnical Testing Journal, GTJODJ, Vol. 8, No. 3, Sept 1985, pp. 101-110.

APPENDIX B

STRESS-STRAIN CURVES
(from LOAD-DISPLACEMENT)

The following pages contain plots of the axial stress versus axial strain obtained from the load-displacement data. The tests for which curves are presented are listed below with the corresponding page where the graph can be found.

T25.2.13
STRESS vs STRAIN from LOAD -DISPLACEMENT

T25.2.15
STRESS vs STRAIN from LOAD-DISPLACEMENT

B-2
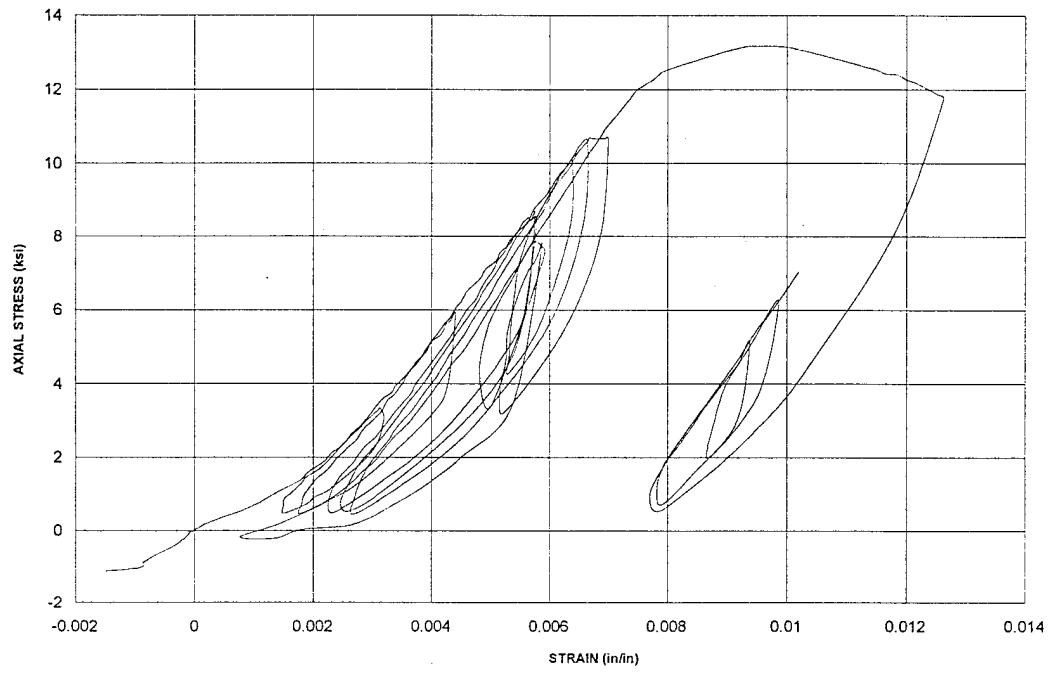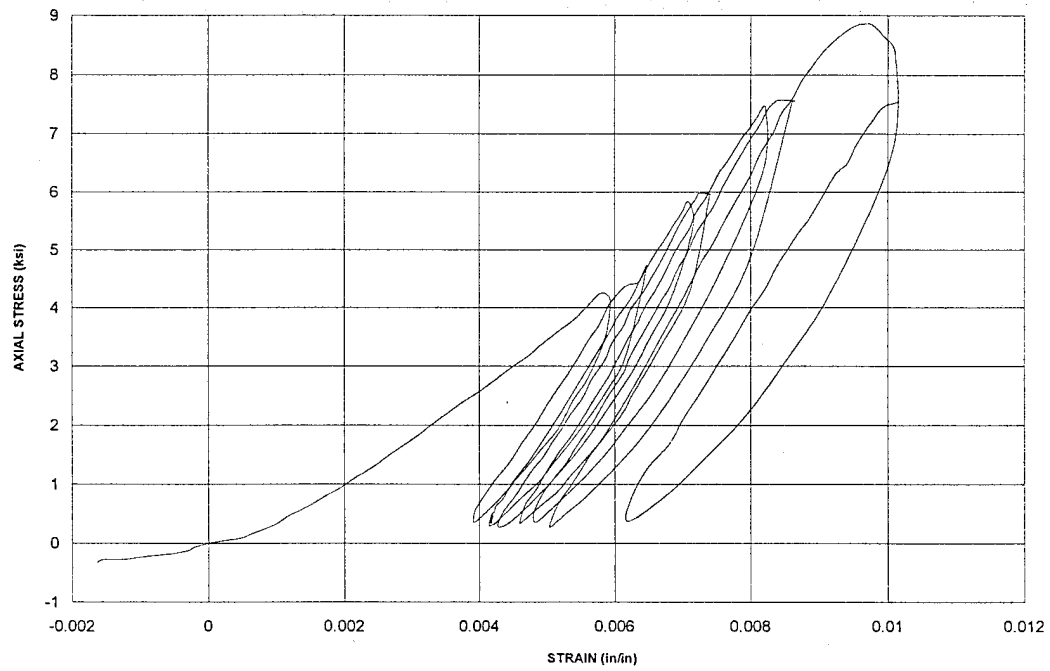
T25.2.16
STRESS vs STRAIN from LOAD-DISPLACEMENT

T25.2.17
STRESS vs STRAIN from LOAD-DISPLACEMENT

B-3
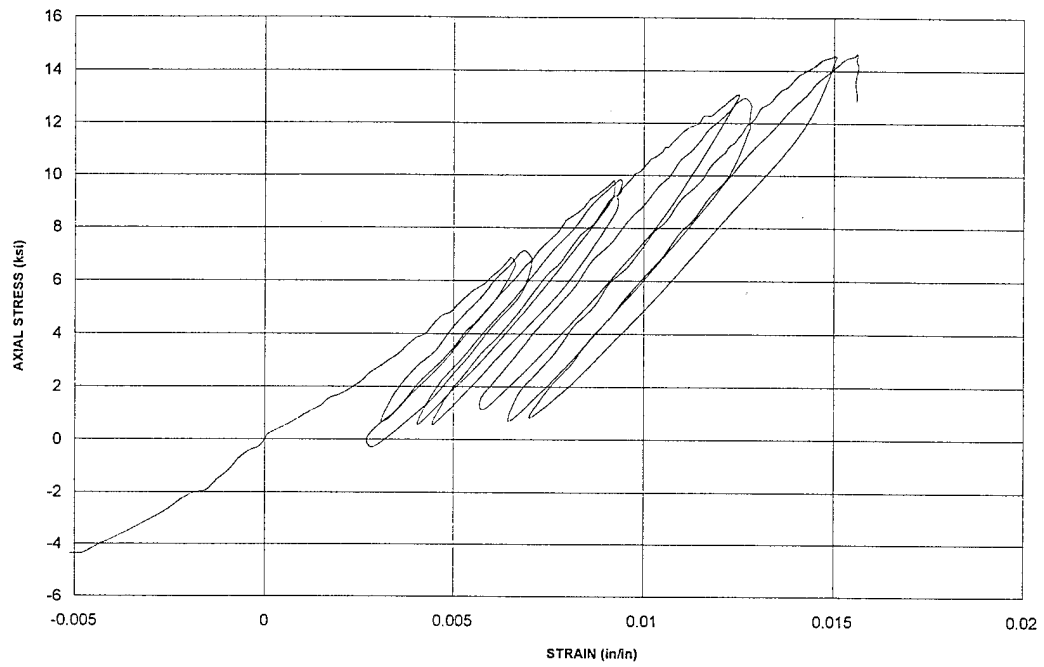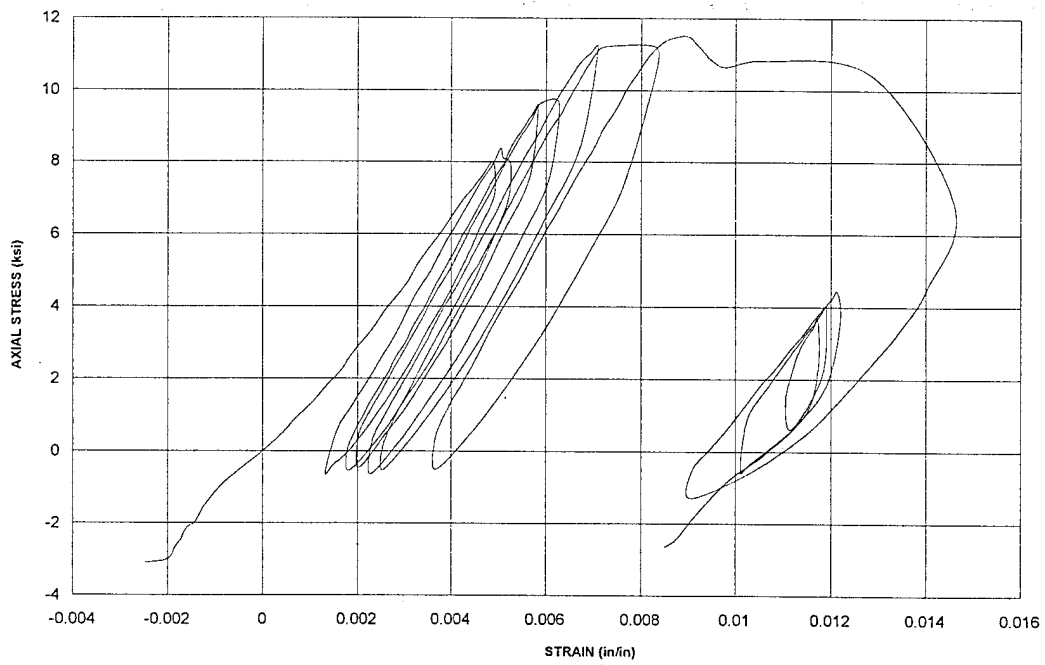
T25.2.19
STRESS vs STRAIN from LOAD-DISPLACEMENT

T25.2.23
STRESS vs STRAIN from LOAD-DISPLACEMENT

B-4
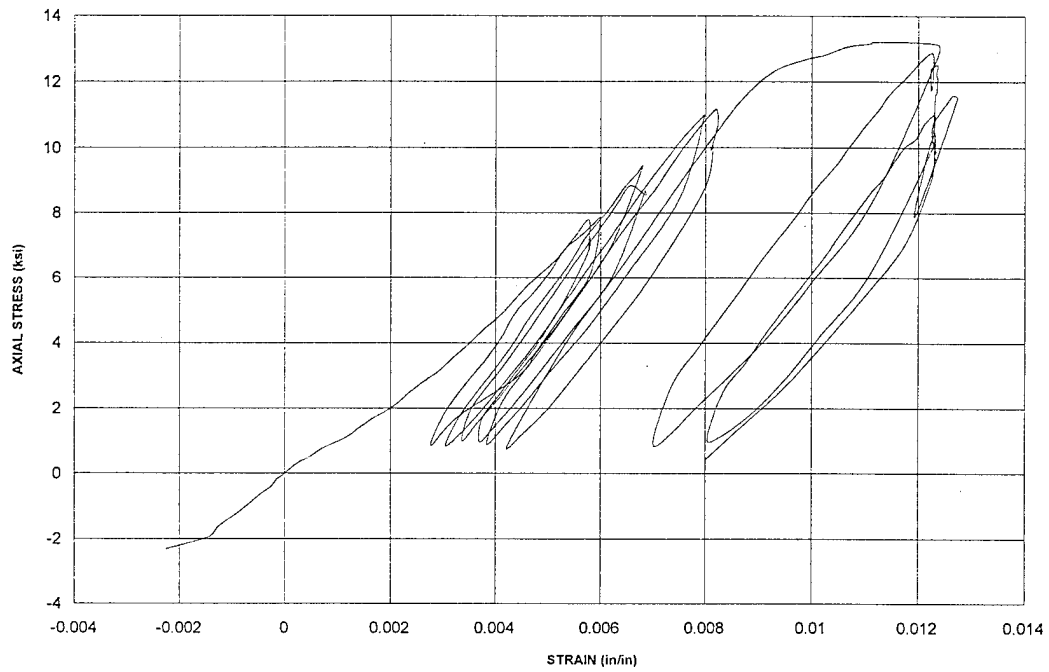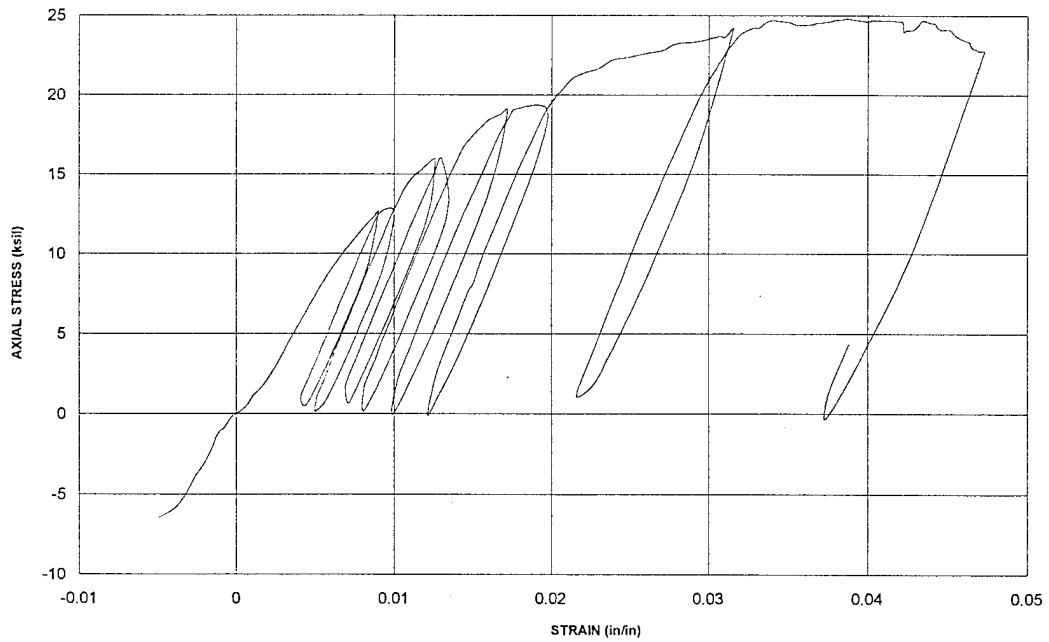
T25.3.13
STRESS vs STRAIN from LOAD-DISPLACEMENT

T25.3.15
STRESS vs STRAIN from LOAD-DISPLACEMENT

B-5
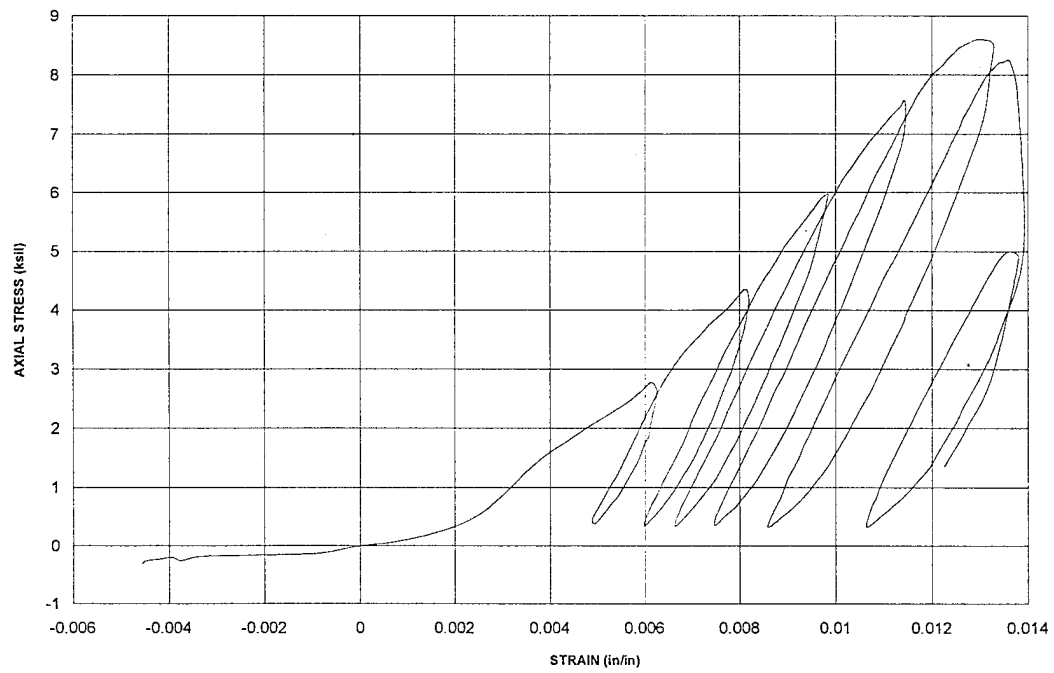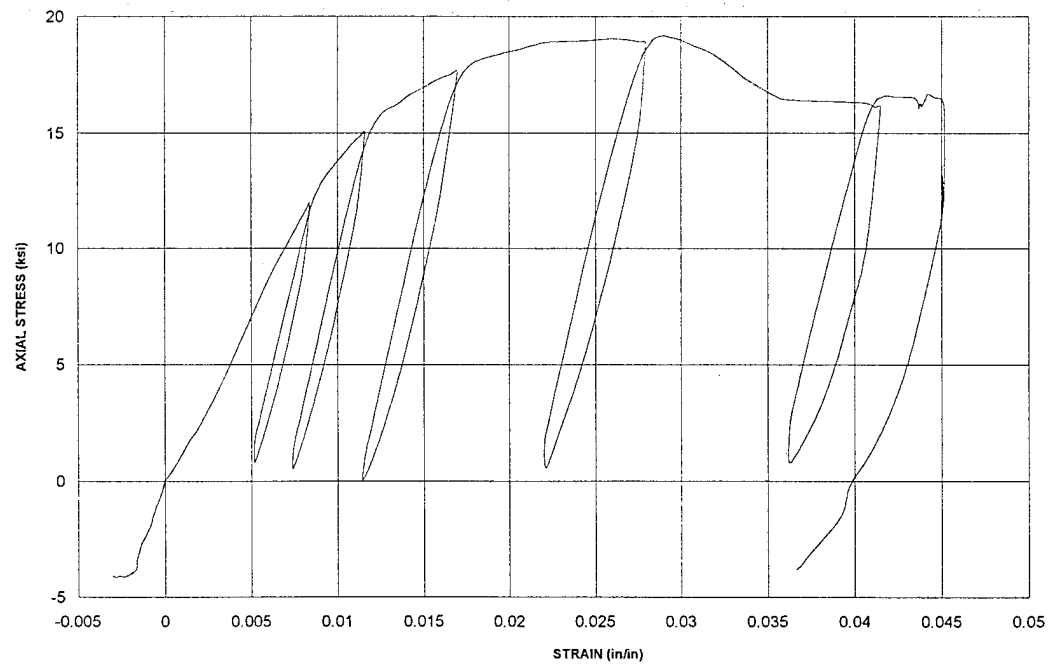
T25.3.17
STRESS vs STRAIN from LOAD-DISPLACEMENT

T25.3.18
STRESS vs STRAIN from LOAD-DISPLACEMENT

B-6
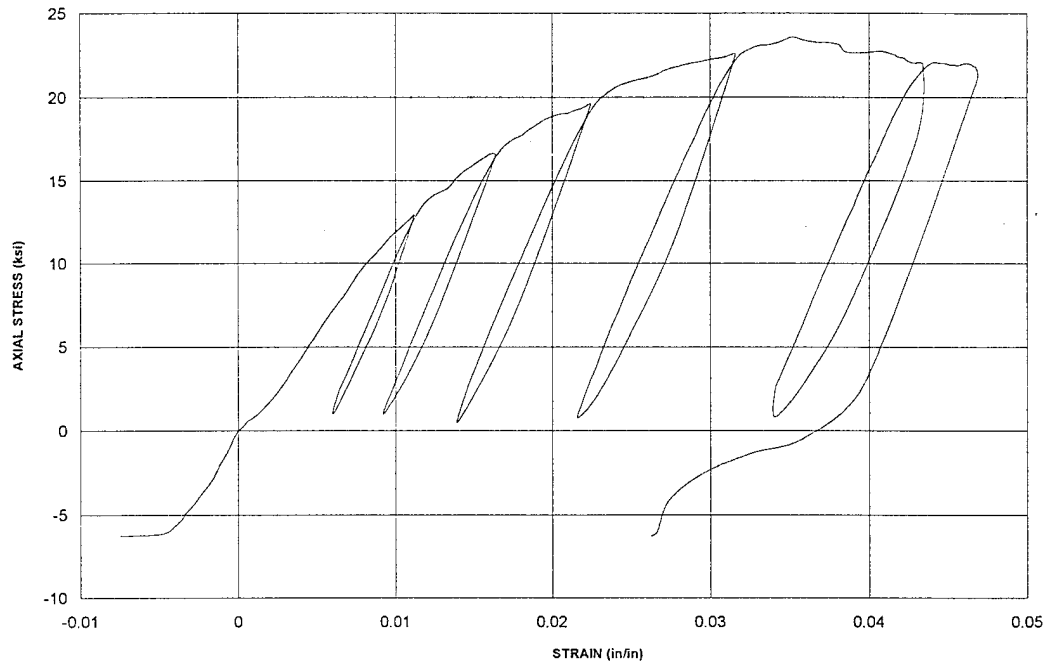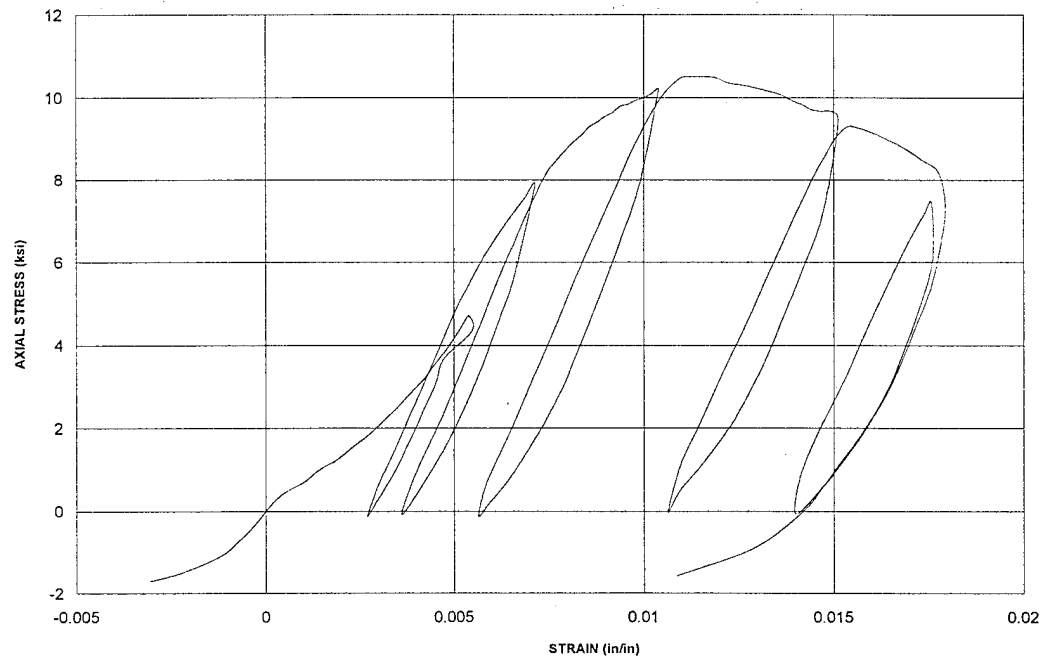
T25.3.21
STRESS vs STRAIN from LOAD-DISPLACEMENT
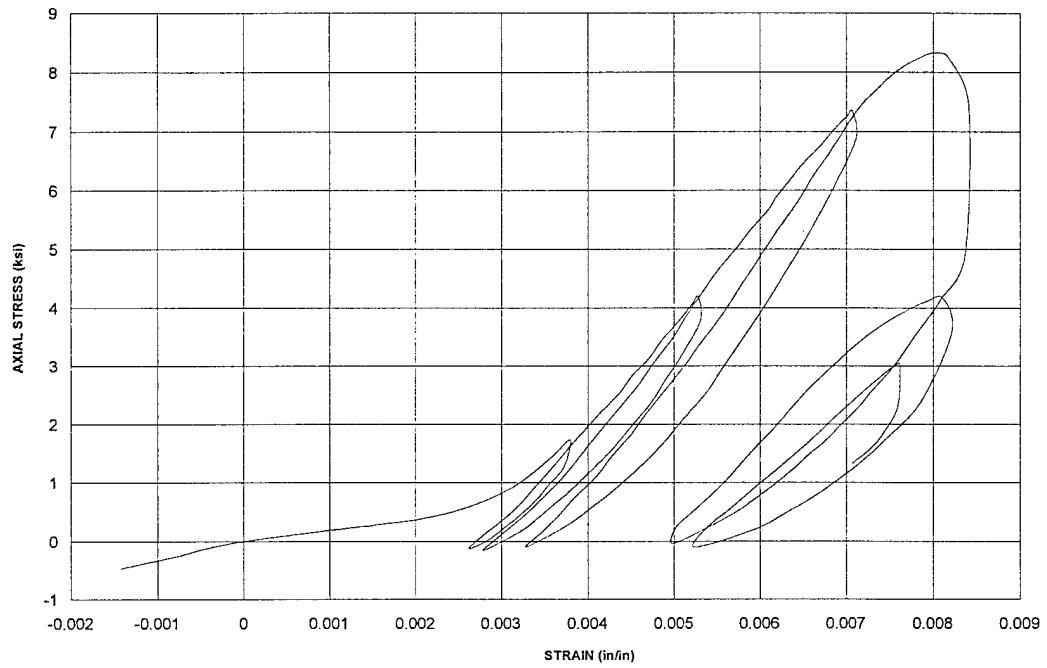
T25.3.22
STRESS vs STRAIN from LOAD-DISPLACEMENT
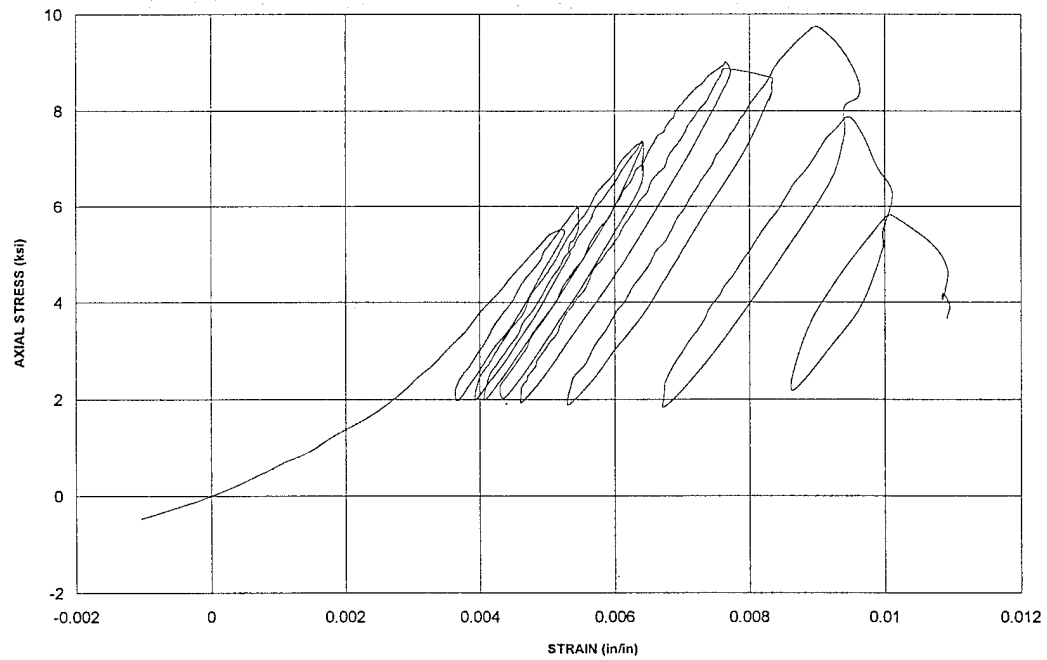
T25.4.6
STRESS vs STRAIN from LOAD-DISPLACEMENT
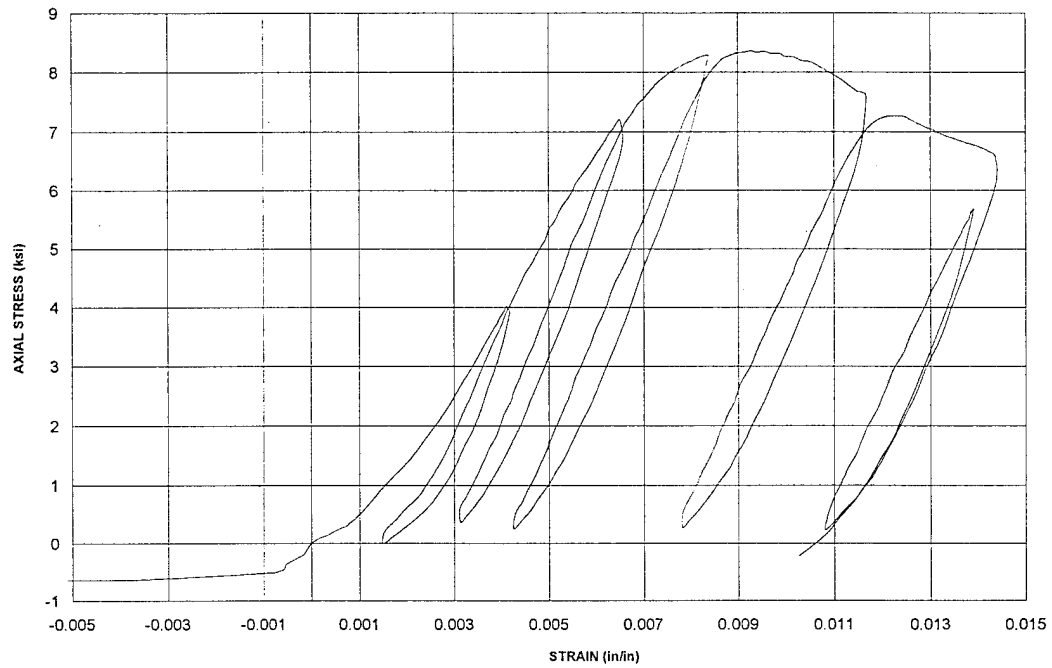
T25.4.7
STRESS vs STRAIN from LOAD-DISPLACEMENT
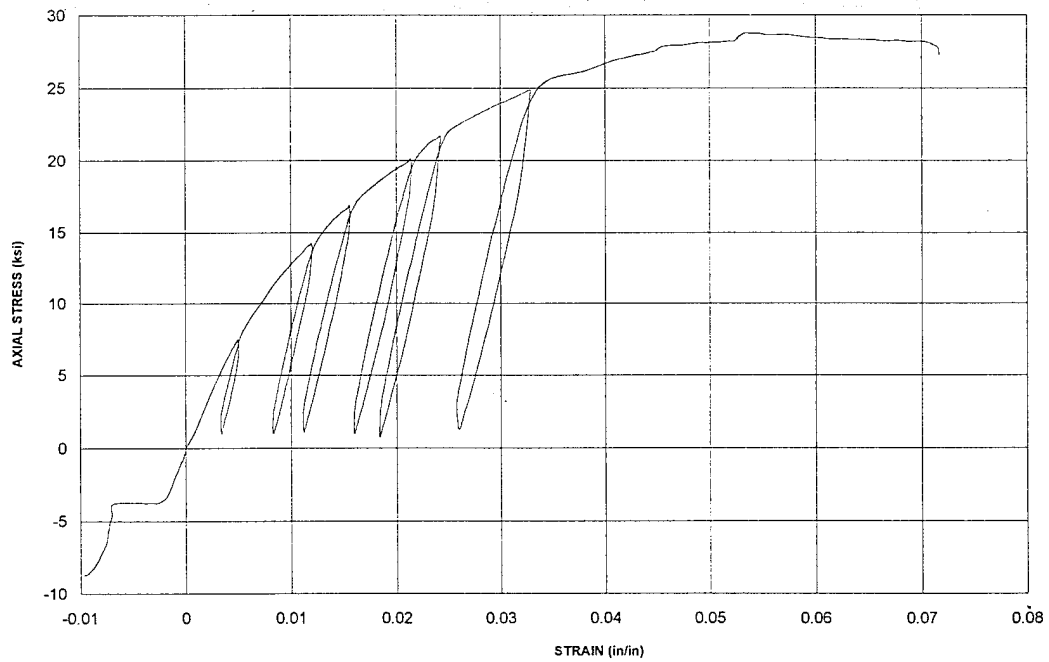
T25.4.8
STRESS vs STRAIN from LOAD-DISPLACEMENT
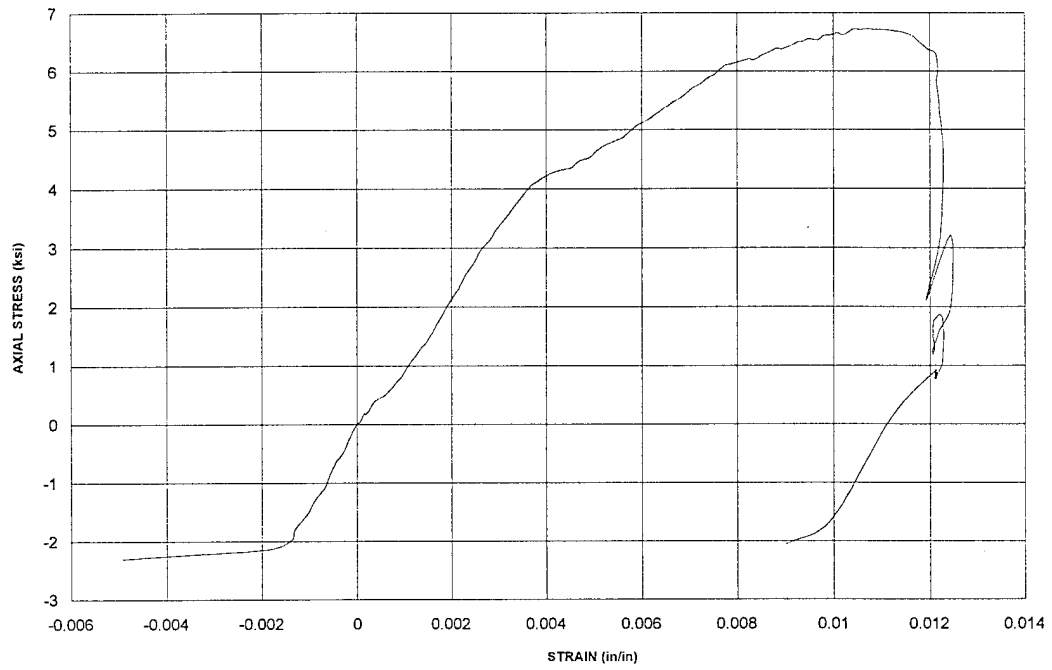
T25.4.15
STRESS vs STRAIN from LOAD-DISPLACEMENT

B-9
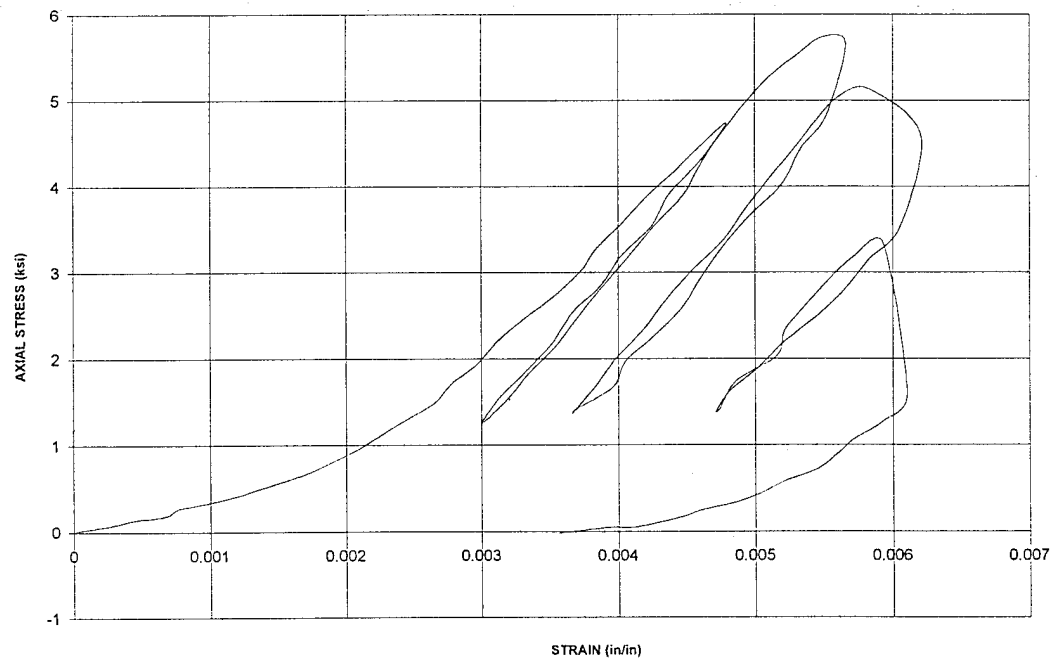
T25.4.16
STRESS vs STRAIN from LOAD-DISPLACEMENT

T25.4.18
STRESS vs STRAIN from LOAD-DISPLACEMENT

B-10
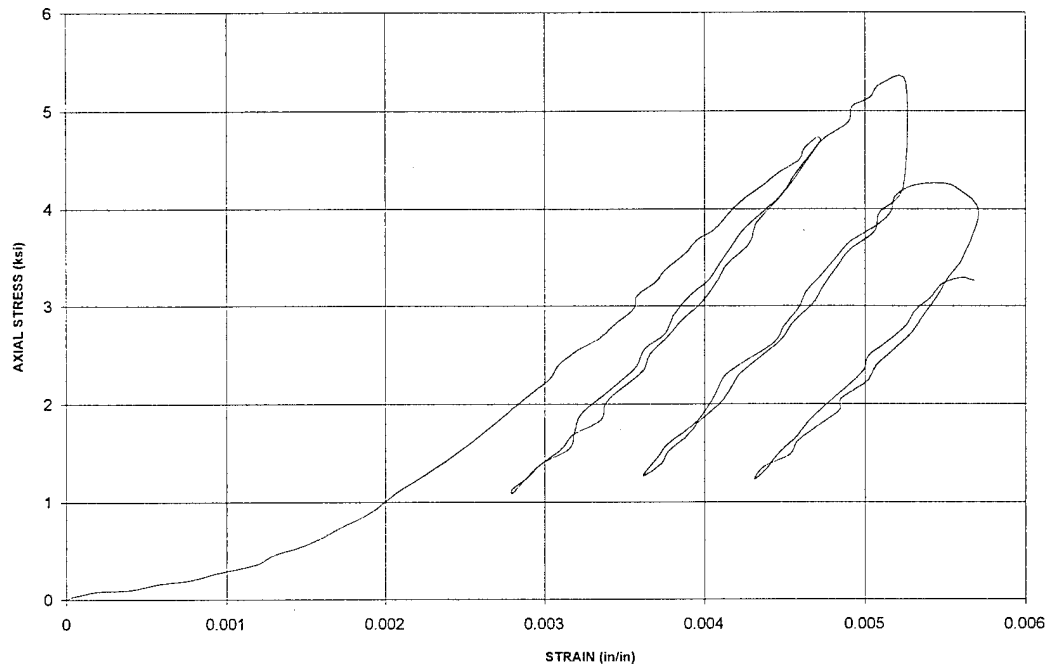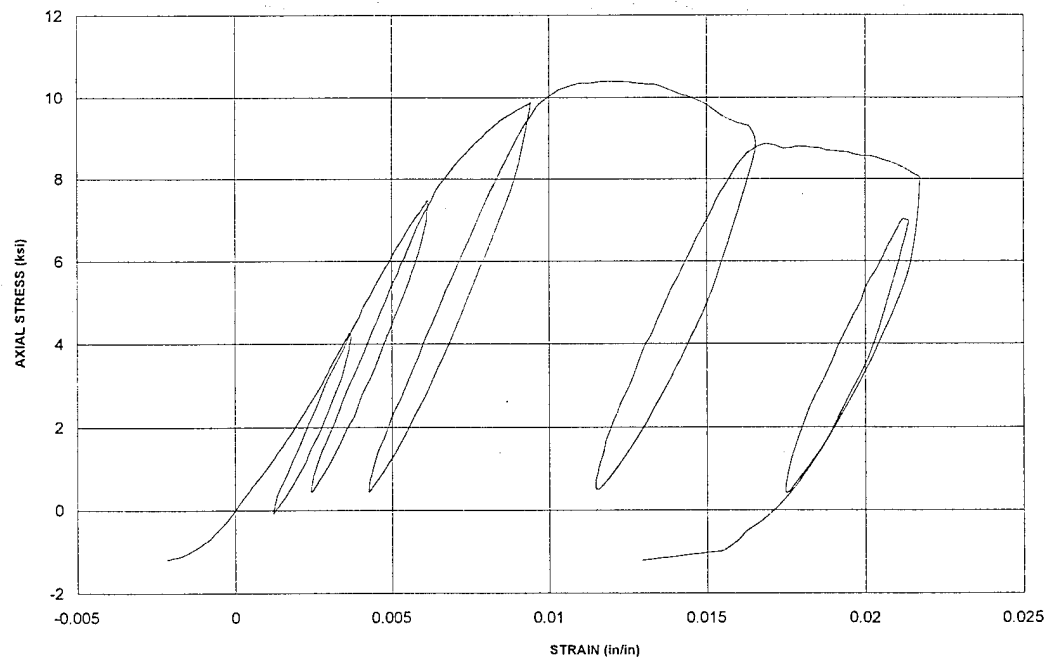
T25.4.19
STRESS vs STRAIN from LOAD-DISPLACEMENT
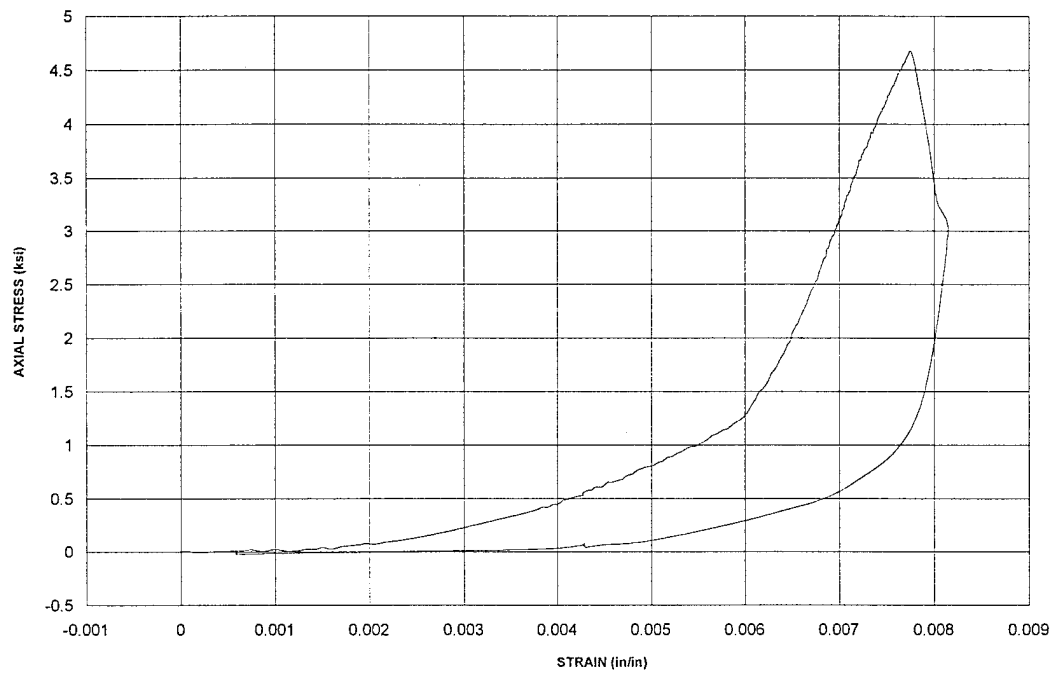
B3.1
STRESS vs STRAIN from LOAD-DISPLACEMENT
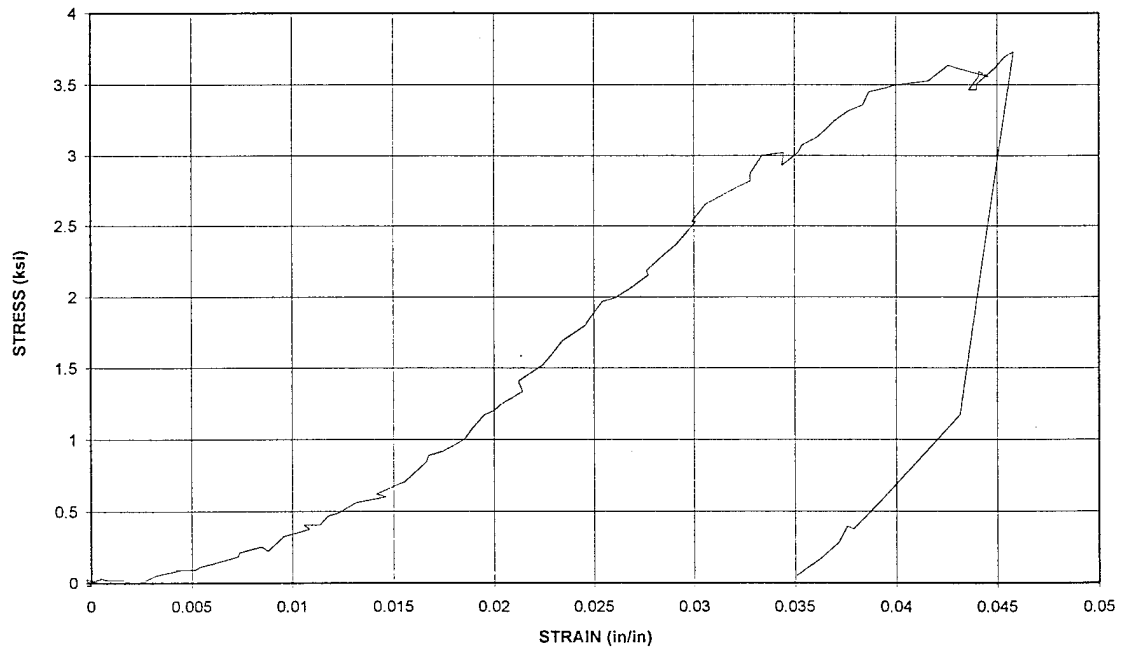
APPENDIX C

STRESS-STRAIN CURVES
(from STRAIN GAUGES)

The following pages contain plots of the axial stress versus axial and volumetric strains obtained from strain gauges. In cases where the axial strain gauge broke or malfunctioned the lateral strain is shown in lieu of the volumetric strain. If the lateral gauge broke or malfunctioned then the axial data alone is shown for that set of gauges. For each test the stress-strain curves for the gauges located at the middle of the specimen are located at the top of the page while the curves for the gauges located at the bottom (end) of the specimen are located at the bottom of the page. The tests for which curves are presented are listed below with the corresponding page where the graph can be found.

T25.2.13
STRESS vs STRAIN at MID HEIGHT

T25.2.13
STRESS vs STRAIN at SPECIMEN BOTTOM (END)
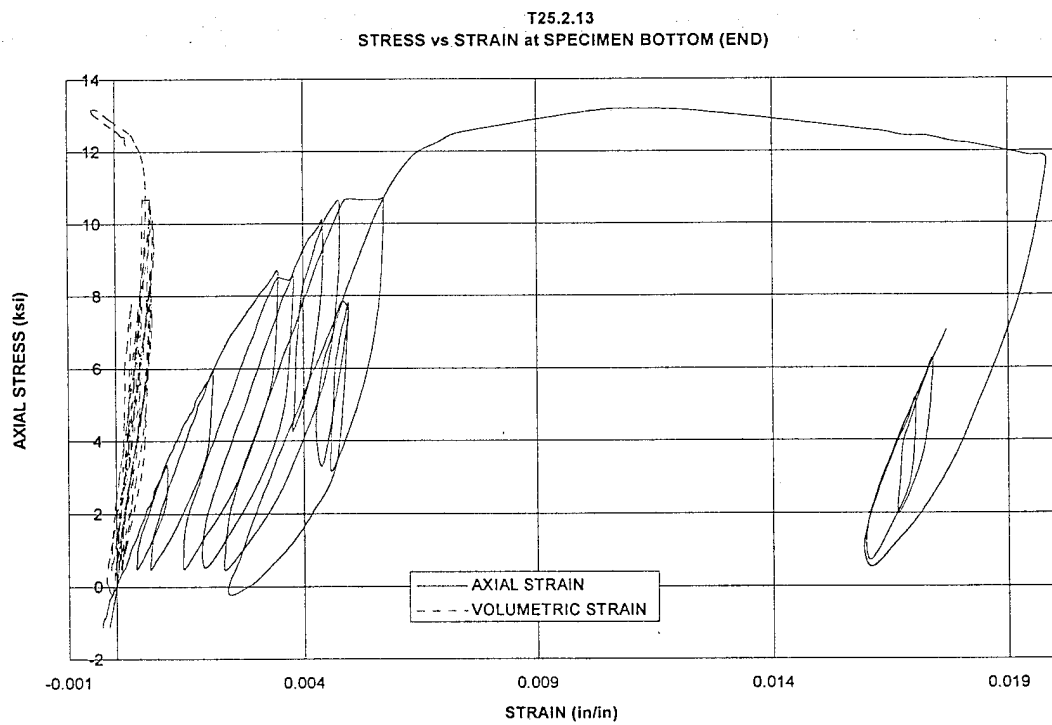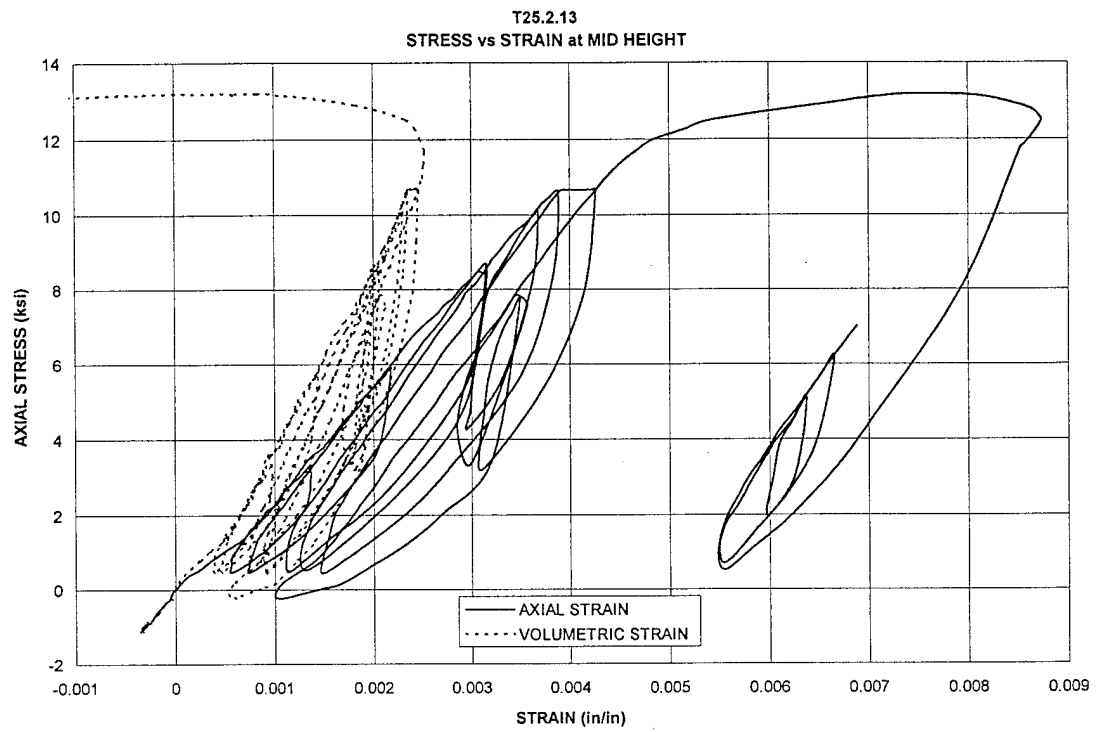
T25.2.15
STRESS vs STRAIN at MID HEIGHT
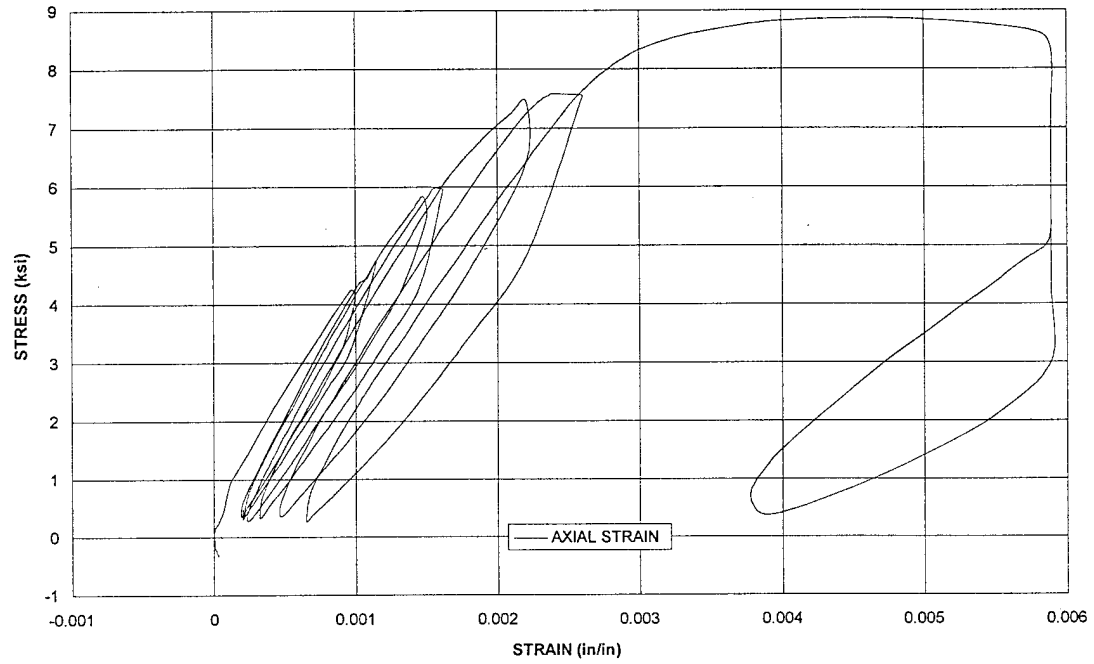
T25.2.15
STRESS vs STRAIN at SPECIMEN BOTTOM (END)
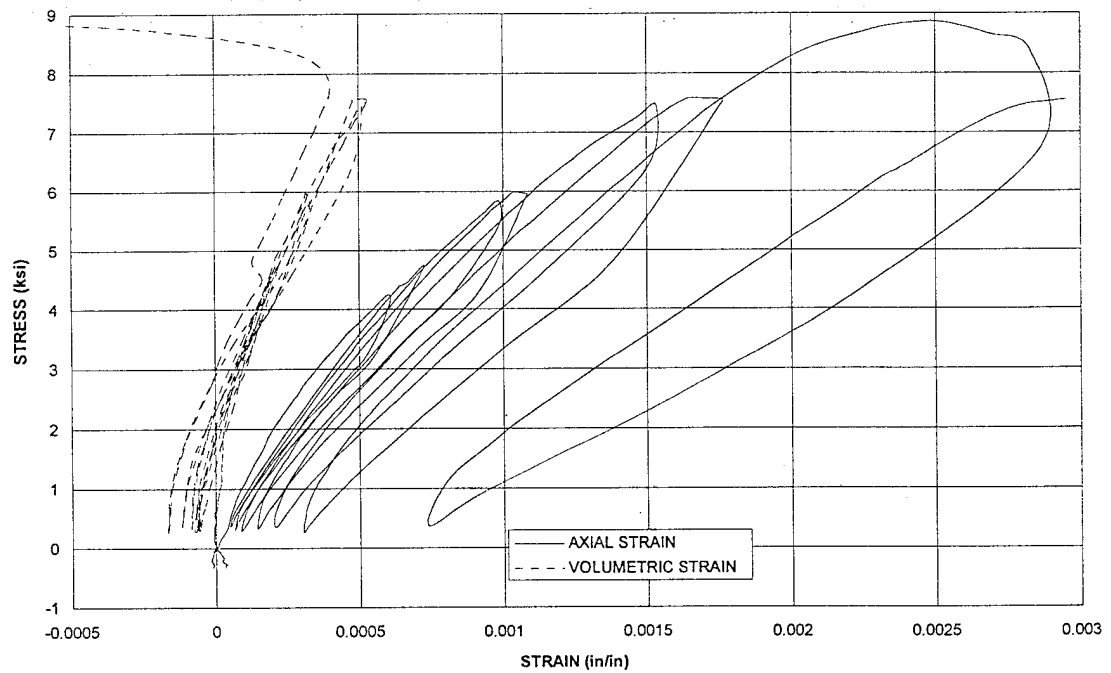
T25.2.16
STRESS vs STRAIN at MID HEIGHT

T25.2.16
STRESS vs STRAIN at SPECIMENBOTTOM (END)

T25.2.17
STRESS vs STRAIN at MID HEIGHT
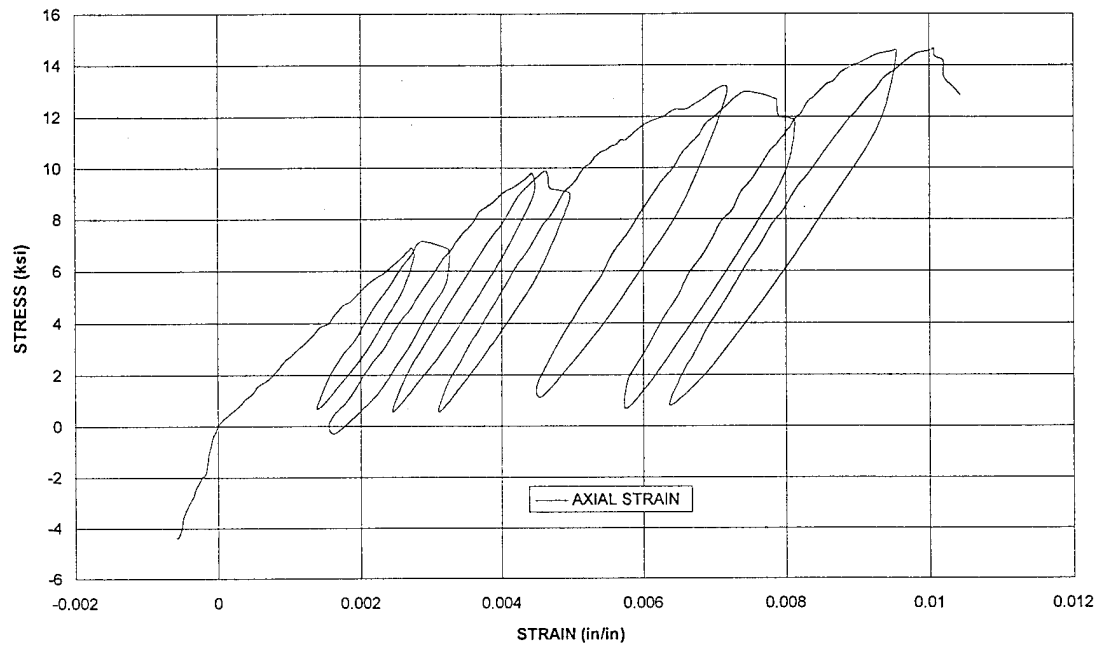
T25.2.17
STRESS vs STRAIN at SPECIMEN BOTTOM (END)
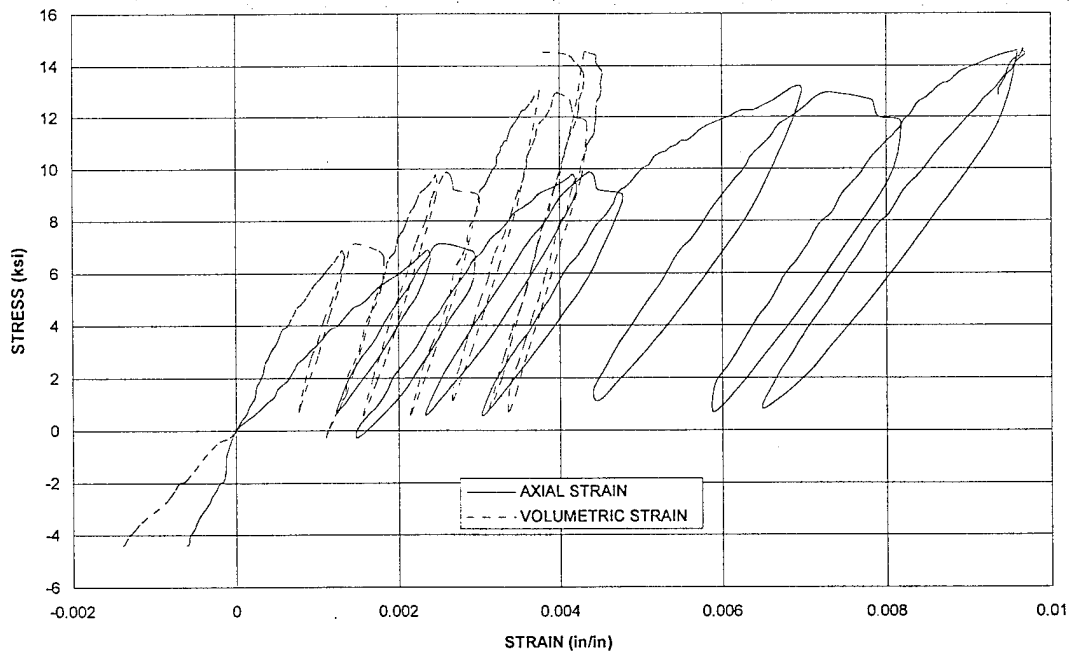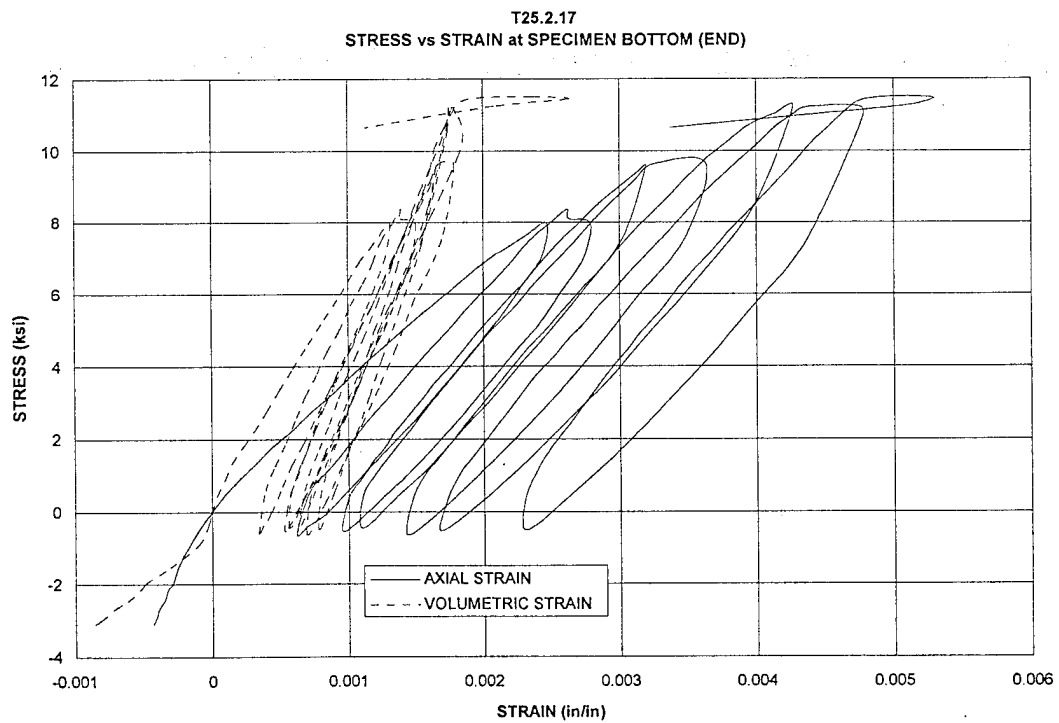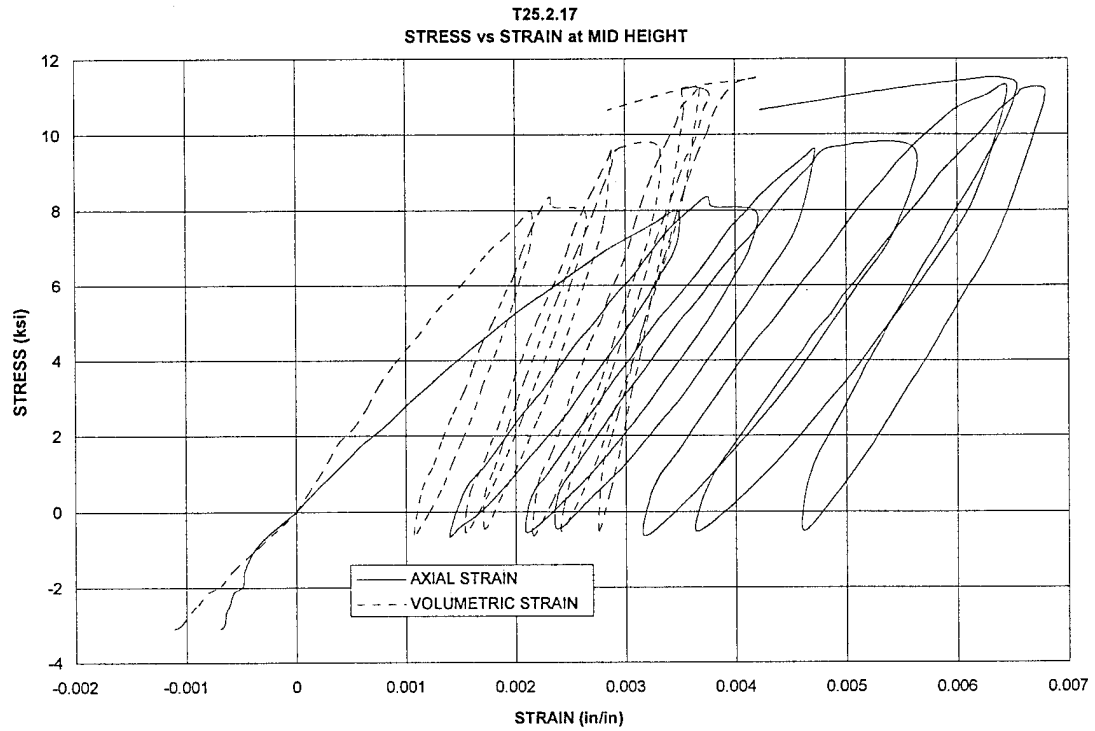
T25.2.19
STRESS vs STRAIN at MID HEIGHT
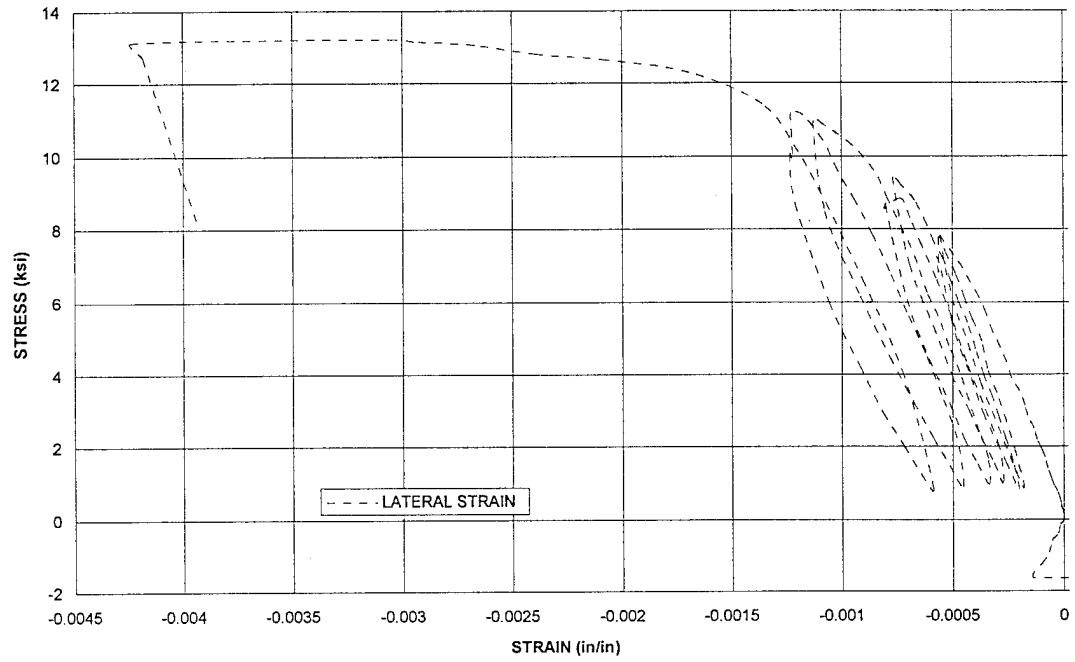
T25.2.19
STRESS vs STRAIN at SPECIMEN BOTTOM (END)
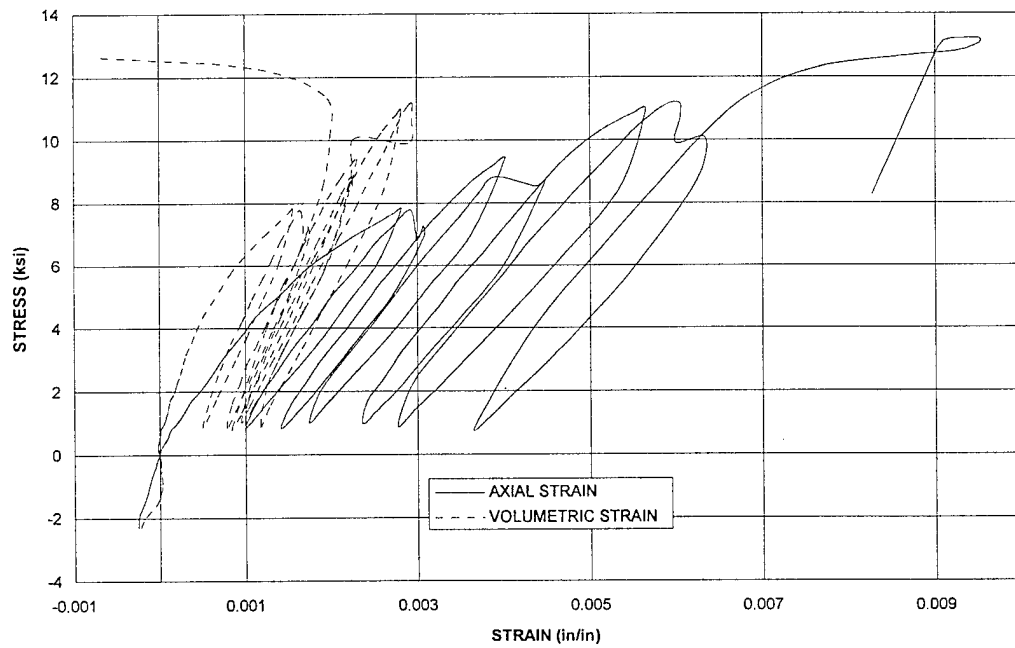
T25.2.23
STRESS vs STRAIN at MID HEIGHT
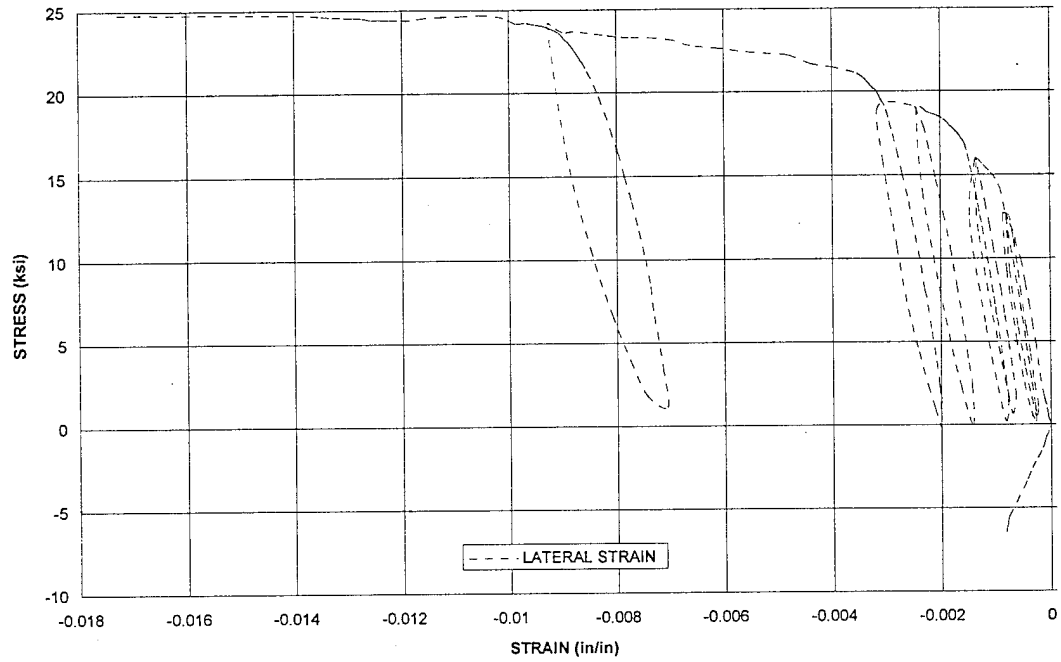
T25.2.23
STRESS vs STRAIN at SPECIMEN BOTTOM (END)
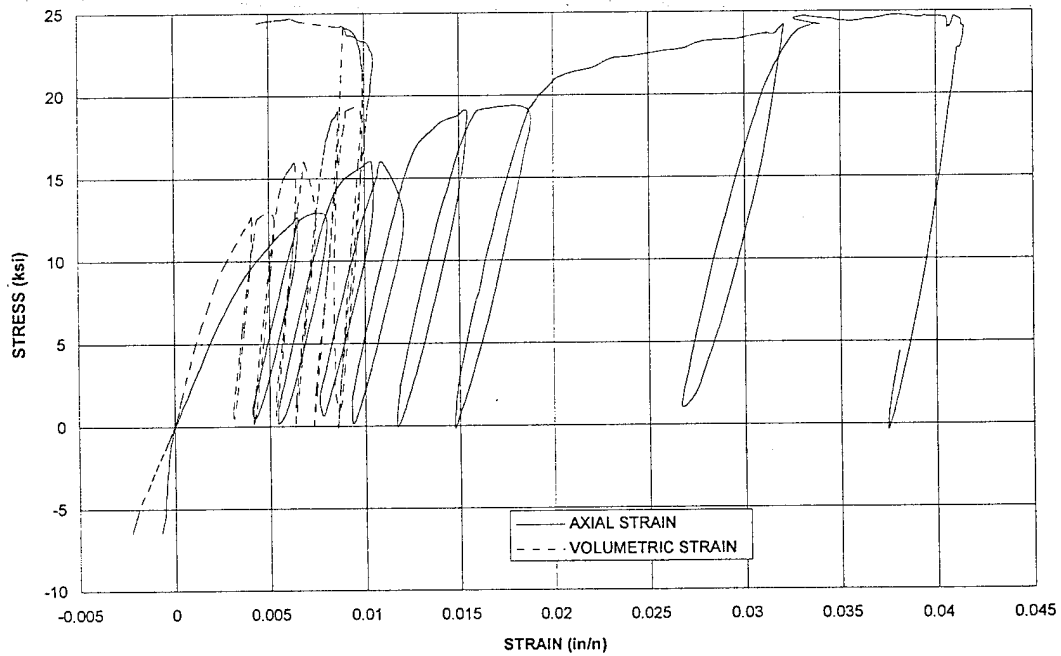
T25.3.13
STRESS vs STRAIN at MID HEIGHT
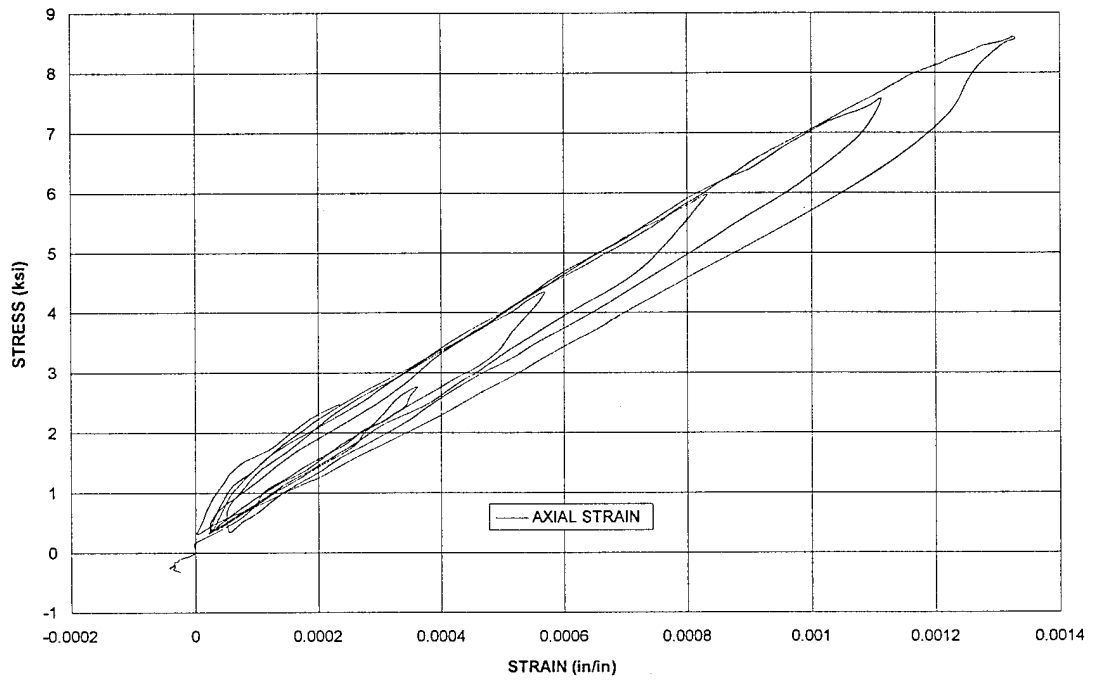
T25.3.13
STRESS vs STRAIN at SPECIMEN BOTTOM (END)
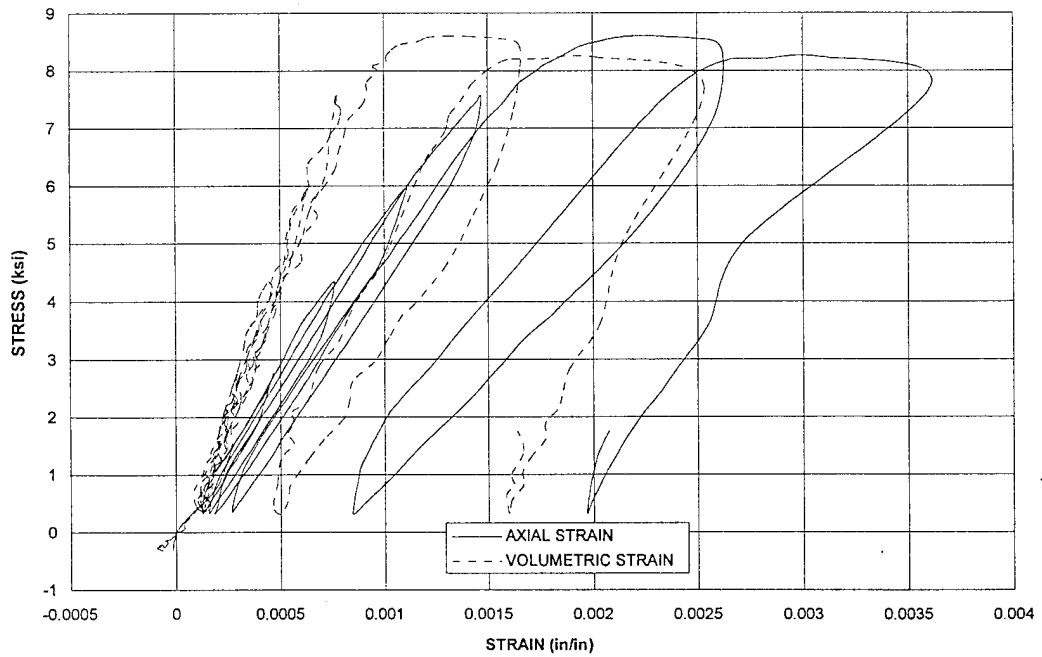
T25.3.15
STRESS vs STRAIN at MID HEIGHT

T25.3.15
STRESS vs STRAIN at SPECIMEN BOTTOM (END)

C-9
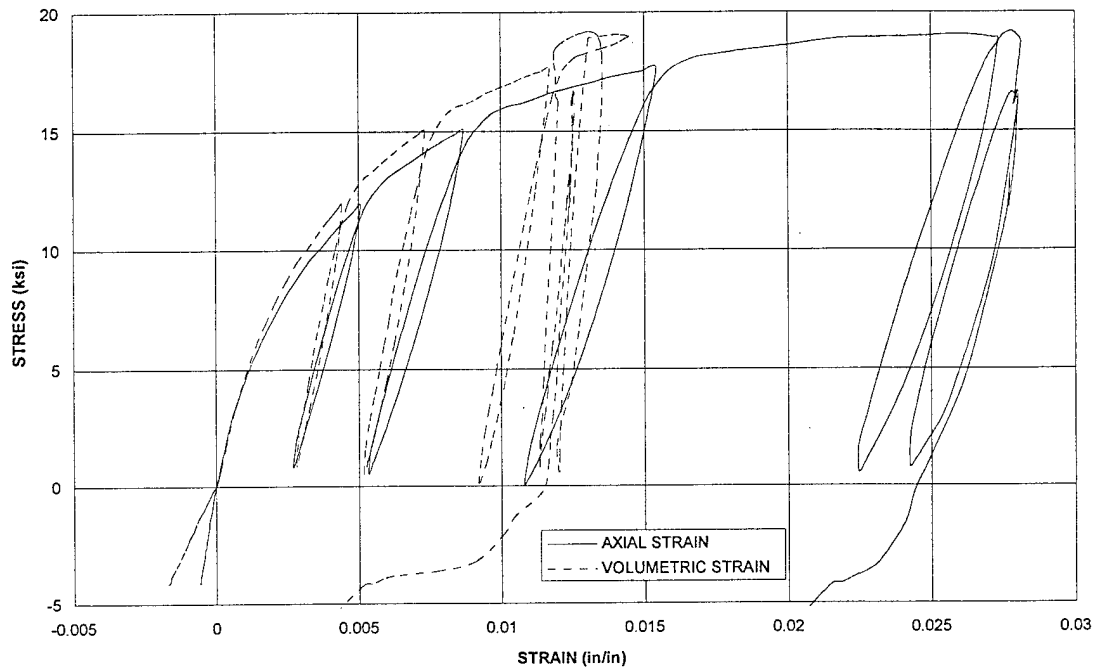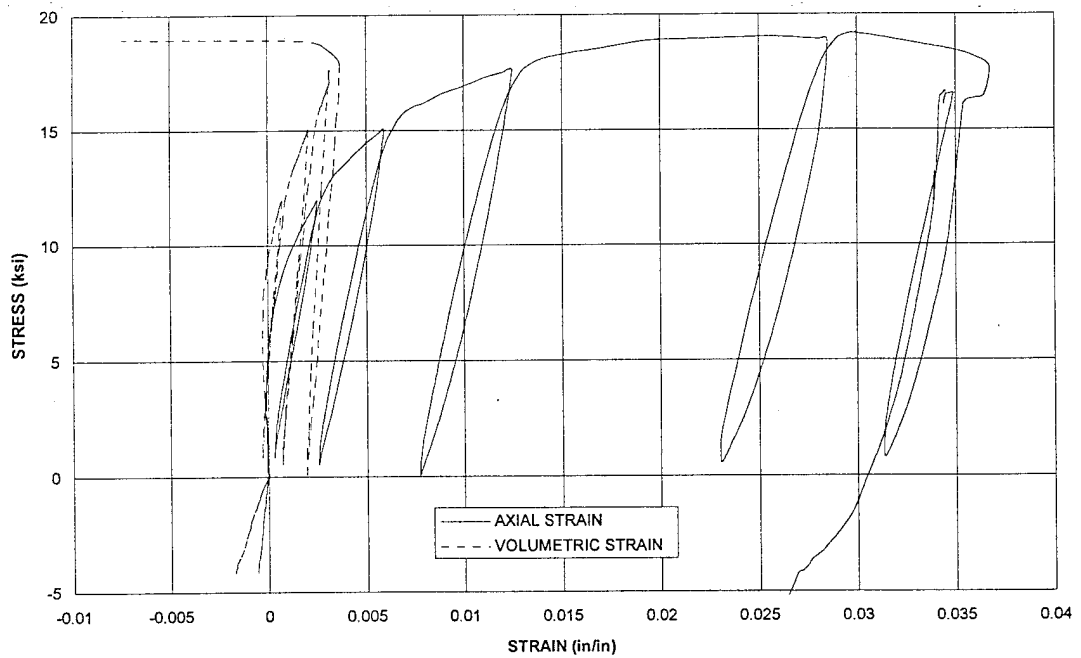
T25.3.17
STRESS vs STRAIN at MID HEIGHT

T25.3.17
STRESS vs STRAIN at SPECIMEN BOTTOM (END)

T25.3.18
STRESS vs STRAIN at MID HEIGHT
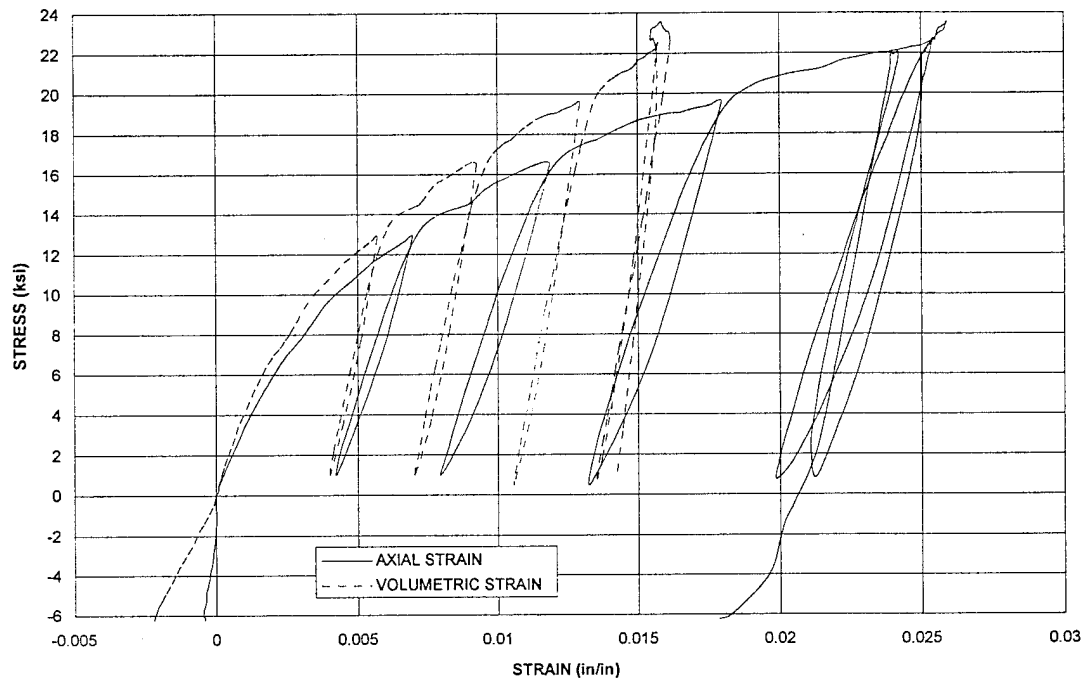
T25.3.18
STRESS vs STRAIN at SPECIMEN BOTTOM (END)
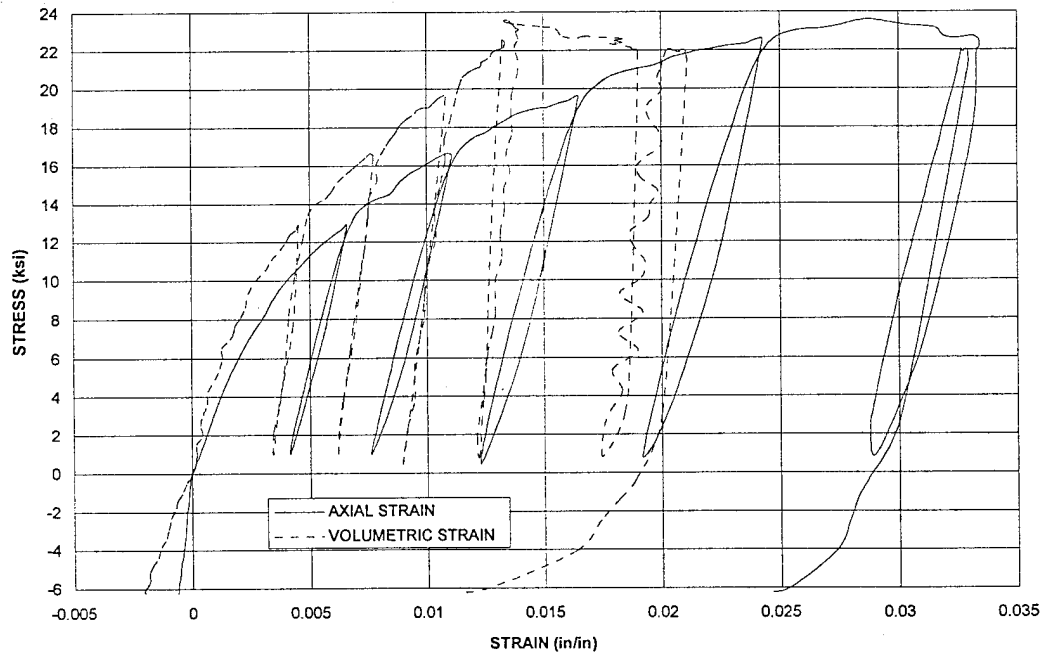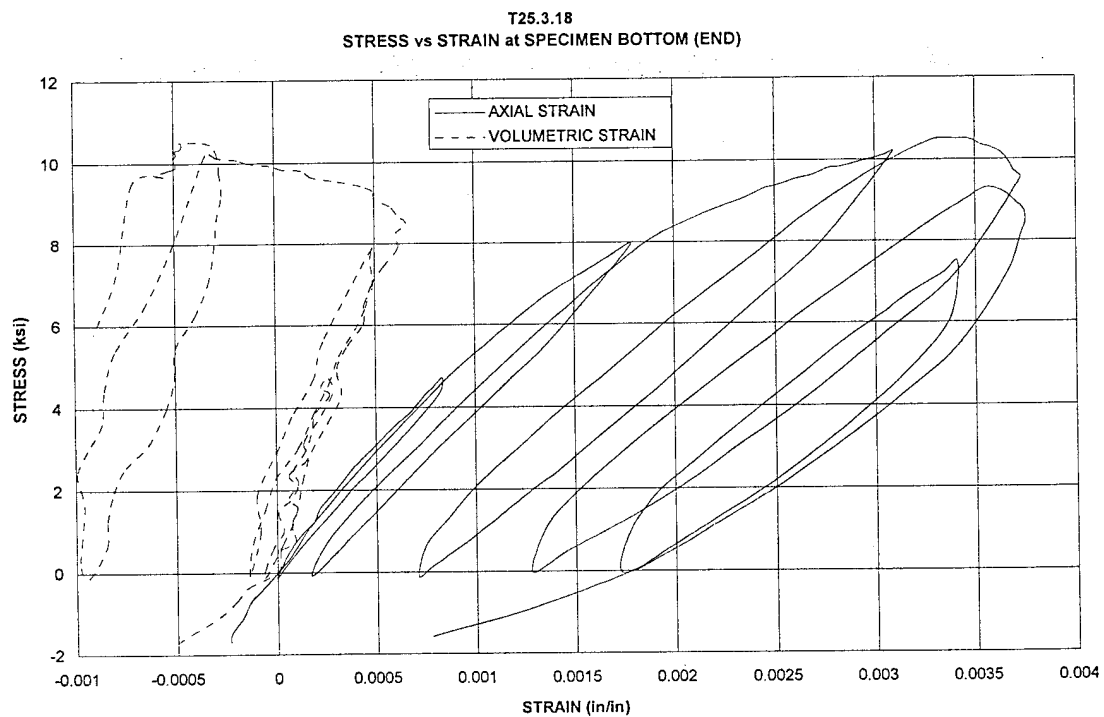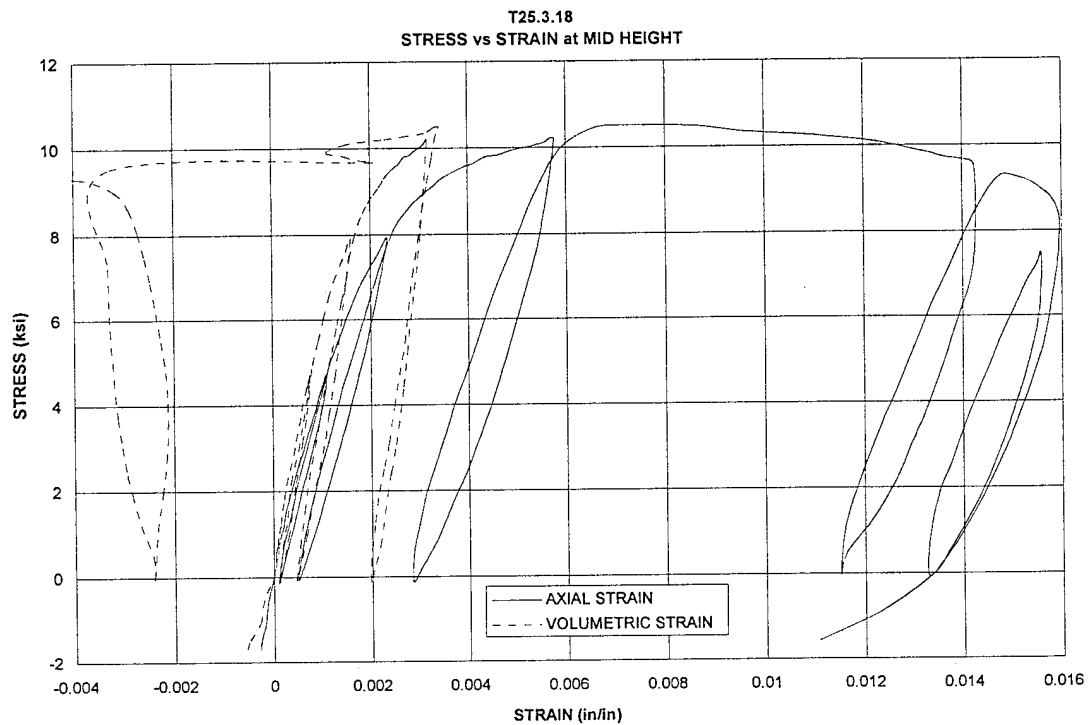
T25.3.21
STRESS vs STRAIN at MID HEIGHT
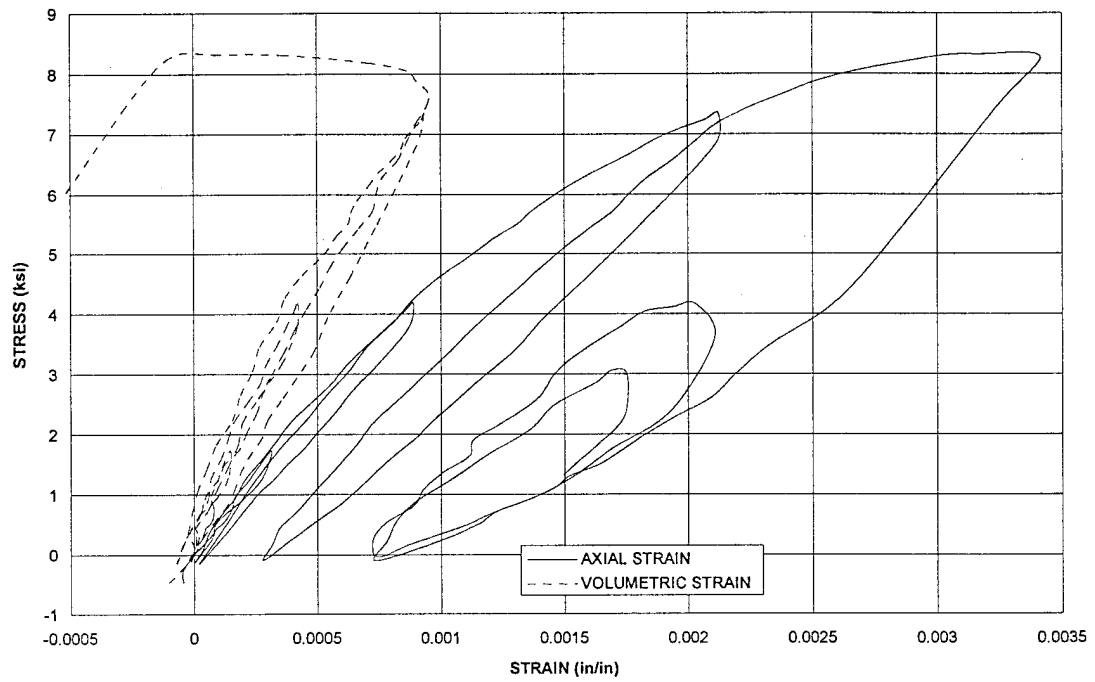
T25.3.21
STRESS vs STRAIN at SPECIMEN BOTTOM (END)
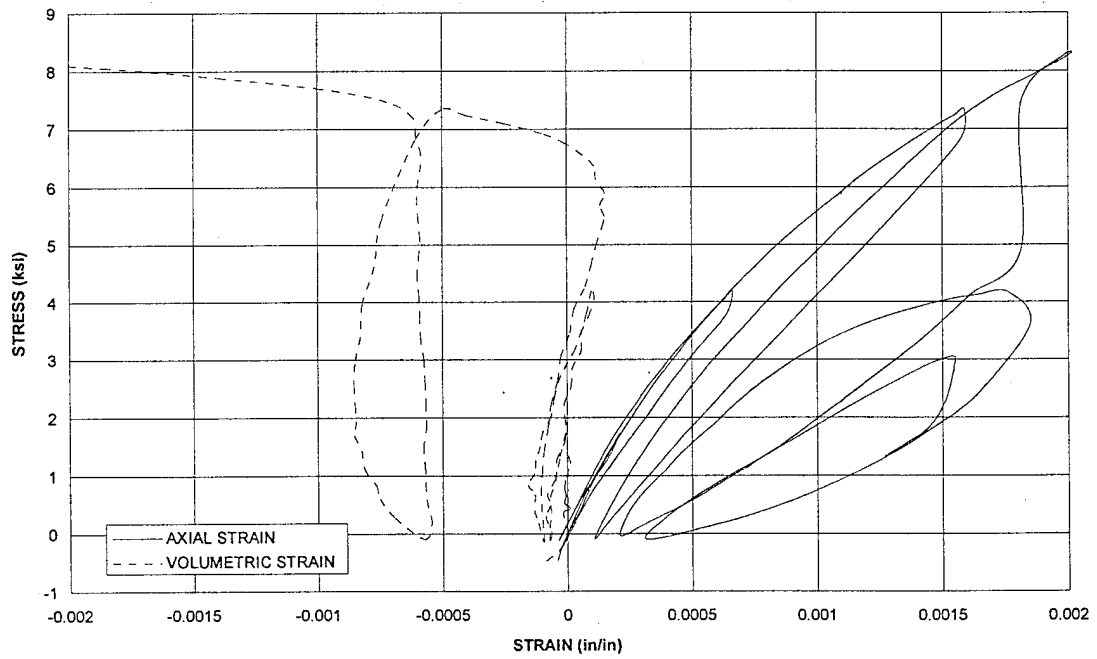
T25.3.22
STRESS vs STRAIN at MID HEIGHT

T25.3.22
STRESS vs STRAIN at SPECIMEN BOTTOM (END)

T25.4.6
STRESS vs STRAIN at MID HEIGHT
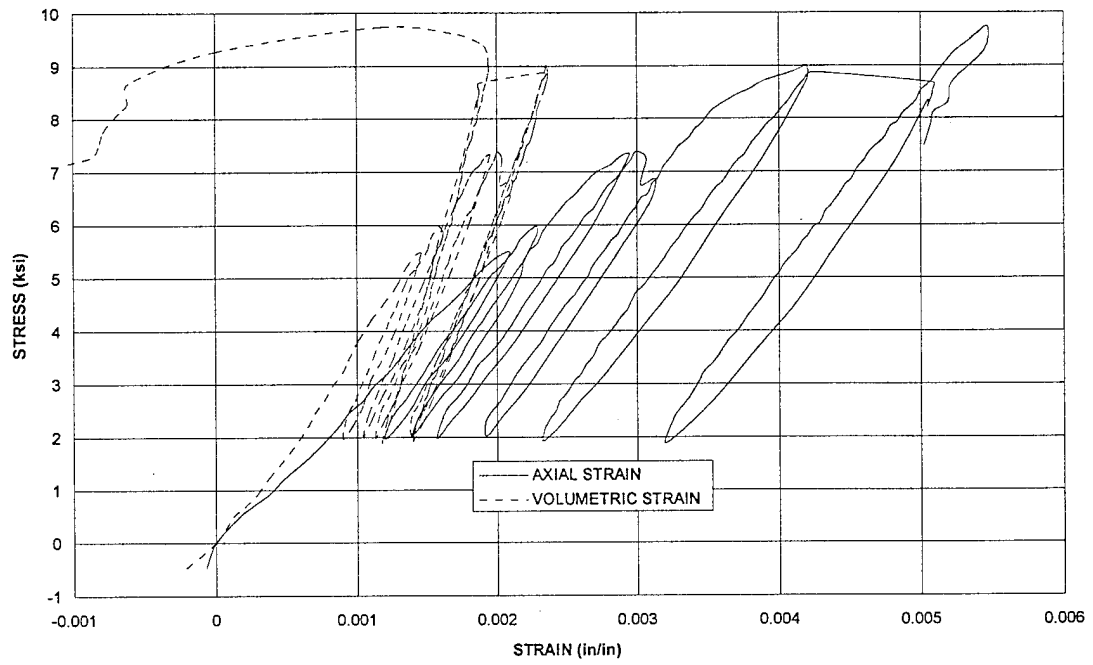
T25.4.6
STRESS vs STRAIN at SPECIMEN BOTTOM (END)
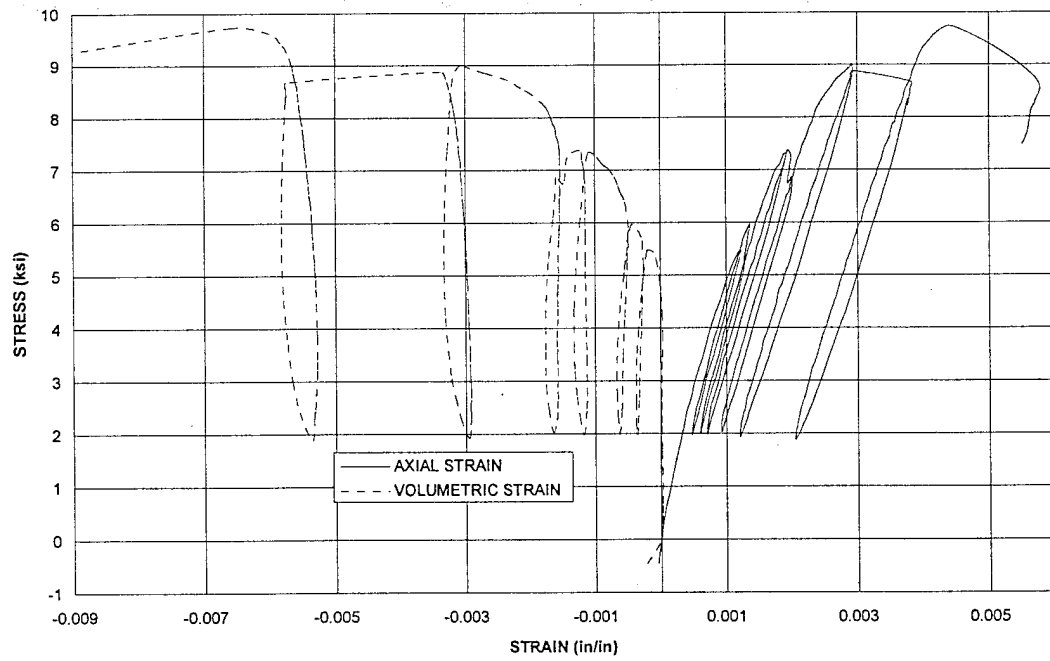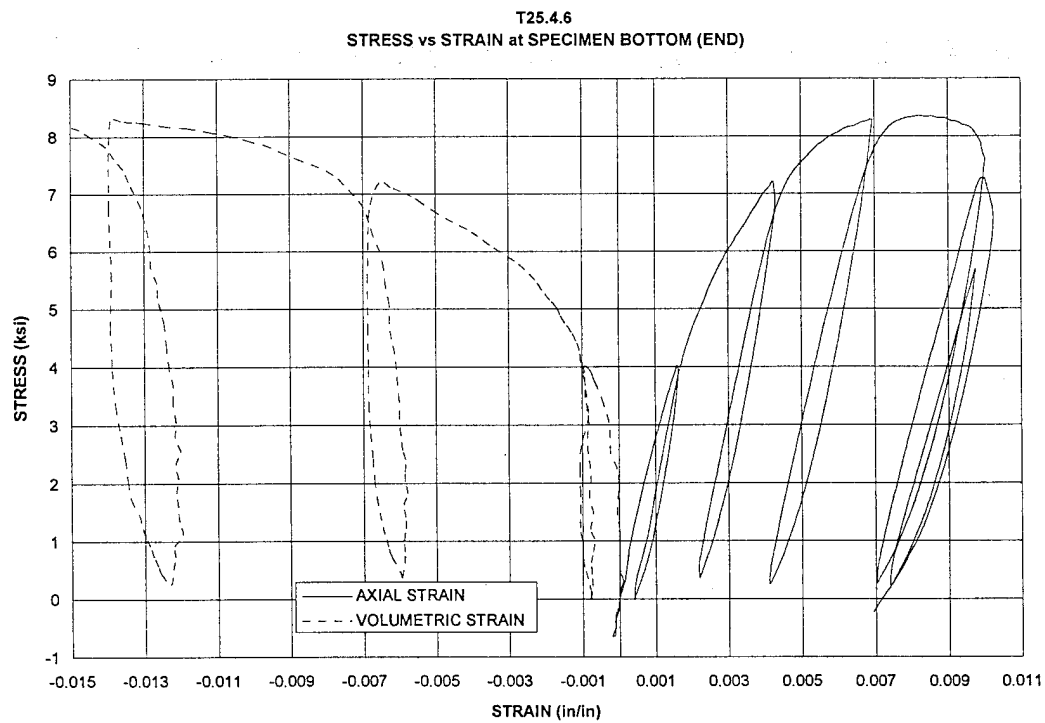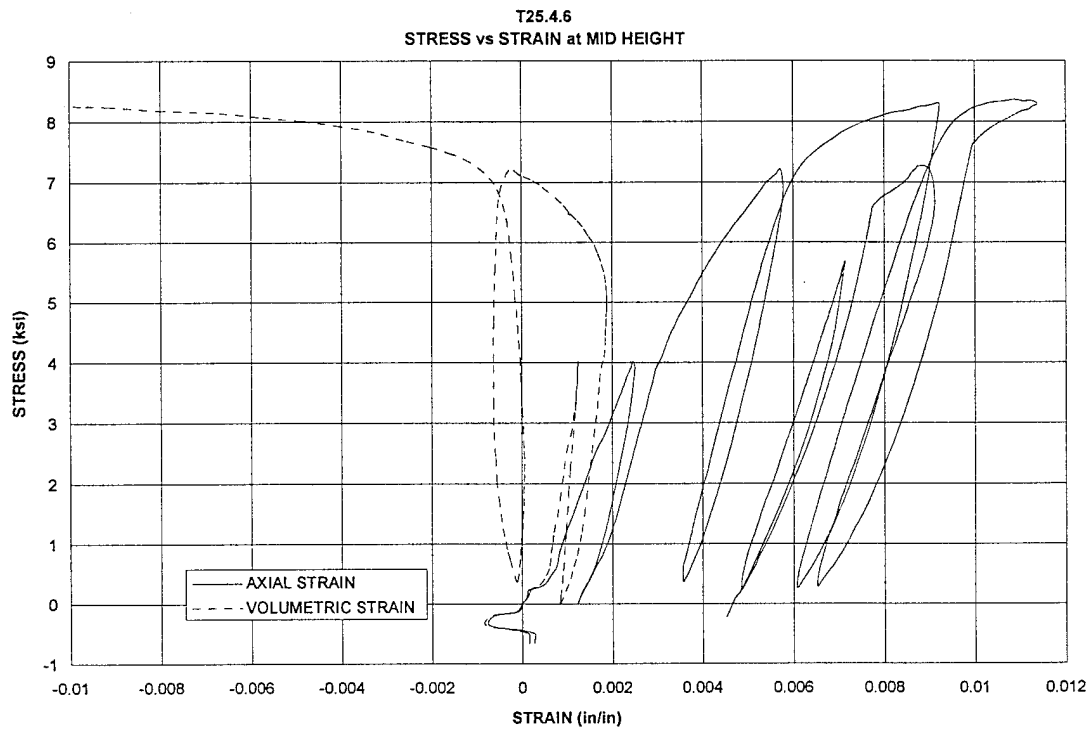
T25.4.7
STRESS vs STRAIN at MID HEIGHT

T25.4.7
STRESS vs STRAIN at SPECIMEN BOTTOM (END)

T25.4.8
STRESS vs STRAIN at MID HEIGHT

T25.4.8
STRESS vs STRAIN at SPECIMEN BOTTOM (END)

T25.4.15
STRESS vs STRAIN at MID HEIGHT

T25.4.15
STRESS vs STRAIN at SPECIMEN BOTTOM (END)

C-17

T25.4.16
STRESS vs STRAIN at MID HEIGHT

T25.4.16
STRESS vs STRAIN at SPECIMEN BOTTOM (END)

C-18
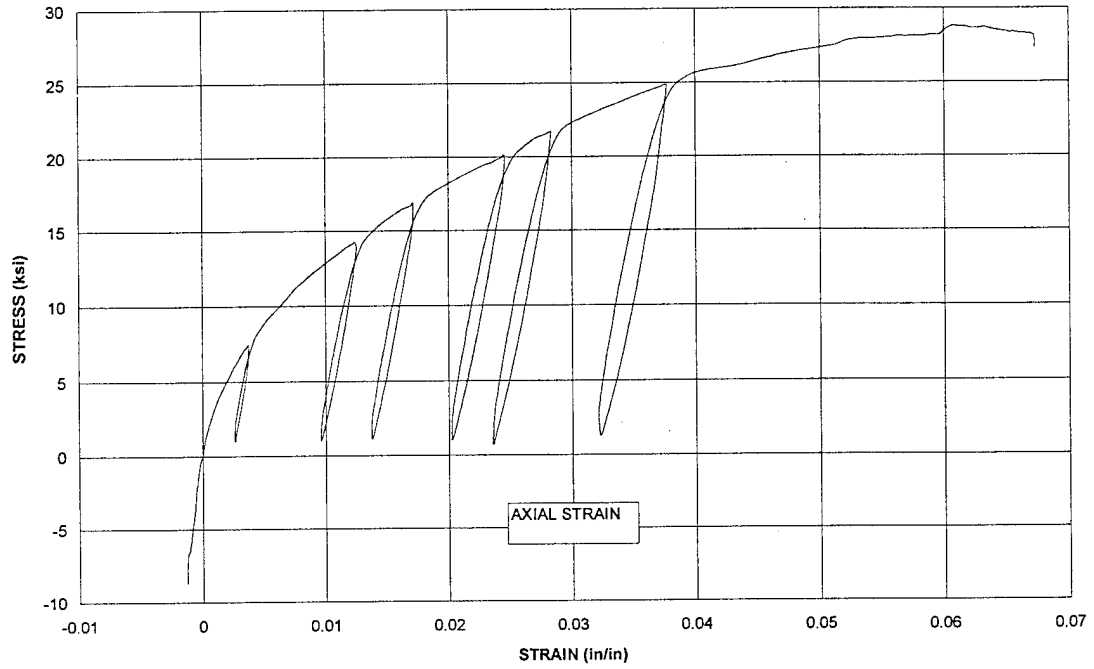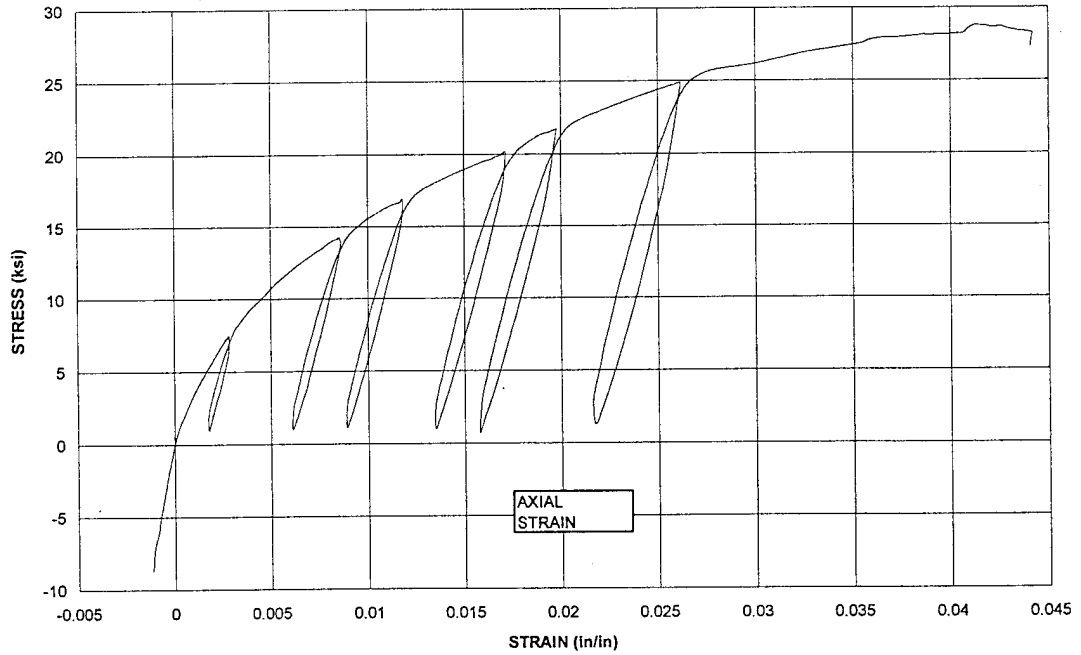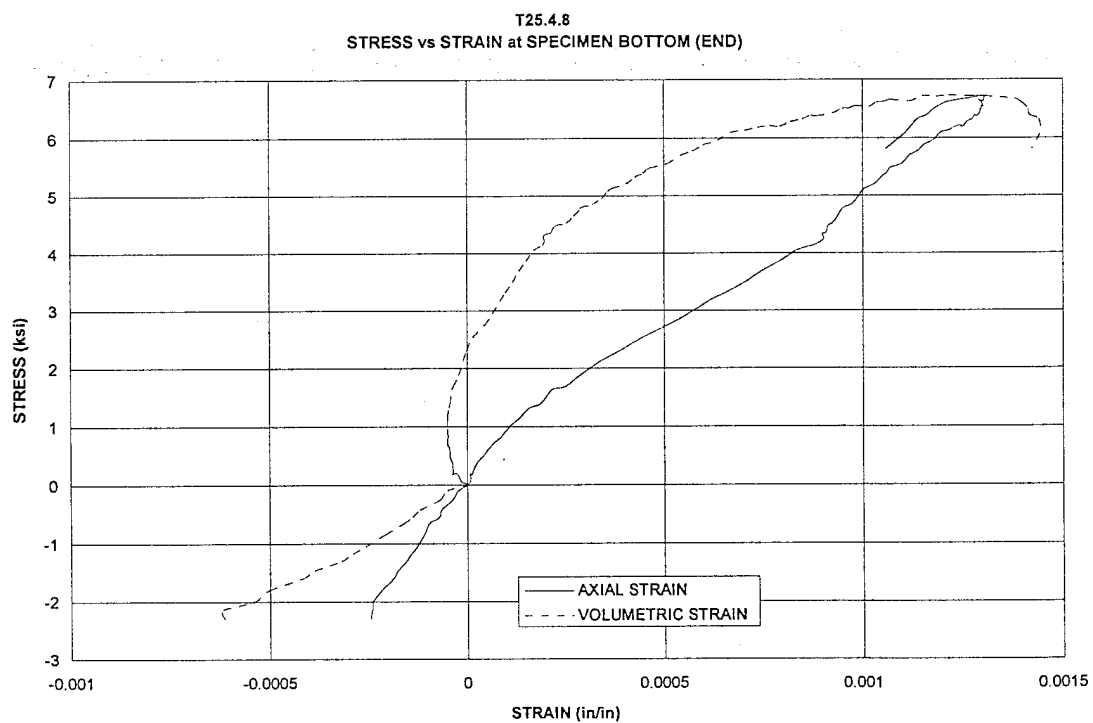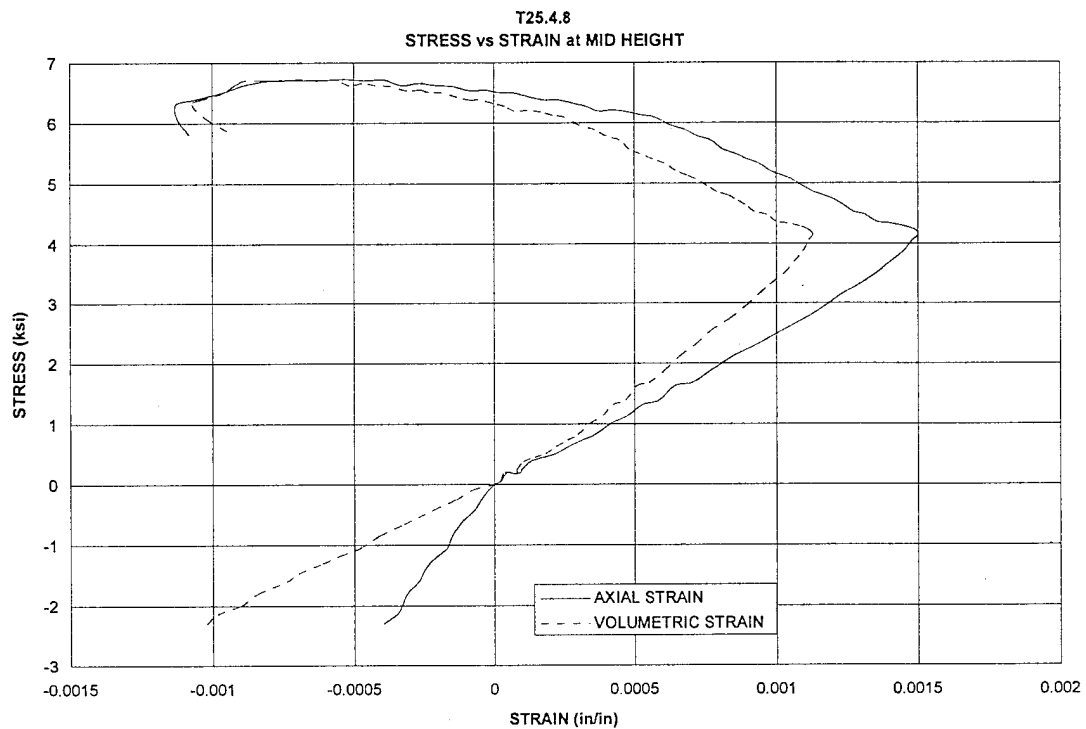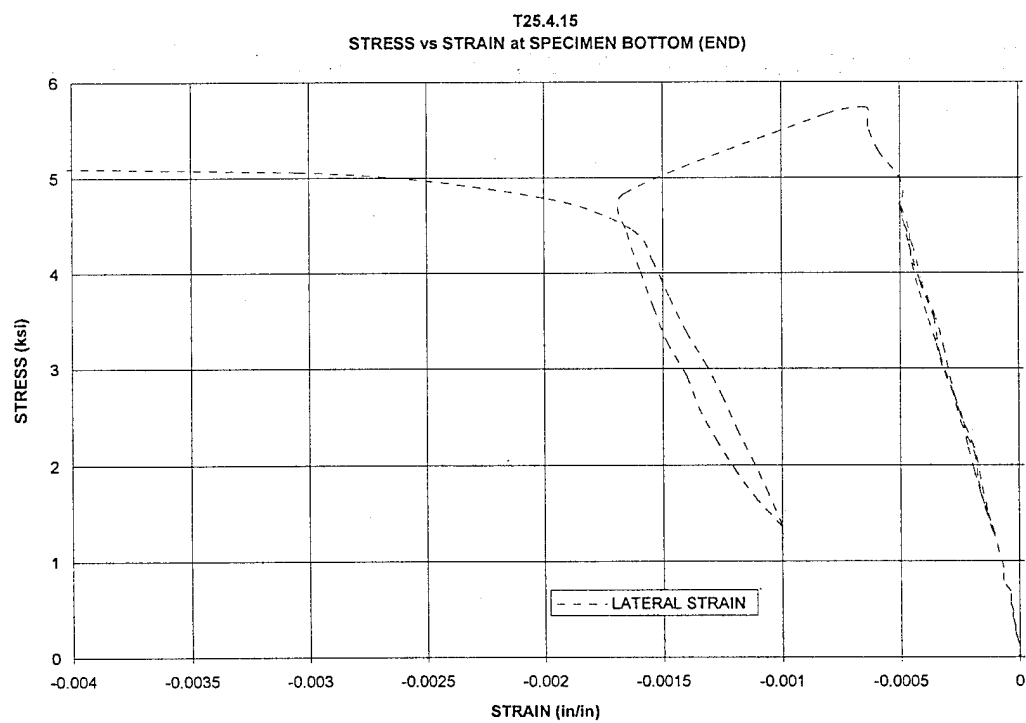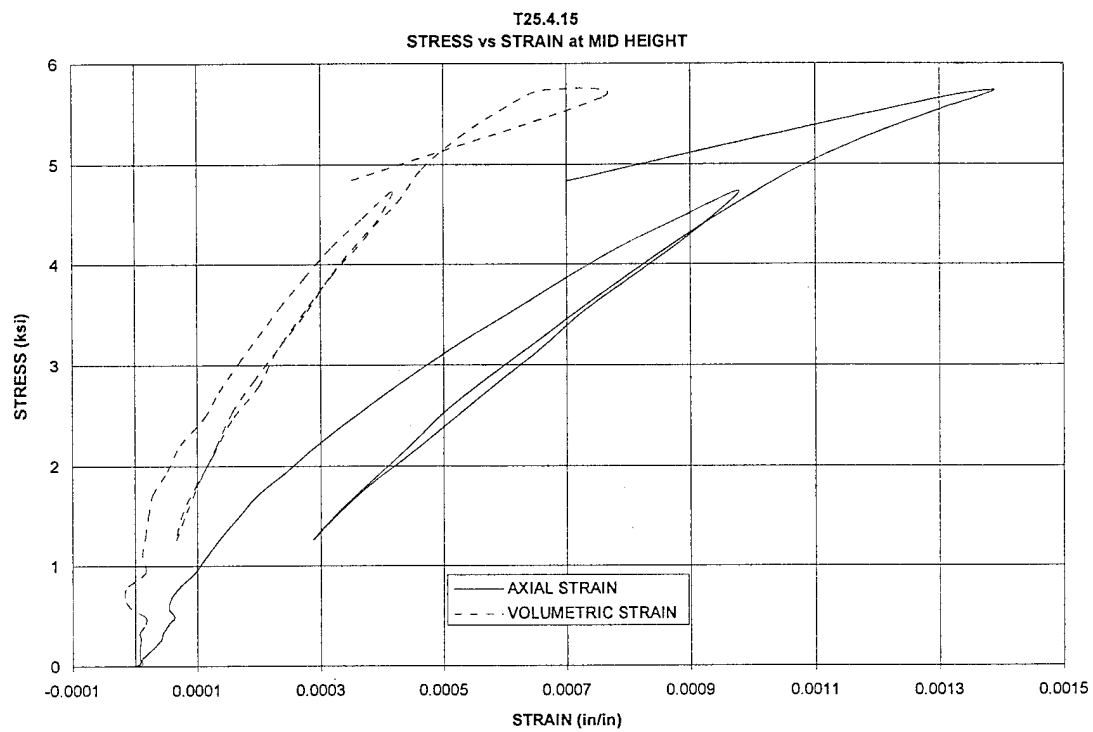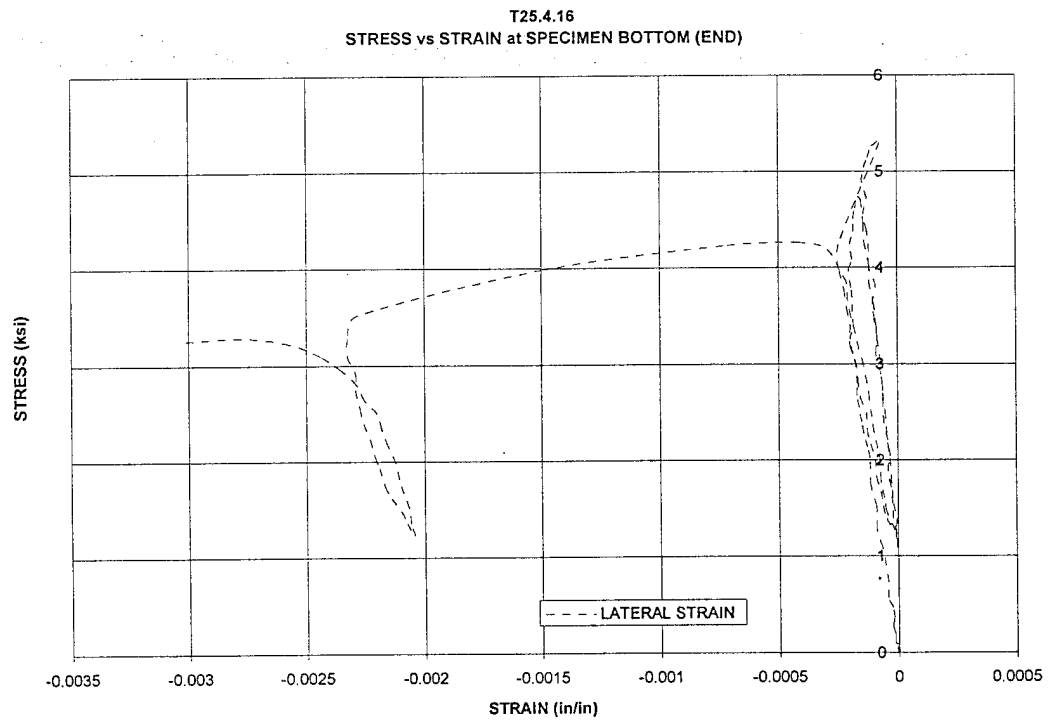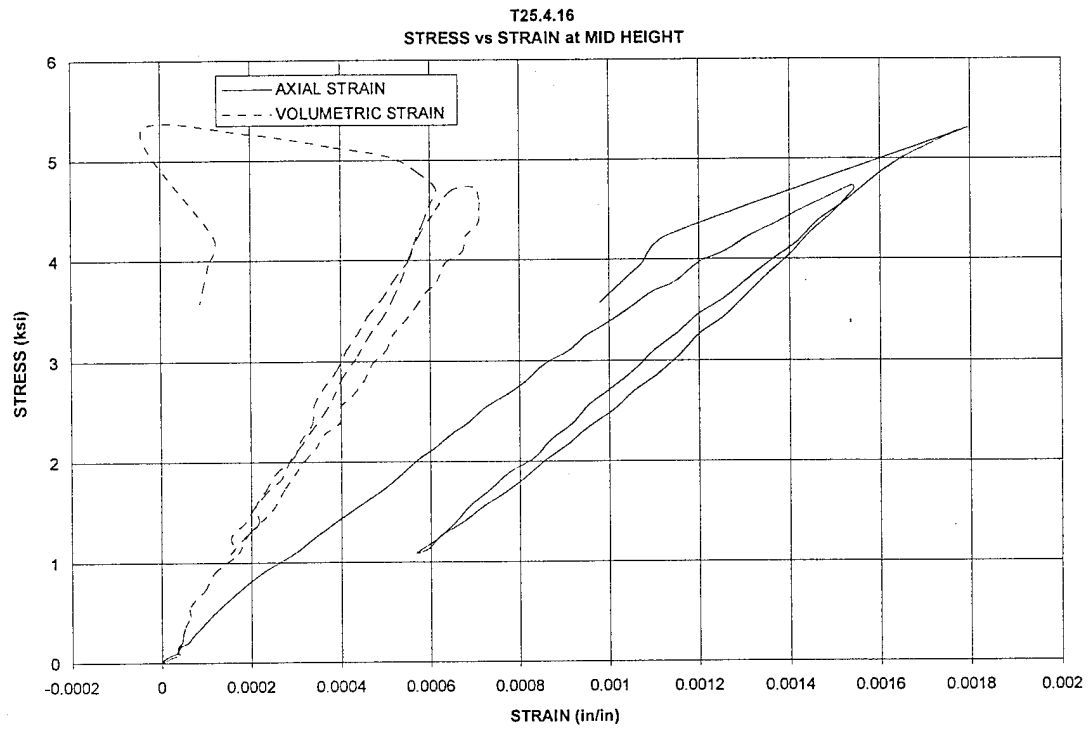
T25.4.18
STRESS vs STRAIN at MID HEIGHT
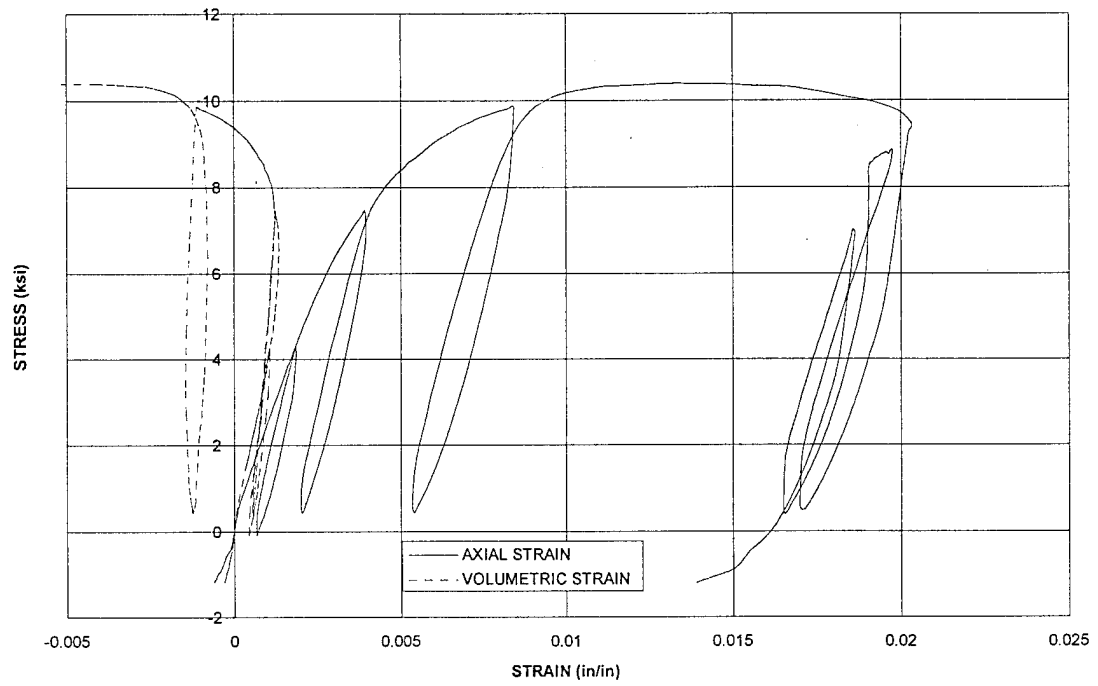
T25.4.18
STRESS vs STRAIN at SPECIMEN BOTTOM (END)
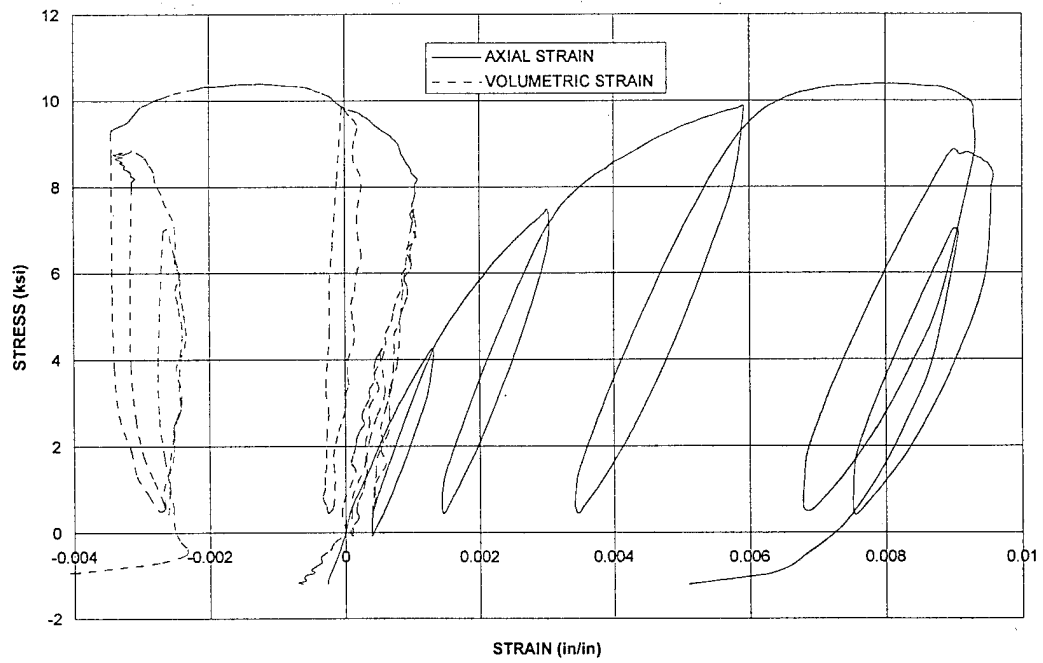
T25.4.19
STRESS vs STRAIN at MID HEIGHT

T25.4.19
STRESS vs STRAIN at SPECIMEN BOTTOM (END)

C-20
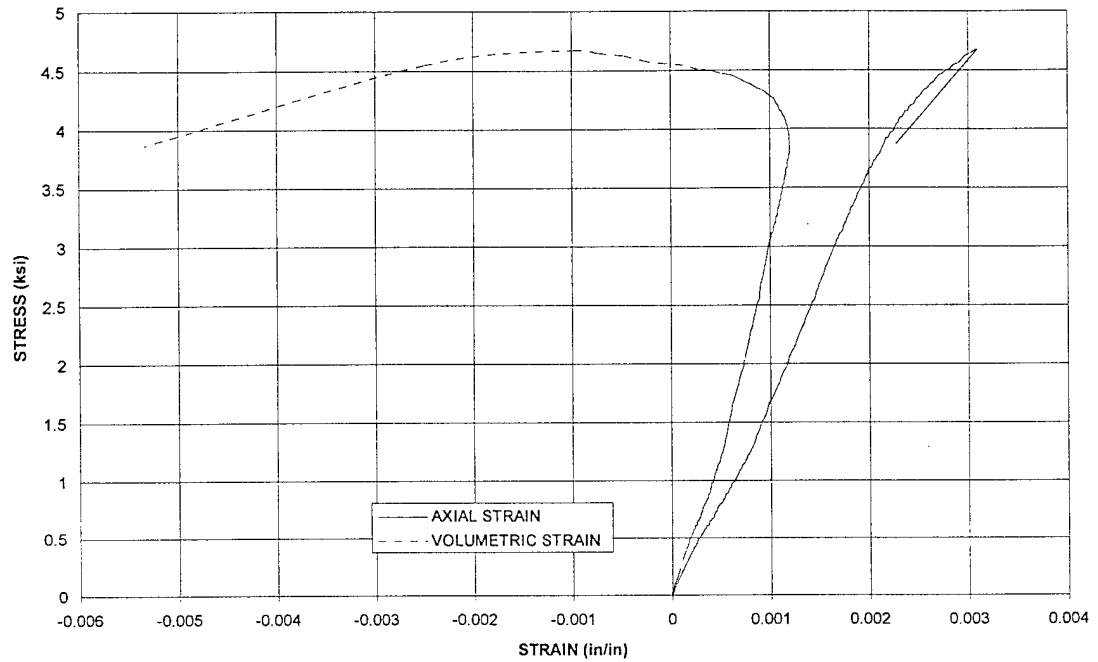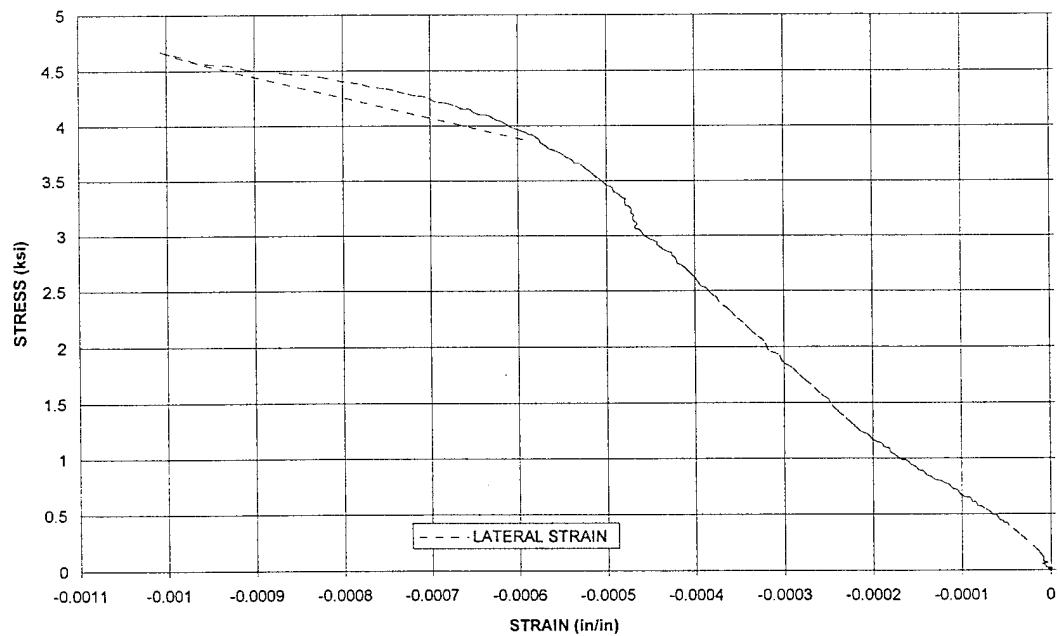
B3.1
STRESS vs STRAIN at MID HEIGHT

B3.1
STRESS vs STRAIN at SPECIMEN BOTTOM (END)

C-21
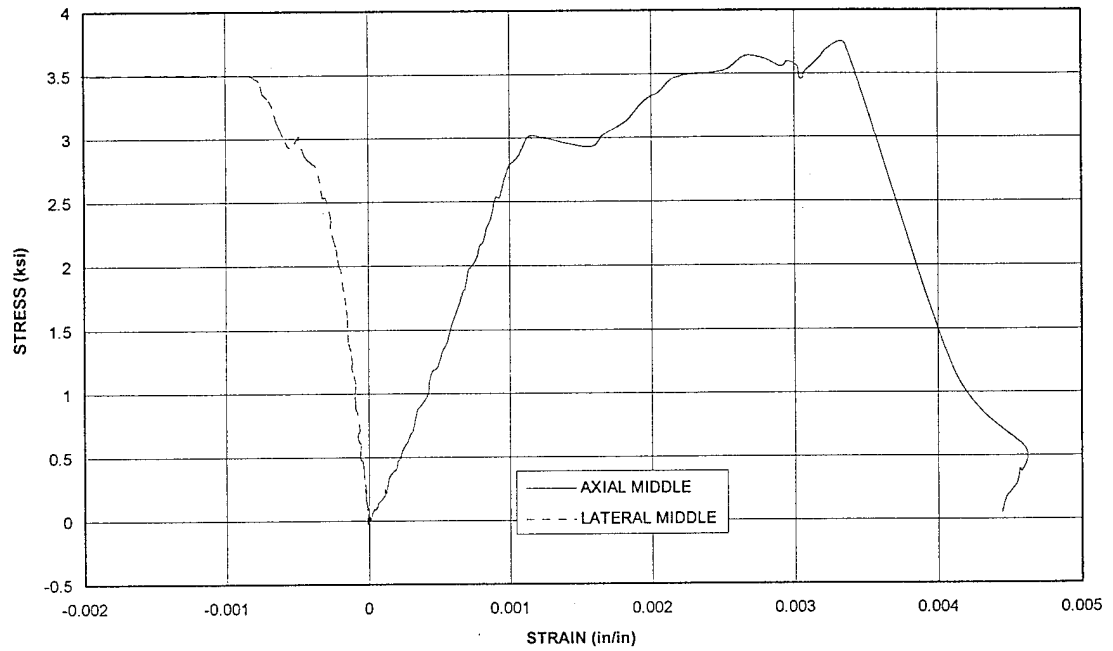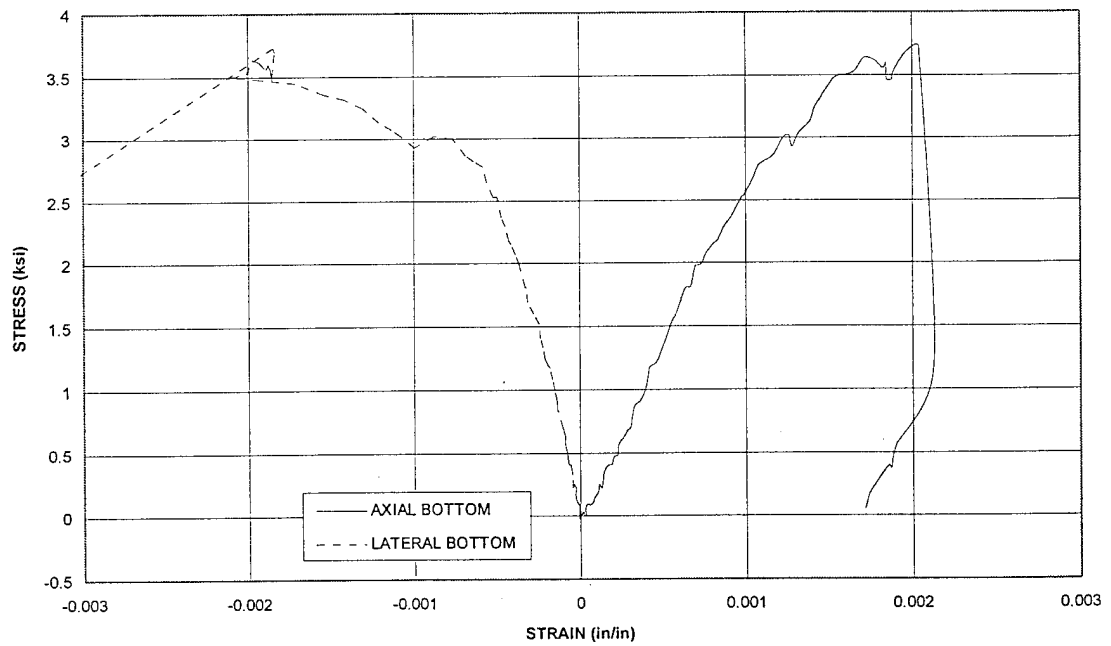
APPENDIX D

GAUGE STRAIN VERSUS DISPLACEMENT STRAIN CURVES

The following pages contain plots of the strain measured from the strain gauges versus the axial strains calculated from the axial displacement. If the gauge broke or malfunctioned then the data is not shown. For each test the curves for the axial gauges located at the top of the page while the curves for the bottom (end) gauges are located at the bottom of the page. The tests for which curves are presented are listed below with the corresponding page where the graph can be found.

T25.2.13
GAUGE STRAIN vs DISPL STRAIN

T25.2.13
GAUGE STRAIN vs DISPL STRAIN

D-2

T25.2.15
GAUGE STRAIN vs DISPL STRAIN

T25.2.15
GAUGE STRAIN vs DISPL STRAIN

T25.2.16
GAUGE STRAIN vs DISPL STRAIN

T25.2.16
GAUGE STRAIN vs DISPL STRAIN

T25.2.17
GAUGE STRAIN vs DISPL STRAIN

T25.2.17
GAUGE STRAIN vs DISPL STRAIN

T25.2.19
GAUGE STRAIN vs DISPL STRAIN

T25.2.19
GAUGE STRAIN vs DISPL STRAIN

T25.2.23
GAUGE STRAIN vs DISPL STRAIN

T25.2.23
GAUGE STRAIN vs DISPL STRAIN

T25.3.13
GAUGE STRAIN vs DISPL STRAIN

T25.3.13
GAUGE STRAIN vs DISPL STRAIN

T25.3.15
GAUGE STRAIN vs DISPL STRAIN

T25.3.15
GAUGE STRAIN vs DISPL STRAIN

T25.3.17
GAUGE STRAIN vs DISPL STRAIN

T25.3.17
GAUGE STRAIN vs DISPL STRAIN

T25.3.18
GAUGE STRAIN vs DISPL STRAIN

T25.3.18
GAUGE STRAIN vs DISPL STRAIN

D-11

T25.3.21
GAUGE STRAIN vs DISPL STRAIN

T25.3.21
GAUGE STRAIN vs DISPL STRAIN
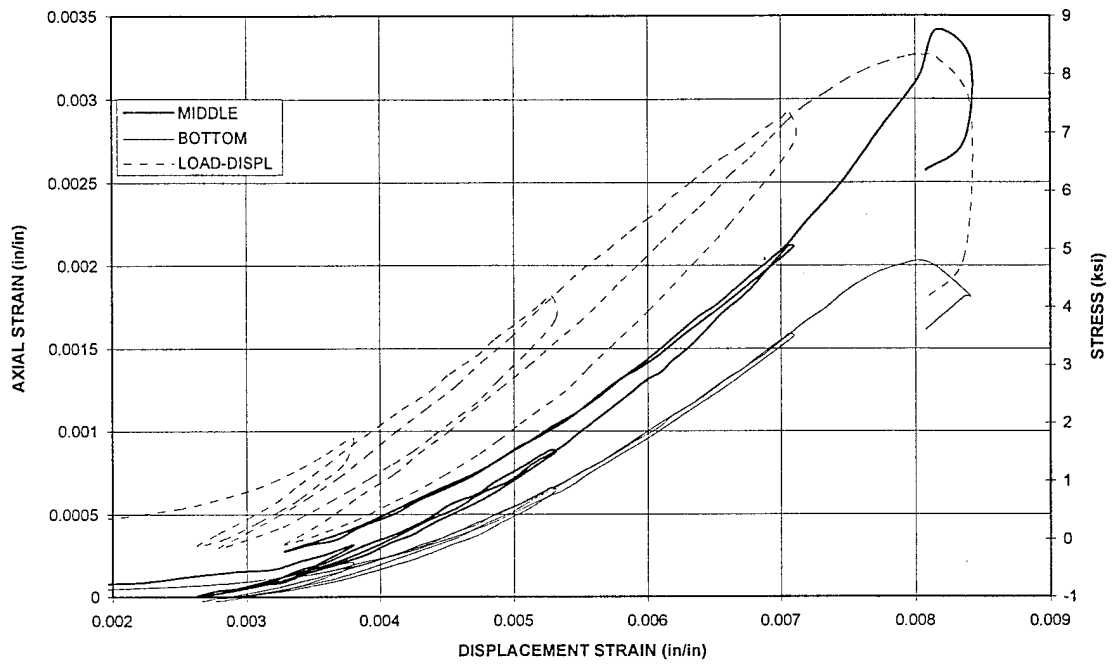
T25.3.22
GAUGE STRAIN vs DISPL STRAIN

T25.3.22
GAUGE STRAIN vs DISPL STRAIN

D-13
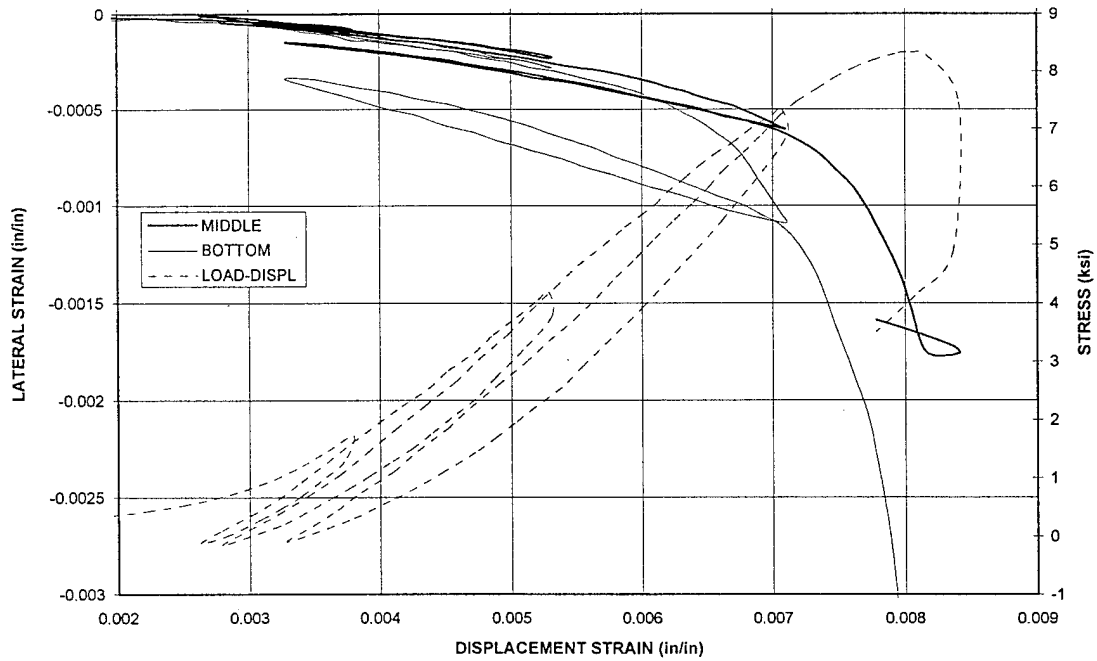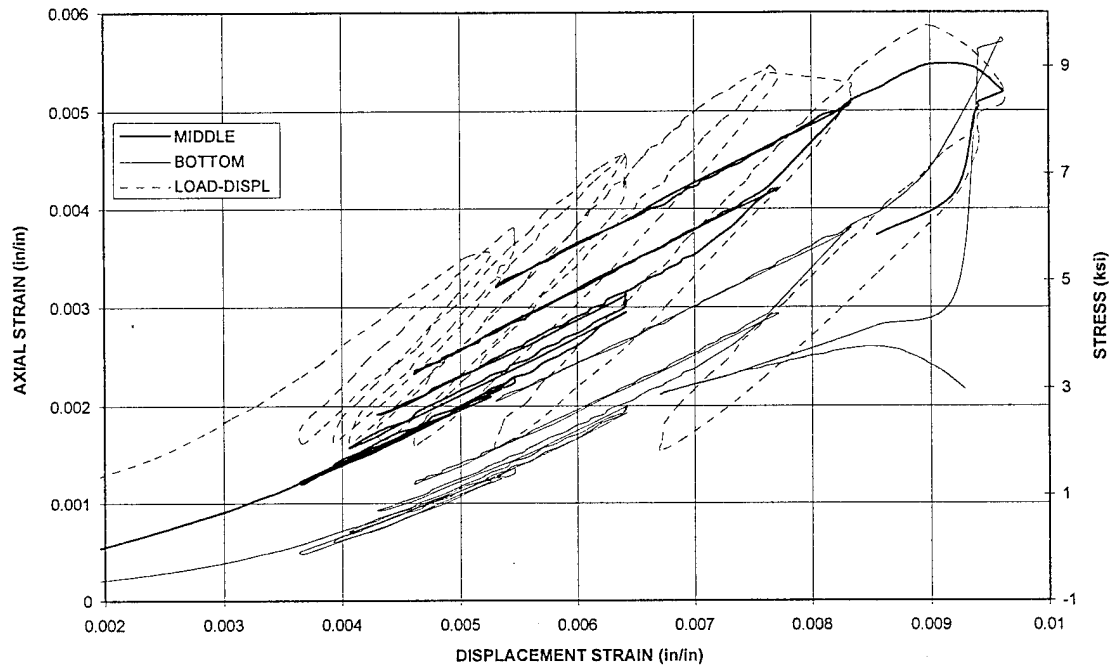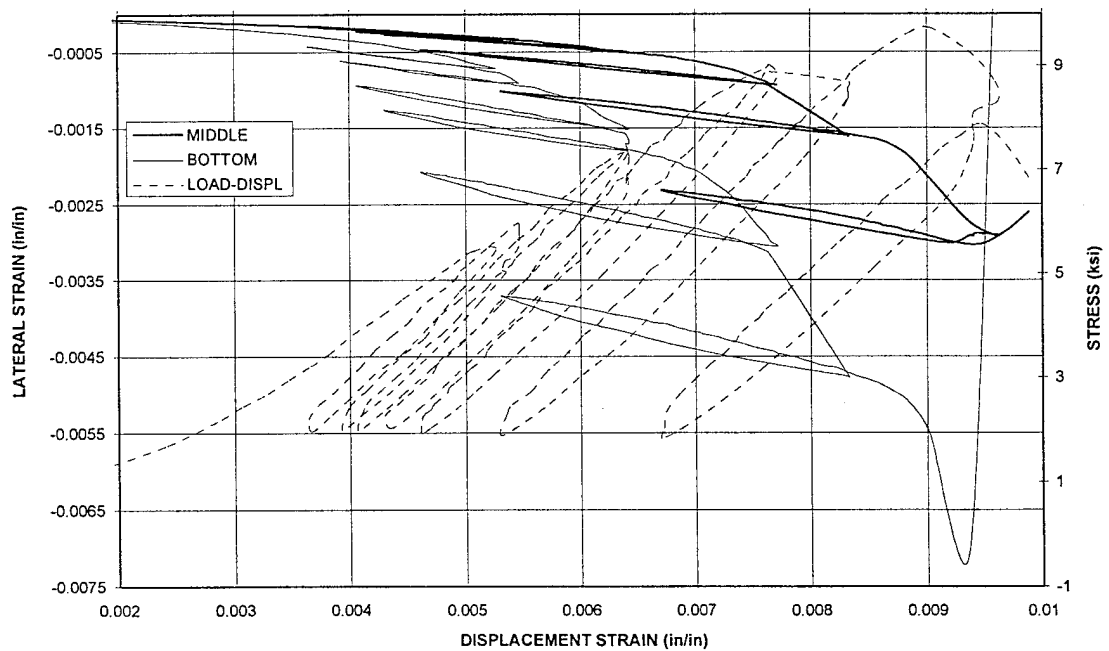
T25.4.6
GAUGE STRAIN vs DISPL STRAIN

T25.4.6
GAUGE STRAIN vs DISPL STRAIN
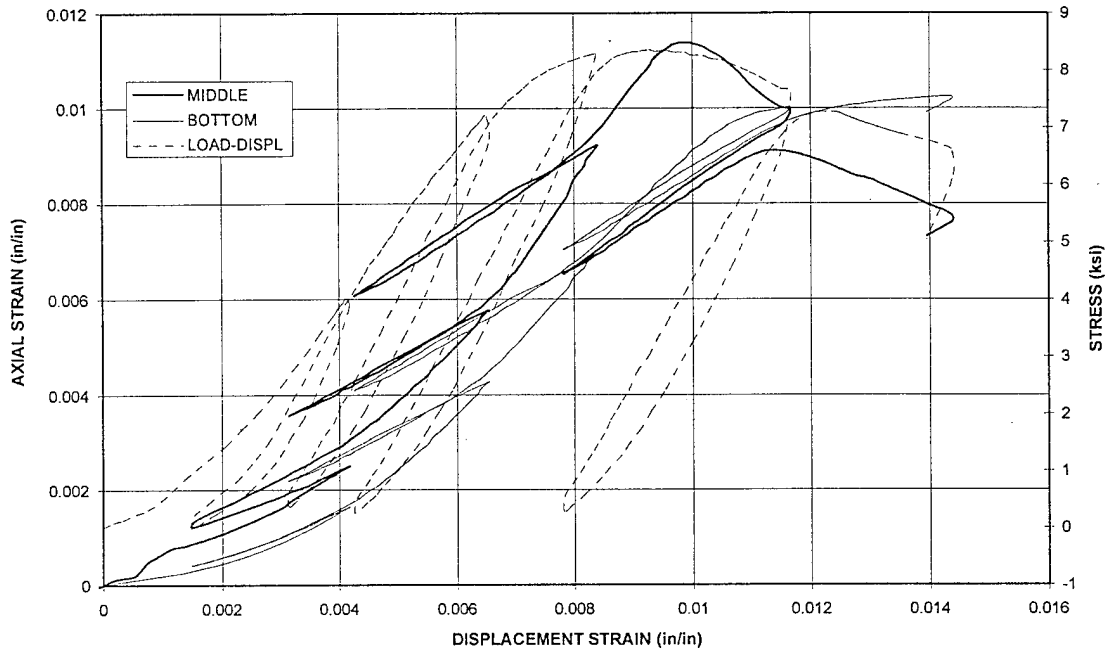
T25.4.7
GAUGE STRAIN vs DISPL STRAIN
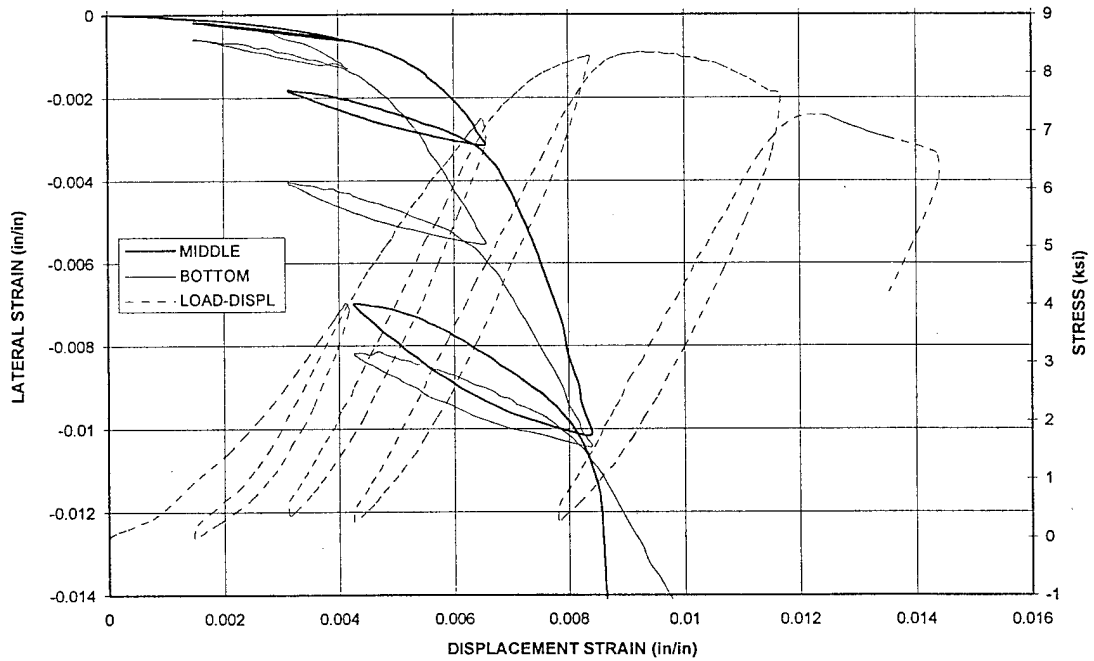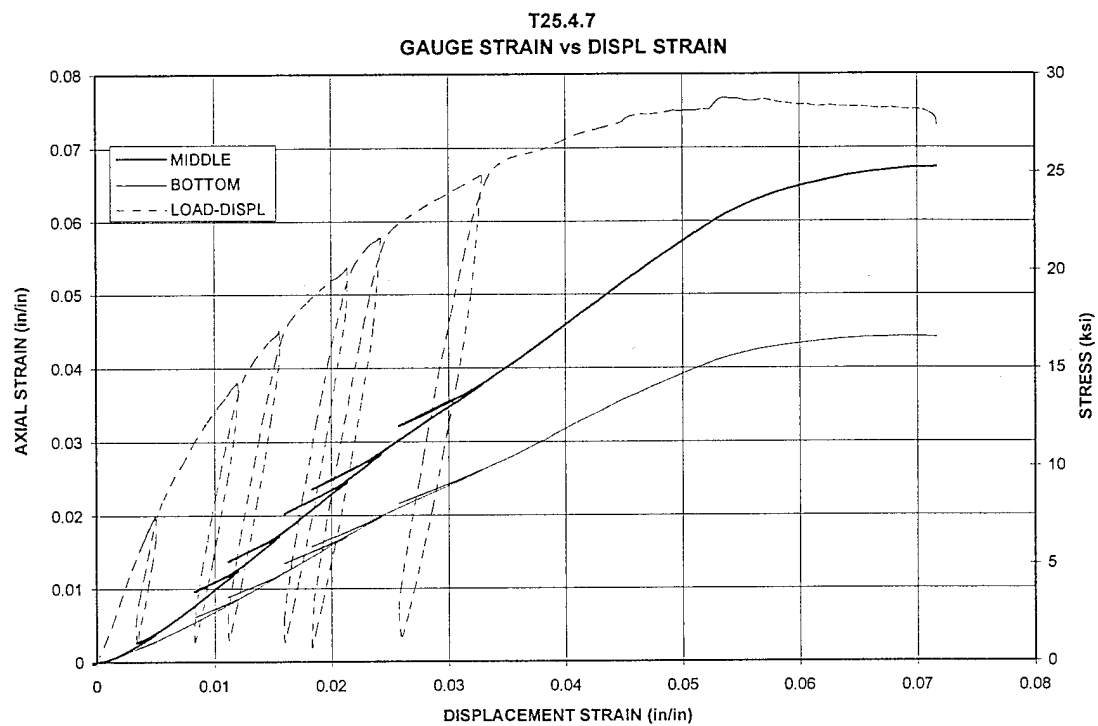
LATERAL GAUGES MALFUNCTIONED

T25.4.8
GAUGE STRAIN vs DISPL STRAIN

T25.4.8
GAUGE STRAIN vs DISPL STRAIN

T25.4.15
GAUGE STRAIN vs DISPL STRAIN

T25.4.15
GAUGE STRAIN vs DISPL STRAIN

D-17

T25.4.16
GAUGE STRAIN vs DISPL STRAIN

T25.4.16
GAUGE STRAIN vs DISPL STRAIN

T25.4.18
GAUGE STRAIN vs DISPL STRAIN

T25.4.18
GAUGE STRAIN vs DISPL STRAIN

D-19
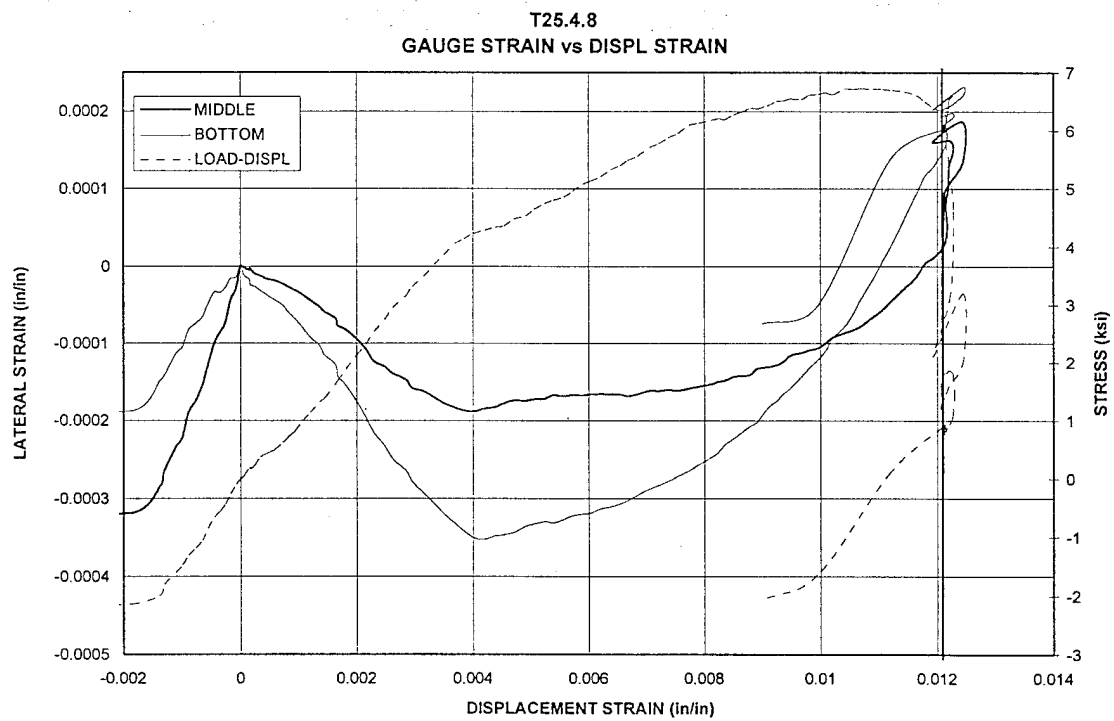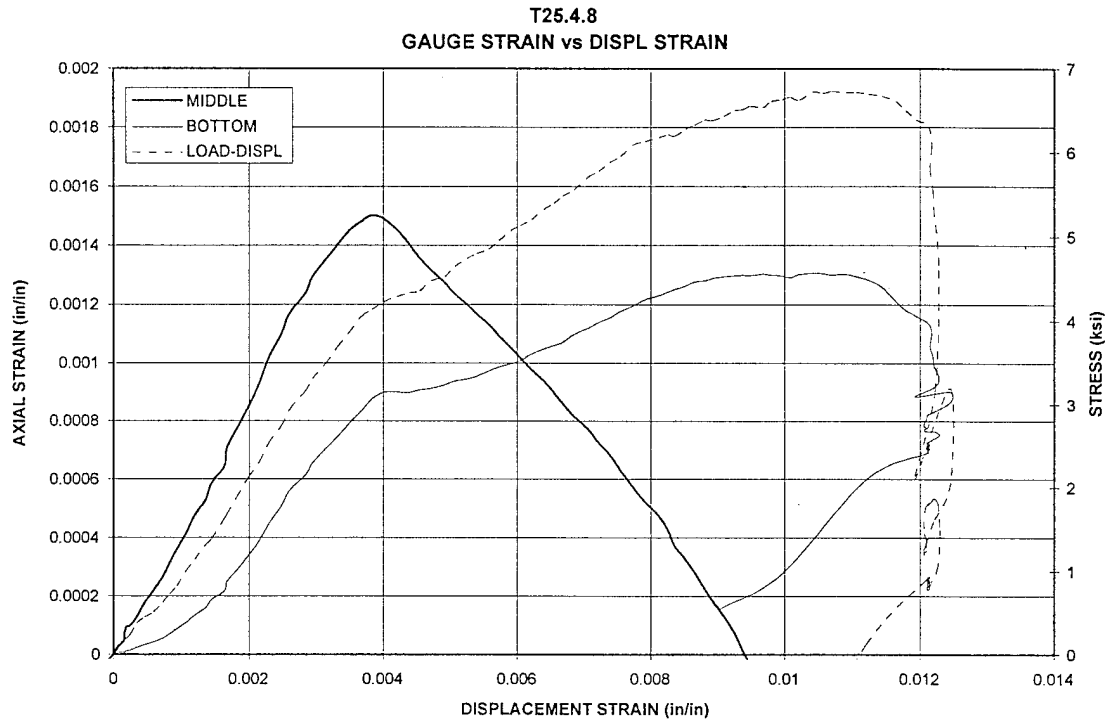
T25.4.19
GAUGE STRAIN vs DISPL STRAIN
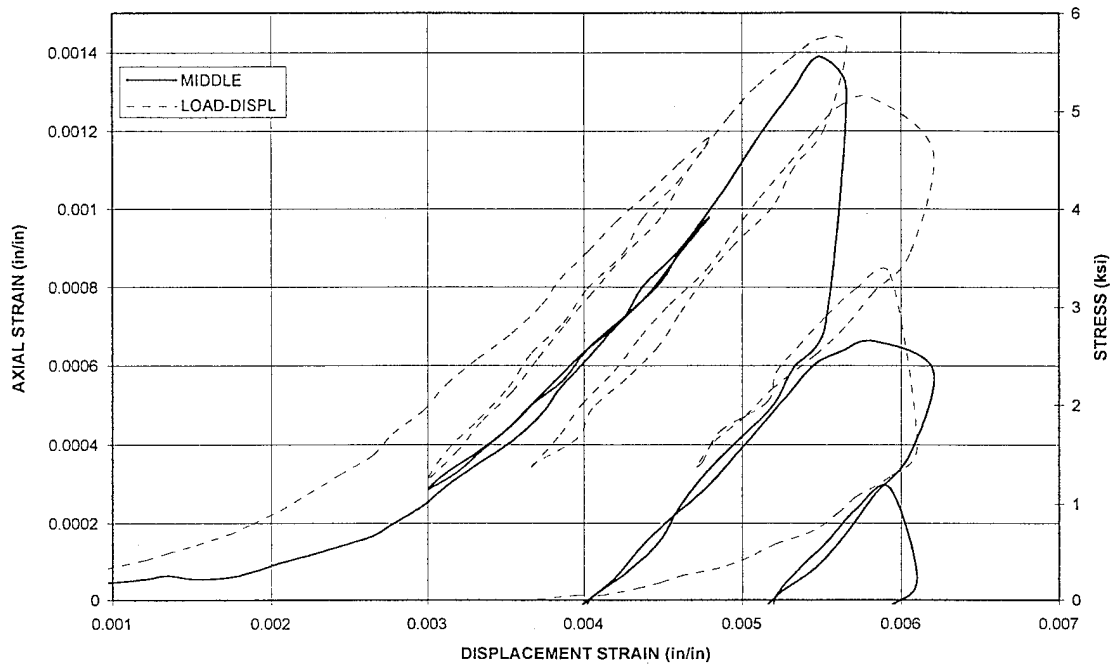
T25.4.19
GAUGE STRAIN vs DISPL STRAIN
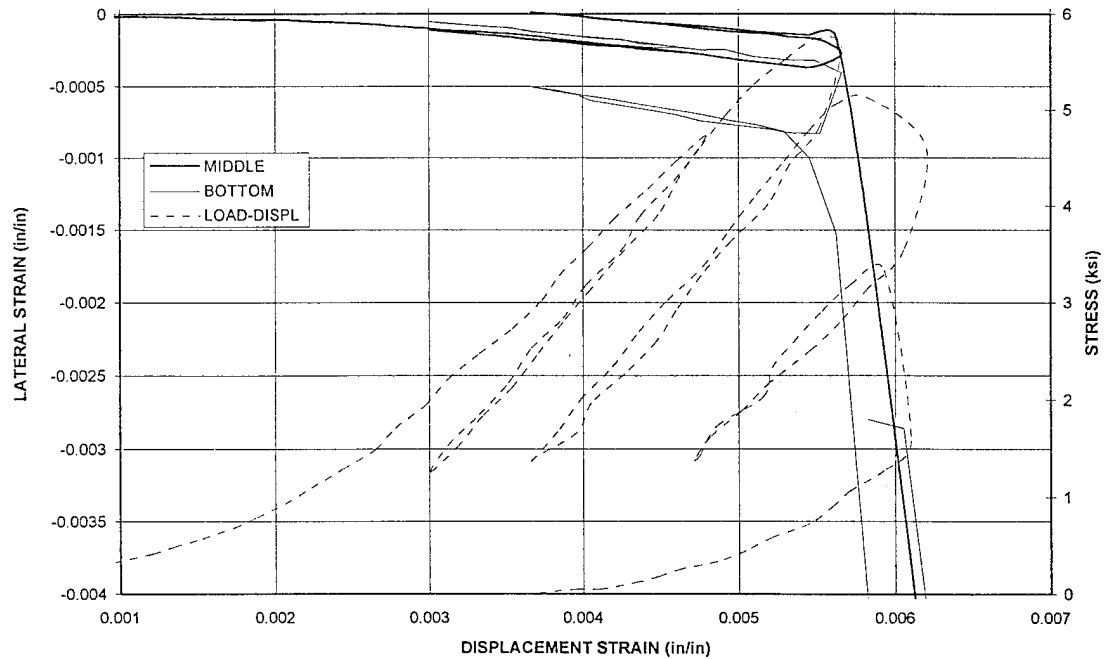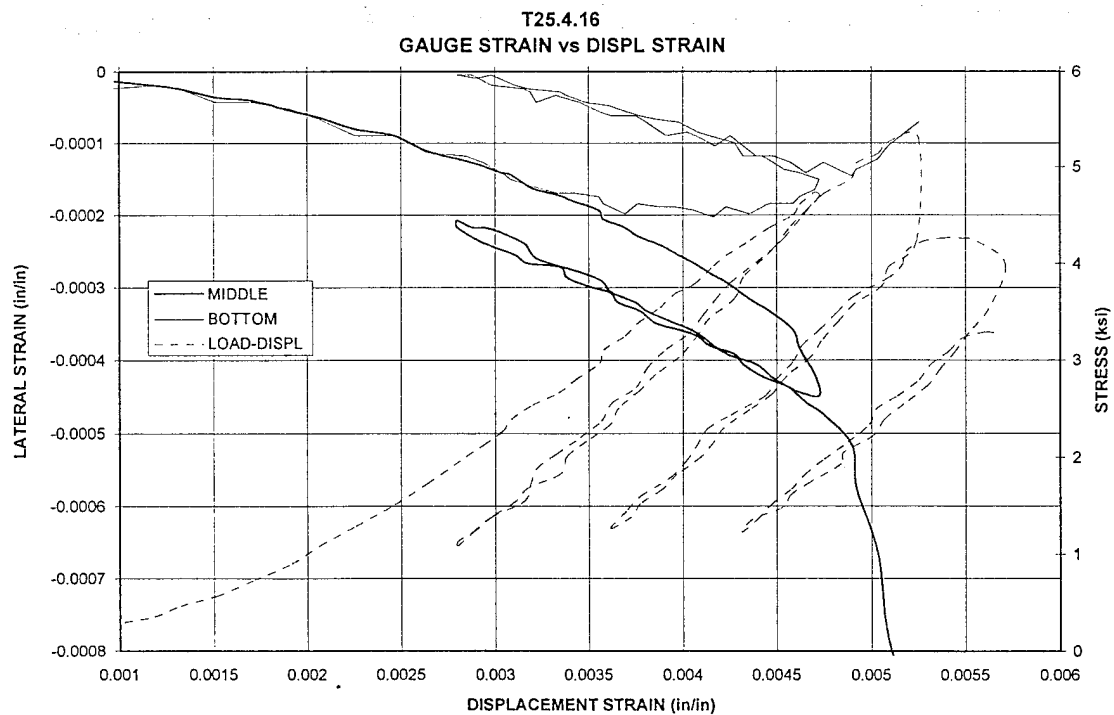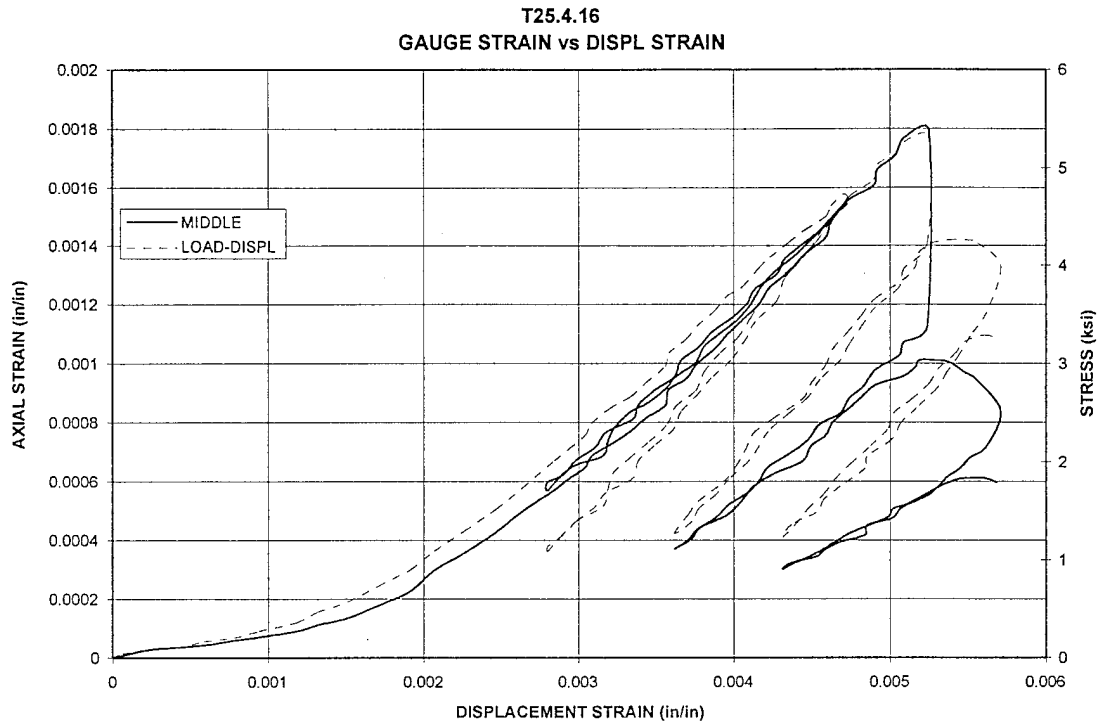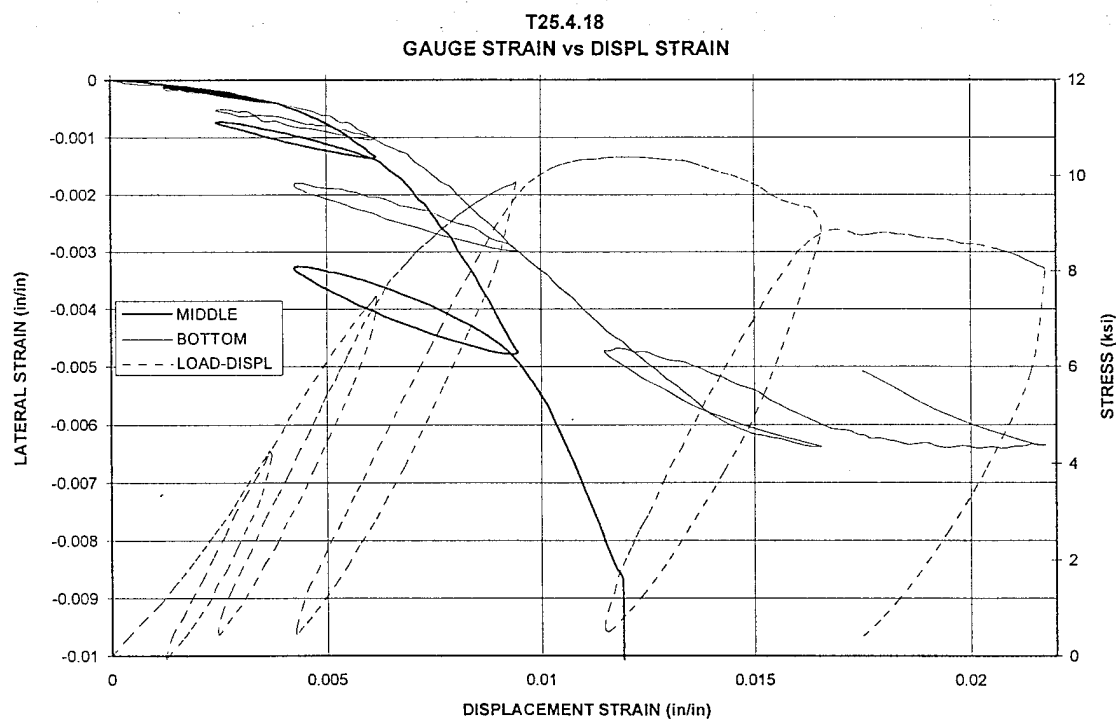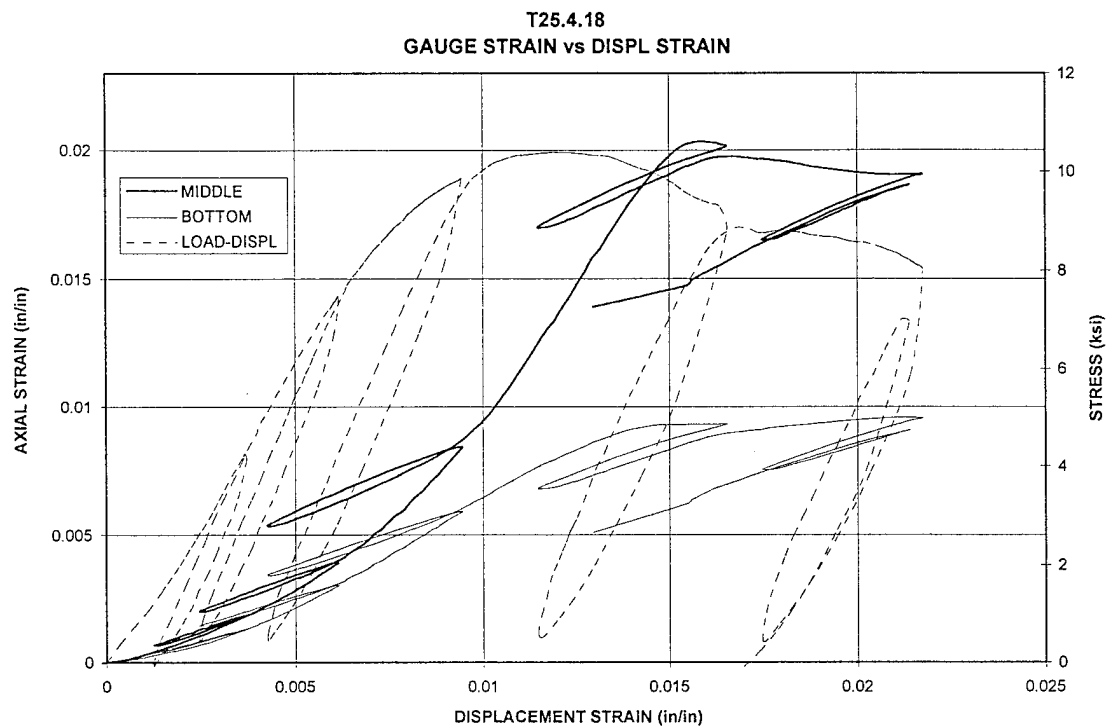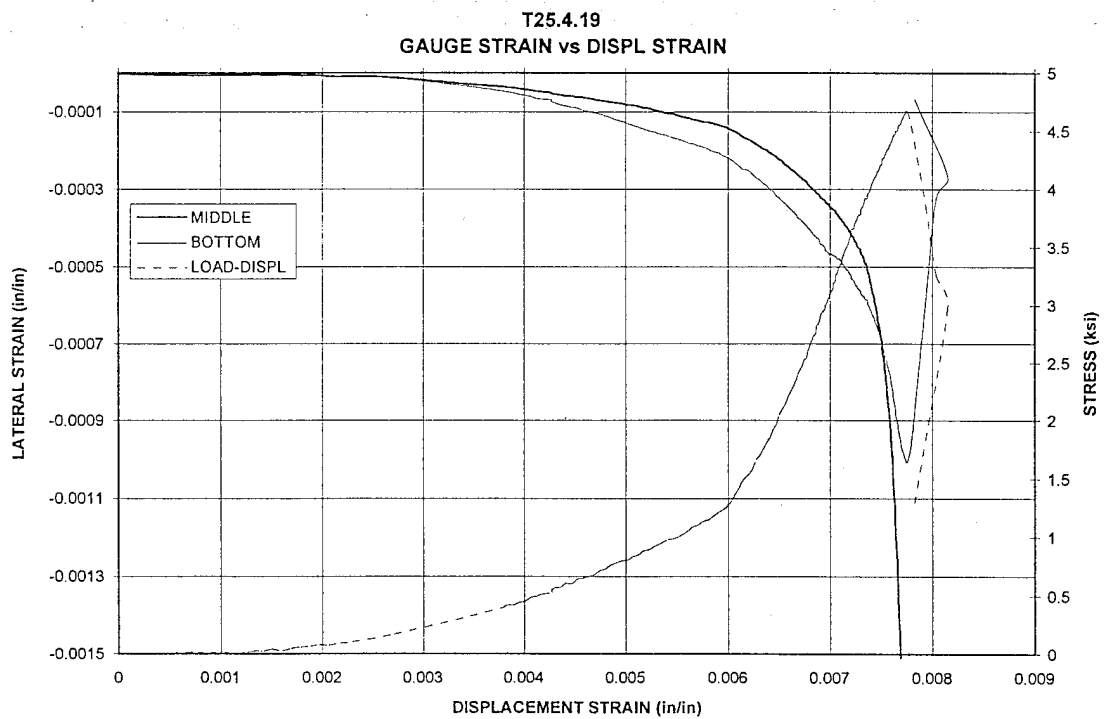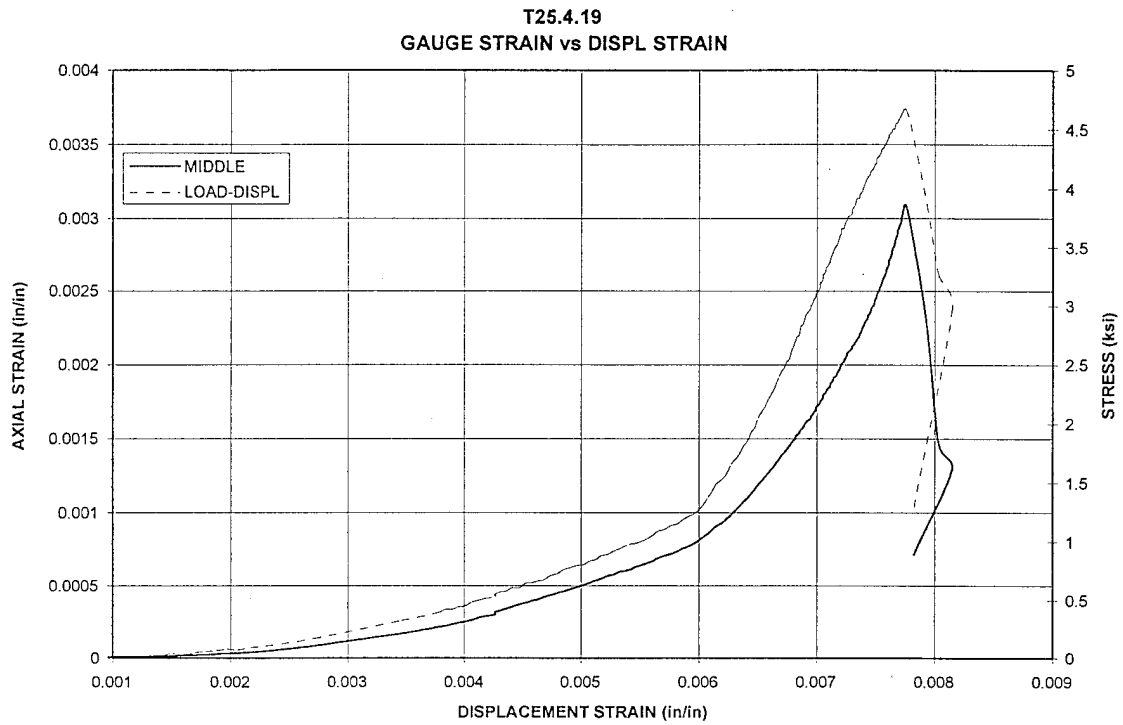
B3.1
GAUGE STRAIN vs DISPLACEMENT STRAIN
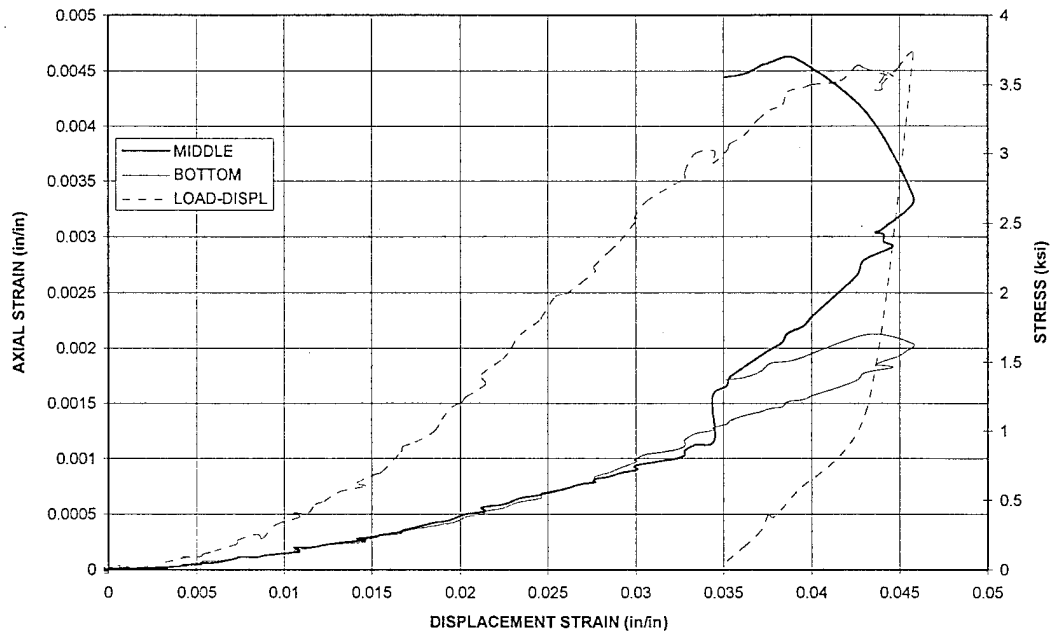
B3.1
GAUGE STRAIN vs DISPLACEMENT STRAIN
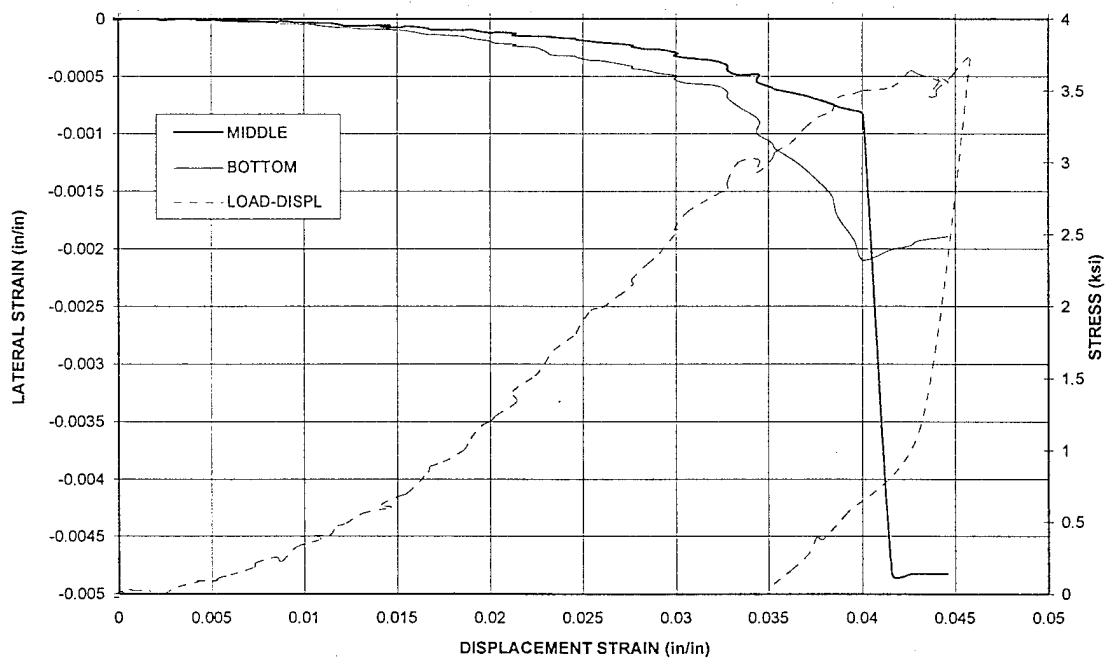
APPENDIX E

PHOTOS OF SPECIMENS

This appendix contains photos of all of the specimens with the exception of T25.3.11. The table below provides test numbers with cooresponding page numers where the photos of that specimen are located.

T25.1.01	E-2	T25.2.01	E-10	T25.3.01	E-15	T25.4.01	E-22
T25.1.02	E-2	T25.2.02	E-10	T25.3.02	E-16	T25.4.02	E-22
T25.1.03	E-2	T25.2.03	E-10	T25.3.03	E-16	T25.4.03	E-22
T25.1.04	E-2	T25.2.04	E-10	T25.3.04	E-17	T25.4.04	E-23
T25.1.05	E-2	T25.2.05	E-10	T25.3.05	E-17	T25.4.05	E-23
T25.1.06	E-2	T25.2.06	E-11	T25.3.06	E-17	T25.4.06	E-23
T25.1.07	E-3	T25.2.07	E-11	T25.3.07	E-18	T25.4.07	E-23
T25.1.08	E-3	T25.2.08	E-11	T25.3.08	E-18	T25.4.08	E-24
T25.1.09	E-3	T25.2.09	E-12	T25.3.09	E-19	T25.4.09	E-24
T25.1.10	E-3	T25.2.10	E-12	T25.3.10	E-19	T25.4.10	E-24
T25.1.11	E-3	T25.2.11	E-12	T25.3.11	N/A	T25.4.11	E-24
T25.1.12	E-4	T25.2.12	E-13	T25.3.12	E-19	T25.4.12	E-25
T25.1.13	E-5	T25.2.13	E-13	T25.3.13	E-19	T25.4.13	E-25
T25.1.14	E-5	T25.2.14	E-13	T25.3.14	E-19	T25.4.14	E-25
T25.1.15	E-6	T25.2.15	E-13	T25.3.15	E-20	T25.4.15	E-26
T25.1.16	E-7	T25.2.16	E-13	T25.3.16	E-20	T25.4.16	E-26
T25.1.17	E-7	T25.2.17	E-14	T25.3.17	E-20	T25.4.17	E-26
T25.1.18	E-7	T25.2.18	E-14	T25.3.18	E-20	T25.4.18	E-27
T25.1.19	E-8	T25.2.19	E-14	T25.3.19	E-20	T25.4.19	E-27
T25.1.20	E-8	T25.2.20	E-14	T25.3.20	E-21	T25.4.20	E-27
T25.1.21	E-9	T25.2.21	E-14	T25.3.21	E-21		
T25.1.22	E-9	T25.2.22	E-15	T25.3.22	E-21		
T25.1.23	E-9	T25.2.23	E-15	T25.3.23	E-22		
T25.1.24	E-10	T25.2.24	E-15	T25.3.24	E-22		
T25.1.25	E-10	T25.2.25	E-15	T25.3.25	E-22		

B3.1	E-28		T1.1	E-31	T3.1	E-33
B3.2	E-28		T1.2	E-31	T3.2	E-34
B3.3	E-28		T1.3	E-31	T3.3	E-34
B3.4	E-29		T1.4	E-32	T3.4	E-34
B3.5	E-29		T2.1	E-32	T4.1	E-34
B3.6	E-30		T2.2	E-32	T4.2	E-35
B3.7	E-30		T2.3	E-33	T4.3	E-35
			T2.4	E-33	T4.4	E-35
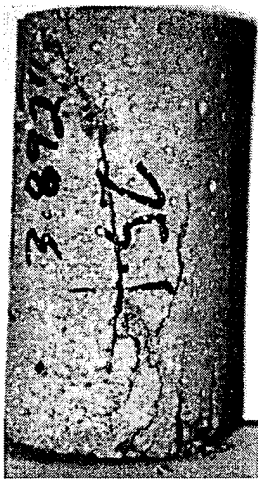
Figure E- 1: T25.1.01
NONE, 0 psi
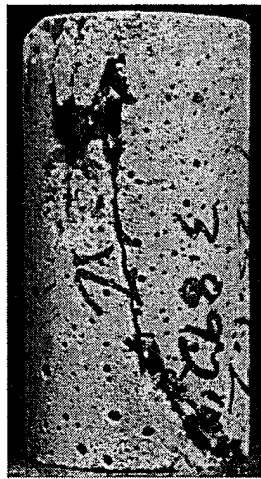
Figure E- 2: T25.1.02
NONE, 0 psi
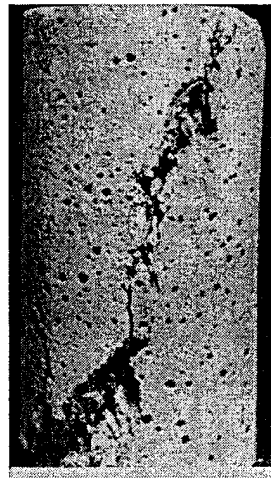
Figure E- 3: T25.1.02
NONE, 0 psi

Figure E- 4: T25.1.03
NONE, 0 psi
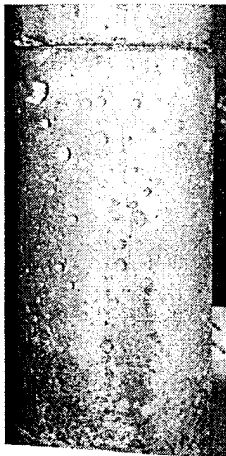
Figure E- 5: T25.1.04
CAP, 0 psi
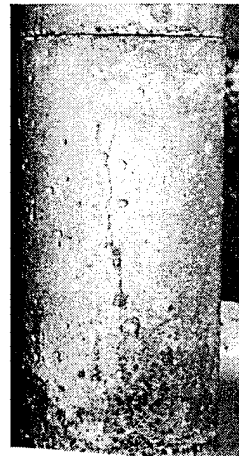
Figure E- 6: T25.1.04
CAP, 0 psi

Figure E- 7: T25.1.05
CAP, 0 psi
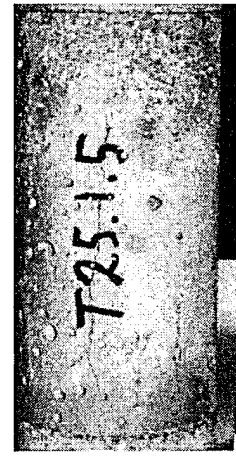
Figure E- 8: T25.1.05
CAP, 0 psi
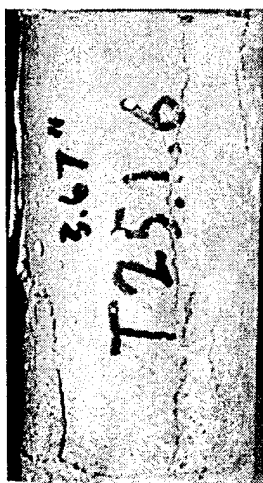
Figure E- 9: T25.1.06
CAP, 0 psi

Figure E- 10: T25.1.06
CAP, 0 psi

Figure E- 11: T25.1.06
CAP, 0 psi

Figure E- 12: T25.1.06
CAP, 0 psi
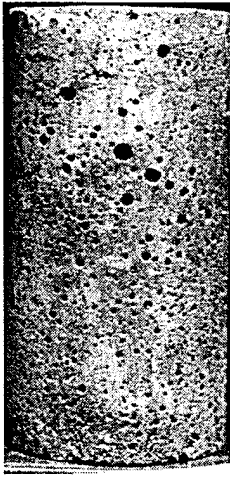
Figure E- 13: T25.1.07 CAP, 9000 psi
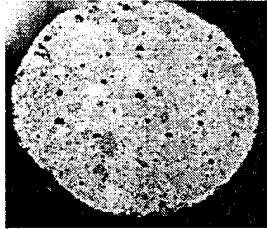
Figure E- 14: T25.1.07 CAP, 9000 psi

Figure E- 15: T25.1.08 CAP, 8000 psi

Figure E- 16: T25.1.08 CAP, 8000 psi

Figure E- 17: T25.1.08 CAP, 8000 psi

Figure E- 18: T25.1.09 CAP, 8000 psi

Figure E- 19: T25.1.09 CAP, 8000 psi

Figure E- 20: T25.1.09 CAP, 8000 psi
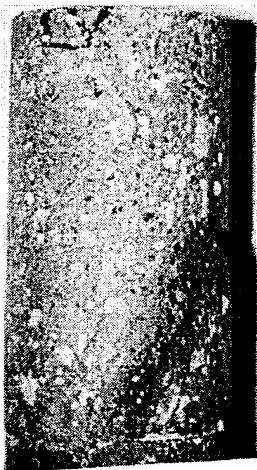
Figure E- 21: T25.1.10 CAP, 6000 psi

Figure E- 22: T25.1.10 CAP, 6000 psi

Figure E- 23: T25.1.11 CAP, 6000 psi
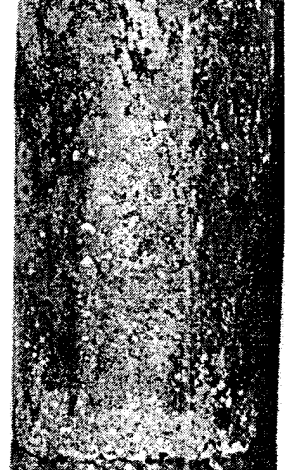
Figure E- 24: T25.1.11 CAP, 6000 psi
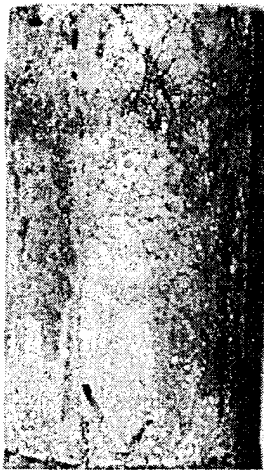
Figure E- 25: T25.1.11
CAP, 6000 psi
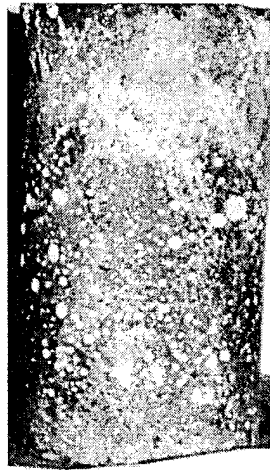
Figure E- 26: T25.1.11
CAP, 6000 psi

Figure E- 27: T25.1.11
CAP, 6000 psi

Figure E- 28: T25.1.11
CAP, 6000 psi
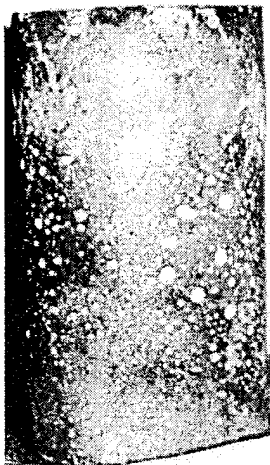
Figure E- 29: T25.1.11
CAP, 6000 psi

Figure E- 30: T25.1.12
CAP, 6000 psi
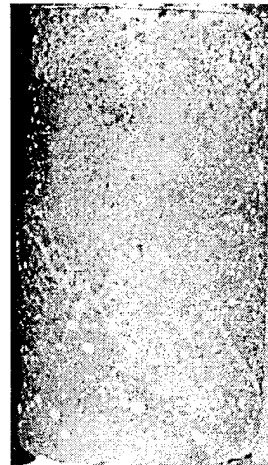
Figure E- 31: T25.1.12
CAP, 6000 psi
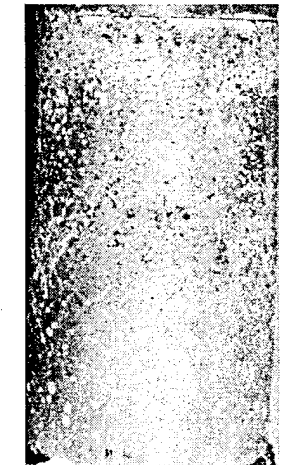
Figure E- 32: T25.1.12
CAP, 6000 psi

Figure E- 33: T25.1.12
CAP, 6000 psi

Figure E- 34: T25.1.12
CAP, 6000 psi
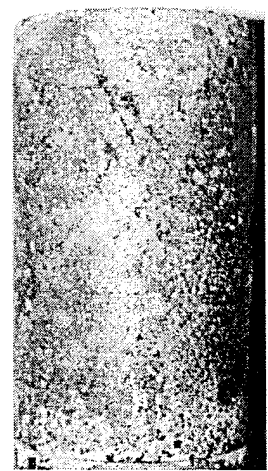
Figure E- 35: T25.1.12
CAP, 6000 psi

Figure E- 36: T25.1.12
CAP, 6000 psi

Figure E- 37: T25.1.12
CAP, 6000 psi
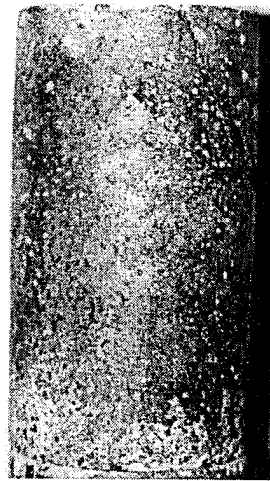
Figure E- 38: T25.1.12
CAP, 6000 psi
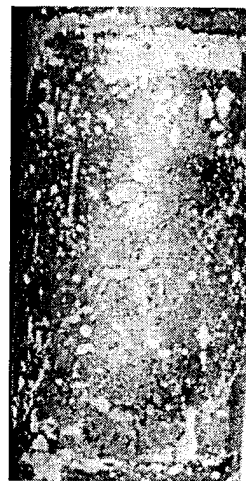
Figure E- 39: T25.1.13
CAP, 4000 psi

Figure E- 40: T25.1.13
CAP, 4000 psi

Figure E- 41: T25.1.13
CAP, 4000 psi

Figure E- 42: T25.1.13
CAP, 4000 psi

Figure E- 43: T25.1.13
CAP, 4000 psi

Figure E- 44: T25.1.13
CAP, 4000 psi

Figure E- 45: T25.1.13
CAP, 4000 psi

Figure E- 46: T25.1.13
CAP, 4000 psi

Figure E- 47: T25.1.13
CAP, 4000 psi

Figure E- 48: T25.1.14
CAP, 4000 psi

Figure E- 49: T25.1.14 CAP, 4000 psi
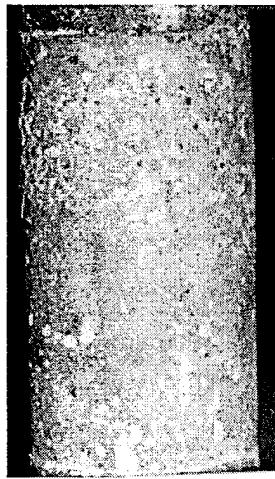
Figure E- 50: T25.1.14 CAP, 4000 psi
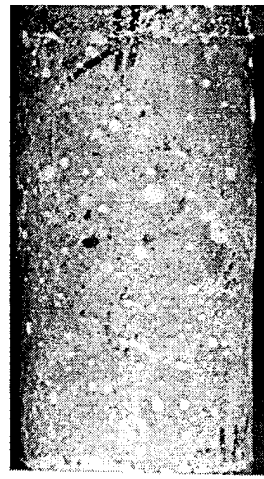
Figure E- 51: T25.1.14 CAP, 4000 psi

Figure E- 52: T25.1.14 CAP, 4000 psi

Figure E- 53: T25.1.14 CAP, 4000 psi

Figure E- 54: T25.1.14 CAP, 4000 psi
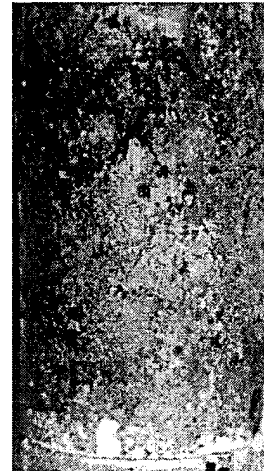
Figure E- 55: T25.1.14 CAP, 4000 psi

Figure E- 56: T25.1.15 CAP, 4000 psi

Figure E- 57: T25.1.15 CAP, 4000 psi

Figure E- 58: T25.1.15 CAP, 4000 psi
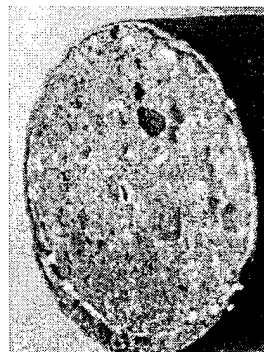
Figure E- 59: T25.1.15 CAP, 4000 psi

Figure E- 60: T25.1.15 CAP, 4000 psi

Figure E- 61: T25.1.15 CAP, 4000 psi
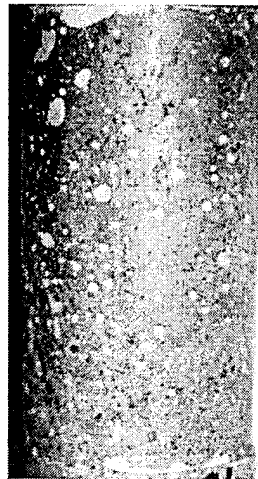
Figure E- 62: T25.1.16 CAP, 2000 psi
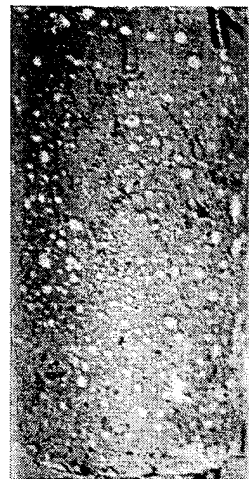
Figure E- 63: T25.1.16 CAP, 2000 psi
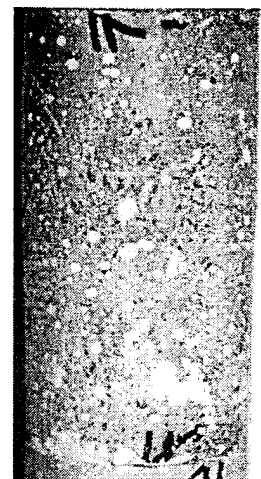
Figure E- 64: T25.1.16 CAP, 2000 psi

Figure E- 65: T25.1.16 CAP, 2000 psi
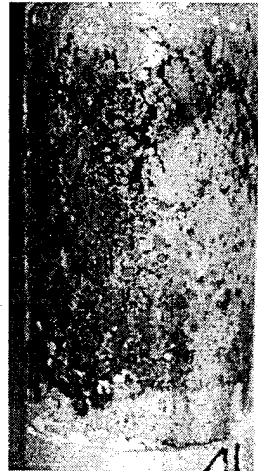
Figure E- 66: T25.1.16 CAP, 2000 psi

Figure E- 67: T25.1.16 CAP, 2000 psi

Figure E- 68: T25.1.17 CAP, 2000 psi

Figure E- 69: T25.1.17 CAP, 2000 psi

Figure E- 70: T25.1.17 CAP, 2000 psi

Figure E- 71: T25.1.17 CAP, 2000 psi

Figure E- 72: T25.1.18 CAP, 2000 psi
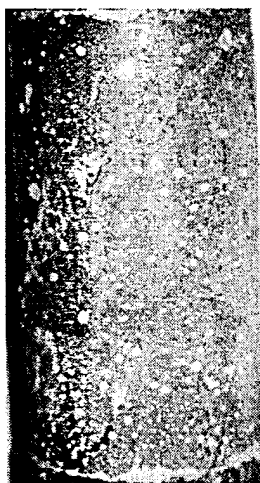
Figure E- 73: T25.1.18
CAP, 2000 psi
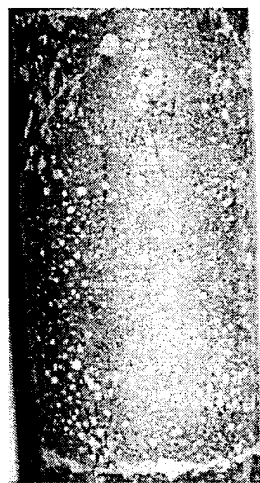
Figure E- 74: T25.1.18
CAP, 2000 psi
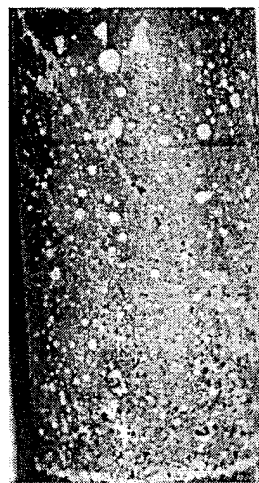
Figure E- 75: T25.1.18
CAP, 2000 psi

Figure E- 76: T25.1.18
CAP, 2000 psi

Figure E- 77: T25.1.19
CAP, 1000 psi
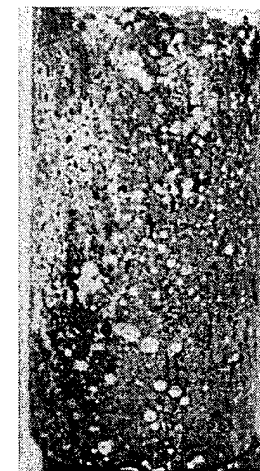
Figure E- 78: T25.1.19
CAP, 1000 psi
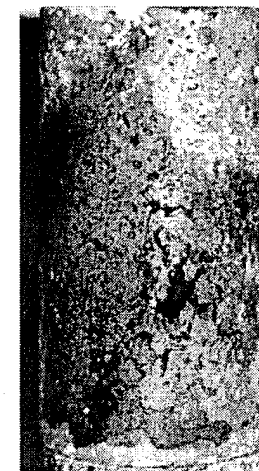
Figure E- 79: T25.1.19
CAP, 1000 psi

Figure E- 80: T25.1.19
CAP, 1000 psi

Figure E- 81: T25.1.19
CAP, 1000 psi
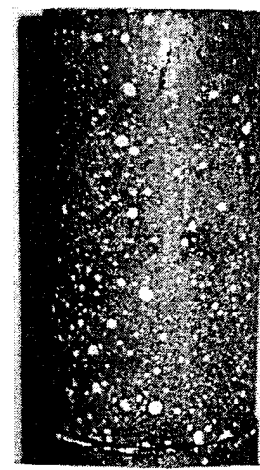
Figure E- 82: T25.1.20
CAP, 1000 psi

Figure E- 83: T25.1.20
CAP, 1000 psi

Figure E- 84: T25.1.20
CAP, 1000 psi

Figure E- 85: T25.1.21 CAP, 1000 psi
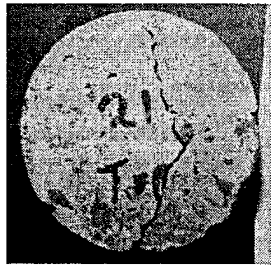
Figure E- 86: T25.1.21 CAP, 1000 psi

Figure E- 87: T25.1.21 CAP, 1000 psi
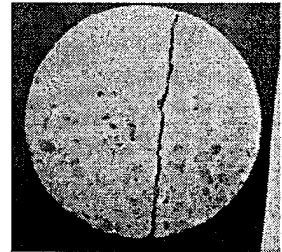
Figure E- 88: T25.1.21 CAP, 1000 psi

Figure E- 89: T25.1.22 CAP, 500 psi
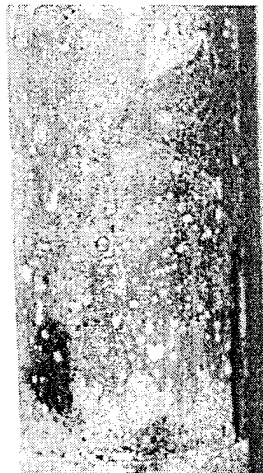
Figure E- 90: T25.1.22 CAP, 500 psi
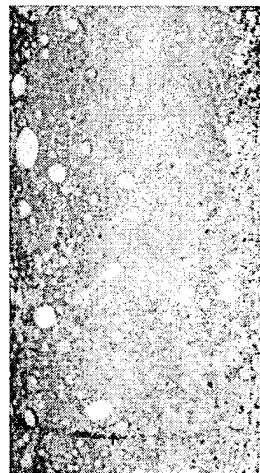
Figure E- 91: T25.1.22 CAP, 500 psi
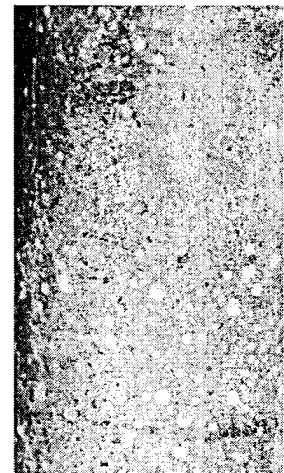
Figure E- 92: T25.1.22 CAP, 500 psi

Figure E- 93: T25.1.23 CAP, 500 psi

Figure E- 94: T25.1.23 CAP, 500 psi

Figure E- 95: T25.1.23 CAP,500 psi

Figure E- 96: T25.1.23 CAP, 500 psi

Figure E- 97: T25.1.24
CAP, 500 psi

Figure E-98: T25.1.24
CAP, 500 psi

Figure E-99: T25.1.25
CAP, 500 psi
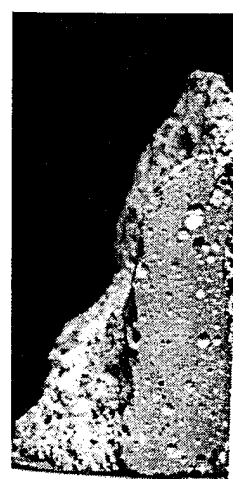
Figure E-100: T25.1.25
CAP, 500 psi

Figure E- 101: 25.1.25
CAP, 500 psi
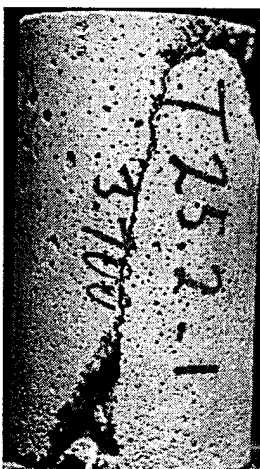
Figure E- 102: T25.2.1
NONE, 0 psi
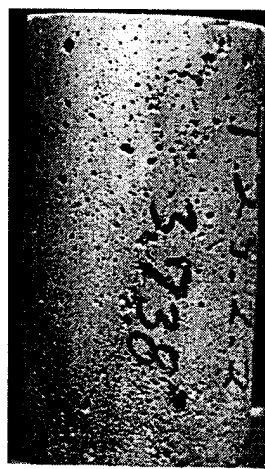
Figure E- 103: T25.2.2
NONE, 0 psi
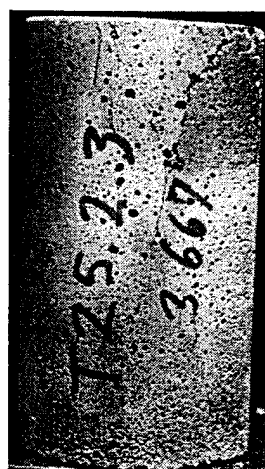
Figure E- 104: T25.2.3
NONE, 0 psi

Figure E- 105: T25.2.4
CAP, 500 psi

Figure E- 106: T25.2.4
CAP, 500 psi

Figure E- 107: T25.2.5
CAP, 500 psi

Figure E- 108: T25.2.5
CAP, 500 psi
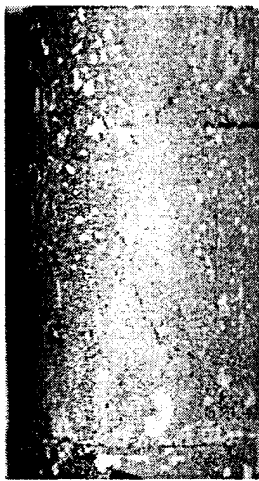
Figure E- 109: T25.2.6 CAP, 500 psi
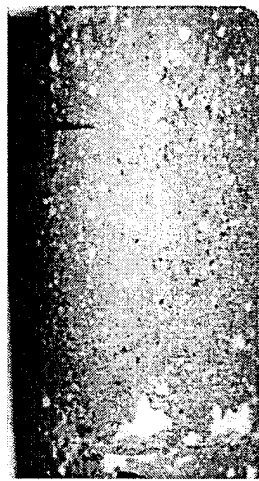
Figure E- 110: T25.2.6 CAP, 500 psi
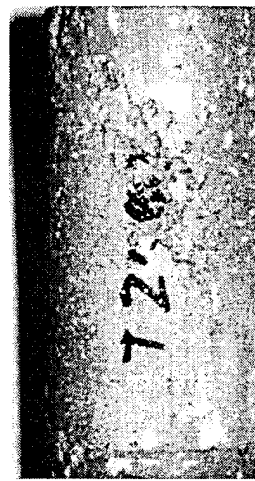
Figure E- 111: T25.2.6 CAP, 500 psi
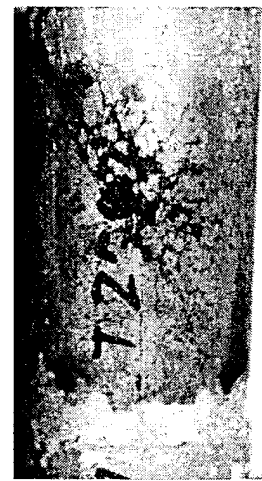
Figure E- 112: T25.2.6 CAP, 500 psi

Figure E- 113: T25.2.7 CAP, 500 psi
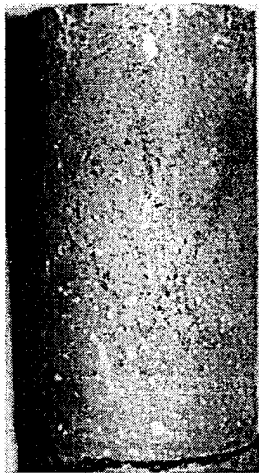
Figure E- 114: T25.2.7 CAP, 500 psi
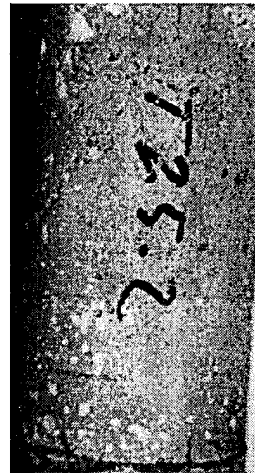
Figure E- 115: T25.2.7 CAP, 500 psi

Figure E- 116: T25.2.7 CAP, 500 psi

Figure E- 117: T25.2.7 CAP, 500 psi

Figure E- 118: T25.2.8 CAP, 0 psi

Figure E- 119: T25.2.8 CAP, 0 psi
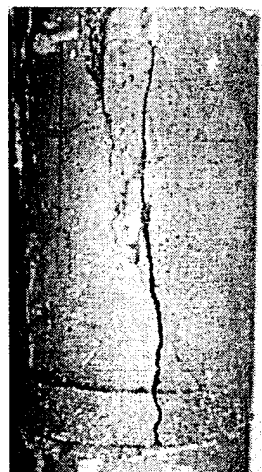
Figure E- 120: T25.2.8 CAP, 0 psi

Figure E-121:T25.2.8 CAP, 0 psi
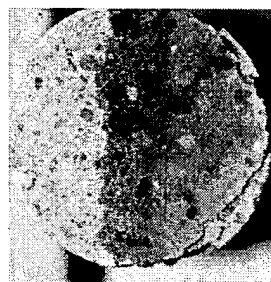
Figure E-122:T25.2.8 CAP, 0 psi

Figure E-123: T25.2.9 CG, 500 psi

Figure E-124: T25.2.9 CG, 500 psi

Figure E-125: T25.2.9 CG, 500 psi
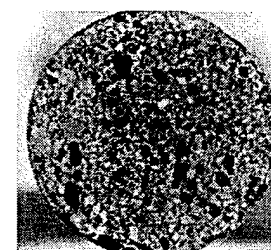
Figure E-126: T25.2.9 CG, 500 psi
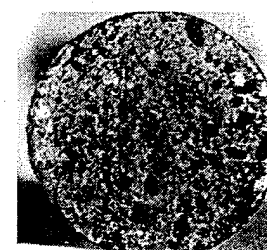
Figure E-127: T25.2.9 CG, 500 psi
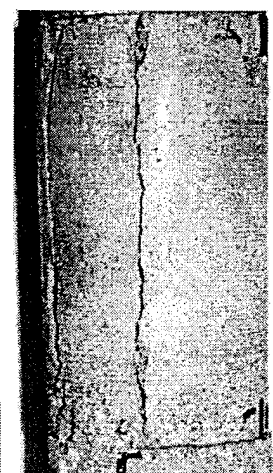
Figure E-128: T25.2.10 CAP, 250 psi

Figure E-129: T25.2.10 CAP, 250 psi
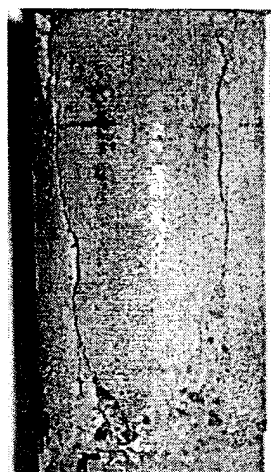
Figure E-130: T25.2.10 CAP, 250 psi
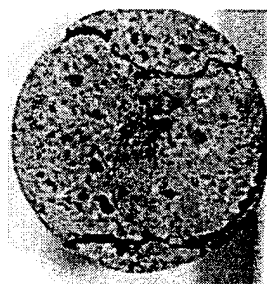
Figure E-131: T25.2.10 CAP, 250 psi
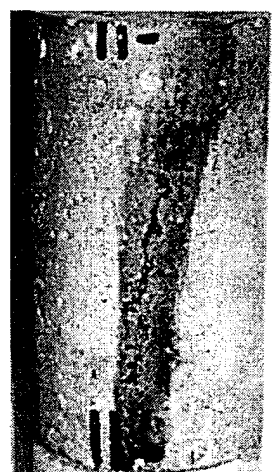
Figure E-132: T25.2.11 CAP, 250 psi
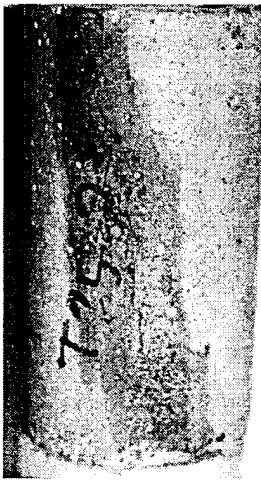
Figure E-133: T25.2.11
CAP, 250 psi
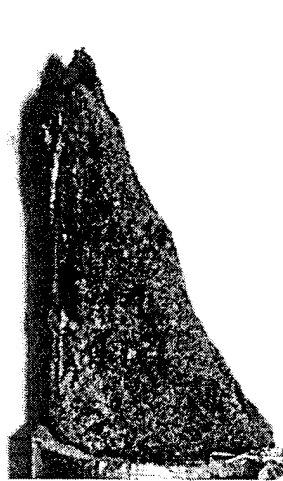
Figure E-134: T25.2.12
CAP, 250 psi

Figure E-135: T25.2.12
CAP, 250 psi

Figure E-136: T25.2.12
CAP, 250 psi

Figure E-137: T25.2.13
CAP, 1000 psi
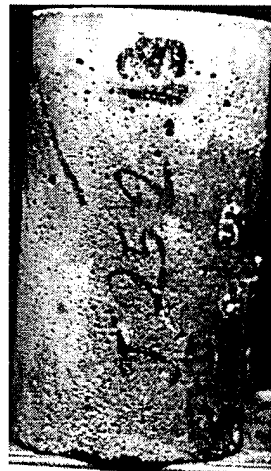
Figure E- 138: T25.2.13
CAP, 1000 psi
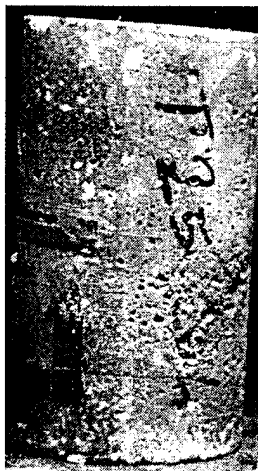
Figure E- 139: T25.2.14
CAP, 2000 psi
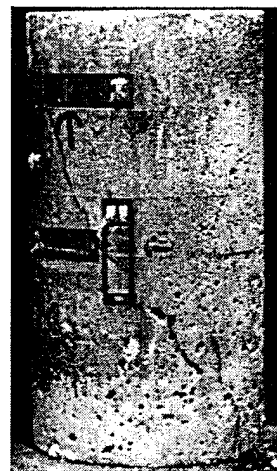
Figure E-140: T25.2.15
CAP, 250 psi
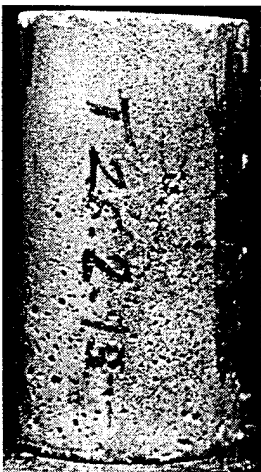
Figure E-141: T25.2.15
CPGP, 250 psi
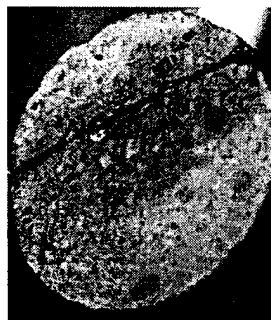
Figure E-142: T25.2.15
CG, 250 psi

Figure E-143: T25.2.16
CG, 4000 psi
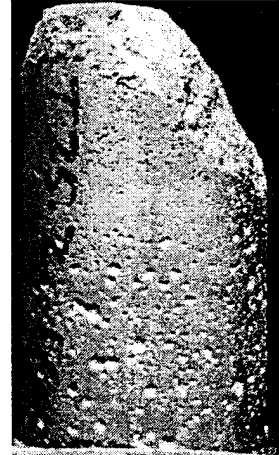
Figure E-144: T25.2.16
CG, 4000 psi

Figure E-145: T25.2.17 CG, 2000 psi
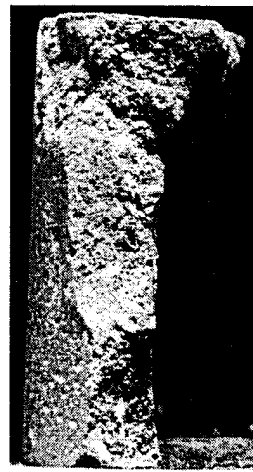
Figure E-146: T25.2.17 CG, 2000 psi

Figure E-147: T25.2.18 CG, 500 psi

Figure E- 148: T25.2.18 CAP, 500 psi
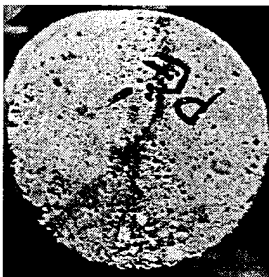
Figure E-149: T25.2.18 CAP, 500 psi

Figure E-150: T25.2.19 CG, 2000 psi

Figure E-151: T25.2.19 CG, 2000 psi
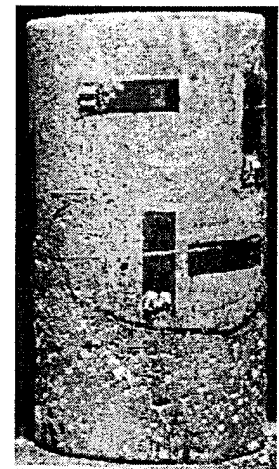
Figure E-152: T25.2.20 CPGP, 4000 psi
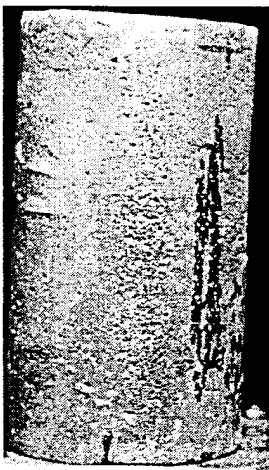
Figure E-153: T25.2.20 CPGP, 4000 psi

Figure E-154: T25.2.20 CPGP, 4000 psi

Figure E-155: T25.2.21 CG, 2000 psi

Figure E-156: T25.2.21 CG, 2000 psi

Figure E-157: T25.2.22 CAP, 2000 psi
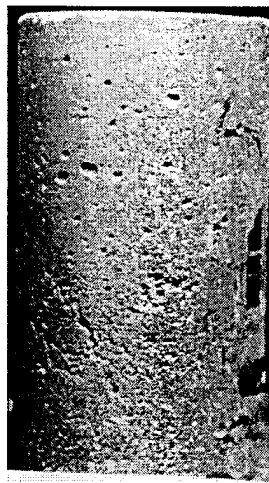
Figure E-158: T25.2.22 CAP, 2000 psi

Figure E-159: T25.2.23 CAP, 6000 psi
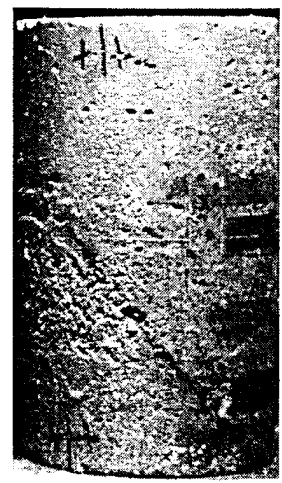
Figure E-160: T25.2.23 CAP, 6000 psi

Figure E-161: T25.2.23 CAP, 6000 psi

Figure E-162: T25.2.23 CAP, 6000 psi
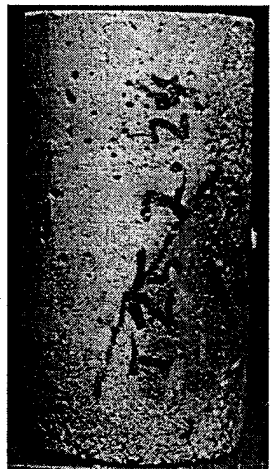
Figure E-163: T25.2.24 CG, 500 psi

Figure E-164: T25.2.24 CG, 500 psi

Figure E-165: T25.2.25 CG, 2000 psi

Figure E-166: T25.2.25 CG, 2000 psi
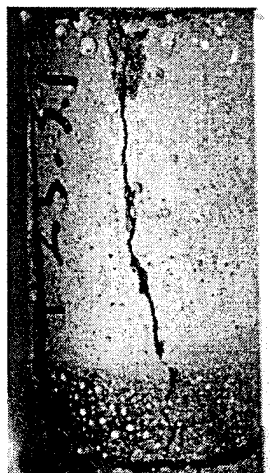
Figure E-167: T25.3.1 CG, 0 psi

Figure E-168: T25.3.1 CG, 0 psi

Figure E-169: T25.3.1 CG, 0 psi
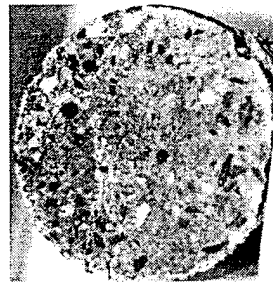
Figure E-170: T25.3.1 CG, 0 psi
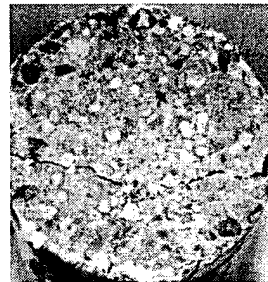
Figure E-171: T25.3.1 CG, 0 psi
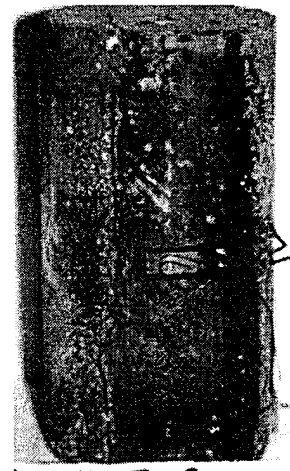
Figure E-172: T25.3.2 NONE, 0 psi
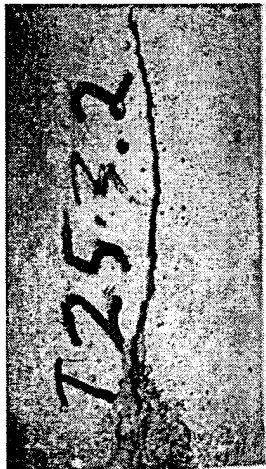
Figure E-173: T25.3.2 NONE, 0 psi

Figure E-174: T25.3.2 NONE, 0 psi
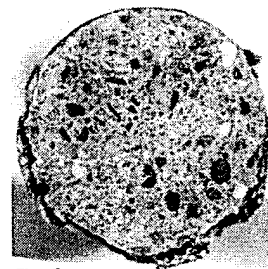
Figure E-175: T25.3.2 NONE, 0 psi
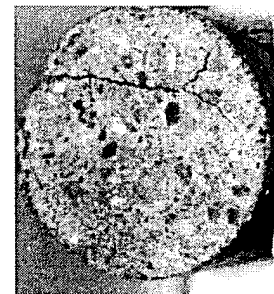
Figure E-176: T25.3.2 NONE, 0 psi

Figure E-177: T25.3.3 PGP, 0 psi

Figure E-178: T25.3.3 PGP, 0 psi
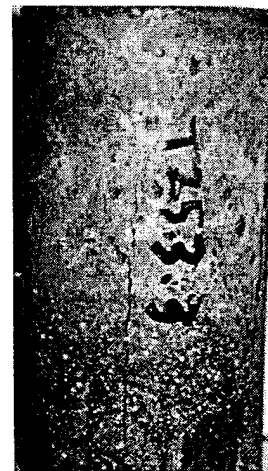
Figure E-179: T25.3.3 PGP, 0 psi
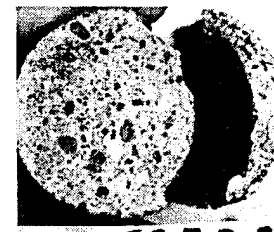
Figure E-180: T25.3.3 PGP, 0 psi
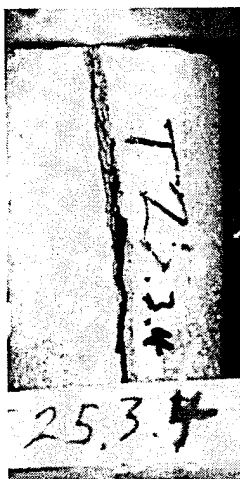
Figure E-181: T25.3.4 RUBBER, 0 psi

Figure E- 182: T25.3.4 RUBBER, 0 psi
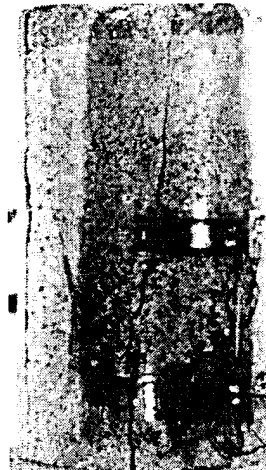
Figure E- 183: T25.3.4 RUBBER, 0 psi

Figure E- 184: T25.3.4 RUBBER, 0 psi

Figure E- 185: T25.3.4 RUBBER, 0 psi
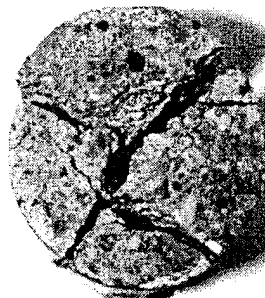
Figure E- 186: T25.3.4 RUBBER, 0 psi
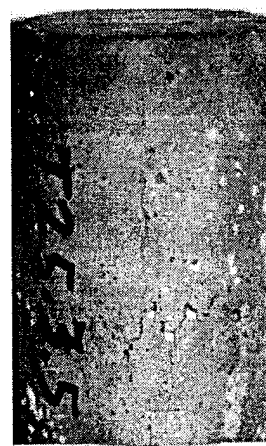
Figure E- 187: T25.3.5 NONE, 0 psi

Figure E- 188: T25.3.5 NONE, 0 psi

Figure E- 189: T25.3.5 NONE, 0 psi
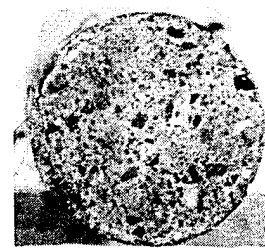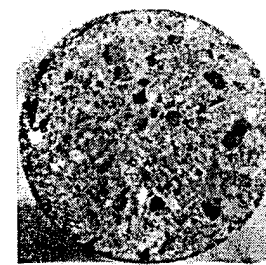

Figure E- 190: T25.3.5 NONE, 0 psi

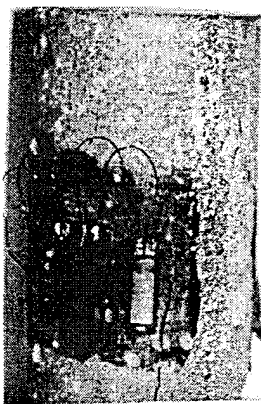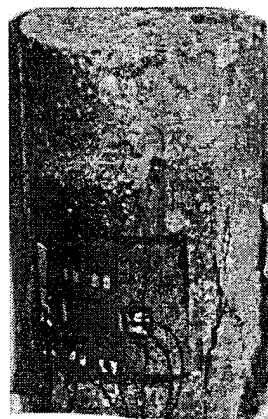Figure E- 191: T25.3.5 NONE, 0 psi
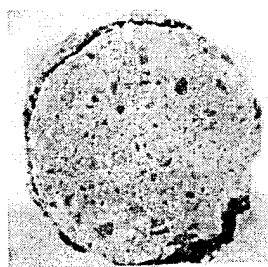

Figure E- 192: T25.3.6 NONE, 0 psi

Figure E- 193: T25.3.6 NONE, 0 psi

Figure E- 194: T25.3.6 NONE, 0 psi

Figure E- 195: T25.3.7 NONE, 0 psi

Figure E- 196: T25.3.7 NONE, 0 psi

Figure E- 197: T25.3.7 NONE, 0 psi

Figure E- 198: T25.3.7 NONE, 0 psi

Figure E- 199: T25.3.7 NONE, 0 psi
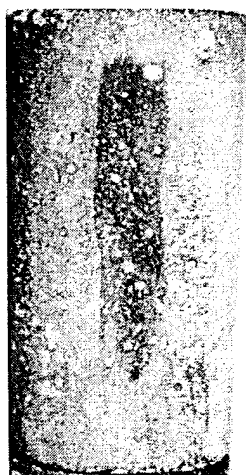
Figure E- 200: T25.3.8 CPGP, 0 psi

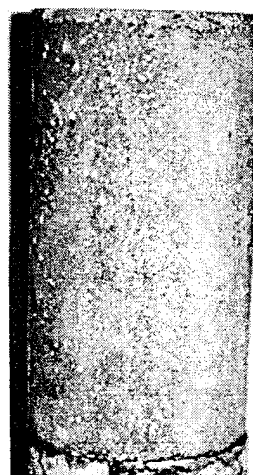**Figure E- 201: T25.3.8 CPGP, 0 psi**
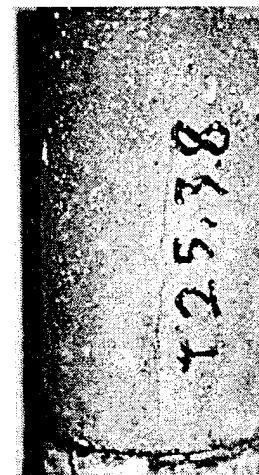
Figure E- 202: T25.3.8 CPGP, 0 psi

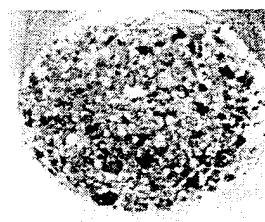**Figure E- 203: T25.3.8 CPGP, 0 psi**

Figure E- 204: T25.3.8 CPGP, 0 psi

Figure E- 205: T25.3.9 CPGP, 250 psi
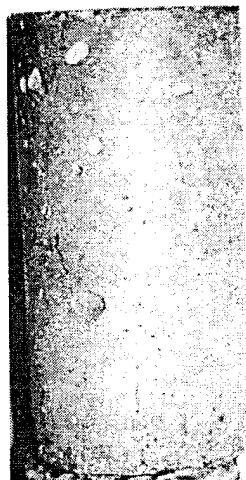

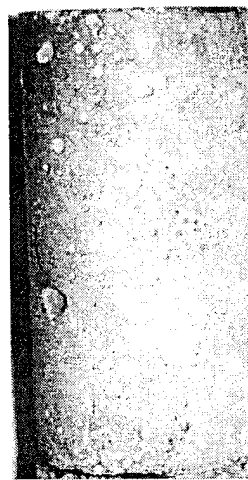Figure E- 206: T25.3.9 CPGP, 250 psi

Figure E- 207: T25.3.9 CPGP, 250 psi
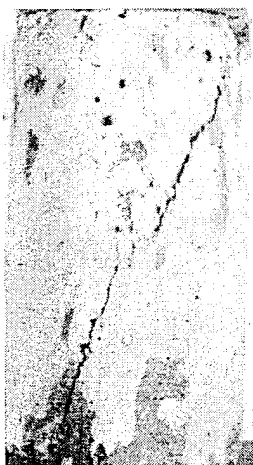

Figure E- 208: T25.3.10 CPGP, 500 psi

Figure E-209: T25.3.10 CPGP, 500 psi

Figure E-210: T25.3.12 CPGP, 6000 psi
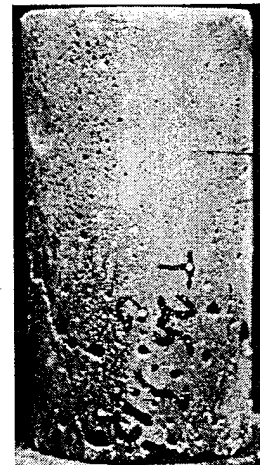

Figure E-211: T25.3.12 CPGP, 6000 psi

Figure E-212: T25.3.13 CPGP, 250 psi

Figure E-213: T25.3.13 CPGP, 250 psi

Figure E-214: T25.3.13 CPGP,250 psi

Figure E-215: T25.3.13 CPGP, 250 psi
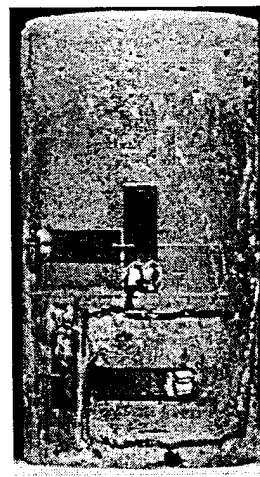
Figure E-216: T25.3.14 CPGP, 500 psi
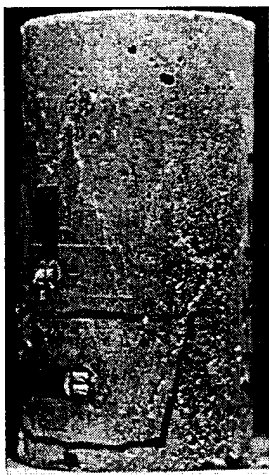
Figure E-217: T25.3.14
CPGP, 500 psi

Figure E-218: T25.3.14
CPGP, 500 psi

Figure E-219: T25.3.15
CG, 4000 psi

Figure E-220: T25.3.15
CG, 4000 psi

Figure E-221: T25.3.15
CG, 4000 psi

Figure E-222: T25.3.16
CG, 2000 psi

Figure E-223: T25.3.17
CG, 6000 psi

Figure E-224: T25.3.17
CG, 6000 psi

Figure E-225: T25.3.17
CG, 6000 psi

Figure E-226: T25.3.18
CPGP, 1000 psi
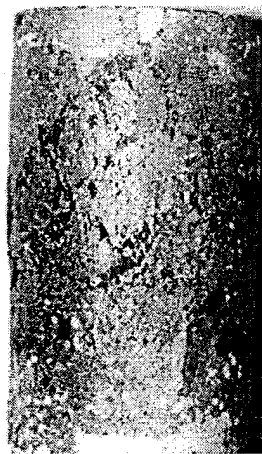
Figure E-227: T25.3.18
CPGP, 1000 psi
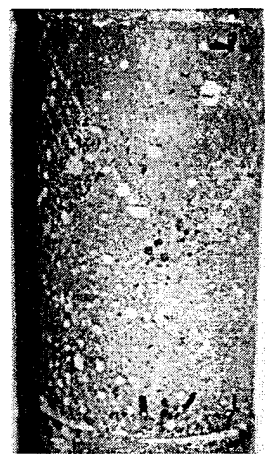
Figure E-228: T25.3.19
CG, 0 psi

Figure E-229: T25.3.19
CG, 0 psi

Figure E-230: T25.3.20
CPGP, 1000 psi
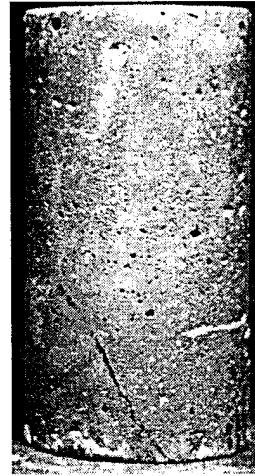
Figure E-231: T25.3.20
CPGP, 1000 psi

Figure E-232: T25.3.20
CPGP, 1000 psi
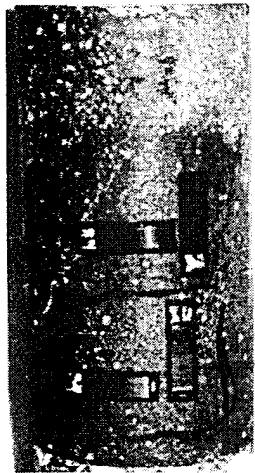
Figure E-233: T25.3.21
CG, 250 psi

Figure E-234: T25.3.21
CG, 250 psi

Figure E-235: T25.3.21
CG, 250 psi

Figure E-236: T25.3.21
CG, 250 psi

Figure E-237: T25.3.22
CG, 500 psi

Figure E-238: T25.3.22
CG, 500 psi
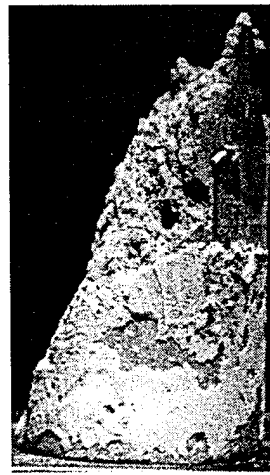
Figure E-239: T25.3.22
CG, 500 psi
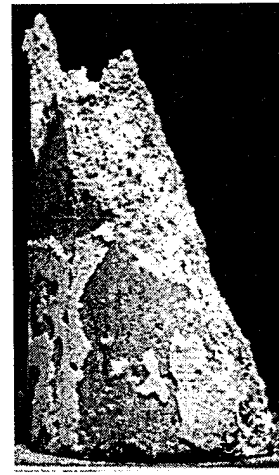
Figure E-240: T25.3.22
CG, 500 psi

Figure E-241: T25.3.23 CPGP, 4000 psi

Figure E-242: T25.3.23 CPGP, 4000 psi
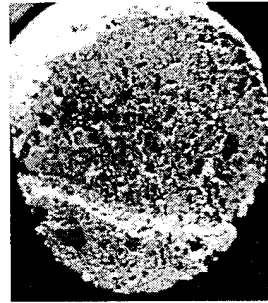
Figure E-243: T25.3.23 CPGP, 4000 psi

Figure E-244: T25.3.24 CPGP, 6000 psi

Figure E-245: T25.3.25 CPGP, 2000 psi
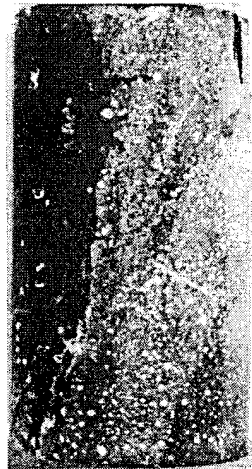
Figure E-246: T25.3.25 CPGP, 2000 psi

Figure E-247: T25.4.01 CAP, 500 psi

Figure E-248: T25.4.02 CAP, 500 psi

Figure E-249: T25.4.02 CAP, 500 psi

Figure E-250: T25.4.02 CAP, 500 psi
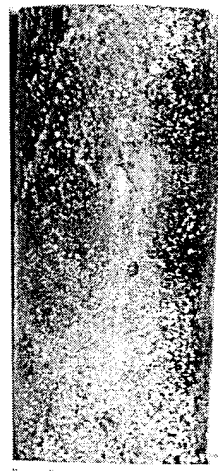
Figure E-251: T25.4.03 CAP, 500 psi
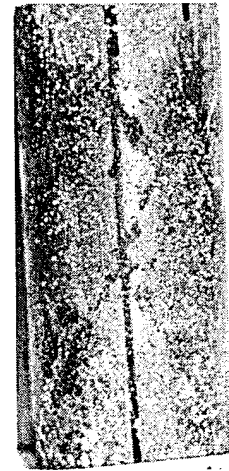
Figure E-252: T25.4.03 CAP, 500 psi

Figure E-253: T25.4.03 CAP, 500 psi
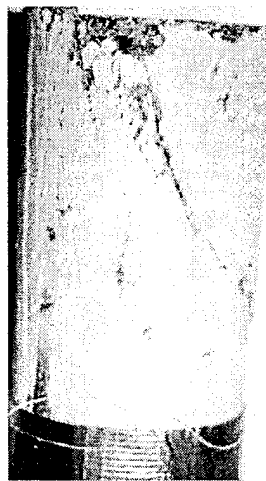
Figure E-254: T25.4.04 CAP, 500 psi
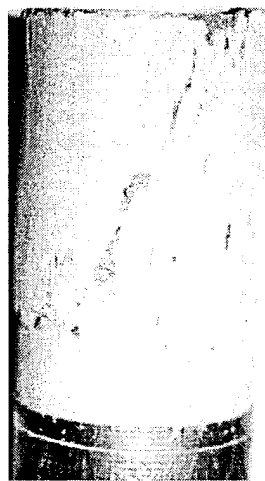
Figure E-255: T25.4.04 CAP, 500 psi
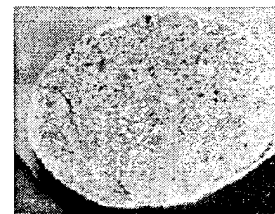
Figure E-256: T25.4.04 CAP, 500 psi

Figure E-257: T25.4.05 CG, 0 psi

Figure E-258: T25.4.06 CG, 500 psi

Figure E-259: T25.4.06 CG, 500 psi

Figure E-260: T25.4.06 CG, 500 psi

Figure E-261: T25.4.06 CG, 500 psi

Figure E-262: T25.4.07 CG, 8000 psi

Figure E-263: T25.4.07 CG, 8000 psi
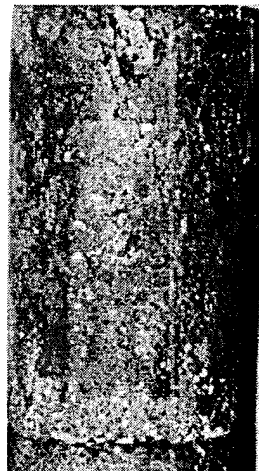
Figure E-264: T25.4.07 CG, 8000 psi
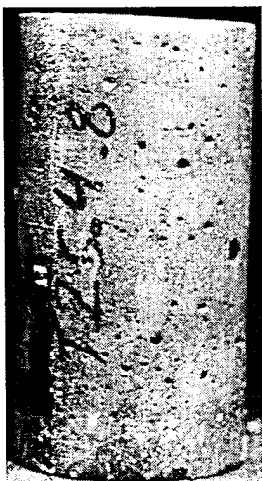
Figure E-265: T25.4.08 CG, 2000 psi

Figure E-266: T25.4.09 CAP, 250 psi

Figure E-267: T25.4.09 CAP, 250 psi

Figure E-268: T25.4.10 PGP, 0 psi

Figure E-269: T25.4.10 PGP, 0 psi
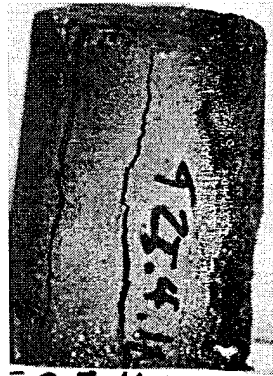
Figure E-270: T25.4.10 PGP, 0 psi
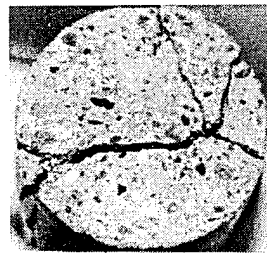
Figure E-271: T25.4.10 PGP, 0 psi

Figure E-272: T25.4.10 PGP, 0 psi
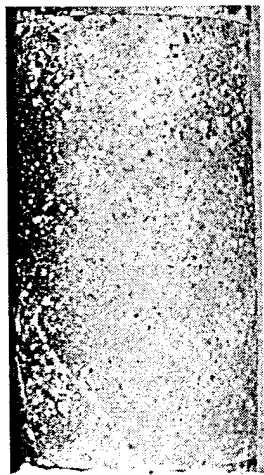

Figure E-273: T25.4.11 PGP, 0 psi

Figure E-274: T25.4.11 PGP, 0 psi
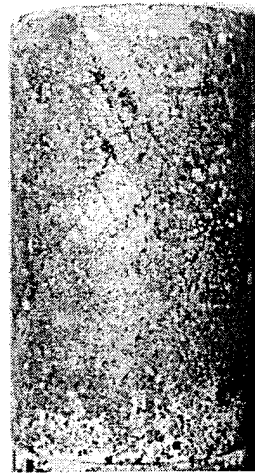
Figure E-275: T25.4.11 PGP, 0 psi

Figure E-276: T25.4.11 PGP, 0 psi
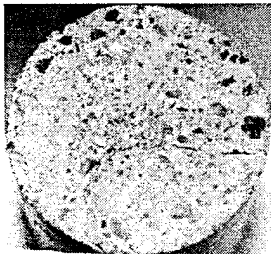
Figure E-277: T25.4.11 PGP, 0 psi
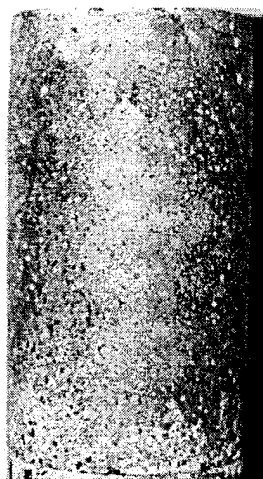
Figure E-278: T25.4.12 CAP, 0 psi
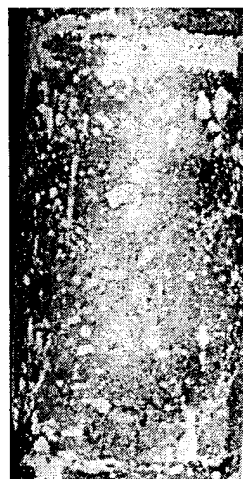
Figure E-279: T25.4.12 CAP, 0 psi
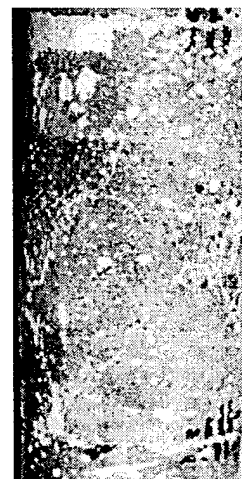
Figure E-280: T25.4.12 CAP, 0 psi
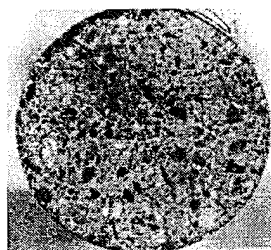
Figure E-281: T25.4.12 CAP, 0 psi

Figure E-282: T25.4.13 RUB, 0 psi
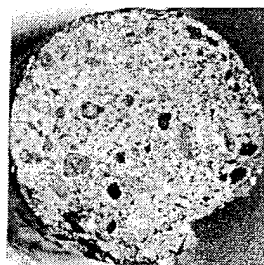
Figure E-283: T25.4.13 RUB, 0 psi

Figure E-284: T25.4.14 CG, 0 psi

Figure E-285: T25.4.14 RUB, 0 psi

Figure E-286: T25.4.14 RUB, 0 psi
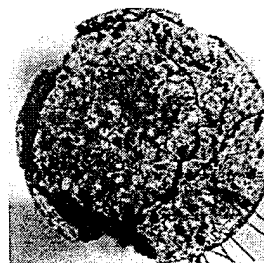
Figure E-287: T25.4.14 RUB, 0 psi
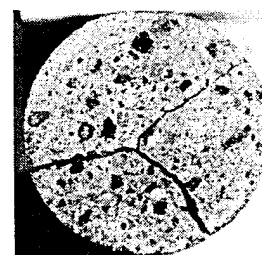
Figure E-288: T25.4.14 RUB, 0 psi

Figure E-289: T25.4.15 CAP, 0 psi

Figure E-290: T25.4.15 CAP, 0 psi

Figure E-291: T25.4.15 CAP, 0 psi

Figure E-292: T25.4.15 CAP, 0 psi
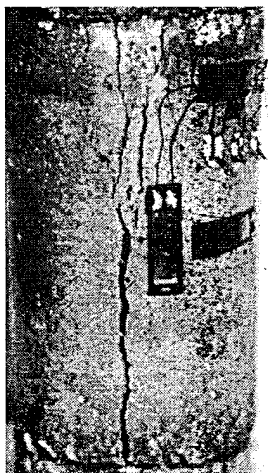
Figure E-293: T25.4.16 CG, 0 psi
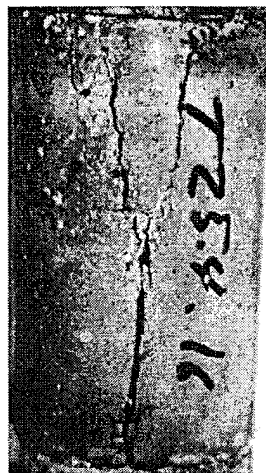
Figure E-294: T25.4.16 CG, 0 psi

Figure E-295: T25.4.16 CG, 0 psi

Figure E-296: T25.4.16 CG, 0 psi
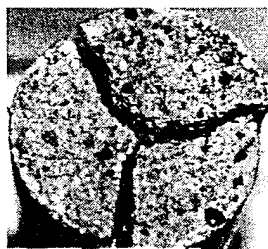
Figure E-297: T25.4.16 CG, 0 psi

Figure E-298: T25.4.17 CAP, 4000 psi

Figure E-299: T25.4.17 CAP, 4000 psi

Figure E-300: T25.4.17 CAP, 4000 psi
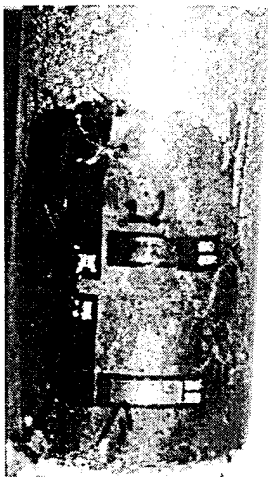
Figure E-301: T25.4.18 CG, 1000 psi

Figure E-302: T25.4.18 CG, 1000 psi
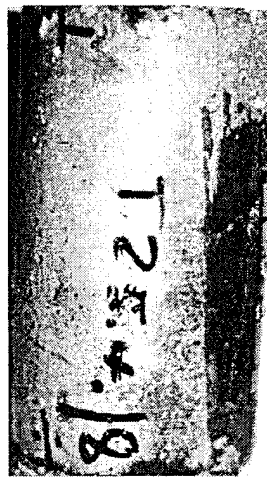
Figure E-303: T25.4.18 CG, 1000 psi

Figure E-304: T25.4.19 CPGP, 0 psi
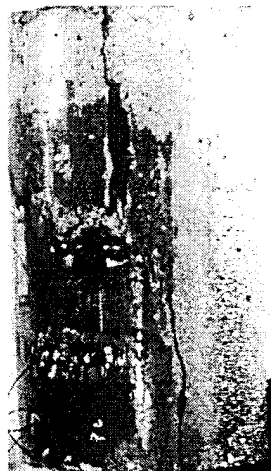
Figure E-305: T25.4.19 CPGP, 0 psi
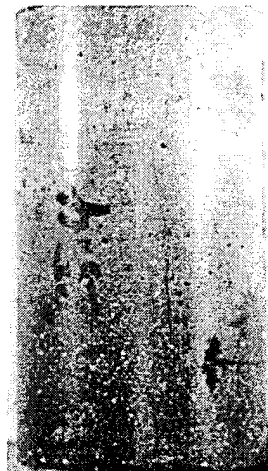
Figure E-306: T25.4.19 CPGP, 0 psi

Figure E-307: T25.4.20 CPGP, 0 psi

Figure E-308: T25.4.20 CPGP, 0 psi

Figure E-309: T25.4.20 CPGP, 0 psi

Figure E-310: T25.4.20 CPGP, 0 psi
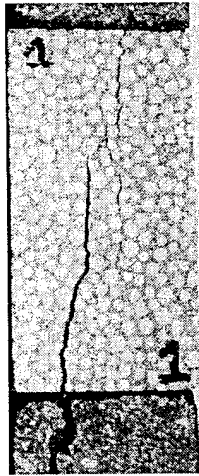
Figure E- 311: B3.1
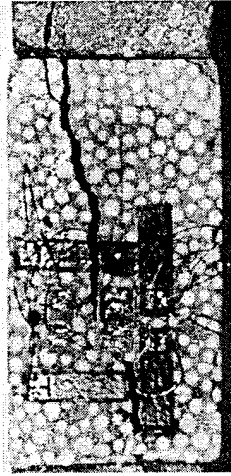
Figure E- 312: B3.1
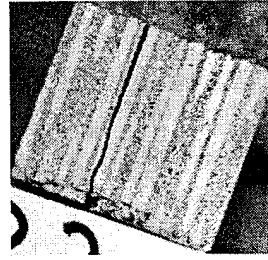
Figure E- 313: B3.1
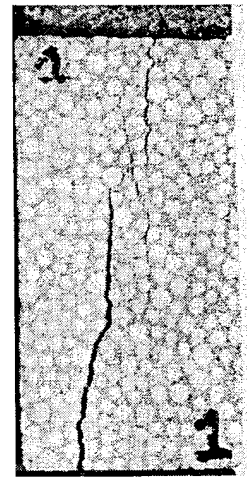
Figure E- 314: B3.1
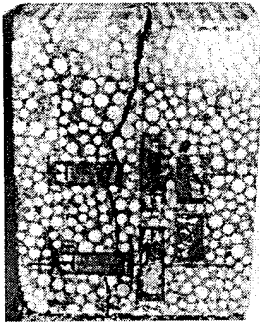
Figure E- 315: B3.2
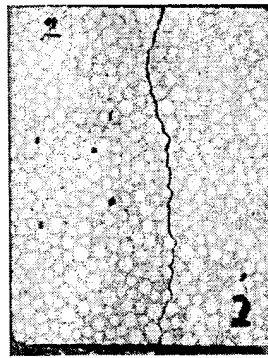
Figure E- 316: B3.2
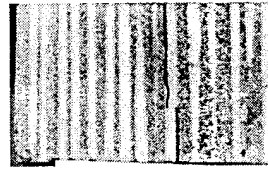
Figure E- 317: B3.2

Figure E- 318: B3.2
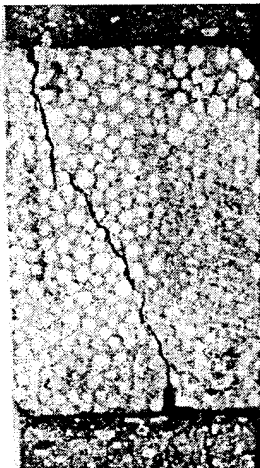
Figure E- 319: B3.3
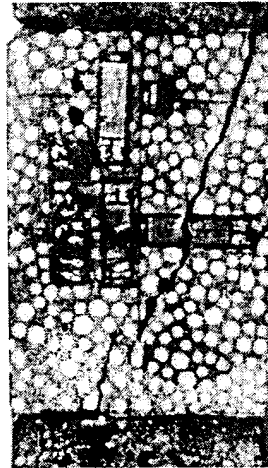
Figure E- 320: B3.3
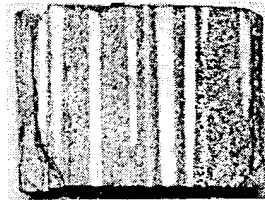
Figure E- 321: B3.3
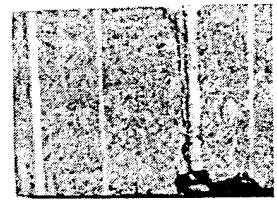
Figure E- 322: B3.3
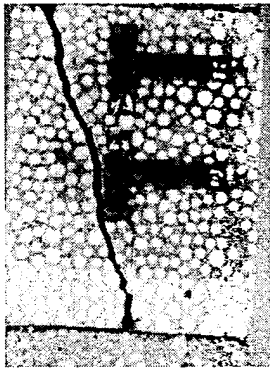
Figure E- 323: B3.4   Figure E- 324: B3.4   Figure E- 325: B3.4   Figure E- 326: B3.4
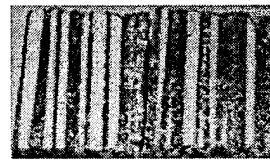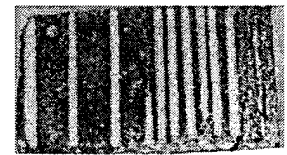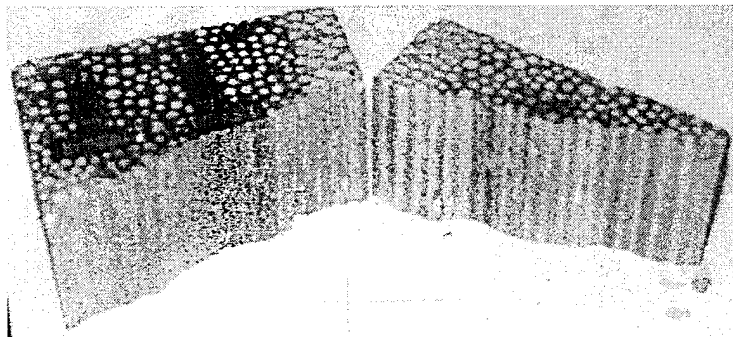
Figure E- 327: B3.4
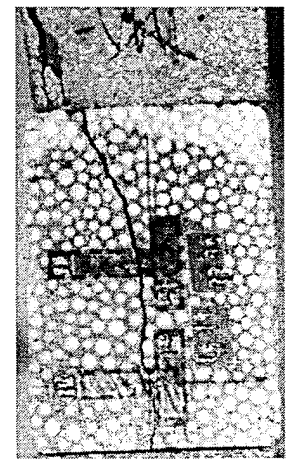
Figure E- 328: B3.5
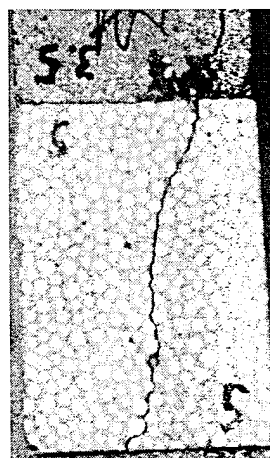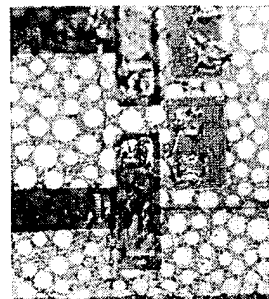
Figure E- 329: B3.5   Figure E- 330: B3.5   Figure E- 331: B3.5   Figure E- 332: B3.5
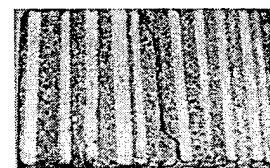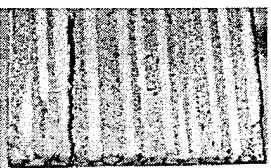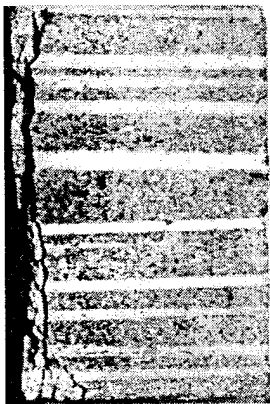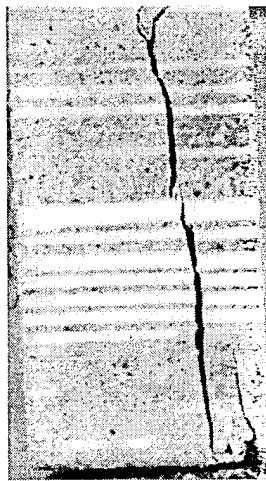
Figure E- 333: B3.6   Figure E- 334: B3.6   Figure E- 335: B3.6   Figure E- 336: B3.6
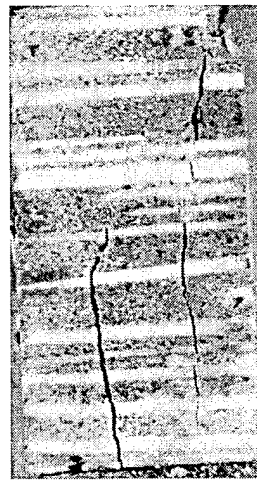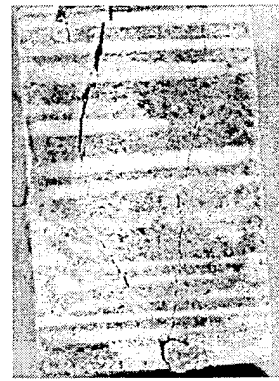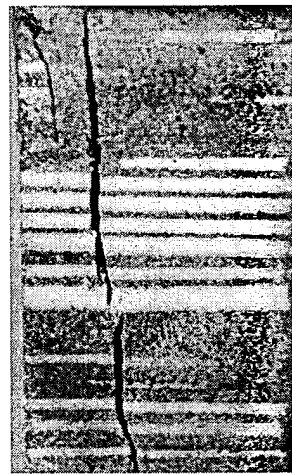
Figure E- 337: B3.6   Figure E- 338: B3.6
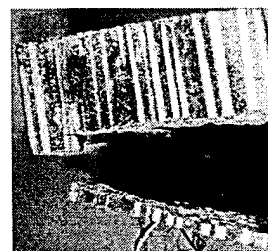
Figure E- 339: B3.7   Figure E- 340: B3.7   Figure E- 341: B3.7
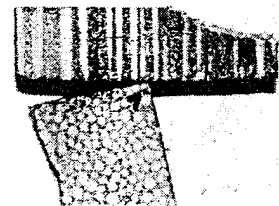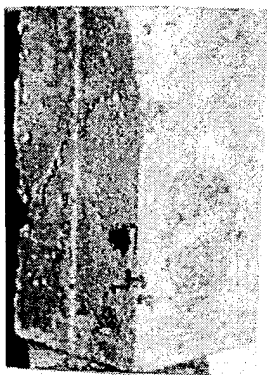
Figure E- 342: TR 1.1
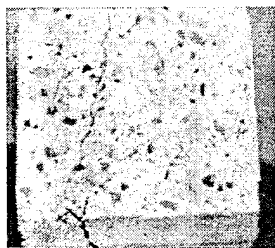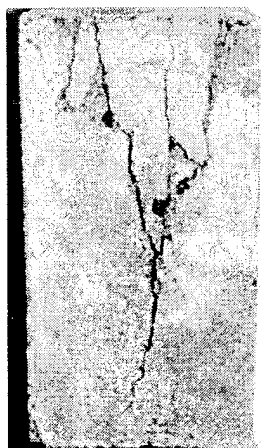
Figure E- 343: TR 1.2   Figure E- 344: TR 1.2   Figure E- 345: TR 1.2   Figure E- 346: TR 1.2
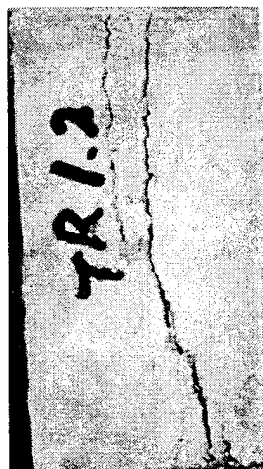
Figure E- 347: TR 1.3   Figure E- 348: TR 1.3   Figure E- 349: TR 1.3   Figure E- 350: TR 1.3

Figure E- 351: TR 1.4   Figure E- 352: TR 1.4   Figure E- 353: TR 1.4   Figure E- 354: TR 1.4
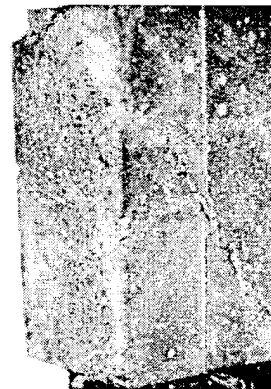
Figure E- 355: TR 2.1   Figure E- 356: TR 2.1   Figure E- 357: TR 2.1
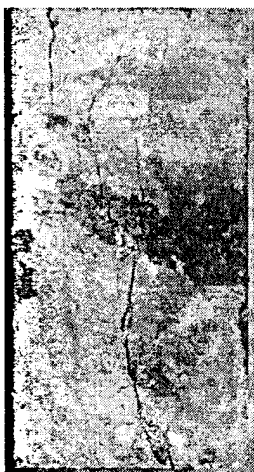
Figure E- 358: TR 2.2   Figure E- 359: TR 2.2   Figure E- 360: TR 2.2   Figure E- 361: TR 2.2
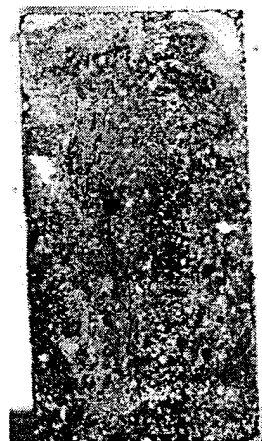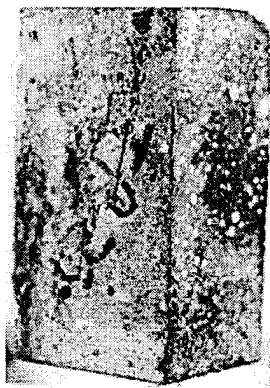
Figure E- 362: TR 2.3   Figure E- 363: TR 2.3   Figure E- 364: TR 2.3   Figure E- 365: TR 2.3
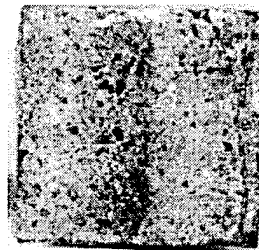
Figure E- 366: TR 2.4

Figure E- 367: TR 3.1
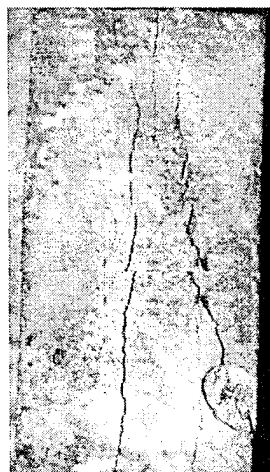
Figure E- 368: TR 3.1   Figure E- 369: TR 3.1   Figure E- 370: TR 3.1   Figure E- 371: TR 3.1
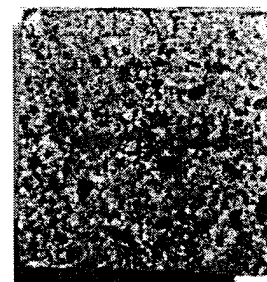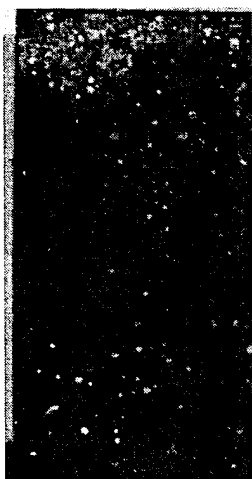
Figure E- 372: TR 3.2

Figure E- 373: TR 3.3

Figure E- 374: TR 3.3

Figure E- 375: TR 3.4

Figure E- 376: TR 3.4
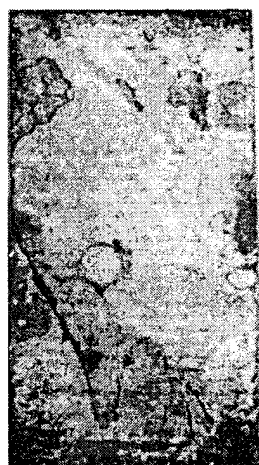
Figure E- 377: TR 3.4
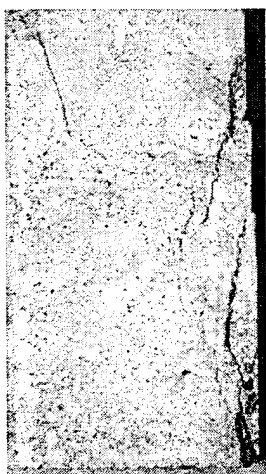
Figure E- 378: TR 4.1
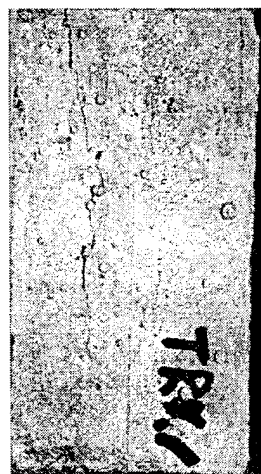
Figure E- 379: TR 4.1
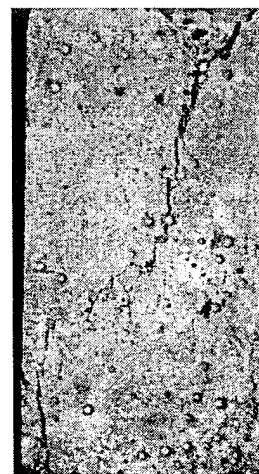
Figure E- 380: TR 4.1
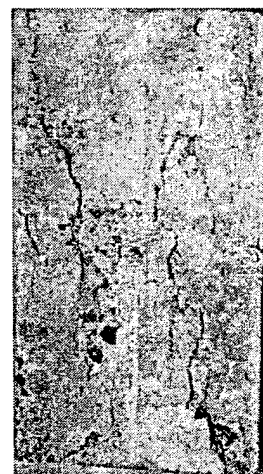
Figure E- 381: TR 4.1

Figure E- 382: TR 4.2
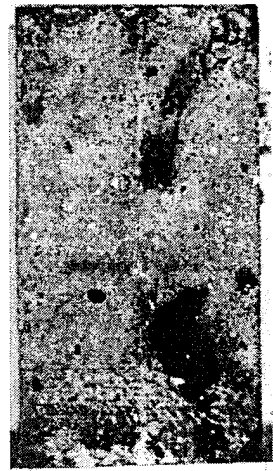
Figure E- 383: TR 4.3
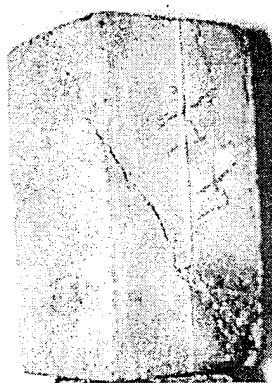
Figure E- 384: TR 4.4   Figure E- 385: TR 4.4

APPENDIX F

CONSTITUTIVE MODEL DRIVER PROGRAM

This appendix contains the list of FORTRAN code used to perform the numerical analysis on a plasticity model discussed in section 5 of this dissertation. Several versions of the code were used during the analysis. This version was the last one used in the analysis. The code contains a main driver program called DISDRV.FOR. This main driver calls up the subroutine CONSTIT which in turn calls up several other subroutines: ISOHARD, LOCAL, DETER3, and DETER4.

The main driver program gets input from a data file and output to several data files. The data in the input file tells the program what the material properties are, the load path(s) to be considered, the increments of strain to be applied, and the criteria for ending each portion of the load path; i.e. apply equal strain to all direction until a prescribed mean pressure is attained. To accomplish the application of the strain increments to the model the driver calls the subroutine CONSTIT.

CONSTIT contains the constitutive model. It applies strain increments to the model then evaluates if the increment puts the new stress state on or out side the limit surface. If it is with in the limit surface the program proceeds elastically. If the State is on the limit surface the rate of change of PHI, the limit surface parameter is evaluated to see if the material is moving along the limit surface elastically or plastically. If the strain increment is plastic the program determines the amount of plastic deformation by calculating DLAMBDA that put the stress state back on to the limit surface. ISOHARD is used to apply the hardening (softening) function. The program then forms the tangent stiffness tensor in matrix form (4X4) and calculated the determinant of the tangent stiffness and symmetric portion of the tangent stiffness. The program then calls subroutine LOCAL before returning to the driver program.

LOCAL calculates the determinant of the acoustic tensor and the symmetric portion of the acoustic tensor. This accomplished by setting up the vector n such that it varies across three planes, X_1-X_2, X_1-X_3, X_2-X_3, one degree at a time from 0 to 180 degrees. For example the vector n was set $= \cos \vartheta \, \underline{i} + \sin \vartheta \, \underline{j} + 0 \, \underline{k}$ for the X_1-X_2 plane the angle ϑ, was changed from 0° to 180° in increments of 1°; thus, moving from the positive X_1 direction to the negative X_1 direction. At each possible angle the acoustic tensor was formulated and the determinant of the symmetric portion of the tensor and the tensor itself were calculated. The values of the determinant versus the angle were stored for later use. Figure 5-5 provides an example of the output put in graphical form.

```fortran
C DISDRVB.FOR
C THIS PROGRAM IS A DRIVER PROGRAM.
C THIS PROGRAM IS USED AS A DRIVER FOR
C CONSTITUTIVE MODEL PROGRAMS
C THIS PROGRAM DRIVES THE SUBROUTINE CONSTIT
C
C COMMON BLOCKS
      IMPLICIT REAL*8 (A-H,P-Z)
      CHARACTER*72 ITITLE
      CHARACTER*12 FILOUT,FILEP,FILEP1,FILEP2,FILEP3
      CHARACTER*4 FILIN
      INTEGER NC,NMAX
C
   COMMON /MATPRO/ YM,PR,H0,HL,EPBARL,Q,AL,E1,E2,TG,G0,E(3,3,3,3),PR2
      COMMON /STRESS/ SG11,SG22,SG33,SG12,P
      COMMON /STRAIN/ STT11,STT22,STT33,STT12,DSTT11,DSTT22
     +          ,DSTT33,DSTT12,STI11,STI22,STI33,STI12
     +          ,STE11,STE22,STE33,STE12,STIVOL,STEVOL
     +          ,STTVOL,EPS,QEP
    COMMON /MISCW/ IPSS,IEL,ITER,H,EPBAR,NITER
   + ,DETC,DETCT
      COMMON /LOCAL/ THEDA(3),DET(3),C(3,3,3,3),IP,IPL
C
C DIMENSION ARRAYS
C
C
C ASKUSER FOR THE INPUT AND OUTPUT FILE NAMES
C
      WRITE(*,*) 'INPUT THE DATA FILENAME'
      READ(*,10) FILIN
      OPEN (1,FILE=FILIN,STATUS='OLD')
      OPEN (4,FILE='FILOUT.DAT',STATUS='NEW')
      WRITE (4,72) FILIN,'.ANS'
      WRITE (4,72) FILIN,'.CSV'
      WRITE (4,72) FILIN,'1.CSV'
      WRITE (4,72) FILIN,'2.CSV'
      WRITE (4,72) FILIN,'3.CSV'
      CLOSE (4,STATUS='KEEP')
      OPEN (4,FILE='FILOUT.DAT',STATUS='OLD')
      READ(4,10) FILOUT
      READ (4,10) FILEP
      READ (4,10) FILEP1
      READ (4,10) FILEP2
      READ (4,10) FILEP3
      CLOSE (4,STATUS='DELETE')
     WRITE(*,*)'THE OUTPUT WILL BE PLACED IN THE FOLLOWING FILES'
      WRITE(*,*)FILOUT
      WRITE(*,*)FILEP
      WRITE(*,*)FILEP1
      WRITE(*,*)FILEP2
      WRITE(*,*)FILEP3
      OPEN (2,FILE=FILOUT,STATUS='NEW')
C
C SET FORMATS
```

```
C
 72     FORMAT (A,A)
C
 10     FORMAT (A)
 20      FORMAT ('CYCLE =',1X,I5,43X,A7,G10.4,A4,G10.4)
 17     FORMAT (25X,A7,29X,A8)
 15     FORMAT (A7,1X,4(G10.4,1X),4X,A7,G10.4)
 25     FORMAT (A,' = ',I5)
 30     FORMAT (2(A,' = ',G10.4,5X))
 35     FORMAT (24(A,','))
 37     FORMAT (15(G10.4,','),I5,',',8(G10.4,','))
 45     FORMAT (A,' = ',G10.4)
 57     FORMAT (12X,4(A2,9X))
 55     FORMAT (5(G10.4,1X))
399     FORMAT (46(I3,A))
C
C OPEN PLOT FILE
C
        OPEN(3,FILE=FILEP,STATUS='NEW')
        OPEN(5,FILE=FILEP1,STATUS='NEW')
        OPEN(6,FILE=FILEP2,STATUS='NEW')
        OPEN(7,FILE=FILEP3,STATUS='NEW')
C
C GET INFO FROM THE INPUT FILE
C
        READ (1,10,END=1000) ITITLE
        READ(1,*) YM
        READ(1,*) PR
        READ(1,*) H0
        READ(1,*) HL
        READ(1,*) EPBARL
        READ(1,*) Q
        READ (1,*) AL
        READ (1,*) EPS
        WRITE(2,10) ITITLE
        WRITE(2,30) 'YM',YM,'PR',PR
        WRITE(2,30) 'H0',H0,'HL',HL
        WRITE(2,30) 'EPBARL',EPBARL,'Q',Q
        WRITE(2,30) 'ALPHA',AL
        WRITE (2,30) 'EPS',EPS
        WRITE(2,10) ' '
C
C PUT HEADER ON THE PLOT FILE
C
        WRITE(3,10) ITITLE
        WRITE(5,10) ITITLE
        WRITE(6,10) ITITLE
        WRITE(7,10) ITITLE
        WRITE(5,10) 'DET(N*C*N) VS THEDA'
        WRITE(6,10) 'DET(N*C*N) VS PHI'
        WRITE(7,10) 'DET(N*C*N) VS BETA'
        WRITE(5,10) '1,2 PLANE'
        WRITE(6,10) '1,3 PLANE'
        WRITE(7,10) '2,3 PLANE'
```

```
      WRITE(5,10) 'THEDA'
      WRITE(6,10) 'PHI'
      WRITE(7,10) 'BETA'
      WRITE(5,10) 'DEGREES'
      WRITE(6,10) 'DEGREES'
      WRITE(7,10) 'DEGREES'
      WRITE(5,399)(I,',', I=0,180,4)
      WRITE(6,399)(I,',', I=0,180,4)
      WRITE(7,399)(I,',', I=0,180,4)
       WRITE(3,35) 'STE11','STE22','STE33','STE12','STT11'
    + ,'STT22','STT33','STT12','STEVOL','STTVOL','SG11','SG22'
    + ,'SG33','SG12','P','NITER','DETC','DETCT','THEDA','DET(1)'
    + ,'PHI','DET(2)','BETA','DET(3)','EP'
C
C INITIALIZE PARAMETERS
C
      STT11=0
      STT22=0
      STT33=0
      STT12=0
      STI11=0
      STI22=0
      STI33=0
      STI12=0
      STE11=0
      STE22=0
      STE33=0
      STE12=0
      SG11=0
      SG22=0
      SG33=0
      SG12=0
      STTVOL=0
      STIVOL=0
      EPBAR = 0
      STEVOL = 0
      IPTH=0
C
C SETUP ALL OF THE ELASTICITY PARAMETERS
C
      PR1=1.-PR
      PR2=PR/PR1
      PR3=1.+PR
      PR4=1./(PR3*(1.-2.*PR))
      E1=YM*PR1*PR4
      E2=YM*PR*PR4
      TG=YM/PR3
      G0=TG/2
C
C SETUP THE ELASTICITY TENSOR
C
      DO 510 I=1,3
      DO 520 J=1,3
      DO 530 K=1,3
```

```
        DO 540 L=1,3
        E(I,J,K,L)=0
540   CONTINUE
530   CONTINUE
520   CONTINUE
510   CONTINUE
        DO 550 I=1,3
        E(I,I,I,I)=E1
550   CONTINUE
        DO 560 I=1,3
        DO 570 J=1,3
        IF (I .EQ. J) GOTO 570
        E(I,I,J,J)=E2
570   CONTINUE
560   CONTINUE
        DO 580 I=1,3
        DO 590 J=1,3
        IF (I .EQ. J) GO TO 590
        E(I,J,I,J)=G0
        E(I,J,J,I)=G0
        E(J,I,J,I)=G0
        E(J,I,I,J)=G0
590   CONTINUE
580   CONTINUE
C
200     CONTINUE
        IPTH=IPTH+1
C
C READ IN THE LOAD STEP DATA
C
C D11X - STRAIN INCREMENT IN THE X DIRECTION
C D22X - STRAIN INCREMENT IN THE Y DIRECTION
C D33X - STRAIN INCREMENT IN THE Z DIRECTION
C D12X - STRAIN INCREMENT IN THE XY DIRECTION
C SGL  - STRESS EXIT LEVEL
C PL   - PRESSURE EXIT LEVEL
C IPSS - 1 UNIAXIAL STRESS
C       2 PLANE STRESS
C       3 3D STRAIN WITH PRINCIPAL STRAIN IN X DIRECTION
C NMAX - MAXIMUM # OF ITERATIONS FOR THIS STRESS PATH
C
C ITEST- 1 STRESS EXIT TEST
C       2 PRESSURE EXIT TEST
C       3 NO EXIT TEST
C IR   - 0 ADDITIONAL STRESS PATH, WILL REPEAT INPUT
C         AFTER COMPLETION OF THIS PATH
C       1 NO ADDITIONAL STRESS PATHS
C IWL  - WTITE OUT DATA EVERY IWL STEPS
C IPL  - STORE DATAEVERY IPL STEPS
C IEL  - 0 NOT ELESTIC MATERIAL
C       1 ELASTIC MATERIAL
C
C
C READ IN DATA
```

```
C
      READ (1,*,END=1000) D11X
      READ (1,*,END=1000) D22X
      READ (1,*,END=1000) D33X
      READ (1,*,END=1000) D12X
      READ (1,*,END=1000) SGL
      READ (1,*,END=1000) PL
      READ (1,*,END=1000) IPSS
      READ (1,*,END=1000) NMAX
      READ (1,*,END=1000) ITEST
      READ (1,*,END=1000) IR
      READ (1,*,END=1000) IWL
      READ (1,*,END=1000) IPL
      READ (1,*,END=1000) IEL
C
C WRITE THE DATA
C
      WRITE(2,45) 'D11X',D11X
      WRITE(2,45) 'D22X',D22X
      WRITE(2,45) 'D33X',D33X
      WRITE(2,45) 'D12X',D12X
      WRITE(2,45) 'SGL',SGL
      WRITE(2,45) 'PL',PL
      WRITE(2,25) 'IPSS',IPSS
      WRITE(2,25) 'NMAX',NMAX
      WRITE(2,25) 'ITEST',ITEST
      WRITE(2,25) 'IR',IR
      WRITE(2,25) 'IWL',IWL
      WRITE(2,25) 'IPL',IPL
      WRITE(2,25) 'IEL',IEL
       WRITE(2,10)' '
       WRITE(2,10)' '
      WRITE(2,17) 'STRAINS','STRESSES'
      WRITE(2,57) '11','22','33','12'
C
      IP = 0
      IW = 0
      DO 500 NC = 1 ,NMAX
       IP =IP + 1
       IW =IW + 1
       DSTT11 = D11X
       DSTT22 = D22X
       DSTT33 = D33X
       DSTT12 = D12X
C
C   CALL CONSTITUTIVE LAW SUBROUTINE CONSTIT
C
      CALL CONSTIT
C
C OR IF(IP .EQ. IPL) REMENMBER TO RESET IW & IP TO 0
C
      IF (IW .EQ.IWL .OR. NC .EQ. 1) THEN
       IW=0
      WRITE (2,20) NC,'SG11 = ',SG11,'P = ',P
```

```fortran
      WRITE (2,15) 'ELASTIC',STE11,STE22,STE33,STE12,'SG22 = '
     + ,SG22
      WRITE (2,15) 'PLASTIC',STI11,STI22,STI33,STI12,'SG33 = '
     + ,SG33
      WRITE (2,15) 'TOTAL',STT11,STT22,STT33,STT12,'SG12 = '
     + ,SG12
      WRITE (2,10) ' '
      ENDIF
      IF (IP .EQ. IPL .OR. NC .EQ. 1) THEN
      IP=0
      WRITE(3,37) STE11,STE22,STE33,STE12,STT11
     + ,STT22,STT33,STT12,STEVOL,STTVOL,SG11,SG22
     + ,SG33,SG12,P,NITER,DETC,DETCT,THEDA(1),DET(1)
     + ,THEDA(2),DET(2),THEDA(3),DET(3),QEP
      ENDIF
C
C
      GO TO (300,400,500) ITEST
C
 300    IF(ABS(SG11) .GE. SGL) GO TO 600
      GOTO 500
 400    IF (ABS(P) .GE. PL) GO TO 600
      GOTO 500
 500    CONTINUE
C
 600    CONTINUE
      WRITE (2,20) NC,'SG11 = ',SG11,'P = ',P
      WRITE (2,15) 'ELASTIC',STE11,STE22,STE33,STE12,'SG22 = '
     + ,SG22
      WRITE (2,15) 'PLASTIC',STI11,STI22,STI33,STI12,'SG33 = '
     + ,SG33
      WRITE (2,15) 'TOTAL',STT11,STT22,STT33,STT12,'SG12 = '
     + ,SG12
      WRITE (2,10) ' '
      WRITE(3,37) STE11,STE22,STE33,STE12,STT11
     + ,STT22,STT33,STT12,STEVOL,STTVOL,SG11,SG22
     + ,SG33,SG12,P,NITER,DETC,DETCT,THEDA(1),DET(1)
     + ,THEDA(2),DET(2),THEDA(3),DET(3),QEP
      IF (IR .NE. 1) GOTO 200
C
C
C
 1000    CONTINUE
C
C
C
      STOP
      END
```

```
C SUBROUTINE CONSTIT
C
C
C NEWBETA.FOR
C------------------------------------------------------------
C LIMIT SURFACE
C PHI = SG11 - 3.65 ((SG22+SG33)/2)+ 2.74*EXP(-6.35(SG22+SG33)/2) - H(EPBAR)
C NON-ASSOCIATED FLOW
C       | 1      0       0   |
C   M = | 0    -BETA     0   |
C       | 0      0     -BETA |
C
C   BETA = 3.5*EXP(-2*(SG22+SG33)/2)+1.2*EXP(-.04*(SG22+SG33)/2)
C
C H(EPBAR)=H0                              EPBAR<=0
C H(EPBAR)=H0 + (HL-H0)*SIN((PI/2)*(EPBAR/EPBARL)^Q)   0<EPBAR<=EPBARL
C H(EPBAR)=-AL*(EPBAR-EPBARL)+HL                EPBARL<EPBAR
C
C COMPRESSION IS POSSITIVE
C MEAN PRESSURE P = 1/3 (SG11+SG22+SG33)
C THIS MODEL IS FOR SG11 >= (SG22 = SG33)
C------------------------------------------------------------
C
C  PLASTIC VERSION FOR FRICTIONAL MATERIALS
C  ONE PRINCIPAL COMPONENT OF STRAIN REQUIRED
C  OPTIONS FOR CONSTITUTIVE EQUATIONS
C    IPSS=1  (UNIAXIAL STRESS)
C    IPSS=2  (PLANE STRESS)
C    IPSS=3  (3D STRAIN {TRIAXIAL STRESS})
C
C  THIS VERSION ASSUMES TOTAL STRAIN INCREMENTS ARE SPECIFIED
C    IEL=1   PURELY ELASTIC
C
C    PR = POISSON'S RATIO
C    YM = YOUNGS MODULUS
C    TG = 2*MODULUS OF RIGIDITY
C
C------------------------------------------------------------
C
C
C THIS PROGRAM IS FOR ISOTROPIC MATERIALS
C THIS MODEL IS FOR TRIAXIAL COMPRESSION
C
C
    SUBROUTINE CONSTIT
    IMPLICIT REAL*8 (A-H,P-Z)
    COMMON /MATPRO/ YM,PR,H0,HL,EPBARL,Q,AL,E1,E2,TG,G0,E(3,3,3,3),PR2
    COMMON /STRESS/ SG11,SG22,SG33,SG12,P
    COMMON /STRAIN/ STT11,STT22,STT33,STT12,DSTT11,DSTT22,DSTT33
   +         ,DSTT12,STI11,STI22,STI33,STI12,STE11,STE22
   +         ,STE33,STE12,STIVOL,STEVOL,STTVOL,EPS,QEP
    COMMON  /MISCW/ IPSS,IEL,ITER,H,EPBAR,NITER
   +,DETC,DETCT
    COMMON  /LOCAL/ THEDA(3),DET(3),C(3,3,3,3),IP,IPL
```

```
      DIMENSION QM(3,3),QN(3,3),QC(4,4),GAM(3,3,3,3)
      DIMENSION QCT(4,4),INDX(4)
      REAL*8 QMSQ
C
      DATA ITERM/400/,THIRD/0.33333333/
C
C  INITIALIZE VARIABLES FOR THIS STEP
C
      NITER=0
      DLAMB = 0.0
      PI=3.141592654
      ITER=0
C
C    INITIALIZE VARIABLES FOR NEW DLAMBS SEARCH ROUTINE
C
      QM11=1
      DLAMBMIN=0
      DLAMBMAX=(STE11 + DSTT11)/QM11
C
C  SET THE INITIAL STRESSES EQUAL TO THE CURRENT STRESSSES
C
      SGZ11=SG11
      SGZ22=SG22
      SGZ33=SG33
      SGZ12=SG12
C
C  SET THE INITIAL INELASTIC STRAIN INCREMENTS TO BE ZERO
C
      DSTI11=0.0
      DSTI22=0.0
      DSTI33=0.0
      DSTI12=0.0
C
C  SET THE ELASTIC STRAIN INCREMENTS TO BE THE NEW TOTAL STRAIN INCREMENT
C
      DSTE11=DSTT11
      DSTE22=DSTT22
      DSTE33=DSTT33
      DSTE12=DSTT12
C
C  STRAIN CALCULATIONS FOR UNIAXIAL STRESS
C
      IF(IPSS.EQ.1) THEN
         DSTE22=-PR*DSTE11
         DSTE33=DSTE22
C
C  STRAIN CALCULATIONS FOR PLANE STRESS
C
       ELSE
        IF (IPSS.EQ.2) DSTE33=-PR2*(DSTE11+DSTE22)
       ENDIF
C
C INITIALIZE DEPBAR
C
```

```fortran
      DEPBAR=0
      EPBARZ=EPBAR
C
C   UPDATE THE STRESSES
C
   10 CONTINUE
      DSG11=E1*DSTE11+E2*(DSTE22+DSTE33)
      DSG22=E1*DSTE22+E2*(DSTE11+DSTE33)
      DSG33=E1*DSTE33+E2*(DSTE11+DSTE22)
      DSG12=TG*DSTE12
      SG11=SGZ11+DSG11
      SG22=SGZ22+DSG22
      SG33=SGZ33+DSG33
      SG12=SGZ12+DSG12
      P=THIRD*(SG11+SG22+SG33)
C
C
      ITER=ITER+1
C
C  CHECK FOR ELASTIC PROBLEM (IEL=1)
C
      IF (IEL.EQ.1) GO TO 30
C
C   EVALUATE THE LIMIT FUNCTION
C
C CALCULATE DEPBAR AND EPBAR
C
      DEPBAR=(2*(DSTI11**2+DSTI22**2+DSTI33**2+2*DSTI12**2)/3)**.5
      EPBAR=EPBARZ+DEPBAR
C
C GET H FROM HARDENING SUBROUTINE
C
      CALL ISOHARD
C
C CALC (PHI)
C
C    WRITE (*,*) 'CALC PHI'
      PHI=SG11-3.65*((SG22+SG33)/2)+2.74*EXP(-3.175*(SG22+SG33))-H
C
C
      PTEST=PHI/HL
C
C  CHECK FOR ELASTIC CASE IN CONJUNCTION WITH THE FIRST ITERATION
C    IN OTHER WORDS THIS STEP MAY BE PURELY ELASTIC
C
      IF(ITER.EQ.1.AND.PTEST.LT.EPS) GO TO 30
C
C  CHECK FOR PLASTIC SOLUTION
C
      IF(ITER.GT.1.AND.ABS(PTEST).LT.EPS) GO TO 30
C
C NEED TO FIND DELTA LAMDA BY DLAMDA=-F/FPRIME
C WHERE FPRIME =-(DF/DS):E:M - EP
C N = (DF/DS)
```

```
C
C SET UP N=(DPHI)/D(SIGMA)DENOTED BY QN
C
      QN11=1.0
      QN22=-1.825-2.74*3.175*EXP(-3.175*(SG22+SG33))
      QN33=-1.825-2.74*3.175*EXP(-3.175*(SG22+SG33))
      QN12=0.0
C
C SETUP M DENOTED BY QM
C
      BETA = 3.5*EXP(-2*(SG22+SG33)/2)+1.2*EXP(-.04*(SG22+SG33)/2)
      QM11=1.0
      QM22=-BETA
      QM33=-BETA
      QM12=0.0
C
C CALCULATE E:N
C
      IF (ITER .EQ. 1) THEN
      SPR11=E1*QN11+E2*(QN22+QN33)
      SPR22=E1*QN22+E2*(QN11+QN33)
      SPR33=E1*QN33+E2*(QN11+QN22)
      SPR12=TG*QN12
C
C NOW CALCULATE EP
C
C
C FIRST CALCULATE ((2/3)* [EP]:[M])/EPBAR
C
      IF (EPBAR .NE. 0) THEN
C
      QMSQ=QM11*(STI11 + DSTI11)
      QMSQ=QMSQ+QM22*(STI22 + DSTI22)
      QMSQ=QMSQ+QM33*(STI33 + DSTI33)
      QMSQ=QMSQ+2*QM12*(STI12 + DSTI12)
      QMSQ=2*QMSQ/3
      QMSQ=QMSQ/EPBAR
      ELSE
      QMSQ = 1
      ENDIF
C
C NOW GET EP
C
C     WRITE (*,*) 'EPBAR =',EPBAR,' EPBARL =',EPBARL
      IF (EPBAR .LE. 0.0 ) THEN
      QEP = 0.0
      ELSE
         IF (EPBAR .LE. EPBARL) THEN
         A=(HL-H0)*(Q*PI/2)*((EPBAR)**(Q-1))*((EPBARL)**(-Q))
         QEP=A*QMSQ*COS(((EPBAR/EPBARL)**Q)*PI/2)
         ELSE
          A=-AL
           QEP=A*QMSQ
         ENDIF
```

```fortran
          ENDIF
C
C  COMPUTE PHI PRIME = - M:E:N - EP
C
      PHIPRM=-(SPR11*QM11+SPR22*QM22+SPR33*QM33+
     +     2*SPR12*QM12) - QEP
C
      IF(PHIPRM.GE.0) THEN
C
C  RETURN WITH AN ERROR MESSAGE
C
          WRITE (*,*) ' '
          WRITE (*,*) '***********************************'
          WRITE (*,*) '*                           *'
          WRITE (*,*) '*  PROBLEM IN ELSTRS WITH PHIPRM  *'
          WRITE (*,*) '*   BEING CALCULATED AS POSITIVE  *'
          WRITE (*,*) '*                           *'
          WRITE (*,*) '***********************************'
          WRITE (*,*) ' '
      ENDIF
C
      ENDIF
C
C  COMPUTE DLAMDA USING SECANT APPROXIMATION
C
C
      DLAMBZ=DLAMBS
      IF(ITER.GT.1) THEN
          IF ((PHIZ-PHI) .LE. 0) THEN
              WRITE (*,*) 'PHIZ-PHI <= 0'
              WRITE (*,*) NITER
              WRITE (*,*) PHI
              WRITE (*,*) PHIZ
              WRITE (*,*) H
              WRITE (*,*) EPBAR
              WRITE (*,*) DLAMBS
          ENDIF
          DLAMBS=DLAMBZ*PHI/(PHIZ-PHI)
      ELSE
          DLAMBS = -.1*PHI/PHIPRM
      ENDIF
C
C
      PHIZ=PHI
C
C    WRITE(*,*) 'CALC STRAIN INCREMENTS'
C
C  COMPUTE THE INELASTIC STRAIN INCREMENTS
C
      SUBI11=DLAMBS*QM11
      SUBI22=DLAMBS*QM22
      SUBI33=DLAMBS*QM33
      SUBI12=DLAMBS*QM12
C
```

```fortran
C  COMPUTE TOTAL INELASTIC STRAIN
C
      DSTI11=SUBI11
      DSTI22=SUBI22
      DSTI33=SUBI33
      DSTI12=SUBI12
C
C  COMPUTE THE ELASTIC STRAIN INCREMENT
C
      DSTE11=DSTT11-SUBI11
      DSTE22=DSTT22-SUBI22
      DSTE33=DSTT33-SUBI33
      DSTE12=DSTT12-SUBI12
C
C  ADJUST FOR SPECIAL CONDITIONS (ACCORDING TO STRESS PATH CHOSEN)
C
      IF(IPSS.EQ.1) THEN
         DSTE22=-PR*DSTE11
         DSTE33=DSTE22
       ELSE
         IF (IPSS.EQ.2) DSTE33=-PR2*(DSTE11+DSTE22)
       ENDIF
       IF(ITER.LE.ITERM) GO TO 10
C
C  UPDATE STRAINS
C
   30 CONTINUE
      STI11=STI11+DSTI11
      STI22=STI22+DSTI22
      STI33=STI33+DSTI33
      STI12=STI12+DSTI12
      STIVOL=STI11+STI22+STI33
C
      STE11=STE11+DSTE11
      STE22=STE22+DSTE22
      STE33=STE33+DSTE33
      STE12=STE12+DSTE12
      STEVOL=STE11+STE22+STE33
C
      DSTT11=DSTI11+DSTE11
      DSTT22=DSTI22+DSTE22
      DSTT33=DSTI33+DSTE33
      DSTT12=DSTI12+DSTE12
C
      STT11=STT11+DSTT11
      STT22=STT22+DSTT22
      STT33=STT33+DSTT33
      STTVOL=STT11+STT22+STT33
C
C
C
      SG11=E1*STE11+E2*(STE22+STE33)
      SG22=E1*STE22+E2*(STE11+STE33)
      SG33=E1*STE33+E2*(STE11+STE22)
```

```
      SG12=TG*STE12
      EPBAR=(2*(STI11**2+STI22**2+STI33**2+2*STI12**2)/3)**.5
      IF(IP .EQ. IPL) THEN
C
C NOW CALCULATE K
C
C SET UP N=(DPHI)/D(SIGMA)DENOTED BY QN
C
      QN11=1.0
      QN22=-1.825-2.74*3.175*EXP(-3.175*(SG22+SG33))
      QN33=-1.825-2.74*3.175*EXP(-3.175*(SG22+SG33))
      QN12=0.0

C
C SETUP M DENOTED BY QM
C
      BETA = 3.5*EXP(-2*(SG22+SG33)/2)+1.2*EXP(-.04*(SG22+SG33)/2)
      QM11=1.0
      QM22=-BETA
      QM33=-BETA
      QM12=0.0
C
C CALCULATE E:N
C
      SPR11=E1*QN11+E2*(QN22+QN33)
      SPR22=E1*QN22+E2*(QN11+QN33)
      SPR33=E1*QN33+E2*(QN11+QN22)
      SPR12=TG*QN12
C
C  CALC QK = N:E:M
C
      QK=(SPR11*QM11+SPR22*QM22+SPR33*QM33+
     +      2*SPR12*QM12)
C
C CALCULATE [M] IN MATRIX FORM
C
      DO 710 I=1,3
      DO 720 J=1,3
      QM(I,J)=0
 720  CONTINUE
 710  CONTINUE
      QM(1,1)=QM11
      QM(2,2)=QM22
      QM(3,3)=QM33
      QM(1,2)=QM12
      QM(2,1)=QM12
C
C NOW SETUP [N] IN MATRIX FORM
C
      DO 730 I=1,3
      DO 740 J=1,3
      QN(I,J)=0
 740  CONTINUE
 730  CONTINUE
```

```fortran
      QN(1,1)=QN11
      QN(2,2)=QN22
      QN(3,3)=QN33
      QN(1,2)=QN12
      QN(2,1)=QN12
C
C NOW CALCULATE EP
C
C
C FIRST CALCULATE ((2/3)* [EP]:[M])/EPBAR
C
      IF (EPBAR .NE. 0) THEN
C
      QMSQ=QM11*STI11
      QMSQ=QMSQ+QM22*STI22
      QMSQ=QMSQ+QM33*STI33
      QMSQ=QMSQ+2*QM12*STI12
      QMSQ=2*QMSQ/3
      QMSQ=QMSQ/EPBAR
C
C     WRITE (*,*) 'QMSQ =',QMSQ
C
      ELSE
      QMSQ=1
      ENDIF
C
C NOW GET EP
C
      WRITE (*,*) 'EPBAR =',EPBAR,' EPBARL =',EPBARL
       IF (EPBAR .LE. 0.0 ) THEN
       QEP = 0.0
       ELSE
         IF (EPBAR .LE. EPBARL) THEN
         A=(HL-H0)*(Q*PI/2)*((EPBAR)**(Q-1))*((EPBARL)**(-Q))
         QEP=A*QMSQ*COS(((EPBAR/EPBARL)**Q)*PI/2)
         ELSE
          A=-AL
          QEP=A*QMSQ
         ENDIF
       ENDIF
C     WRITE(*,*) 'A =',A,' ESTAR =',ESTAR
C
C     WRITE (*,*) 'QEP = ',QEP
C     WRITE (*,*) 'CALC THE TENSOR C'
C NOW CALCULATE THE TENSOR C AND THE MATRIX REPRESENTATION [C]
C
C     WRITE (*,*) 'CALC GAMMA'
C     GAMMA = E:N (X) M:E
C
C FIRST CALC GAMMAS
C
      DO 610 I=1,3
      DO 620 J=1,3
      DO 630 II=1,3
```

```fortran
      DO 640 JJ=1,3
      GAM(I,J,II,JJ)=0
      DO 650 K=1,3
      DO 660 L=1,3
      DO 670 M=1,3
      DO 680 N=1,3
      GAM(I,J,II,JJ)=GAM(I,J,II,JJ)+E(I,J,K,L)*QM(K,L)*
     +QN(M,N)*E(M,N,II,JJ)
  680 CONTINUE
  670 CONTINUE
  660 CONTINUE
  650 CONTINUE
  640 CONTINUE
  630 CONTINUE
  620 CONTINUE
  610 CONTINUE
C
C     WRITE (*,*) 'CALC C TENSOR'
C
C NEXT FORM THE TENSOR C
C
      DO 810 I=1,3
      DO 820 J=1,3
      DO 830 K=1,3
      DO 840 L=1,3
      IF (DLAMBS .GT. 0.0) THEN
        C(I,J,K,L)=E(I,J,K,L)-GAM(I,J,K,L)/(QK+QEP)
      ELSE
        C(I,J,K,L)=E(I,J,K,L)
      ENDIF
  840 CONTINUE
  830 CONTINUE
  820 CONTINUE
  810 CONTINUE
C
C     WRITE (*,*) 'CALC [C]'
C
C FORM [C]
C
      DO 850 I=1,3
      DO 860 J=1,3
      QC(I,J)=C(I,I,J,J)
  860 CONTINUE
  850 CONTINUE
      DO 870 I=1,3
      QC(I,4)=C(I,I,1,2)+C(I,I,2,1)
      QC(4,I)=C(1,2,I,I)
  870 CONTINUE
      QC(4,4)=C(1,2,1,2)+C(1,2,2,1)
C
C     WRITE (*,*) 'CALC [CT]'
C
C FORM [CT] = [C]+[C]TRANSPOSE
C
```

```
      DO 410 I=1,4
      DO 420 J=1,4
      QCT(I,J)= QC(I,J)+QC(J,I)
  420 CONTINUE
  410 CONTINUE
C
C DEBUG WRITE STATEMENTS
C
C     WRITE (*,*) 'K =',QK,'EP =',QEP
C     WRITE (*,*) 'C(1,1,1,1)= ', C(1,1,1,1)
C     WRITE (*,*) 'C(2,2,2,2)= ', C(2,2,2,2)
C     WRITE (*,*) 'C(3,3,3,3)= ', C(3,3,3,3)
C     WRITE (*,*) 'C(1,1,2,2)= ', C(1,1,2,2)
C     WRITE (*,*) 'C(1,1,3,3)= ', C(1,1,3,3)
C     WRITE (*,*) 'C(2,2,1,1)= ', C(2,2,1,1)
C     WRITE (*,*) '          ', QC(1,1),QC(1,2),QC(1,3)
C     WRITE (*,*) '   QC()= ', QC(2,1),QC(2,2),QC(2,3)
C     WRITE (*,*) '          ', QC(3,1),QC(3,2),QC(3,3)
C
C END DEBUG WRITE STATEMENTS
C
C     WRITE (*,*) 'EVAL DET [C]'
C
C EVALUTE DET[C]
C
      CALL DETER4(QC,DETC)
C
C     WRITE (*,*) 'EVALUATE DET [CT]'
C
C EVALUATE DET[C+CTRAN]
C
      CALL DETER4(QCT,DETCT)
C
C FIND N*C*N AND EVALUATE DET [N*C*N]
C
      CALL LOC
      ENDIF
C
C
      NITER=NITER +ITER -1
C
C RETURN THE DRIVER PROGRAM
C
      RETURN
      END
```

```
C
C LOCAL.FOR
C
C THIS PROGRAM CALCULATES N*C*N FOR VARIOUS N AND
C COMPUTES THE DETERMINANT OF THE RESULT AND OF THE
C SYMMETRIC PORTIO OF THE RESULT.
C IF THE DET IS ZERO THEN THEN THE PROGRAM STOPS
C
C
C
      SUBROUTINE LOC
      IMPLICIT REAL*8 (A-H,P-Z)
      COMMON /LOCAL/ THEDA(3),DET(3),C(3,3,3,3),IP,IPL
      COMMON /STRESS/ SG11,SG22,SG33,SG12,P
      DIMENSION TN(3),DETP(181),INDX(3),T(3,3)
      PI=3.141592654
C     WRITE (*,*) 'COMING INTO LOCAL'
C
C START WITH THE 1,2 PLANE
C
      DO 10 I=0,180
      THEDA(1)=I*PI/180
      TN(1)=COS(THEDA(1))
      TN(2)=SIN(THEDA(1))
      TN(3)=0
C
C CALCULATE T=N*C*N
C
      DO 20 J=1,3
      DO 30 K=1,3
      T(J,K)=0
      DO 40 L=1,3
      DO 50 M=1,3
      T(J,K)=T(J,K)+TN(L)*TN(M)*C(L,J,K,M)
 50   CONTINUE
 40   CONTINUE
 30   CONTINUE
 20   CONTINUE
C
C CALCULATE THE SYMMETRIC PART OF T
C
      DO 21 J=1,3
      DO 23 K=1,3
      T(J,K)=.5*(T(J,K)+T(K,J))
 23   CONTINUE
 21   CONTINUE
C
C CALCULATE THE DETERMINANT
C
C     WRITE (*,*) 'GOING TO LUDCMP FROM LOC'
      CALL DETER3(T,D)
C     CALL LUDCMP(T,3,3,INDX,D)
C     WRITE (*,*) 'COMING TO LOC FROM LUDCMP'
C     DO 60 J=1,3
```

```
C       D=D*T(J,J)
C60     CONTINUE
        DET(1)=D
C
C
C
      DETP(I+1)=DET(1)
      IF(DET(1) .EQ. 0) GO TO 1000
C
C
C
C
        IF(I .EQ. 0) THEN
          THEDMN=THEDA(1)
          DETMIN=DET(1)
        ELSE
          IF(DET(1) .LT. DETMIN) THEN
            THEDMN=THEDA(1)
            DETMIN=DET(1)
          ENDIF
        ENDIF
 10     CONTINUE
C
C PRINTOUT TO A FILE THEDA VS DET(1)
C
      IF (IP .EQ. IPL) THEN
      WRITE(5,22)(DETP(J+1),J=0,180,4)
      ENDIF
 22   FORMAT(46(G10.4,','))
        DET(1)=DETMIN
        THEDA(1)=THEDMN
C
C NOW DO THE 1,3 PLANE
C
      DO 110 I=0,180
      THEDA(2)=I*PI/180
      TN(1)=COS(THEDA(2))
      TN(3)=SIN(THEDA(2))
      TN(2)=0
C
C CALCULATE T=N*C*N
C
      DO 120 J=1,3
      DO 130 K=1,3
      T(J,K)=0
      DO 140 L=1,3
      DO 150 M=1,3
      T(J,K)=T(J,K)+TN(L)*TN(M)*C(L,J,K,M)
 150    CONTINUE
 140    CONTINUE
 130    CONTINUE
 120    CONTINUE
C
C CALCULATE THE SYMMETRIC PART OF T
```

```
C
      DO 121 J=1,3
      DO 122 K=1,3
      T(J,K)=.5*(T(J,K)+T(K,J))
 122    CONTINUE
 121    CONTINUE
C
C CALCULATE THE DETERMINANT
C
C     WRITE (*,*) 'GOING TO LUDCMP FROM LOC'
      CALL DETER3(T,D)
C     CALL LUDCMP(T,3,3,INDX,D)
C     WRITE (*,*) 'COMING TO LOC FROM LUDCMP'
C     DO 160 J=1,3
C      D=D*T(J,J)
C160    CONTINUE
      DET(2)=D
C
C
C
    DETP(I+1)=DET(2)
     IF (DET(2) .EQ. 0) GO TO 1000
C
C
C
     IF(I .EQ. 0) THEN
      THEDMN=THEDA(2)
      DETMIN=DET(2)
     ELSE
      IF(DET(2) .LT. DETMIN) THEN
       THEDMN=THEDA(2)
       DETMIN=DET(2)
      ENDIF
     ENDIF
 110    CONTINUE
C
C PRINTOUT TO A FILE THEDA VS DET(2)
C
     IF (IP .EQ. IPL) THEN
     WRITE(6,22)(DETP(J+1),J=0,180,4)
     ENDIF
      DET(2)=DETMIN
      THEDA(2)=THEDMN
C
C NOW DO THE 2,3 PLANE
C
     DO 210 I=0,180
     THEDA(3)=I*PI/180
     TN(2)=COS(THEDA(3))
     TN(3)=SIN(THEDA(3))
     TN(1)=0
C
C CALCULATE T=N*C*N
C
```

```fortran
      DO 220J=1,3
      DO 230 K=1,3
      T(J,K)=0
      DO 240 L=1,3
      DO 250 M=1,3
      T(J,K)=T(J,K)+TN(L)*TN(M)*C(L,J,K,M)
250   CONTINUE
240   CONTINUE
230   CONTINUE
220   CONTINUE
C
C CALCULATE THE SYMMETRIC PART OF T
C
      DO 221 J=1,3
      DO 222 K=1,3
      T(J,K)=.5*(T(J,K)+T(K,J))
222   CONTINUE
221   CONTINUE
C
C CALCULATE THE DETERMINANT
C
      CALL DETER3(T,D)
C
C     DO 260 J=1,3
C     D=D*T(J,J)
C260    CONTINUE
      DET(3)=D
C
C
C
      DETP(I+1)=DET(3)
      IF (DET(3) .EQ. 0) GO TO 1000
C
C
C
      IF(I .EQ. 0) THEN
       THEDMN=THEDA(3)
       DETMIN=DET(3)
      ELSE
       IF(DET(3) .LT. DETMIN) THEN
        THEDMN=THEDA(3)
        DETMIN=DET(3)
       ENDIF
      ENDIF
210   CONTINUE
C
C PRINTOUT TO A FILE THEDA VS DET(3)
C
      IF (IP .EQ. IPL) THEN
      WRITE(7,22)(DETP(J+1),J=0,180,4)
      ENDIF
       DET(3)=DETMIN
       THEDA(3)=THEDMN
C
```

```
C
C
 1000    CONTINUE
C       WRITE (*,*) 'LEAVING LOC'
        RETURN
        END
```

```
C ISOSOFT4.FOR
C THIS SUBROUTINE US USED BY THE SUBROUTINE CONSTIT TO
C RETURN THE VALUE OF THE ISOTROPIC SOFTENING FUNCTION
C FOR EACH STRAIN STEP
C
      SUBROUTINE ISOHARD
      IMPLICIT REAL*8 (A-H,P-Z)
    COMMON /MATPRO/ YM,PR,H0,HL,EPBARL,Q,AL,E1,E2,TG,G0,E(3,3,3,3)
      COMMON /MISCW/ IPSS,IEL,ITER,H,EPBAR,NITER,DETC,DETCT
      DATA PI/3.1415927/
      IF (EPBAR .LE. 0) THEN
      H=H0
      ELSE
       IF (EPBAR .GT. 0 .AND. EPBAR .LE. EPBARL) THEN
        H=H0+(HL-H0)*SIN(PI*((EPBAR/EPBARL)**Q)/2)
       ELSE
        H=-AL*(EPBAR-EPBARL)+HL
       ENDIF
      ENDIF
      IF (H .LT. 0) H = 0
      RETURN
      END
```

```
C DETER3.FOR
C DETER3 CALCULATES THE DETEMIONANT OF A 3X3 MATRIX
C
C
      SUBROUTINE DETER3(A,D)
      IMPLICIT REAL*8 (A-H,P-Z)
      DIMENSION A(3,3)
C
C
C
      B=A(1,1)*A(2,2)*A(3,3)
      C=A(1,2)*A(2,3)*A(3,1)
      D=A(1,3)*A(2,1)*A(3,2)
      E=A(3,1)*A(2,2)*A(1,3)
      F=A(3,2)*A(2,3)*A(1,1)
      G=A(3,3)*A(2,1)*A(1,2)
C
      D=B+C+D-E-F-G
      RETURN
      END
```

```
C DETER4.FOR
C DETER4 CALCULATES THE DETEMIONANT OF A 4X4 MATRIX
C
C
      SUBROUTINE DETER4(A,D)
      IMPLICIT REAL*8 (A-H,P-Z)
      DIMENSION A(4,4)
C
C
C
      B=A(2,2)*A(3,3)*A(4,4)
      C=A(2,3)*A(3,4)*A(4,2)
      D=A(2,4)*A(3,2)*A(4,3)
      E=A(4,2)*A(3,3)*A(2,4)
      F=A(4,3)*A(3,4)*A(2,2)
      G=A(4,4)*A(3,2)*A(2,3)
C
      D1=A(1,1)*(B+C+D-E-F-G)
C
C
C
      B=A(2,1)*A(3,3)*A(4,4)
      C=A(2,3)*A(3,4)*A(4,1)
      D=A(2,4)*A(3,1)*A(4,3)
      E=A(4,1)*A(3,3)*A(2,4)
      F=A(4,3)*A(3,4)*A(2,1)
      G=A(4,4)*A(3,1)*A(2,3)
C
      D2=-A(1,2)*(B+C+D-E-F-G)
C
C
      B=A(2,1)*A(3,2)*A(4,4)
      C=A(2,2)*A(3,4)*A(4,1)
      D=A(2,4)*A(3,1)*A(4,2)
      E=A(4,1)*A(3,2)*A(2,4)
      F=A(4,2)*A(3,4)*A(2,1)
      G=A(4,4)*A(3,1)*A(2,2)
C
      D3=A(1,3)*(B+C+D-E-F-G)
C
C
      B=A(2,1)*A(3,2)*A(4,3)
      C=A(2,2)*A(3,3)*A(4,1)
      D=A(2,3)*A(3,1)*A(4,2)
      E=A(4,1)*A(3,2)*A(2,3)
      F=A(4,2)*A(3,3)*A(2,1)
      G=A(4,3)*A(3,1)*A(2,2)
C
      D4=-A(1,4)*(B+C+D-E-F-G)
C
C
      D=D1+D2+D3+D4
      RETURN
      END
```

SELECTED BIBLIOGRAPHY

P. W. Abels and C. H. Hu "Flexural Microcracking in Unreinforced Concrete Beams," ACI Journal, Oct 71, Vol. 68, pp. 779-786

S. Ahmad and S. P. Shah "Complete Triaxial Stress-Strain Curves for Concrete," North Western University, Department of Civil Engineering, Evanston IL.

K. M. Alexander, J. Wardlaw, and D. J. Gilbert "Aggregate-Cement Bond, Cement Paste Strength and the Strength of Concrete," Proceedings of the International Conference on "The Structure of Concrete," London, September 1965, pp. 59-81

N. McN. Alford, G. W. Groves, and D. D. Double "Physical Properties of High Strength Cement Pastes," Cement and Concrete Research, 1982, Vol. 12, pp. 349-358

J. R. F. Arthur "Industrial Radiography in Soil Mechanics, "British Journal of Non-destructive Testing, Vol. 29, No. 1, Jan 1977, pp. 9-13

K. Asaga and D. M. Roy "Rheological Properties of Cement Mixes: IV. Effects of Superplasticizers on Viscosity and Yield Stress," Cement and Concrete Research, 1980, Vol. 10, pp. 287-295

G. A. Balmer "Shearing Strength of Concrete Under High Triaxial Stress - Computation of Mohr's Envelope as a Curve," Structural Research Laboratory Report No. SP-23, U.S. Department of the Interior, Bureau of Reclamation, 28 Oct 1949, 26 pp.

G. A. Balmer "Strength and Elastic Properties of Black Canyon Dam Concrete and Rock - Boise Project, Idaho," Concrete Laboratory Report No. Sp-36, U.S. Department of the Interior, Bureau of Reclamation, 24 Nov 1952, 27 pp.

G. A. Balmer "Shear Strength and Elastic Properties of Soil-Cement Mixtures under Triaxial Loading," Proceedings of the ASTM, Vol. 58, 1958, pp. 1187-1204

J. P. Bardet "Orientation of Shear Bands in Frictional Soils," Journal of Engineering Mechanics, Vol. 117, No. 7, July 1991, pp. 1466-1484

Z. P. Bazant "Recent Advances in Failure Localization and Nonlocal Models," Proceeding of the International Conference on "Micro Mechanics of Failure of Quasi-Brittle Materials," ed. S. P. Shah, S. E. Swartz, and M. L. Wang, June 1990, pp. 12-129

P. Bertacchi and R. Bellotti, "Experimental Research on Deformation and Failure of Concrete Under Triaxial Loads," RILEM international symposium , Cannes, 1972, "The deformation and the Rupture of Solids Subjected to Multiaxial Stresses", pp. 37-52

D. Bigoni and T. Hueckel "Uniqueness and Localization-I. Associative and Non-Associative ElastoPlasticity," Int. J. Solids Structures, Vol. 28, No. 2, 1991, pp. 197-213

D. Bigoni and T. Hueckel "Uniqueness and Localization-II. Coupled ElastoPlasticity," Int. J. Solids Structures, Vol. 28, No. 2, 1991, pp. 215-224

D. L. Bloem and R. D. Gaynor "Effects of Aggregate Properties on Strength of Concrete," Journal of the ACI, October 1963, Vol. 60, pp. 1429-1454

W. F. Brace "Brittle Fracture of Rocks," Proceedings of the International Conference on the "State of Stress in the Earth's Crust," 1964, pp. 111-174

O. Buyukozturk, A. H. Nilson, and F. O. Slate "Stress-Strain Response and Fracture of a Concrete Model in Biaxial Loading," ACI Journal, August 1971, Vol. 68, pp. 590-599

S. Chatterji, N. Thaulow, and P. Christensen "Formation of Shrinkage Cracks in Thin Specimens of Cement Paste," Cement and Concrete Research, 1981, Vol. 11, pp. 155-157

S. Chatterji "Probable Mechanisms of Crack Formation at Early Ages of Concrete: A Literature Survey," Cement and Concrete Research, 1982, Vol. 12, pp. 371-376

K. T. Chau and J. W. Rudnicki "Bifurcation of Compressible Pressure-Sensitive Materials in Planes Strain Tension and Compression," J. Mech. Phys. Solids, Vol. 38, No. 6, 1990, pp. 875-898

J. Chinn and R. M. Zimmerman, "Behavior of Plan Concrete Under Various High Triaxial Compression Loading Conditions," Air Force Weapons Laboratory Technical Report No. WLTR 64-163, 10 May 1965

L. E. Clark, K. H. Gerstle, and L. G. Tulin "Effect of Strain Gradient on the Stress-Strain Curve of Mortar and Concrete," ACI Journal, September 1967, Vol. 64, pp. 580-586

W. A. Cordon and H. A. Gillespie "Variables in Concrete Aggregates and Portland Cement Paste which Influence the Strength of Concrete," Journal of the ACI, August 1963, Vol. 60, pp. 1029-1049

R. de Borst "Numerical Methods for Bifurcation Analysis in Geomechanics," Ingenieur-Archiv, Vol. 59, 1989, pp. 160-174

R. de Borst "Simulation of Localization Using Cosserat Theory," Delft University of Technology, Department of Civil Engineering, Netherlands, 1990

R. de Borst, Pankaj, and N. Bicanic "A Note on Singularity Indicators for Mohr-Coulomb Type Yield Criteria," Computers and Structures, Vol. 39, 1991, pp. 219- 220

J. Desrues and R. Chambon "Shear Band Analysis for Granular Materials: The Question of Incremental Non-Linearity," Ingenieur-Archiv, Vol. 59, 1989, pp. 187-196

S. Diamond "Very High Strength Cement-Based Materials - A prospective," Materials Research Society Symposia Proceedings, Vol. 42, "Very High Strength Cement Based Materials," ed. J. F. Young, 1985, pp. 233-243

E. Dingsoyp, T. Mosberg, and J. F. Young "Influence of Aggregates on the Strength and Elastic Modulus of High Strength Mortars Containing Microsilica," Materials Research Society Symposia Proceedings, Vol. 42, "Very High Strength Cement Based Materials," ed. J. F. Young, 1985, pp. 212-218

D. C. Drucker "A More Fundamental Approach to Stress-Strain Relations," Proc. First U.S. National Congress of Applied Mechanics, American Society of Mechanical Engineers, 1951, pp. 487-491

D. C. Drucker "Limit Analysis of Two and Three Dimensional Soil Mechanics Problems," J. Mech. Phys. Solids, Vol. 1, 1953, pp. 217-226

D. E. Dunn, L. J. LaFountain, and R. E. Jackson "Porosity Dependence and Mechanism of Brittle Fracture in Sandstones," Journal of Geophysical Research, Vol. 78, No. 14, 10 May 1973, pp. 2403-2417

R. H. Evans and M. S. Marthe "Microcracking and Stress-Strain Curves for Concrete in Tension," Materiaux et Constructions, January-February 1968, pp. 61-64

P. H. Feenstra, R. de Borst, and J.G. Rots "Numerical Study on Crack Dilitancy. I: Models and Stability Analysis," ASCE Journal of Engineering Mechanics, Vol. 117, No. 4, April 1991, pp. 733-753

R. G. Galloway, "Modeling Strain Rate Effects in Plain Concrete," Ph.D. Dissertation, University of New Mexico, May 1989

K. H. Gerstle, D. L. Linse, P. Bertacchi, M. D. Kotsovos, H. Y. Ko, J. B. Newman, P. Rossi, G. Schickert, M. A. Taylor, L. A. Traina, R. M. Zimmerman, and R. Bellotti "Behavior of Concrete Under Multiaxial Stress States," Journal of the Engineering Mechanics Division, ASCE, Dec 1980, pp. 1383-1403

J. Glucklich "Fracture of Plain Concrete," Journal of the Engineering Mechanics Division, Proceedings of the American Society of Civil Engineers, December, 1963, EM 6, pp. 127-138

J. Glucklich "The Effect of Microcracking on Time-Dependent Deformation and the Long-term Strength of Concrete," Proceedings of the International Conference on "The Structure of Concrete," London, September 1965, pp. 176-189

H. Goldstein and J. E. Wilkins, Jr. "Calculation of Penetration of Gamma Rays," U.S. Atomic Energy Comm., NYO-3075, 1954

V. S. Gopalaratnam and S. P. Shah "Softening Response of Plain Concrete in Direct Tension," Journal of the ACI, Vol. 82, 1985, pp. 310-323

J. Gramberg "The 'Ellipse-with-Notch' Theory to Explain Axial Cleavage Fracturing of Rocks," Int. Journ. Rock Mech. Min. Sci., Vol. 7, pp. 537-559

J. L. Granju and J. C. Maso "Hardened Portland Cement Pastes, Modelisation of the Micro-Structure and Evolution Laws of Mechanical Properties: I- Basic Results," Cement and Concrete Research, 1984, Vol. 14, pp. 249-256

S. J. Green and S. R. Swanson "Static Constitutive Relations for Concrete," AFWL-TR-72-244, 1973, Air Force Weapons Laboratory, Kirtland AFB, NM.

P. Grubl "Fracture Behavior of Lightweight Aggregate Concrete Under Multiaxial Compressive Stress," Materials Research Society Symposia Proceedings, Vol. 42, "Very High Strength Cement Based Materials," ed. J. F. Young, 1985, pp. 183-191

A. Grudemo "Microcracks, Fracture Mechanism, and Strength of the Cement Paste Matrix," Cement and Concrete Research, 1979, Vol. 9, pp. 19-34

R. Halmshaw "Physics of Industrial Radiology," American Elsevier Publishing Company Inc., 1966, pp. 142-143

E. A. Hansen "Real Time TV-Holography Observations of the Fracture Process Zone," Proceeding of the International Conference on "Micro Mechanics of Failure of Quasi-Brittle Materials," ed. S. P. Shah, S. E. Swartz, and M. L. Wang, June 1990, pp. 504-513

T. C. Hansen "Influence of Aggregate and Voids on the Modulus of Elasticity of Concrete, Cement Mortar, and Cement Paste," Journal of the ACI, Feb 1965, Vol. 62, pp. 193-215

T. C. Hansen and K. E. C. Nielsen "Influence of Aggregate Properties on Concrete Shrinkage," Journal of the ACI, July 1965, Vol. 62, pp. 783-793

W. C. Hansen "Porosity of Hardened Portland Cement Paste," Journal of the ACI, January 1963, vol. 60, pp. 141-155

H. C. Heard "Transition from Brittle Fracture to Ductile Flow in Solenhofen Limestone as a function of Temperature, Confining Pressure, and Interstitial Fluid Pressure," Rock Deformation, ed. Griggs and Handin, Geological Society of America, 1 March 1960, pp. 193-226

W. T. Hester "Microstructure as a Tool for Proportioning High-Strength Concrete Mixes," Materials Research Society Symposia Proceedings, Vol. 42, "Very High Strength Cement Based Materials," ed. J. F. Young, 1985, pp. 193-200

A. Hilerborg, M. Modeer, and P-E Petersson "Analysis of Crack Formation and Crack Growth in Concrete by Means of Fracture Mechanics and Finite Elements," Cement and Concrete research, 1976, Vol. 6, pp. 773-782

R. Hill "On Discontinuous Plastic States, with Special Reference to Localized Necking in Thin Sheets," Jnl. Mech. Phys. Solids, Vol. 1, 1952, pp. 19-30

R. Hill "On the Limits Set by Plastic Yielding to the Intensity of Singularities of Stress," J. Mech. Phys. Solids, Vol. 2, 1954, pp. 278-285

R. Hill "New Horizons in the Mechanics of Solids," Journal of the Mechanics and Physics of Solids, 1956, Vol. 5, pp. 66-74

R. Hill "On the Problem of Uniqueness in the Theory of a Rigid-Plastic Solid-II," Journal of the Mechanics and Physics of Solids, 1956, Vol. 5, pp. 1-8

R. Hill "On the Problem of Uniqueness in the Theory of a Rigid-Plastic Solid-III," Journal of the Mechanics and Physics of Solids, 1957A, Vol. 5, pp. 153-161

R. Hill "On Uniqueness and Stability in the Theory of Finite Elastic Strain," Journal of the Mechanics and Physics of Solids, 1957B, Vol. 5, pp. 229-241

R. Hill "Stability of Rigid-Plastic Solids," Journal of the Mechanics and Physics of Solids, 1957C, Vol. 6, pp. 1-8

R. Hill "A Generalized Theory of Uniqueness and Stability in Elastic-Plastic Solids," Journal of the Mechanics and Physics of Solids, 1958, Vol. 6, pp. 236-249

R. Hill "Some Basic Principles in the Mechanics of Solids without a Natural Time," J. Mech. Phys. Solids, Vol. 7, 1959, pp. 209-225

R. Hill "Uniqueness in General Boundary-Value Problems For Elastic or Inelastic Solids," J. Mech. Phys. Solids, Vol. 9, 1961, pp. 114-130

R. Hill "Uniqueness Criteria and Extremum Principles in Self-Adjoint Problems of Continuum Mechanics," J. Mech. Phys. Solids, Vol. 10, 1962, pp. 185-194

R. Hill "Constitutive Laws and Waves in Rigid/Plastic Solids," Journal of the Mechanics and Physics of Solids, 1962, Vol. 10, pp. 89 to 98

R. Hill "Eigenmodal Deformations in Elastic/Plastic Continua," J. Mech. Phys. Solids, Vol. 15, 1967, pp. 371-386

R. Hill "On Constitutive Inequalities for Simple Materials - I," J. Mech. Phys. Solids, Vol. 16, 1968, pp. 299-242

R. Hill "On Constitutive Inequalities for Simple Materials - II," J. Mech. Phys. Solids, Vol. 16, 1968, pp. 315-322

R. Hill and J. W. Hutchinson " Bifurcation Phenomena in the Plane Tension Test," Journal of the Mechanics and Physics of Solids, 1975, Vol. 23, pp. 239 to 264

A. Hoenig "The Behavior of a Flat Elliptical Crack in an Anisotropic Elastic Body," Journal of Solid Structures, 1978, Vol. 14, pp. 925-934

H. Horii and S. Nemat-Nasser "Overall Moduli of Solids with Microcracks: Load-induced Anisotropy," Journal Mech. Phys. Solids, Vol. 31, 1983, No. 2, pp. 155-171

H. Horii and S. Nemat-Nasser "Compression-Induced Microcrack Growth in Brittle Solids: Axial Splitting and Shear Failure," Journal of Geophysical Research, Vol. 90, 10 March 1985, No. B4, pp. 3105-3125

H. Horii and S. Nemat-Nasser "Brittle Failure in Compression: Splitting, Faulting and Brittle-Ductile Transition," Phil. Trans. Royal Soc. London., Vol. 319, 1986, pp. 337-374

H. Horii and S. Nirmalendran "Roles of Microcracking and Bridging in Fracture of Quasi-Brittle Materials," Proceeding of the International Conference on "Micro Mechanics of Failure of Quasi-Brittle Materials," ed. S. P. Shah, S. E. Swartz, and M. L. Wang, June 1990, pp. 569-578

E. R. Hoskins "The Failure of Thick-walled Hollow Cylinders of Isotropic Rock," Int. Journal Rock Mech. Min. Sci., Vol. 6, pp. 99-125

T. T. C. Hsu, F. O. Slate, G. M. Sturman, and G. Winter "Microcracking of Plain Concrete and the Shape of the Stress-Strain Curve," Journal of the ACI, February 1963, Vol. 60, pp. 209-223

T. T. C. Hsu "Mathematical Analysis of Shrinkage Stresses in a Model of Hardened Concrete," Journal of the ACI, March 1963, Vol. 60, pp. 371-388

T. T. C. Hsu and F. O. Slate "Tensile Bond Strength Between Aggregate and Cement Paste or Mortar," Journal of the ACI, April 1963, Vol. 60, pp. 465-485

R. E. Hunt, " Geotechnical Engineering Techniques and Practices," McGraw-Hill Book Co., 1986

M. A. Iqbal and E. M. Krokosky "Interaction Stresses In Composite Systems," Journal of the Engineering Mechanics Division, Proceedings of the ASCE, December 1970, EM 6, pp. 825-845

R. Jones "Cracking and Failure of Concrete Test Specimens Under Uniaxial Quasi-Static Loading" Proceedings of the International Conference on "The Structure of Concrete," London, September 1965, pp. 125-130

V. Kadlecek and Z. Spetla "Effect of Size and Shape of Test Specimens on the Direct Tensile Strength of Concrete," RELIM Bulletin, September 1967, No 36, pp. 175-187

M. F. Kaplan "Flexural and Compressive Strength of Concrete as Affected by the Properties of Coarse Aggregates," Journal of the ACI, Vol. 55, May 1959, pp. 1193-1208

M. F. Kaplan "Strains and Stresses of Concrete at Initiation of Cracking and Near Failure," Journal of the ACI, July 1963, Vol. 60, pp. 853-879

O. A. Kayyali "Porosity and Compressive Strength of Cement Paste in Sulphate Solution," Cement and Concrete Research, vol. 19 , 1989, pp. 423-433

K. Kendall and J. D. Birchall "Porosity and its Relationship to the Strength of Hydraulic Cement Pastes," Materials Research Society Symposia Proceedings, Vol. 42, "Very High Strength Cement Based Materials," ed. J. F. Young, 1985, pp. 143-148

L. I. Knab, H. N. Walker, J. R. Clifton, and E. R. Fuller, Jr. " Fluorescent Thin Section to Observe the Fracture Zone in Mortar," Cement and Concrete Research, 1984, Vol. 14, pp. 339-344

D. Kolymbas and G. Rombach "Shear Band Formation in Generalized Hypoelasticity," Ingenieur-Archiv, Vol. 59, 1989, pp. 117-186

V. I. Kondaurov, L. V. Nikitin, and E. I. Ryzhak "Damage and Instability in Geomaterials," Ingenieur-Archiv, Vol. 59, 1989, pp. 245-252

M. D. Kotsovos "Effect of Testing Techniques on the Post-Ultimate Behavior of Concrete in Compression," Materiaux et Constructions, 1983, vol. 16, No. 91, pp. 3-12

D. Krajcinovic "Damage Mechanics," Mechanics of Materials, Vol. 8, 1989, pp. 117-197

H. Kupfer, H. K. Hilsdorf, and H. Rusch "Behavior of Concrete Under Biaxial Stresses," ACI Journal, August 1969, vol. 66, pp. 656-666

J. F. Labuz and J. M. Bridell, "Reducing Frictional Constraint in Compression Testing Through Lubrication," paper submitted to Experimental Mechanics on 9/3/91

P. V. Lade "Experimental Observations of Stability, Instability, and Shear Planes in Granular Materials," Ingenieur-Archiv, Vol. 59, 1989, pp. 114-123

K. E. Loland "Continuous Damage Model for Load-Response Estimation of Concrete," Cement and Concrete Research, 1980, Vol. 10, pp. 395-402

F. D. Lydon and A. H. Mahawish "Strength and Permeability Results from a Range of Concretes," Cement and Concrete Research, Vol. 19, 1989, pp. 366-376

J. Mandel "Conditions de Stabilité at Postulat de Drucker," IUTAM Symposium Grenoble 1964 on Rheology and Soil Mechanics, eds. J. Kravtchenko and P. M. Sirieys, Springer-Verlag, 1966, pp. 58-68

B. K. Marsh and R. L. Day "Some Difficulties in the Assessment of Pore-Structure of High Performance Blended Cement Pastes," Materials Research Society Symposia Proceedings, Vol. 42, "Very High Strength Cement Based Materials," ed. J. F. Young, 1985, pp. 114-121

T. Maruyama "Stress Fields in the Neighborhood of a Crack," Bulletin of the Earthquake Research Institute, Vol. 47 (1969), PP. 1-29

R. C. McMaster, The Society for Nondestructive Testing "Nondestructive Testing Handbook," 1959, Vol.1, pp. 13.17-15.39

M. D. Meiser and R. E. Tressler "Failure Modes in Low Density Aluminus Cement Bonded Composites," Cement and Concrete Research, 1982, Vol. 12, pp. 279-288

B. L. Meyers, F. O. Slate, G. Winter "Relationship Between Time-Dependent Deformation and Microcracking of Plain Concrete," ACI Journal, January 1969, pp. 60-68

J. P. Miles "Bifurcation in Plastic Flow Under Uniaxial Tension," J. Mech. Phys. Solids, Vol. 19, 1971, pp. 89-102

J. P. Miles "The Initiation of Necking in Rectangular Elastic/Plastic Specimens Under Uniaxial and Biaxial Tension," J. Mech. Phys. Solids, Vol. 23, 1975, pp. 197-213

L. L. Mills "A Study of the Strength of Concrete Under Combined Compressive Loads," Ph.D. Dissertation, 1967, New Mexico State University, Las Cruces, New Mexico

L. L. Mills and R. M. Zimmerman "Compressive Strength of Plain Concrete Under Multiaxial Loading Conditions," ACI Journal, October 1970, Vol. 67, pp. 802-807

S. Mindess and S. Diamond "A Preliminary SEM Study of Crack Propagation in Mortar," Cement and Concrete Research, 1980, Vol. 10, pp. 509-519

S. Mindess "The Effect of Specimen Size on the Fracture Energy of Concrete," Cement and Concrete Research, 1984, Vol. 14, pp. 431-436

K. Mogi "Deformation and Fracture of Rocks Under Confining Pressure (2) Elasticity and Plasticity of Some Rocks," Bulletin of the Earthquake Research Institute, Vol. 43 (1965), pp. 349-379

K. Mogi "Pressure Dependence of Rock Strength and Transition from Brittle Fracture to Ductile Flow," Bulletin of the Earthquake Research Institute, Vol. 44 (1966), pp. 215-232

S. A. Murrell "The Effect of Triaxial Stress Systems on the Strength of Rocks at Atmospheric Temperatures," Geophys. J. R. Astron. Soc., Vol. 10, 1965, pp. 231-281

M. K. Neilsen and H. L. Schreyer "Bifurcations in Elastic-Plastic Materials," The International Journal of Solids and Structures, Vol. 30, N0. 4, 1993, pp. 521-544

M. K. Neilsen and H. L. Schreyer "Bifurcations in Elastic-Damaging Materials," Damage Mechanics and Localization, AMD-Vol. 142, Edited by J. W. Ju and K. C. Valanis, The American Society of Mechanical Engineers, NY, NY, 1992, pp. 109-123

S. Nemat-Nasser, M. Obata "A Microcrack Model of Dilatancy in Brittle Materials," Journal of Applied Mechanics, Vol. 55, March 1988

J. B. Newman "Apparatus for Testing Concrete Under Multiaxial States of Stress," Magazine of Concrete Research, December 1974, Vol. 26, No. 89, pp. 229-238

K. Newman "Criteria for the Behaviour of Plain Concrete Under Complex States of Stress," Proceedings of the International Conference on "The Structure of Concrete," London, ed. A.E. Brooks and K. Newman, September 1965, pp. 255-274

M. Ortiz "A Constitutive Theory for the Inelastic Behavior of Concrete," Mechanics of Materials, Vol. 4, 1985, pp. 67-93

N. S. Ottosen and K. Runesson "Properties of Discontinuous Bifurcation Solutions in Elasto-Plasticity," Int. Journ. Solids Structures, 1991, Vol. 27, No. 4, pp. 401-421

N. S. Ottosen and K. Runesson "Discontinuous Bifurcations in a Non-Associated Mohr Material," Mechanics of Materials, 1991B, pp. 255-265

R. Palaniswamy and S. P. Shah "Fracture and Stress-Strain Relationship of Concrete Under Triaxial Compression," Journal of the Structures Division, ASCE, May 1974, ST5, pp. 901-916

R. Palaniswamy and S. P. Shah "Deformation and Failure of Hardened Cement Paste Subjected to Multiaxial Stresses," Proceedings of the RILEM International Symposium: "The Deformations and the Rupture of Solids Subjected to Multiaxial Stresses", 1972, pp. 169-179

M. S. Patterson "Experimental Rock Deformation: The Brittle Field," Springer-Velag, Berlin Heidelberg New York, 1978

A. Pauw "Static Modulus of Elasticity of Concrete as Affected by Density," Journal of the ACI, Dec 1960, pp. 679-683

D. Peric "Localized Deformation and Failure Analysis of Pressure Sensitive Granular Materials," Ph.D. Dissertation, University of Colorado, July 1990

P-E. Petersson "Fracture Energy of Concrete: Method of Determination," Cement and Concrete Research, 1980, Vol. 10, pp. 78-89

P-E. Petersson "Fracture Energy of Concrete: Practical Performance and Experimental Results," Cement and Concrete Research, 1980, Vol. 10, pp. 91-101

P-E. Petersson "Crack Growth and Development of Fracture Zones in Plain Concrete and Similar Materials," Report #: LUTVDG/(TVBM-1006)/1-174/(1981), Lund Institute of Technology, Sweden, 1981

S. Popovics "Effect of Porosity on the Strength of Concrete," Journal of Materials, Vol. 4, No. 2, June 1969, pp. 356-371

S. Popovics "New Formulas for the Prediction of the Effect of Pporosity on Concrete Strength," ACI Journal, March-April 1985, vol. 82, pp. 136-146

B. Raniecki "Uniqueness Criteria in Solids with Non-Associated Plastic Flow Laws at Finite Deformations," Bulletin de L'Academie Polonaise Des Sciences, 1979, Vol. 27, pp. 391-399

B. Raniecki, and O. T. Bruhns "Bounds to Bifurcation Stresses in Solids with Non-Associated Plastic Flow Law at Finite Strain," J. Mech. Phys. Solids, Vol. 29, No. 2, 1981, pp. 153-172

H. W. Reinhardt, H. A. W. Cornelissen "Post-Peak Cyclic Behavior of Concrete in Uniaxial Tensile and Alternating Tensile and Compressive Loading," Cement and concrete Research, 1984, Vol.14, pp. 263-270

L. Resende "A Damage Mechanics Constitutive Theory for the Inelastic Behavior of Concrete," Computer Methods in Applied Mechanics and Engineering, 1987, Vol. 60, pp. 57-93

J. R. Rice "The Localization of Plastic Deformation," Theoretical and Applied Mechanics, 14th IUTAM Congress, ed. W. T. Koiter North-Holland Pub. Co., 1976, pp. 207-220

J. R. Rice and J. W. Rudnicki "A Note on Some Features of the Theory of Localization of Deformation," Int. J. Solids Structures, Vol. 16, 1980, pp. 597-605

F. E. Richart, A. Brandtzaeg, and R. L. Brown, " A Study of the Failure of Concrete Under Combined Compressive Stresses," University of Illinois Engineering Experiment Station, Bulletin No. 185, November 1928

K. H. Roscoe, J. R. F. Arthur, R. G. James "The Determination of Strains in Soils By an X-Ray Method," Civil Engineering and Public Works Review, July 1963, pp. 873-876

I. Rosenthal and J. Glucklich "Strength of Plain Concrete Under Biaxial Stress," ACI Journal, Nov. 1970, Vol. 67, pp. 903-914

D. M. Roy and G. M. Idorn "Relation Between Strength, Pore Structure and Associated Properties of Slag-Containing Cementitious Materials," Materials Research Society Symposia Proceedings, Vol. 42, "Very High Strength Cement Based Materials," ed. J. F. Young, 1985, pp. 114-121

J. W. Rudnicki and J. R. Rice "Conditions for the Localization of Deformation in Pressure-Sensitive Dilatant Materials," J. Mech. Phys. Solids, Vol. 23, 1975, pp. 371-394

C. G. Sammis and M. F. Ashby "The failure of Brittle Porous Solids Under Compressive Stress States," Acta Metall, 1986, Vol. 34, No. 3, pp. 511-526

S. D. Santiago and H. K. Hilsdorf, "Fracture Mechanisms of Concrete Under Compressive Loads," Cement and Concrete Research, 1973, Vol. 3, pp. 363-388

R. Scavuzzo, H. V. Cornelius, K. H. Gerstle, H. Y. Ko, T. Stankowski "Simple Formulation of Concrete Response to Multiaxial load Cycles," Proc. Int. Conf. "Constitutive Laws for Engineering Materials," 1983, pp. 421-426

R. Scavuzzo, T. Stankowski, K. H. Gerstle, H. Y. Ko "Stress-Strain Curves for Concrete under Multiaxial Load Histories," Department of Civil Engineering, University of Colorado, NSF Grant CME 80-010508, August 1983

G. Schickert "On the Influence of Different Load Application Techniques on the Lateral Strain and Fracture of Concrete," Cement and Concrete Research, 1973, Vol. 3, pp. 487-494

H. L. Schreyer and J. E. Bean "Plasticity Models for Soils, Rock and Concrete," Report for the New Mexico Engineering Research Institute, University of New Mexico, 1987

H. L. Schreyer "Analytical Solutions for Nonlinear Strain-Gradient Softening and Localization," Journal of Applied Mechanics, Sept 1990, Vol. 57, pp. 522-528

H. L. Schreyer and M. K. Neilsen "Analytical and Numerical Tests for Loss of Material Stability," International Journal for Numerical Methods in Engineering, To appear, 1996

S. P. Shah and F. O. Slate "Internal Microcracking, Mortar-Aggregate Bond and the Stress-Strain Curve of Concrete," Proceedings of the International Conference on "The Structure of Concrete," London, September 1965, pp. 82-92

S. P. Shah and G. Winter "Inelastic Behavior and Fracture of Concrete," Journal of the ACI, September 1966, pp. 925-930

S. P. Shah and S. Chandra "Fracture of Concrete Subjected to Cyclic and Sustained Loading," ACI Journal, October 1970, pp. 816-825

S. P. Shah and F. J. McGarry "Griffith Fracture Criterion and Concrete," Journal of the Engineering Mechanics Division, Proceedings of the ASCE, December 1971, EM 6, pp. 1663-1676

S. P. Shah and R. Sankar "Internal Cracking and Strain-Softening Response of Concrete under Uniaxial Compression," ACI Mat. Journal, May-June 1987, Vol. 84, pp. 200-212

G. C. Sih, et al "Fracture Mechanics of Concrete: Material Characterization and Testing," ed. by A. Carpinteri and A. R. Ingraffea, 1984

F. O. Slate and S. Olefski "X-Rays for Study of Internal Structure and Microcracking of Concrete," Journal of the ACI, May 1963, Vol. 60, pp. 575-587

Z. Spetla and V. Kadlecek "Effect of the Slenderness on Direct Tensile Strength of Concrete Cylinders and Prisms," RELIM Bulletin, December 1966, No 33, pp. 403-412

D. C. Spooner and C. D. Pomeroy "Energy Dissipation in the Compression of Cement Paste and Concrete," Cement and Concrete Research, 1973, Vol. 3, pp. 481-486

D. C. Spooner, C. D. Pomeroy, and J. W. Dougill " Damage and Energy Dissipation in Cement Pastes in Compression," Magazine of Concrete Research, March 1976, Vol. 28, No. 94, pp. 21-29

D. C. Spooner and J. W. Dougill "A Quantitative Assessment of Damage Sustained in Concrete During Compressive Loading," Magazine of Concrete Research, September 1975, Vol. 27, No. 92, pp. 151-160

T. Stankowski and K. H. Gerstle "Simple Formulation of Concrete Behavior under Multiaxial Load Histories," ACI Journal, March-April 1985, pp. 213-221

E. Stein, R. Lammering, and W. Wagner "Stability Problems in Continuum Mechanics and Their Numerical Computation," Ingenieur-Archiv, Vol. 59, 1989, pp. 89-105

B. Storakers "Bifurcation and Instability Modes in Thick-Walled Rigid-Plastic Cylinders Under Pressure," J. Mech. Phys. Solids, Vol. 19, 1971, pp. 339-351

S. Storen and J. R. Rice "Localized Necking in Thin Sheets," J. Mech. Phys. Solids, Vol. 23, 1975, pp. 421-441

P. C. Strange and A. H. Bryant "The Role of Aggregate in the Fracture of Concrete," Journal of Material Science, 1979, Vol. 14, pp. 1863-1868

P. Stroeven "Geometric Probability Approach to the Examination of Microcracking in Plain Concrete," Journal of Material Science, 1979, Vol. 14, pp. 1141-1151

L. Struble and J. Skalny "A Review of the Cement-Aggregate Bond," Cement and Concrete Research, 1980, Vol. 10, pp. 277-286

G. M. Sturman (et al), S. P. Shah, and G. Winter "Effects of flexural Strain Gradients on the Microcracking and Stress-Strain Behavior of Concrete," Journal of the ACI, July 1965, Vol. 62, pp. 805-821

R. N. Swamy and C. V. S. Kameswara Rao "Fracture Mechanism in Concrete Systems under Uniaxial Loading," Cement and Concrete Research, 1973, Vol. 3, pp. 413-427

S. E. Swartz, "Dye Techniques to Reveal the Fracture Surface Concrete in Mode I," Experimental Techniques, May/June 1991, pp. 29-34

R. B. Tait (et al), S. Diamond, S. A. S. Akers, and S. Mindess "Microprocess Failure Zone Studies Using an in Situ Scanning Electron Microscope Double Torsion Test Facility," Proceeding of the International Conference on "Micro Mechanics of Failure of Quasi-Brittle Materials," ed. S. P. Shah, S. E. Swartz, and M. L. Wang, June 1990, pp. 33-42

C. Tashiro and H. Urushima "Strength Development and Pore Size Distribution of Cement Paste Cured with High Hydrostatic Pressure," Cement and Concrete Research, 1984, Vol. 14, pp. 318-322

J. J. Taylor "Application of Gamma Ray Build-up Data to Shield Design," WAPD Memo, RM-217, 25 January 1954

P. S. Theocaris and J. N. Prassianakis "The Mohr Envelope of Failure for Concrete: a Study of Its Tension-Compression Part," Magazine of Concrete Research, June 1974, Vol. 26, no. 87, pp. 73-82

J. M. Torrenti (et al), J. Desrues, P. Acker, C. Boulay "Application of Stereophotogrammetry to the Strain Localization in Concrete Compression," Proc. of the France-US workshop on " Strain Localization and Size Effect Due to Cracking and Damage," 1988

V. Tvergaard, A. Needleman, and K. K. Lo "Flow Localization in the Plane Strain Tensile Test," J. Mech. Phys. Solids, Vol. 29, No. 2, 1981, pp. 115-142

J. G. M. Van Mier "Strain-Softening of Concrete Under Multiaxial Loading Conditions," Ph.D. Dissertation , 1984, University of Eindhoven, The Netherlands.

J. G. M. Van Mier "Internal Crack Detection in Single Edge Notched Concrete Plates Subjected to Uniform Boundary Displacement," Proceeding of the International Conference on "Micro Mechanics of Failure of Quasi-Brittle Materials," ed. S. P. Shah, S. E. Swartz, and M. L. Wang, June 1990a, pp. 33-42

J. G. M. Van Mier "Fracture Process Zone in Concrete: A Three Dimensional Growth Process," 8th Bianual European Conference on Fracture, "Fracture Behavior and Design Of Materials and Structures," Torino, Italy, Oct 1990b, pp. 567-572

I. Vardoulakis "Shear-Banding and Liquefaction in Granular Materials on the Basis of a Cosserat Continuum Theory," Ingenieur-Archiv, Vol. 59, 1989, pp. 106-113

I. Vardoulakis and B. Graf, "Calibration of Constitutive Models for Granular Materials Using Data form Biaxial Experiments," Geotechnique, Vol. 35, No. 3, 1985, pp. 288-317

P. A. Vermeer "The Orientation of Shear Bands in Biaxial Tests," Geotechnique, Vol. 40, No. 2, 1990, pp. 230-236

W. D. Vile "The strength of Concrete Under Short-term Static Biaxial Stress," Proceedings of the International Conference on "The Structure of Concrete," London, September 1965, pp. 275-288

R. A. Vonk, H. S. Rutten, J. G. M. Van Mier, H. J. Fijnemen "Size Effects in Softening of Concrete Loaded in Compression," 8th Bianual European Conference on Fracture, "Fracture Behavior and Design Of Materials and Structures," Torino, Italy, Oct 1990, pp. 767-772

S. Walker and D. L. Bloem "Effect of Aggregate Size on Properties of Concrete," Journal of the ACI, Sept 1960, pp. 283-298

P. F. Walsh "Crack Initiation in Plain Concrete," Magazine of Concrete Research, March 1976, Vol.28, No. 94, pp. 37-41

M. L. Wang (et al), H. L. Schreyer, and C. A. Rutland "Internal Deformation Measurements with the Use of Real Time X-Rays," Proceeding of the International Conference on "Micro Mechanics of Failure of Quasi-Brittle Materials," ed. S. P. Shah, S. E. Swartz, and M. L. Wang, June 1990, pp. 81-94

W. R. Wawersik and W. F. Brace "Post-Failure Behavior of a Granite and Diabase," Rock Mechanics, Vol. 3, 1971, pp. 61-85

W. R. Wawersik, J. W. Rudnicki, W. A. Olsson, D. J. Holcomb, and K. T. Chau "Localization of Deformation in Brittle Rock: Theoretical and Laboratory Investigations," Proceeding of the International Conference on "Micro Mechanics of Failure of Quasi-Brittle Materials," Ed by S. P. Shah, S. E. Swartz, and M. L. Wang, June 1990, pp. 115-124

W. R. Wawersik and C. Fairhurst "A Study of Brittle Rock Fracture in Laboratory Compression Experiments," Int. Journ. Rock Mech. Min. Sci., Vol. 7, 1970, pp. 561-575

M. Wecharatana and S. P. Shah " Double Torsion Tests for Studying Slow Crack Growth of Portland Cement Mortar," Cement and Concrete Research, 1980, Vol. 10, pp. 833-844

G. B. Welch "Factors Influencing the Tensile Strains and Flexural Failure of Plain Concrete," Proceedings of the International Conference on "The Structure of Concrete," London, September 1965, pp. 525-533

G. B. Welch "Tensile strains in unreinforced Concrete Beams," Magazine of Concrete Research, March 1966, Vol. 18, No. 54, pp. 9-18

R. M. Williams and J. C. Uy "Ceramic Material Characterization," Proceedings of the Fifth Army Materials Technology Conference Held March 21-25 1977, "Ceramics for High Performance Applications - II," ed. by J. J. Burke, E. N. Lenoe, R. N. Katz,, , Brook Hill Pub. Co., 1978, pp. 162-167

R. K. S. Wong and J. R. F. Arthur "Determination and Uses of Strain Distributions in Sand Samples," Geotechnical Testing Journal, GTJODJ, Vol. 8, No. 3, Sept 1985, pp. 101-110

S. Yazdani "A Unified Plasticity and Damage Mechanics Model for Plain Concrete," Ph.D. Dissertation, 1987, The University of New Mexico

S. Yazdani and H. L. Schreyer "An Anisotropic Damage Model with Dilatation for Concrete," Mechanics of Materials, Vol. 7, 1988, pp. 231-244

V. A. Yerlici "Behavior of Plain Concrete Under Axial Tension," Journal of the ACI, August 1965, Vol. 62, pp. 987-991

H. Yiun-Yuan, D. Wei, and L. Ping "The Influence of Pore-Structure on the Compressive Strength of Hardened Cement Paste," Materials Research Society Symposia Proceedings, Vol. 42, "Very High Strength Cement Based Materials," ed. J. F. Young, 1985, pp. 123-131

J. W. Zaitsev and F. H. Wittmann "Fracture of Porous Viscoelastic Materials Under Multiaxial State of Stress," Cement and Concrete Research, 1973, Vol. 3, pp. 389-395

Y. B. Zaitev and F. H. Wittmann "Simulation of Crack Propagation and Failure of Concrete," Materiaux et Constructions, 1981, Vol. 14, No. 83, pp. 357-364

A. J. Zielinski "Model for Tensile Fracture of Concrete at High Rates of Loading," Cement and Concrete Research, 1984, Vol.14, pp. 215-224

A. J. Zielinski, H. W. Reinhardt "Stress-Strain Behavior of Concrete and Mortar at High Rates of Tensile Loading," Cement and Concrete Research, 1982, Vol. 12, pp. 309-319

R. M. Zimmerman "The effects of various types of lateral restraint on the Triaxial Behavior of Plain Concrete", Ph.D. dissertation , University of Colorado, 1965.

R.M. Zimmerman, "Major Factors Affecting the Multiaxial Compressive Strength of Plain Concrete," Proceedings of the RILEM international symposium: "The Deformations and the Rupture of Solids Subjected to Multiaxial Stresses", 1972, pp. 257-272

R. M. Zimmerman and L. A. Traina, "Strength and Deformation Response of Concrete Under Multiaxial Loadings - Cooperative Project", Final report # ENG 74 - 12097 for National Science Foundation, May 1977